INVESTIGATION OF MAGNETIC PROPERTIES OF ELECTRICAL STEEL AND TRANSFORMER CORE AT HIGH FLUX DENSITIES

A dissertation submitted to The University of Manchester

for the degree of PhD

in the Faculty of Engineering and Physical Sciences

2015

QI TANG

SCHOOL OF ELECTRICAL AND ELECTRONIC ENGINEERING

Contents

Word count: 44,083

LIST OF TABLES

LIST OF FIGURES

Abstract

In a power transformer, the electrical steel core serves as a low reluctance path for the main magnetic flux linking primary and secondary windings. It is also one of the most costly components, whose properties are vital to design an efficient and reliable transformer. Normally, power transformers are predominantly operated within the linear portion of the core steel's magnetisation curve with the maximum flux density limited at a certain value in the knee area. Nowadays, more technical challenges from the core saturation are raised, which are caused by the geomagnetically induced currents or the normal operation of Quadrature Boosters. The substantial power losses generated at such high flux densities can lead to the core overheating and consequential thermal degradation of the surrounding insulation, and even transformer failure.

The characteristics of transformer core in deep saturation, however, are not readily available from measurements, and neither are the current IEC standards applicable above 1.8 Tesla for the measurement of magnetic properties of electrical steels owing to measurement difficulties, such as magnetic flux waveform stabilization. The simulation studies often need to extrapolate the steel's magnetisation curve to high flux densities, which brings uncertainties to the results. In addition, the industry has often adopted a conservative transformer core design due to the insufficient knowledge of core loss and temperature rise under the extreme scenario.

In order to fill the knowledge gap of electrical steels and transformer cores at high flux densities, this thesis uses an improved single strip test bench developed at Wolfson Centre for Magnetics to measure the magnetic properties of modern grain-oriented electrical steels up to 2.0 T under AC magnetisation up to 400 Hz. Based on the latest measurement results, a new single explicit expression is proposed to approximate and predict the AC magnetisation curve accurately over a wide range up to 2.0 T. A simple and accurate power loss separation algorithm is also proposed to identify the percentages of hysteresis loss, eddy current loss and anomalous loss, and predict the power loss at high flux densities.

The finite element computational method based on Maxwell's equations together with the measured magnetic properties of electrical steels up to 2.0 T leads to a more accurate predication for the distribution of magnetic flux and core losses in the power transformer core at high flux densities. The effects of core joint types, overlapping techniques, air gaps on the magnetic flux distribution are investigated in both 2D and 3D core corner joints. The distributions of the main flux, the leakage flux and the power loss in the core and the clamping structures are also obtained.

DECLARATION

No portion of the work referred to in the thesis has been submitted in support of an application for another degree or qualification of this or any other university or other institute of learning.

COPYRIGHT STATEMENT

Acknowledgement

I would first like to express my sincere appreciation to my supervisor Prof Zhongdong Wang for her valuable guidance, consistent encouragements and patience throughout my PhD project.

I would also like to thank Prof Paul Jarman, Dr Philip Anderson, and Prof Anthony Moses for their very helpful technical supports during this project and great efforts in the successful collaboration between Cardiff and Manchester University.

The financial sponsorship from National Grid is highly appreciated for the full scholarship during this PhD project.

I would like to express my deep gratitude to my parents and all friends for their continuous support during this gratifying four years at The University of Manchester.

Special thanks to my wife Minhua and the amazing little one Guanhe for your endless and powerful love!

1 INTRODUCTION

1.1 BACKGROUND

In a power transformer, the electrical steel core serves as a low reluctance path for the main magnetic flux linking primary and secondary windings. It is also one of the most costly components, whose properties are vital in order to design an efficient and reliable transformer. Normally, power transformers are predominantly operated within the linear portion, with the maximum flux density limited at a certain value in the knee area of the core steel's magnetisation curve. The basic goal of a design is to retain a reasonable amount of linearity and to stay just below flux density values that would incur excessive losses.

On March 13, 1989, two failed transformers in Hydro-Quebec led to a blackout, which was caused by the half-saturation effects of a severe geomagneticly induced current (GIC) [1]. GIC is a quasi-direct current (frequency ≤1 Hz) flowing on the earth surface, which is induced by the fluctuating ionospheric current system. It is the ground end of the complex chain starting from the solar activities [2]. Fig. 1.1 sketches the mechanism of the half-saturation caused by GIC. Affected by the quasi-DC GIC, the magnetic flux is offset, which shifts the operating point of a transformer up to the saturation region of the magnetisation curve during the positive half cycle, driving the transformer into the half-cycle saturation and drawing an enomorous reactive current. It has been recognised that refining operational guidance based on the knowledge of transformer core in saturation would possibly reduce the risk of transformer failures when GIC occurs, and this would bring a huge business benefit.

Quadrature boosters (QBs), also known as phase-shifting transformers, are very often the most economic approach for the power flow management [3], [4]. QBs allow us to control the power flow, and to optimise the load sharing across the network. The power flow control capacity of QBs is largely determined by the flux limits of the transformer core. For a 400kV, 2750 MVA QB, its power flow control capability will rise by 13.6% if the designed flux limit increases to 1.95 T from 1.9 T (see Appendix 1). Due

to the insufficient knowledge of core loss and temperature rise where a core is in deep saturation, conservative assumptions are made at the design stage of QBs for the values of flux limits. A better understanding of core saturation, will not only fully utilise the capacity of QBs, but also reduce the failure risk of QBs. It could save millions of pounds for the replacement of a 400kV 2750MVA QB alone – no mention to the other consequential costs [5].

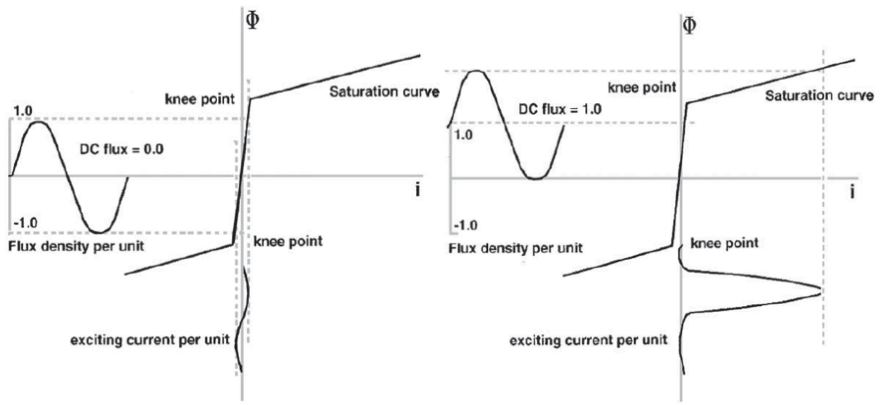

Fig. 1.1 The half-saturation issue caused by GIC [6].

The above two technical challenges together with the DC biased saturation problem of HVDC converter transformers and the saturation issue of current transformers do require us to have a better knowledge of saturation scenarios in transformer cores. As shown in Fig. 1.2, since the first power transformer was developed in the 1880s, considerable research and development has been conducted to the electrical steels in order to build transformer cores towards lower core losses, as an example, there is a constant effort to improve the manufacturing process in order to obtain higher permeability and lower losses. The major technical breakthrough is based on a better understanding of the microstructure of the steel.

The techniques (e.g. Epstein and Single Sheet Tester) to measure the magnetic properties of electrical steels are regulated in IEC standards 60404 series. Unfortunately, the properties of electrical steels in deep saturation are still not clear because the standard measurement methods are inapplicable for the flux higher than 1.8 T. Hence, the simulation studies often need to extrapolate the steel's magnetisation curve to high flux densities, which brings uncertainties to the results.

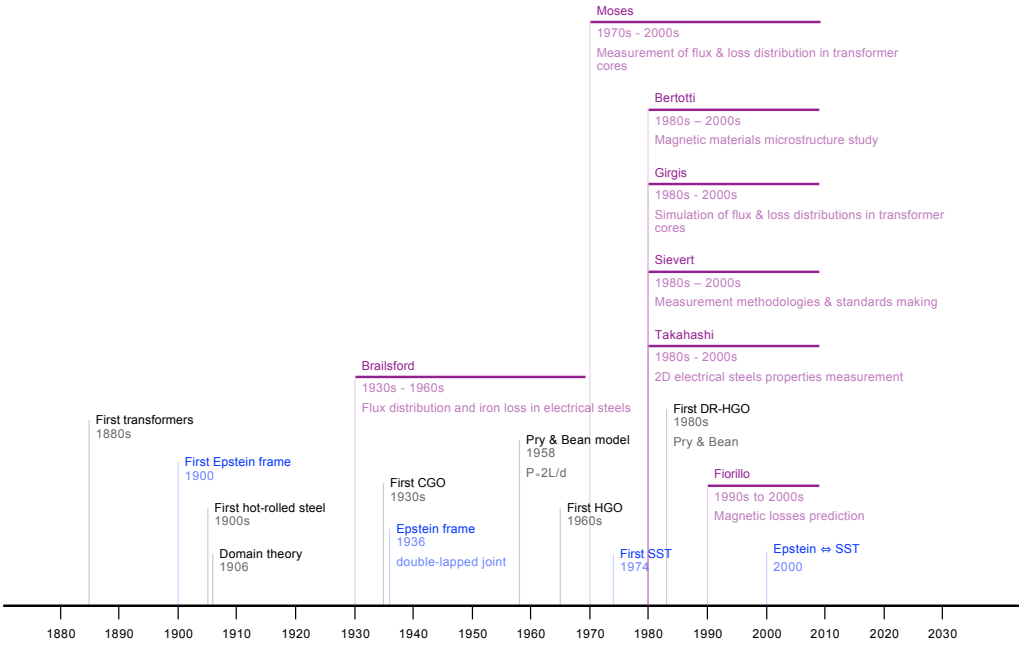

Fig. 1.2 Milestones of the invention and researches on the electrical steels.

Furthermore, at high flux densities, substantial core losses would be generated. The consequent hotspots might lead to thermal degradation of the surrounding insulation and even transformer failure. In order to forecast the positions of hotspots in deep saturation, the power loss distribution in the transformer core and its adjacent metal components must be identified. In addition to the essential magnetisation curve and the power loss characteristics of the electrical steels at high flux densities, the distributions of the magnetic flux and the power losses are also affected by the following factors: core type, core joint type, core window ratio, joint overlapping and gaps, etc.

Consequently, a good model and design for the power transformer core thus demand detailed investigations at high flux densities.

1.2 Objectives and Achievements

The main purpose of this PhD research project is to fill the knowledge gap of electrical steels and transformer cores at high flux densities. This knowledge will help build the magnetic properties of electrical steel materials and transformer core into a more accurate mathematical model for the real size transformer at high flux densities.

The specific objectives and achievements for this project are listed as follows:

- Measure magnetic properties of electrical steels at high flux densities

The fundamental information required to investigate the behaviour of power transformers at high flux densities is the magnetic properties of electrical steels including the magnetisation curve and the power loss curve. An automatic test bench (improved single strip tester) developed at Wolfson Centre for Magnetics was used to conduct the measurements on modern grain-oriented electrical steels up to 2.0 T under AC magnetisation at various frequencies. The magnetic properties of two commercial grain-oriented steel samples are successfully obtained.

- Approximate and predict the AC magnetisation curve with a single explicit function

The nonlinear magnetisation curve expressed in a single explicit function is often required by the simulation software, and it is also particularly useful to yield accurate results as well as to save computer time. Besides, a good function for the magnetisation curve will help minimise the extrapolation errors in the case that the measurement data at high flux densities are unavailable from manufacturers. Hence, a new simple explicit empirical function is proposed here. The advantages in both approximation and prediction are verified when comparing with other ten popular approximation functions for the magnetic properties in the full range of the operating flux.

- Identify the percentages of hysteresis loss, eddy current loss and anomalous loss with the power loss separation techniques, and build the expression function for the power loss curve at high flux densities

The separated power losses will benefit the prediction of the specific power loss at high flux densities and the transformer core loss studies with the finite element method. So far, the popular power loss separation algorithms have not been tested on the latest commercial grain-oriented steels, particularly at high flux densities.

Based on the measured power loss curve up to 2.0 T, the improved two frequency power loss separation algorithm is proposed here, which is simple, efficient, and accurate to give the total power loss curve together with the three loss components.

- Simulate the distributions of magnetic flux and power loss in the transformer core with finite element method

The finite element computational method based on Maxwell's equations together with the measured magnetic properties of electrical steels up to 2.0 T leads to a more accurate predication for the distribution of magnetic flux and core losses in the power transformer core at high flux densities. The effects of joint types, overlapping techniques, air gaps on the magnetic flux distribution are investigated in both 2D and 3D core corner joints. The distributions of the main flux and leakage flux in the core and adjacent metal components (clamping structures) are obtained. The power losses at each element are then calculated based on the magnetic flux values. The studies reveal that the high local power losses generated by the clamping structures would be the major source of the hotspots when the core is in deep saturation.

1.3 Outline

The outline of this thesis is briefly summarised in the following:

Chapter 1 Introduction

This chapter introduces the background for this PhD research project. The objectives and achievements for the PhD project are also highlighted.

Chapter 2 Magnetism and Magnetic Materials

This chapter first reviews the history of magnetic theory, introducing the relevant laws of physics used by power transformers. Following that, the electromagnetic terms used throughout the thesis together with their mathematical relationships are presented. The magnetisation process and hysteresis phenomenon for the ferromagnetic materials are also described.

Chapter 3 Grain-oriented Electrical Steels and Power Transformer Cores

This chapter first reviews the development of grain-oriented electrical steels. The manufacturing and processing of the grain-oriented electrical steels, together with their microstructures, are explained in detail. The core-type power transformers and its core construction process with the grain-oriented electrical steel are introduced. The different joint configurations for power transformers are also compared. The equivalent electric circuit model for power transformers is introduced, and its shortcomings under the core deep saturation scenarios are then discussed.

Chapter 4 Measurement of Magnetic Properties of Electrical Steels

This chapter first reviews the development of Epstein frame, and the standardised Epstein frame in IEC 60404-2. The measurement principle and the digital DAQ test bench with Epstein method built in the laboratory at The University of Manchester are described in detail. The measurement results using Epstein method, together with discussions on the measurement uncertainties and other issues at high flux densities are presented. Following that, the standard single sheet tester in IEC 60404-3 is introduced. An improved compact single strip tester (SST) was described, which is intensively used in this thesis to conduct the measurements of electrical steels at high flux densities. The test results validated the advantage of the improved compact SST developed at Wolfson Centre for Magnetics on the measurement of the magnetic properties in deep saturation.

Chapter 5 Electrical Steel's Magnetisation Curve Approximation and Prediction

Based on the measured magnetisation curve of the modern commercial grain-oriented (GO) electrical steels over a wide range up to 2.00 T using the proposed improved compact SST in Chapter 4, the 10 most popular approximation equations used previously are critically evaluated in this chapter. A new simple explicit empirical function is then proposed. Its performance verifications are also given in terms of both approximation and prediction capabilities, in case that the high flux density data are not available from steel manufacturers.

Chapter 6 Electrical Steel's Power Loss Separation and Prediction

This chapter first compares the popular hysteresis loss models. Jiles-Atherton model is discussed and implemented in a 3D model using COMSOL. The effect of the constant permeability assumption for the GO steel, compared with the realistic changing permeability, on the eddy current loss calculation is investigated. Using the measured power loss curves for the CGO and HGO steels up to 2.0 T from 50 Hz to 400 Hz, different power loss separation algorithms are tested and compared. In addition, a new simple power loss separation algorithm is proposed, and its performance is verified with the latest experimental results.

Chapter 7 Calculation of Distribution of Magnetic Flux and Power Loss with FEM

This chapter first conducts a brief introduction on the numerical computation with the finite element method and the commercial application package – COMSOL Multiphysics. The derivation of differential equations used in COMSOL is illustrated as well. The realistic scenario of magnetic flux transfer is considered, including the effects of stacking air gaps, joint air gaps, and the anisotropic characteristics of laminations. The magnetic flux distributions in single-step-lapped (SSL) and multi-step-lapped (MSL) joints in the 2D and 3D models are presented. The effects of higher operating flux densities on the SSL and MSL joints are investigated. In addition, an alternative method is adopted here to successfully reflect the effect of very thin air gaps, which does not produce any mesh difficulties for the 3D 45° mitred corner model. For an "imaginary" single-phase transformer core based on the Schneider 1 MVA 6.6 kV/433 V transformer, the main flux and the leakage flux in the adjacent clamping structures are presented and analysed. The distributions of power losses in both core and clamping structures are also obtained and discussed.

Chapter 8 Conclusions and Future Work

This chapter highlights the main conclusions of this thesis and provides the recommendations for the future work.

2 MAGNETISM AND MAGNETIC MATERIALS

2.1 INTRODUCTION

This chapter first reviews the history of magnetism, introducing the relevant laws of physics behind power transformers. Following that, the frequently-used electromagnetic terms with the mathematical relationships among them are presented. A detailed magnetisation process analysis on the ferromagnetic material used to build the power transformer core, based on the domain theory, is thus conducted. The hysteresis phenomenon under AC magnetisation with its inevitable power loss is also explained.

2.2 HISTORICAL BACKGROUND

Magnetism was one of the oldest physical phenomena observed and investigated. The earliest reference to magnetism was found in the 4th-century BC Chinese book of Guiguzi: "The lodestone attracts iron [7]." The book also noted that the people of the state of Zheng knew their geographic position by means of a "south-pointer", which was referred to as Si Nan – an early application of the compass.

The first truly scientific study of magnetism was thought to be made by William Gilbert, who formed a clear picture of the earth's magnetic field, and described the movement of a magnetic needle caused by this field [8]. In 1820, Hans Christian Oersted discovered that electric current produces a magnetic field that encircles the wire. This discovery inspired André-Marie Ampère to formulate a hypothesis that an electric current is the source of every magnetic field. His assumption that magnet comprises rotating "electrodynamic molecules" was made around 80 years before the discovery of the electron and around 100 years before the Rutherford-Bohr model of the atom with orbiting electrons. And in 1826, Ampère formulated one of the fundamental laws of magnetism – Ampère's circuital law [9]:

$$\oint_C \mathbf{H} \cdot \mathrm{d}\mathbf{l} = NI \tag{2.1}$$

Equation (2.1) tells that the magnetic field strength $\mathbf{H}$ in a closed magnetic circuit C is generated by the number of conductors (N) in the circuit, each carrying a current I, as shown in Fig. 2.1.

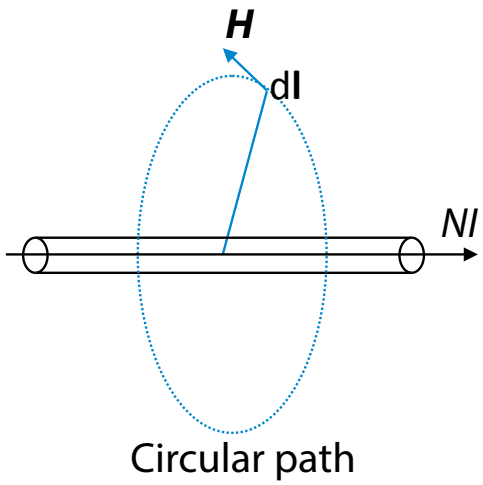

Fig. 2.1 Ampère's circuital law.

In 1831, Michael Farady discovered another fundamental law of magnetism. He stated that if the magnetic flux $\mathbf{\Phi}$ linking an electrical circuit changes, it will induce an electromotive force (emf) V proportional to the rate of change of this flux [10]:

$$V = -\frac{d\mathbf{\Phi}}{dt} \tag{2.2}$$

This effect is called electromagnetic induction. The minus sign in (2.2) implies the Lenz's law, which says the induced voltage is always in a direction opposing the flux change.

This history overview ends at the work "A Treatise on Electricity and Magnetism" published in 1873, where James Clerk Maxwell proposed a set of 20 equations, which were later simplified to a set of just four partial differential equations: two Gauss's, Ampère's and Faraday's [10]. Maxwell's equations describe how electric and magnetic fields are generated and altered by each other, which are fundamental to all analyses of magnetic and electric fields.

2.3 Electromagnetic Terms

In the free space, the presence of a magnetic field $\mathbf{H}$ in an area A generates a magnetic flux $\mathbf{\Phi}$:

$$\mathbf{\Phi} = \mu_0 \mathbf{H} A \tag{2.3}$$

Where μ_0 is the permeability of the free space, i.e. $4\pi \times 10^{-7}$ H/m. The units of $\mathbf{\Phi}$ and $\mathbf{H}$ are Wb (weber) and A/m (ampere per meter) respectively.

The magnetic flux density $\mathbf{B}$ (T, or tesla) is a more commonly used quantity and is defined as:

$$\mathbf{B} = \frac{\mathbf{\Phi}}{A} \tag{2.4}$$

From (2.3) and (2.4), we can see that the relationship between magnetic field strength $\mathbf{H}$ and flux density $\mathbf{B}$ in the free space is:

$$\mathbf{B} = \mu_0 \mathbf{H} \tag{2.5}$$

Magnetic field strength $\mathbf{H}$ and magnetic flux density $\mathbf{B}$ are most commonly used magnetic parameters. Other parameters, for example, permeability, losses, polarization, and magnetisation, are all depending on $\mathbf{H}$ and $\mathbf{B}$.

Although the international system of units (SI) recommends T and A/m, some units such as G (gauss) and Oe (oersted) based on the centimetre-gram-second (CGS) system are still used in many countries, especially in the United States. In the free space, the magnetic field strength of 1 Oe corresponds with the magnetic flux density of 1 G. Table 2.1 summarises the conversion factors between the CGS and the SI units.

Table 2.1 Conversion factors for common magnetic units.

	T	A/m	G	Oe
T	1	7.958×10^{5}	10^{4}	10^{4}
A/m	1.257×10^{-6}	1	1.257×10^{-2}	1.257×10^{-2}
G	10^{-4}	79.58	1	1
Oe	10^{-4}	79.58	1	1

As shown in (2.1), a circular loop of conductor carrying a current is the simplest circuit to generate a magnetic field. This circular current loop is also known as a magnetic dipole for historical reasons. At large distances from the loop, the field produced by such a loop is equivalent to the field produced by two hypothetical magnetic poles of strength p separated by a distance $\mathbf{l}$, the dipole moment $\mathbf{m}$ of such an arrangement is:

$$\mathbf{m} = p\mathbf{l} \tag{2.6}$$

where the pole strength p is defined as below:

$$p = \frac{\mathbf{\Phi}}{\mu_0} \tag{2.7}$$

We can then define a new quantity – the magnetisation $\mathbf{M}$, as the magnetic moment per unit volume of a solid:

$$\mathbf{M} = \frac{\mathbf{m}}{\text{volume}} \tag{2.8}$$

Together with (2.4), (2.6) and (2.7), we have

$$\mathbf{M} = \frac{\mathbf{\Phi l}}{\mu_0 \text{volume}} = \frac{\mathbf{\Phi}}{\mu_0 A} = \frac{\mathbf{B}}{\mu_0} \tag{2.9}$$

From (2.5) and (2.9), we have seen that the magnetic flux density $\mathbf{B}$ consists of two contributions: one from the magnetic field in free space $\mu_0\mathbf{H}$, the other from the

magnetisation of a material $\mu_0\mathbf{M}$. The magnetic induction can therefore be seen as the vector sum of those two:

$$\mathbf{B} = \mu_0 \left(\mathbf{H} + \mathbf{M}\right) \tag{2.10}$$

In order to represent the response of a magnetic material to a magnetic field, we use the permeability, which is defined as:

$$\mu = \frac{\mathbf{B}}{\mathbf{H}} \tag{2.11}$$

In practice, it is convenient to use the relative permeability instead of the permeability to stand for the magnetic properties of the material, which is given as below:

$$\mu_r = \frac{\mu}{\mu_0} \tag{2.12}$$

Therefore, the relative permeability of free space is 1. In engineering practice, the relative permeability of air is also taken as the unit. Magnetic materials can thus be classified based on the values of μ_r [11]. Materials with relative permeability slightly less than one are diamagnetic, such as silver, gold, and copper. If the value of μ_r is slightly greater than one, the material (e.g. aluminium, wolfram, and platinum) is paramagnetic. If the value of μ_r is much higher than one ($>10^3$), they are named as ferromagnetic materials. Examples of ferromagnetic materials include iron, cobalt and nickel. In order to take advantage of the high permeability property, ferromagnetic materials are adopted for the electrical steels to build power transformer cores.

Similar to Ohm's law – the resistance is the ratio of the voltage to the current, the concept of magnetic resistance, named as the reluctance R is developed and defined as:

$$R = \frac{F}{\Phi} \tag{2.13}$$

where F is magneto motive force (MMF) which equals to NI. Recall (2.1), (2.4), (2.11) and (2.12), we have the reluctance of a uniform closed magnetic circuit with the loop length l_m and the cross-sectional area A:

$$R = \frac{l_m}{\mu_0 \mu_r A} \tag{2.14}$$

2.4 Magnetisation in Ferromagnetic Materials

2.4.1 Domain structure and magnetisation curve

A ferromagnetic material under no external field can be divided into a number of small regions called domains. Each domain is spontaneously magnetised to the saturation value, but the magnetisation directions of various domains are randomly distributed so that the specimen as a whole has no net magnetisation. The process of magnetisation is converting the specimen from a multi-domain state into one where a single domain magnetised in the same direction as the applied external field.

The magnetisation curve represents a relationship between the flux density $\mathbf{B}$ and the magnetic field strength $\mathbf{H}$. It contains fundamental information about a given magnetic material, and it is hence usually presented in the material catalogue. This process is illustrated schematically in Fig. 2.2 [11]. The square in Fig. 2.2 encloses a portion of a crystal in which there are parts of four domains, and the solid line boundary separating them is called the domain wall. In the demagnetised state, the four domains are spontaneously magnetised in opposite directions, so that the net magnetisation of this part of the crystal is zero, as shown in Fig. 2.2 (a). An external field H has been applied in Fig. 2.2 (b), causing the upper domain to grow at the expense of the lower ones by downward motion of the domain walls. For a small magnetic field, the material returns to its previous state without hysteresis. With larger magnetic field, the domain walls' movements are irreversible, as shown in Fig. 2.2 (c). If the magnetic field is removed, the material will remain partially magnetised due to the new positions of domain walls (the hysteresis appears). In Fig. 2.2 (d), when the magnetic field is further increased, the walls have moved right out of the region considered, and the magnetisation is realised by

rotation of the magnetisation. Eventually, the magnetisation rotates into the direction parallel with the applied field, and the material is fully saturated, as shown in Fig. 2.2 (e).

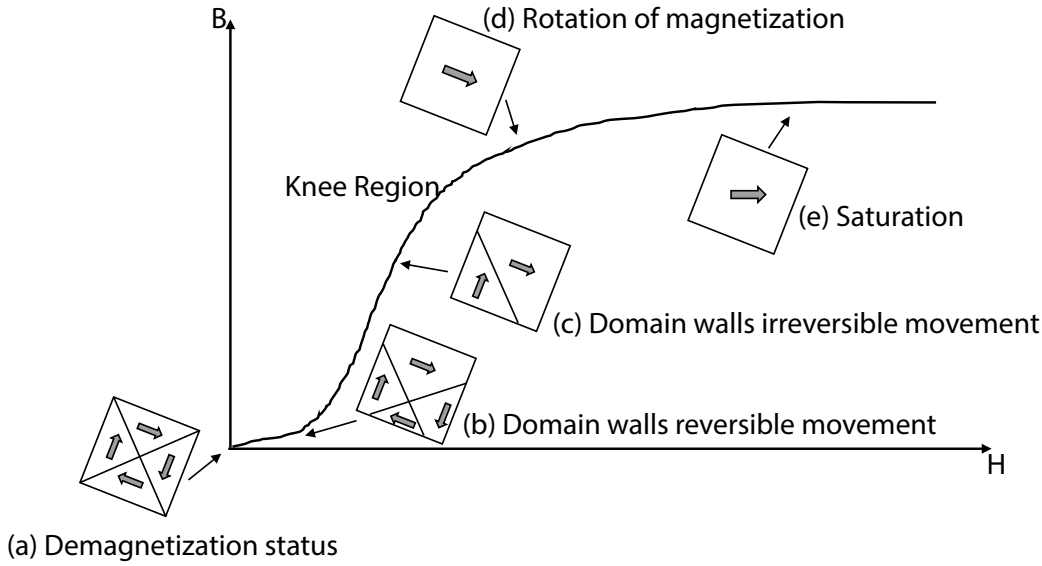

Fig. 2.2 The magnetisation process in a ferromagnetic material.

2.4.2 Hysteresis loop

Under AC excitation, the hysteresis loop, also known as B-H loop, will appear for the ferromagnetic materials, as presented in Fig. 2.3. Starting from a demagnetised state (H=0, B=0), the curve follows the initial magnetisation path from ① to ② (dashed curve) while B increases from zero up to the saturation with the growing H. When H starts to decrease, the return path will be different to the initial magnetisation curve due to the irreversible change of domain wall locations. Therefore, B is higher than zero when H decreases to zero. This magnetisation ③ is called the residual or remanent flux density. In order to obtain zero value of the flux density ④ again, an opposite direction of H is needed to apply. This H is hence called coercive field. If H is increased continuously in negative direction after coercivity point, it will arrive at the opposite tip ⑤. Now H is changed to positive value, the magnetisation will not return to the starting point ①, but it will close the loop at point ② with the path ⑤⑥②. If the material is magnetised by an AC sinusoidal H, the magnetisation will keep following the loop. By changing the peak value of H, a cluster of hysteresis loops will be obtained. Connecting all the tips of these loops, the AC magnetisation curve would be drawn.

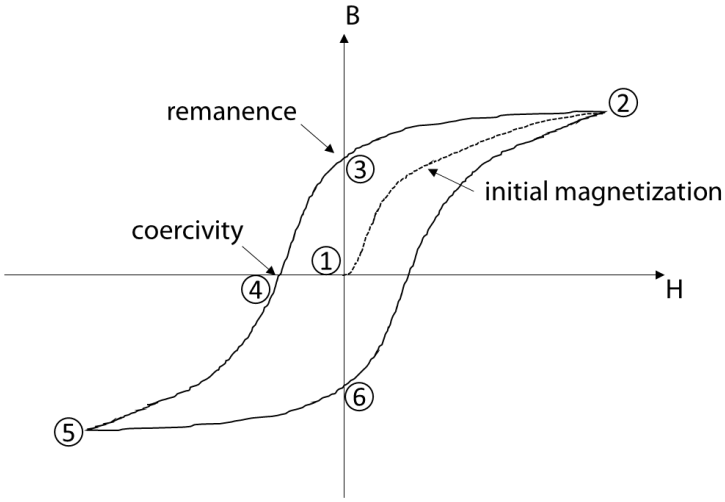

Fig. 2.3 B-H loop for a ferromagnetic material.

2.4.3 Energy loss with magnetisation

The magnetic energy w_m, which brings the specimen from an originally demagnetised condition to the saturation, is given by:

$$w_m = \int_0^B HdB \ \mathrm{J \cdot m^{-3}} \tag{2.15}$$

The area between the magnetisation curve and the B axis is thus a measure of the energy density. Cycling around the B-H loop will take energy proportional to area enclosed. This energy loss, or total power loss can be expressed in the sum of three components: static hysteresis loss, classical eddy current loss, and anomalous loss.

The static hysteresis loss is proportional to the area of static hysteresis loop and the AC magnetisation frequency, which is a characteristic of the material and a function of the peak flux density. Although the Steinmetz hysteresis loss empirical formula is widely used, it has been found the Steinmetz exponent varies a lot with the flux density, which brings difficulties in its application [12], [13]. The classical eddy current loss is related to the loss caused by eddy currents inevitably induced by the main flux B, which is proportional to the squared product of thickness, flux density, and frequency. Hence building up the transformer core with the stacked thin laminations is an easy and efficient way to restrict the eddy current loss. The anomalous loss, or excess loss, was found because there always exists a difference between

the measured power loss and the sum of theoretical calculated hysteresis loss and classical eddy current loss. This discrepancy in the modern grain-oriented steel can be up to 50% of the total core loss at power frequency [14]. The anomalous loss is thought to be proportional to the domain wall spacing and inversely proportional to the sheet thickness [15]. This knowledge finally leads to the birth of the domain refined high-permeability grain-oriented steels with a lower anomalous loss. Further detailed information about the three power loss components together with the algorithm to separate them from the total power loss will be presented in Chapter 6.

In addition, under DC quasi-static magnetisation, only the hysteresis loss exists. Under AC magnetisation, the B-H loop will be wider due to the classical eddy current loss and the anomalous loss. Consequently, the total power loss is higher than that under quasi-static (DC magnetisation) condition.

2.5 Summary

In this chapter, the electromagnetic terms, units system, and the relationships have been presented, followed by a briefing of the development of electromagnetism. The magnetisation process in the ferromagnetic materials was described using the domain structure theory. Inevitable hysteresis loop and the accompanying energy loss under AC magnetisation were also discussed here. The background knowledge in this chapter establishes the base for the later chapters studying on the magnetic properties of electrical steels and transformer cores.

3 Grain-Oriented Electrical Steels and Power Transformer Cores

3.1 Introduction

Modern power transformer cores are all built with grain-oriented electrical steels. A considerable amount of research has been conducted on electrical steels in order to reduce the power loss and improve its magnetic properties. In this chapter, the development of grain-oriented electrical steels is first reviewed. The manufacturing and processing of the grain-oriented electrical steels, together with their microstructures, are explained in detail.

The core-type power transformer and its construction process with grain-oriented electrical steels are then discussed. Transformer core joints are the critical regions to consider where hotspots might arise due to the deviation of the magnetic flux. The different joint configurations for power transformers are hence compared. Taking the leakage flux, iron loss, and copper loss in account, the equivalent electric circuit for power transformers can then be modelled.

3.2 Electrical Steels Manufacturing and Processing

3.2.1 Goss texture

Early power transformer cores were made with high-grade wrought iron in the 1880s [16]. After 20 years, it was recognised that the addition of small amounts of silicon into the iron greatly reduces the hysteresis loss, increases permeability and resistivity, thus reducing the eddy current loss [17]. In order to reduce the eddy current loss, thin electrical steel laminations were also adopted instead. Since then, a considerable research and development efforts have been applied to the electrical steels in order to build transformer cores towards lower core losses [18]–[22].

Electrical steels have a crystalline structure. The external magnetic properties are derived from the magnetic properties of the individual crystals or grains, highly dependent on their orientations. As shown in Fig. 3.1, applying Miller index system for a steel's cube crystal lattice, the cube edge direction, i.e. [001] is the easiest direction of magnetisation. The cube face diagonal [110] is more difficult, and the long diagonal [111] is the most difficult. The ideal electrical steel is thus with high proportion of grains having [001] directions close to the rolling direction and (110) planes close to the lamination plane, which is also named as Goss texture. However, hot-rolled electrical steels (grains were packed together in a random way leading to poor isotropic magnetic properties) were used in power transformer cores until the 1940s [14].

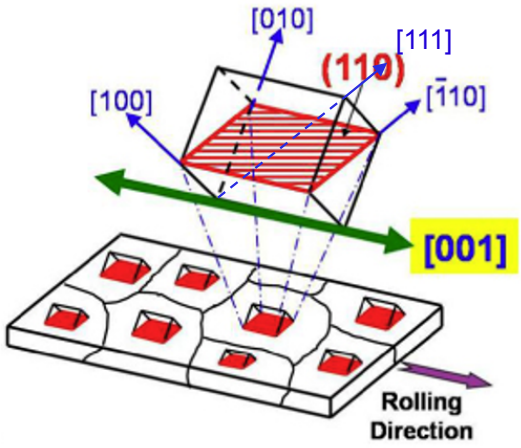

Fig. 3.1 Steel's cube crystal lattice and the ideal grain alignment in grain-oriented electrical steel.

3.2.2 Production of grain-oriented electrical steels

It had been recognised in the early 1920s that the silicon steel crystals were themselves anisotropic, but it was not until 1934 a major breakthrough – rolling process was achieved by N. P. Goss, which made a large proportion of grains in the electrical steels to be aligned with [001] direction. The left-hand of Fig. 3.2 shows the process rout that has formed the basis for the production of conventional grain-

oriented (CGO) steels for many years since they were first commercially produced by AK Steel Corporation in1939 [14].

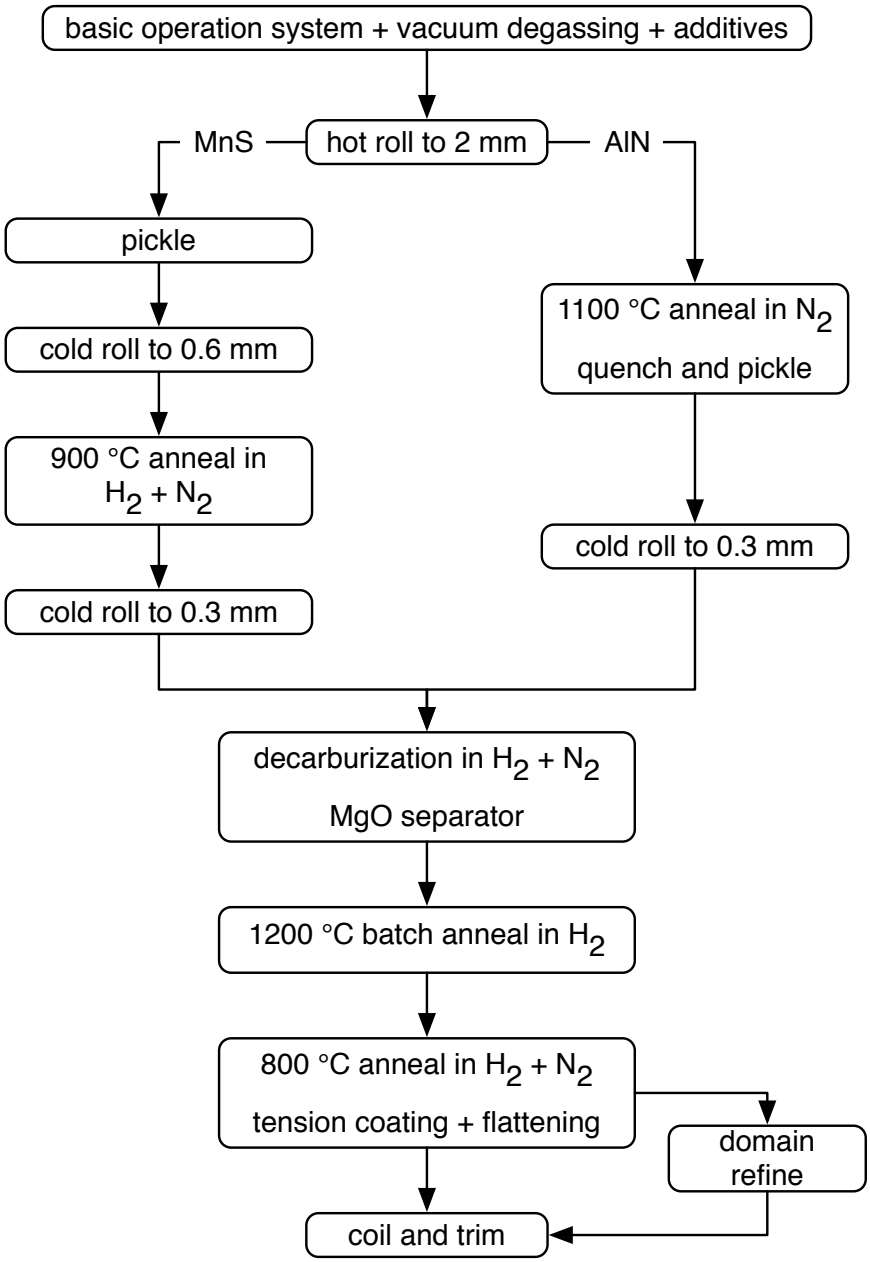

Fig. 3.2 Production route of CGO (via MnS route) and HGO (via AlN route).

The initially 2 mm hot-rolled steel goes through pickling to remove surface oxides and is then cold rolled to about 0.6 mm thickness. The decarburisation anneal is conducted in a nitrogen and hydrogen atmosphere at 900 °C in order to recrystallise and form a thin MgO coating. The next anneal is at 1200 °C for 24 hours. During this

stage, the main grain grows inhibited by the MnS, which is added before pickling. Meanwhile, the MnS particles also retard the growth of other grains. Finally, the material is given a flattening anneal at 800 °C. Although all grains do not have the ideal orientation, most are within 6° of [001](110), which is the best that can be achieved with MnS as a grain growth inhibitor [23].

In 1965, Nippon Steel Corporation announced the revolutionary new electrical steel – high permeability grain-oriented (HGO) steels, whose production is simplified by eliminating one of the cold-rolling stages owing to the introduction of around 0.025% aluminium to the melt and the resulting use of AlN as the grain growth inhibitor, as shown in the right-hand half of Fig. 3.2 [16]. The final product has a better orientation compared to CGO, with most grains within 3° of the ideal, but the grain size, on average 10 mm diameter, is around 2 times larger than that of CGO, as can be seen from Fig. 3.3. The domain images were observed using Bitter technique with a liquid suspension of extremely fine particles of Fe_3O_4. The dark Fe_3O_4 particles are attracted to the regions of nonuniform field, depositing a dark band along the domain wall [11].

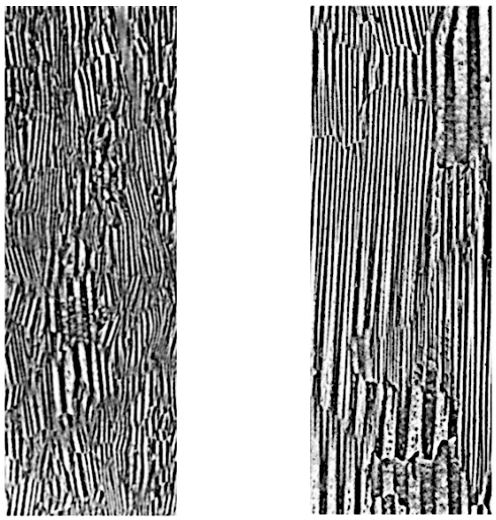

(a) (b)

Fig. 3.3 The static domain images from the domain viewer using Bitter technique: (a) CGO; (b) HGO.

A stress coating is also introduced within HGO, which imparts a tensile stress to the material for reducing eddy current loss that would otherwise be high in a large grain material. However, the lower power loss of HGO is still mainly due to a reduction of 30-40% in hysteresis loss because the eddy current loss of CGO and HGO greater than 0.23 mm thickness are very similar.

It has been recognised for many years that introduction of strain into electrical steels has an effect of subdividing magnetic domains to decrease the domain wall spacing and thus reducing the anomalous loss [15]. One popular solution is the laser-etched methodology: a precisely focused high power laser beam scans across the HGO steel surface rapidly to refine the domains. A further power loss reduction (around 5%-8%) can then be obtained on this domain refined HGO (HGO DR) [23].

Table 3.1 summarised the features of CGO and HGO steels. If the average misalignment is around 6°, and the average grain size is approximately 5 mm, the electrical steels are categorised as the conventional grain-oriented (CGO) steels. The electrical steels with improved characteristics such as less misalignment and much larger grain size are categorised as the high permeability grain-oriented (HGO) steels.

Table 3.1 Brief comparison between CGO and HGO steels.

At 1.7 T	CGO	HGO
Average grain size	5 mm	10 mm
Average misalignment	6°	3°
Typical power loss under 50 Hz	1.25 W/kg	1 W/kg
Typical permeability	1 p.u.	3 p.u.

Under 50 Hz AC magnetisation, HGO will typically achieve 20% lower power loss compared with CGO at 1.7 T. At the same time, HGO normally improves the relative permeability by 300% as well. Thanks to optimisation efforts and technology improvements, HGO steels have been more widely applied with a lower cost.

For a power transformer core, a specific electrical grain-oriented steel will be chosen with an ANSI standard loss evaluation technique called total ownership cost (TOC)

[24]. TOC takes many factors into account, such as the electrical steel costs, no-load/load loss, loading profile, the designed service period, and inflation together with load growth, etc. The simplest form of TOC can be expressed in (3.1), where PP is the transformer purchase price; NLEF is the no-load loss evaluation factor; LLEF is the load loss evaluation factor; P_c is the core no-load loss; P_w is the winding load loss.

$$\mathrm{TOC} = \mathrm{PP} + \mathrm{NLEF} \times P_c + \mathrm{LLEF} \times P_w \tag{3.1}$$

It was reported that for the low or average NLEF (4 $/W), CGO is cost competitive with a lower PP, while for a higher NLEF (7 $/W), HGO becomes a better choice [25].

A market survey of seven contemporary leading manufacturers of grain-oriented electrical steels was made and summarised in Table 3.2. The table demonstrates the corresponding gauges of electrical steel with the lowest power loss, which can be achieved for a certain thickness in the latest product catalogues [26]–[32]. It can be seen that the most popular grain-oriented steels in practice are CGO and HGO with the thickness between 0.23 mm and 0.30 mm, which will thus be selected as the test samples for the measurement and core materials for the simulation in the following chapters.

Table 3.2 Market survey of commercial grain-oriented electrical steels.

Manufacturer	Thickness (mm)	Nippon Steel	POSCO	JFE	AK Steel	ThyssenKrupp	Cogent	ArcelorMittal
CGO	0.18				N/A			
	0.23	M110-23S		M110-23S	M117-23S	M110-23S	M110-23S	M110-23S
	0.27	M120-27S	M110-27S	M120-27S	M124-27S	M120-27S	M120-27S	M114-27S
	0.30	M120-30S	M110-30S	M120-30S	M157-30S	M130-30S	M130-30S	M120-30S
	0.35	M135-35S	M145-35S	M135-35S		M140-35S	M140-35S	M130-35S
HGO	0.20			M085-20P				
	0.23	M080-23P	M080-23P	M080-23P	M080-23P	M085-23P	M085-23P	
	0.27	M090-27P	M090-27P	M090-27P	M090-27P	M090-27P	M090-27P	
	0.30	M100-30P	M095-30P	M105-30P	M100-30P	M100-30P	M100-30P	
	0.35	M115-35P		M115-35P		M125-35P		

3.3 Power Transformer Core

3.3.1 Core-type transformers

In the UK and throughout most of the world, core-type transformers are predominating, whose limbs are surrounded concentrically by the windings. Core-type transformers can have single-phase and three-phase core structures. Dimensional and weight limitations at the site, transportation restrictions, economics of spares and transformer reliability primarily determine whether the transformer required is to be single-phase or three-phase.

Three single-phase transformers cost about 1.5 times the cost of a three-phase transformer having the same total MVA [33]. Due to the considerable economic advantages of a three-phase transformer, most substations up to 500 kV use three-phase transformers. The majority of three-phase power transformers are in three-limb arrangement, having top and bottom yokes equal in cross-section to the wound limbs. With this configuration, it is not necessary to have separate flux-return paths, since the fluxes will summate to zero at all times for a balanced three-phase system. In order to meet the transport height restrictions, the depth of the top and bottom yokes might be reduced 50% by providing a return flux path external to the wound limbs. In this case, the return side yokes should be provided as shown in Fig. 3.4. It will then inevitably increase the size of the core and consequential core losses. If transport restrictions permit, the yoke depth needs not be reduced to half the limb width. The decreased flux density in the yokes will result in a reduction in specific core loss in the yokes. It might be economic if the cost of the core loss saved is greater than the cost of the extra material. Therefore, it is a normal practice to keep the main yoke area 60% and end yoke/end limb area 50% of the main limb area [34].

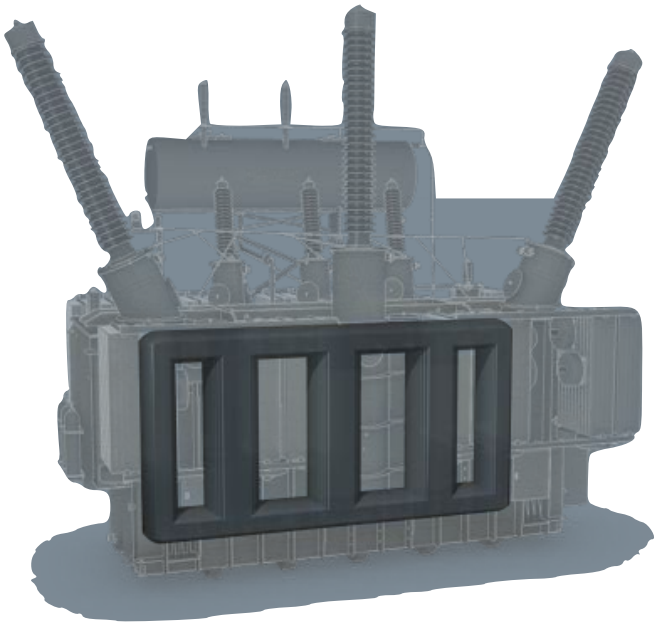

Fig. 3.4 Three-phase power transformer with five limb core [35].

For single-phase transformers, there are three common arrangements in terms of different return-flux path: both-limb wound, centre-limb wound, and cruciform [14]. At the remote ends of rural distribution systems, single-phase transformers with both-limb wound arrangement are often used, where the consumers' load is not great enough to apply a three-phase construction [14]. Single-phase units are also used for the ultra-high voltage large generation power transformers, where power rating demand is sometimes up to 600 MVA. The reason for applying the single-phase transformers at ultra-high voltage is usually to reduce the transport weight and dimensions.

3.3.2 Core construction

Section 3.2.2 has described the developments of electrical steels over the years to reduce the specific core losses. In parallel, transformer manufacturers made their efforts to improve the core designs to better take advantage of the properties of new electrical steels, and also to further reduce losses arising from aspects of the core design.

In stacked transformer cores, the transformer windings are circular cylinders surrounding the limbs. The preferred cross-section of the core is also circular in order to obtain optimum use of space within the windings, and the core is stacked in steps, which approximates a circular cross-section as shown in Fig. 3.5. The approximation depends on how many different widths of electrical steels a manufacturer is going to cut and build. In reality, the manufacturers normally produce a standard range of core cross-sections, named as frame sizes, which may start at 200 mm up to 1 m with progress in 25 mm steps [14]. Hence, it is unlikely that the widths required to give the ideal cross-section for every size of core will be available. For smaller distribution transformers and larger power transformers, the filling rate of the cross-section (the ratio between the total core cross-sectional area and the ideal circular cross-sectional area) is usually over 93% to 95%, respectively [14].

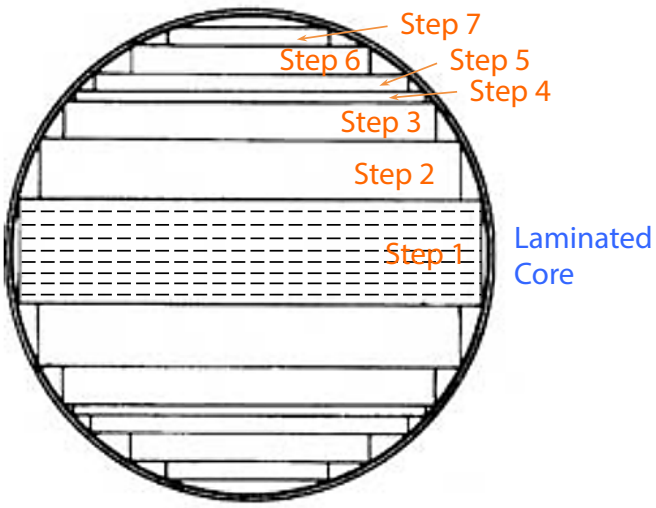

Fig. 3.5 An example of laminated 7-stepped core to approximate a circular cross-section.

The first stage for core construction is the production of the individual electrical steel laminations. Most transformer manufacturers now buy the electrical steels already cut to standard widths by the steel producers, so it is only necessary for them to cut the steels to length [14]. The cutting operation inevitably produces edge burrs. Burrs lead to electrical contact between adjacent electrical steels and the eddy current paths, which increases the core losses. Hence, it was once required to add a burr-grinding

process. Burr-grinding, however, tends to damage the insulation coating, and this damage needs to be repaired by an additional insulation. All these unavoidable handling and burr-grinding operations raise the mechanical stress level, resulting in higher core losses. So a final stress relief annealing need to be conducted by the transformer manufacturers [36]. Nowadays, coils of core steel are loaded onto the computer-controlled cutting machines at one end, and core plates ready for core manufacturing are stacked on pallets at the other end [35]. With modern cutting tools associated with the latest GO steels, burrs less than 0.02 mm are produced so that all the post processing operations can be omitted [14].

Transformer cores are stacked with laminations by hand, which is a labour-intensive process (see Fig. 3.6). In order to stack the core quickly and accurately, the guide pins or jigs are used at suitable positions, which ensures that the corner joints are correctly located. High accuracy of lamination laying and efficient core tightening is required in order to meet the guaranteed losses and noise levels during the tests and later on in service.

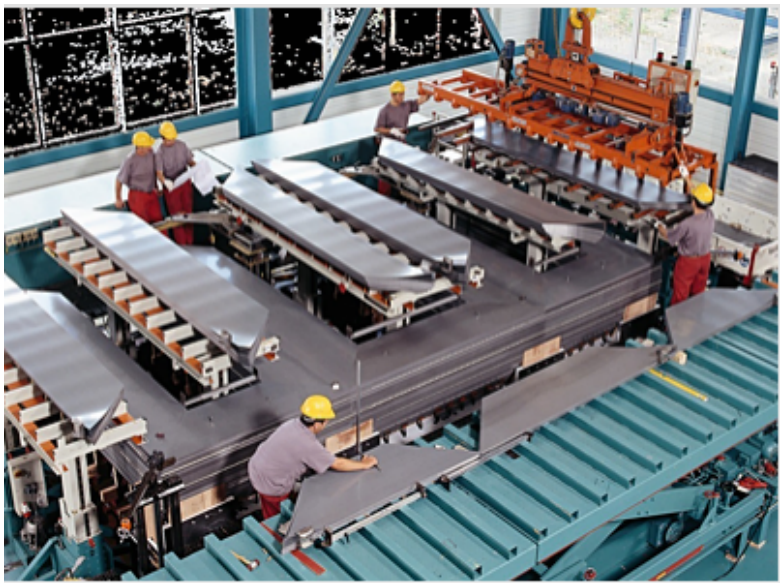

Fig. 3.6 Labour-intensive transformer core stacking [3].

It was normally accepted for laminations to be clamped together to form the complete core by means of steel bolts passing through both limbs and yokes. With the advent of GO steels, it was recognised the significance of boltless design. One

adverse effect using bolts is the increasing mechanical stress due to holes punching through core plates, which raises the core losses as mentioned above. Since the flux deviates from the grain orientation around the bolt holes, this resulting extra loss is undesirable, especially for the latest HGO steels. The loss of effective core cross-section due to the bolts will also lead to an unnecessary increase in the diameter of limbs and yokes. At very high flux densities, the flux may choose the path through the core bolts which brings huge losses. All these four factors together lead designers and manufacturers towards the elimination of core bolts, which are replaced by bands of resin-impregnated glass fibre [37], as shown in Fig. 3.7.

Fig. 3.7 Boltless core tightening with the glass fibre [3].

The core is usually built without the upper yoke as this would only have to be removed before the windings could be fitted. When the core is completed and securely banded, it can then be rocked upright using equipment that is especially designed to avoid unwanted mechanical stresses on the core, as shown in Fig. 3.8. This is a difficult operation due to the weight of the core, which may be up to 200 ton [38]. Once the windings have been fitted, the top yoke can be fitted suitably interlaced in the projecting end of the limb laminations, followed by the top core frames. Axial clamping structure can be then applied to the windings to compress them down to the correct length, together with tie bars linking top and bottom yokes.

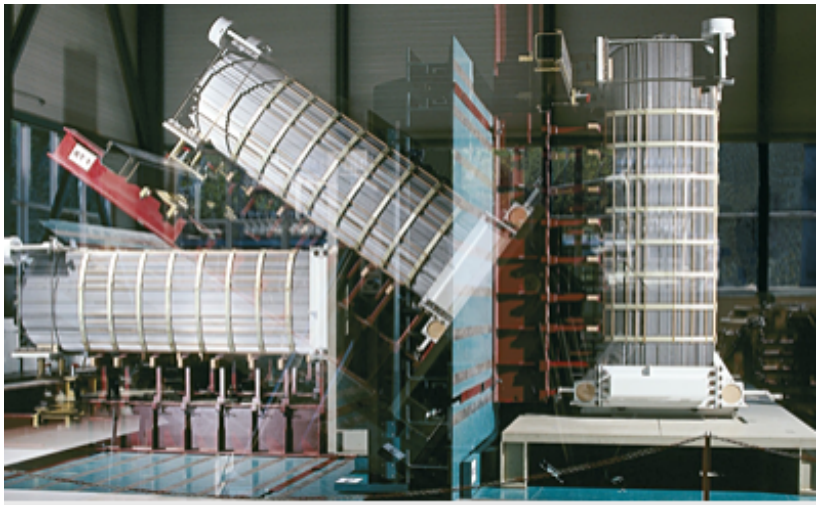

Fig. 3.8 Lifting the core into upright position using special equipment [35].

3.3.3 Overlapping joints

Obviously, the turning of the flux at the top and bottom corners of the core limbs is inevitable. The types of joints that are used in transformer cores are non-mitred, single-step-lapped (SSL) mitred, or multiple-step-lapped (MSL) mitred overlaps. Non-mitred joints, in which the overlap angle is 90°, are quite simple from the manufacturing point of view and can be cut without producing scrap, but the losses in the corner joints are greater since the flux in the joint region cannot flow along the direction of the grain orientation as illustrated in Fig. 3.9(a). Non-mitred joints were commonly adopted in earlier days when hot-rolled material was in use, while they are only used for lower rated transformers nowadays [34].

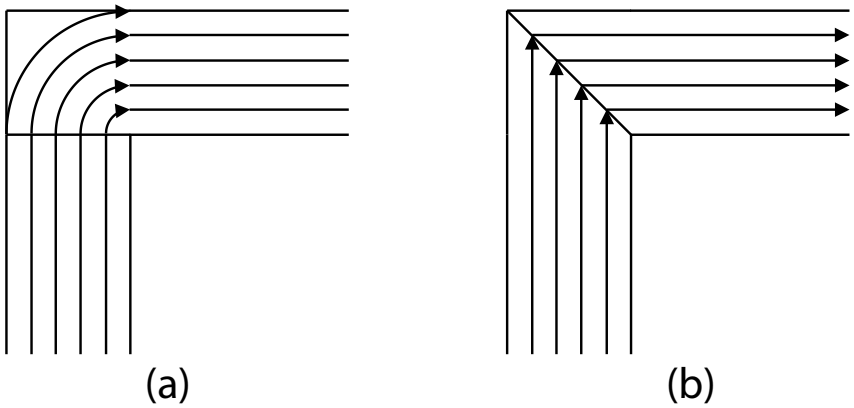

Fig. 3.9 The flux deviation in (a) non-mitred and (b) single-step-lapped core joint.

In order to reduce the effects of change of flux direction, the joint is mitred, i.e. the core plate is cut at an angle. The laminations are most commonly cut at 45°, to minimise the amount of scrap whilst improving the losses in the corners of the core, as shown in Fig. 3.9(b). Similarly, a tall slim core requires less deviation of the flux than a short squat core of the same weight and operating flux density, so the former arrangement is generally preferred because of a lower loss [6]. Meanwhile, when building a core, the laminations are placed in such a way that the gaps between laminations at the joint of the limb and yoke are overlapped by the laminations of the next layer. This provides a lower reluctance path for the magnetic flux as well as giving mechanical security at the joints [10]. The 45° mitred joints always have small isosceles right triangles left out at each corner, as shown in Fig. 3.10. The disadvantage for this arrangement would be some consequential flux distortion – up to 7th harmonics could be detected [37], [39].

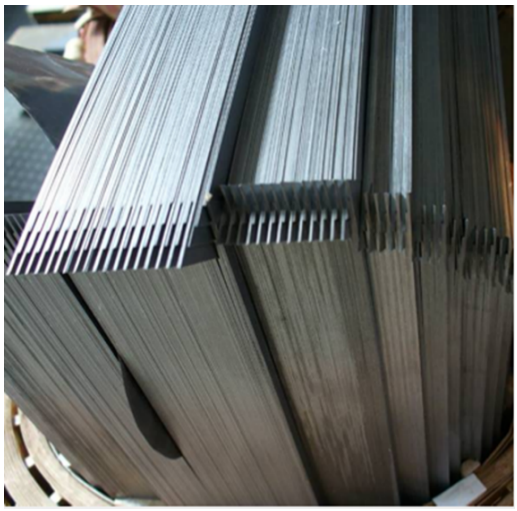

Fig. 3.10 45° mitred multiple-step-lapped transformer core joint.

As the significant proportion of the losses associated with modern transformer cores arises from the yoke to limb joints, MSL joints are now extensively used in power transformers to reduce the losses in these regions. Fig. 3.11 compares a SSL core with a MSL core (5-step-lapped). The MSL arrangement, which allows the flux transfer through the joint to become even smoother than with a SSL joint, thus provides not only lower corner losses, but also a lower noise level. One disadvantage of MSL, however, is that more laminations have to be cut at different lengths, which will

increase the manufacturing costs. Besides, fitting the upper yoke with MSL joints becomes a more complex process requiring greater care and a further increased labour cost. Hence, the step-lapped number is commonly chosen between five and seven to optimise the economics.

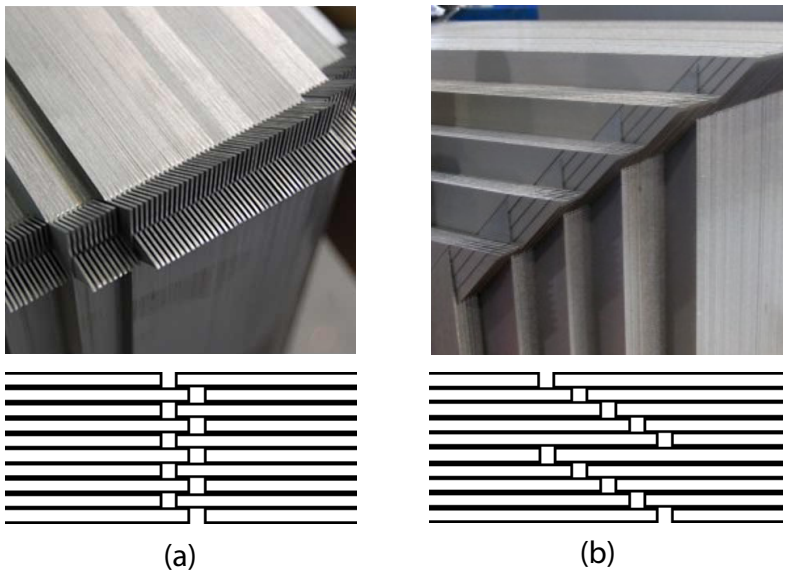

Fig. 3.11 (a) Single-step-lapped and (b) multiple-step-lapped mitred core joints.

3.3.4 Equivalent circuit of a practical transformer

A real transformer differs from the ideal transformer in a number of ways. Magnetic leakage flux is one of them, which has an important effect on the load characteristics of power transformers. When there is a current in the inner coil 1, as shown in Fig. 3.12, most of the flux produced is confined to the core and therefore links all the turns of both windings, which is also called the main flux. The unconfined flux in the air, as shown by the broken lines, is called the leakage flux. Some of the leakage flux links all the turns of coil 1, such as line a (part of coil 2 linkage) and line b (no coil 2 linkage), while another portion of it links only a fraction of the turns of coil 1, such as line c.

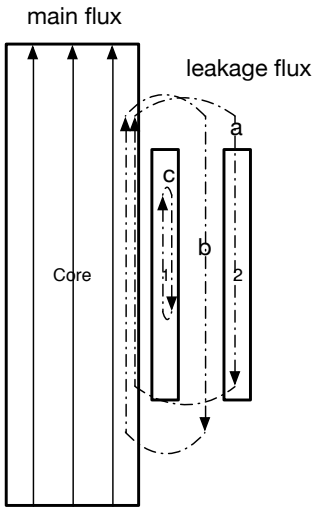

Fig. 3.12 Leakage flux due to the current in inner winding.

Due to the good permeability of transformer core, most of the mutual linkage flux is confined to the core. Because of the magnetic nonlinearity of the iron core, the main flux is not proportional to the MMF. However, a considerable portion of the path length of the leakage flux is in the air and therefore the reluctance of the iron portion of the paths is small compared with those in air. Consequently, the leakage flux can be assumed nearly proportional to the current producing it, and dependent on the geometry configuration of windings and the core. This basic assumption enables us to use a constant leakage inductance to account for the voltage drop induced by the leakage fluxes. The leakage inductance, or more appropriately, the leakage reactance is an important parameter of a power transformer, because it generally controls the short circuit performances of the transformer.

When a transformer is energised without load (i.e. open-circuit), a current is drawn from the voltage source connected to the primary side of the transformer. This no-load current magnetises the core and also generates core losses dissipated in the form of heat. It is composed of two components that are in quadrature with each other – the magnetising current and loss current. The magnetising current component is responsible for the main flux. Due to the non-linear magnetic properties of the iron core, the magnetising current will increase exponentially as the voltage or B increases linearly. Hence, the representing reactance will not be a linear element with the voltage. The consequence of this phenomenon is that the

magnetisation current will be composed of many harmonic components. The loss current component is mainly caused by the core losses with successive reversals of magnetisation of the core steel. There is also a small loss component due to the no-load current flowing in the primary winding. Two resistors are hence used in the equivalent circuit to represent the core losses and the primary winding loss respectively.

Hence, a practical transformer equivalent circuit including all the key parameters discussed earlier, is illustrated in Fig. 3.13. If the main flux is assumed as sinusoidal waveform, and expressed as $\phi = \phi_m \sin(2\pi ft)$, the relationships between the instantaneous as well as rms values of the emf and flux are summarised in (3.2). The phasor diagram of the parameters under the no-load situation is sketched in Fig. 3.14, where the current in the secondary side is null, and there will be no voltage drop on R_2 and X_2. Hence the terminal voltage output is equal to the secondary emf, i.e. $V_2=E_2$.

$$e_1 = N_1 \frac{d\phi}{dt} = N_1 \phi_m 2\pi f \cos(2\pi ft)$$
$$E_1 = \frac{N_1 \phi_m 2\pi f}{\sqrt{2}} = 4.44 f B_m A N_1 \quad (3.2)$$

where:

e_1	emf of primary windings
E_1	rms value of e_1
ϕ	instantaneous main flux
ϕ_m	peak main flux
f	frequency
A	core cross-sectional area
B_m	peak main flux density
N_1	primary winding turns

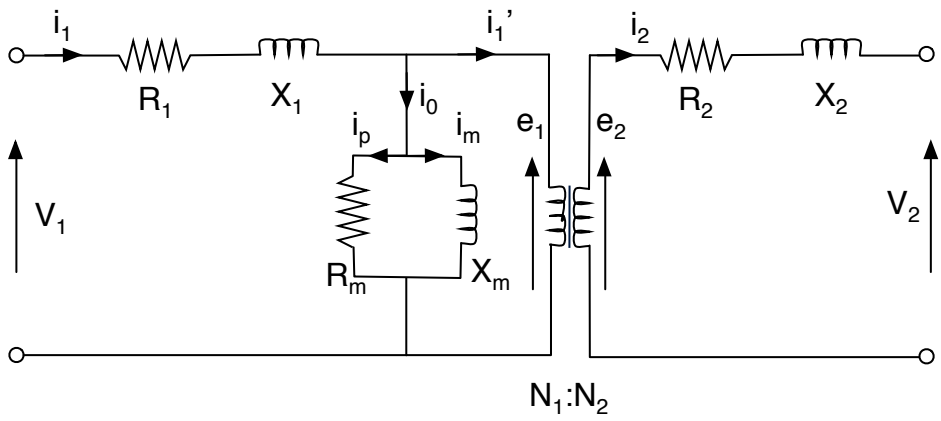

Fig. 3.13 Equivalent circuit of an iron-core transformer.

Where:

R_1,R_2	primary and secondary ohmic resistance
X_1,X_2	primary and secondary reactance
R_p	equivalent resistance representing the core losses
X_m	equivalent reactance representing the core magnetisation
N_1,N_2	primary and secondary winding turns
V_1, V_2	primary and secondary voltage
e_1,e_2	emf of primary and secondary windings
i_1,i_2	primary and secondary current
i_m	magnetisation current
i_p	current supplying the core losses
i_0	no-load current ($i_0=i_m+i_p$)
i_1'	current to neautralise the secondary mmf ($i_1'=i_1-i_0$)

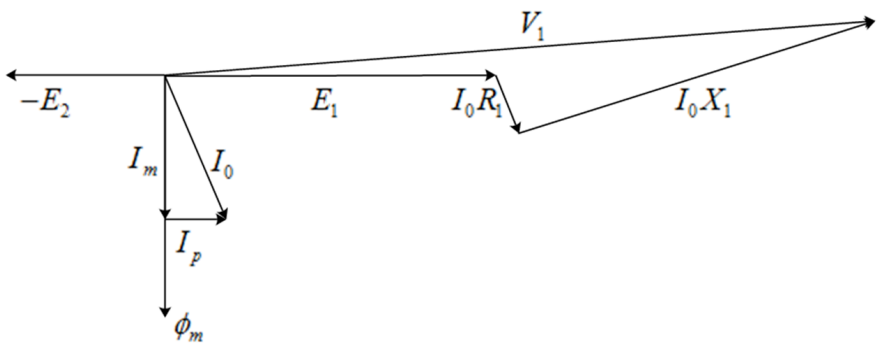

Fig. 3.14 Phasor diagram for the transformer under the no-load situation.

This simple model, however, cannot be used when the transformer goes into deep saturation, since it fails to provide an accurate representation. Firstly, for the calculation of leakage reactances X_1 and X_2, most of the analytical methods are not accurate even under the normal operation. The assumption that both LV and HV windings have exactly the same length, is often made, which is rarely the case in practice [14]. At high flux densities, the leakage reactances are expected to increase as the leakage flux boosts due to the reduction of the transformer core's permeability. The leakage flux flowing in unplanned air paths may link the windings, the tank, and the adjacent structural components, such as bolts and clamping structures. The resulting eddy currents in the non-laminated structural components together with the windings can cause excessive losses and dangerous temperature rise. Besides, the magnetising reactance X_m is not constant, because the magnetisation curve of the transformer core is non-linear. At high flux densities, X_m drops very fast, which attracts a huge amount of highly distorted currents, generating high power losses not only from the core R_m but also from the winding R_1. Hence, the better understanding of the material's magnetisation curve together with the distribution of the main and leakage flux in the transformer is crucially important to modify the equivalent circuit modelling to be a better representation for a power transformer under cases of core saturation.

3.4 Summary

The advantages of CGO and HGO steels with the Goss texture over the previous iron steels have been explained using the crystal lattice model. Most of CGO's grains are within 6° of [001](110), which is the best that can be achieved with MnS as a grain growth inhibitor. For HGO steels, most grains are within 3° of the ideal, and the grain size, on average 10 mm diameter, is around 2 times larger than that of CGO. The modern manufacturing processes for GO steels to achieve a larger grain size and better grain alignment have been thoroughly reported, resulting a sound magnetic property with lower power losses. Under 50 Hz AC magnetisation, HGO will typically achieve 20% lower power loss compared with CGO at 1.7 T. At the same time, HGO normally improves the relative permeability by 300% as well. A market survey of contemporary manufacturers of grain-oriented electrical steels showed the most

popular grain-oriented steels are CGO and HGO with the thickness between 0.23 mm and 0.30 mm, which will thus be selected as the test samples for the measurement and core materials for the simulation in the following chapters.

Dimensional and weight limitations at the site, transportation restrictions, economics of spares and transformer reliability primarily determine whether the transformer required is to be single-phase or three-phase. Due to the considerable economic advantages of a three-phase transformer, most substations up to 500 kV use three-phase transformers. Single-phase units can be used for the ultra-high voltage large generation power transformers to reduce the transport weight and dimensions.

The preferred cross-section of the core is circular in order to obtain optimum use of space within the windings, and the core is thus stacked in steps, which approximates a circular cross-section. For a power transformer core, the filling rate of the cross-section (the ratio between the total core cross-sectional area and the ideal circular cross-sectional area) is usually over 90%.

The four main stages of power transformer core construction have been presented: producing electrical steel laminations; stacking cores with laminations; core tightening and clamping; core lifting and yoke fitting. The difficulties in each stage, such as mechanical stress during lamination cutting and boltless design, were discussed. The three core joint configurations (non-mitred, SSL, MSL) were compared. 45° mitred MSL joint was thought to be a good solution owing to a smoother and lower reluctance path for the magnetic flux as well as a secure mechanical structure at the joints.

The total ownership cost (TOC) takes many factors into account, such as the electrical steel costs, no-load/load loss, loading profile, the designed service period, and inflation together with load growth, etc. For the transformer designer, it is vital to consider both technical specifications and TOC plus labour cost when choosing the specific GOs, transformer core types, and joint configurations, for compliance with the customer's requirement.

The simple equivalent circuit model of a transformer fails to provide an accurate representation, particularly when the transformer goes into deep saturation. Parameters X_1, X_2, R_m, X_m, vary at different flux density levels due to the non-linear characteristics of the core steel. At high flux densities, the leakage flux flowing in unplanned air paths may link the windings, the tank, and the adjacent structural components, such as bolts and clamping structures. The resulting eddy currents in the non-laminated structural components together with the windings can cause dangerous temperature rise. Therefore, it is apparent that a better understanding of both magnetic properties of electrical steels and the flux distribution in the transformer is critical for the power transformer modelling, particularly under the extreme operational conditions.

4 Measurement of Magnetic Properties of Electrical Steels

4.1 Introduction

Since electrical steels in power transformers were rarely designed to work at a peak flux density value above 1.75 T, their properties given by the manufacturers were usually measured up to 1.80 T. However, the overflux challenges do exist when the flux density within a core temporarily exceeds its nominal operating value, as an example, it can occur in quadrature boosters (QBs) during normal operation [40]. Overflux is also the dominating mechanism to cause ferroresonance in a transformer [41]. External factors such as geomagnetically induced currents (GICs) could also trigger half-cycle saturation of high-voltage power transformers [1], [42]. The substantial power loss produced at such high flux densities can lead to core overheating resulting in thermal degradation of the surrounding insulation and even transformer failure. Therefore, there is a growing need for accurately measuring magnetic properties of electrical steels at high flux densities or the so-called deep saturation region in order to have a better understanding of the behaviour of the power transformer core.

Generally, there are three incentives to determine the electrical steels magnetic properties [43]:

- Research on and improvement of the material properties and performance.
- Modelling of the material performance under different magnetisation conditions, i.e. flux density ranges and magnetisation modes, in order to achieve basic input quantities for the performance computation of complex technical devices.
- Characterization of the material by means of the measurements of magnetic loss, permeability and B-H characteristics, to meet requirements of trade and for set-up design calculations.

In order to compare properties of various materials with a good reproducibility – for instance, the same material tested in different laboratories, international standards to precisely determine the condition of the tests are therefore very critical. International Electrotechnical Commission (IEC) standards 60404 series (see Appendix 2) regulates all the aspects of testing magnetic materials. Unfortunately, current IEC standards (60404-2 and 60404-3) that specify the methods of measuring electrical and magnetic properties of commercial electrical steels only cover the tests up to 1.80 T.

This chapter first reviews the development of Epstein frame, and the standardised Epstein frame in IEC 60404-2. The measurement principle and test bench with Epstein method are then described in detail. Results using Epstein method are analysed, together with discussions on measurement uncertainties and issues at high flux densities. Following that, the standard single sheet tester in IEC 60404-3 is introduced. An improved single strip tester was utilised to conduct the measurements at high flux densities. The test results validated the advantage of the improved single strip tester on the magnetic properties measurement in deep saturation region.

4.2 IEC 60404-2 USING EPSTEIN FRAME

The Epstein frame was originally proposed as a 50cm square by Epstein in 1900. Since a smaller 25cm version was proposed by Burgwin in 1936, this measurement technique has been standardised in IEC 60404-2 and widely used in measuring magnetic properties of electric steels [44].

The Epstein frame is schematically shown in Fig. 4.1. A multiple of four sample strips of width 30 mm and length variable from 280 to 320 mm are prepared by cutting, annealing for stress relief, and superposed at the corners to form a complete square. Great care must be devoted to geometrical perfection of the strips, which are required to remain flat after cutting and annealing. The flux continuity at the square corners is ensured by double-lapped joints, as shown in Fig. 4.1. A pressure of 1 N placed on each corner joint provides good and reproducible flux closure.

The fixed windings are composed of four coils connected in series. The primary winding is connected to the power source to provide the magnetisation current. The secondary winding is connected to the voltmeter to measure the peak flux density.

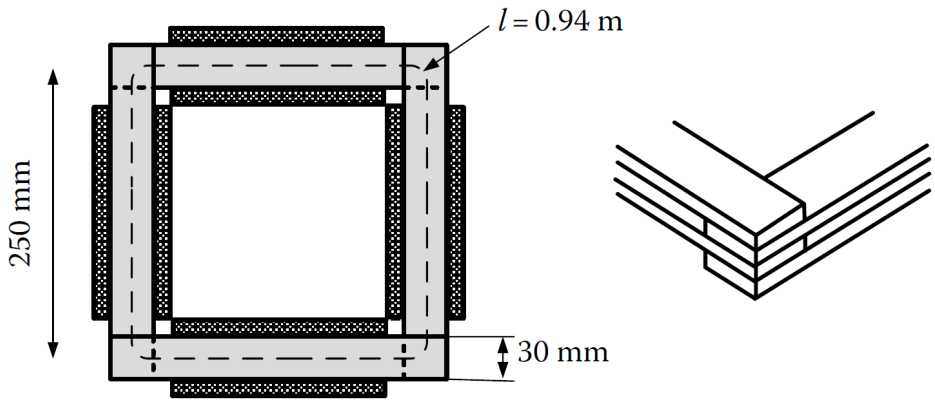

Fig. 4.1 Schematic Epstein frame and the double overlapped corner arrangement.

A decisive argument in favour of the Epstein frame in industrial testing is the easy assembling and disassembling the magnetic circuit, with the sample strips either slipped into or taken out of the winding arrangement.

In the closed sample, the length of mean magnetic path l_m is assumed as 0.94 m, as stipulated in Standard IEC 60404-2. A further discussion on l_m will be given in the next section. The instantaneous magnetic field strength $H(t)$ can then be derived from (2.1), and simplified as (4.1), knowing the magnetisation current $i(t)$ and number of primary winding turns N_1.

$$H(t) = \frac{N_1 i(t)}{l_m} \tag{4.1}$$

The instantaneous flux density $B(t)$ is determined from (2.2), where A is the lamination's cross-sectional area; N_2 is the number of secondary winding turns; $v(t)$ is the measured secondary voltage:

$$B(t) = -\frac{\int v(t)dt}{AN_2} \tag{4.2}$$

A series of hysteresis loops can then be obtained with the scatter of $(H(t),\ B(t))$. If the vertex points of each loops $\left(\widehat{H},\widehat{B}\right)$ are connected, the magnetisation curve, i.e. B-H curve, is thus gained.

The power loss of the Epstein frame core at a certain flux density level can be read conveniently from the wattmeter connected at the primary side, which is similar to the open circuit test on a power transformer.

4.3 Measurement Bench with Epstein Method

A digital test bench with Epstein frame was built to measure the magnetic properties of grain-oriented electrical steels.

The HGO test samples H 105-30 are from ThyssenKrupp company, whose typical core loss is 1.05 W/kg at 1.7 T and the theoretical saturation polarization is around 2.03 T. The dimension of the sample strips are 280 mm × 30 mm × 0.3 mm. Since the internal mechanical stress generated along the cut edges during slitting operation has a highly negative effect on the magnetic properties of the grain-oriented electrical steel, the samples should be prepared with the stress relief annealing in a vacuum furnace, as shown in Fig. 4.2. A typical process is illustrated in Fig. 4.3: the air in the furnace was firstly pumped out until the pressure achieves 10^{-6} atm. Then it was heated up to 810 °C from the room temperature with 250 °C/h. The samples cooled down to the room temperature again with 50 °C/h, followed by dwelling in 810 °C for an hour.

Fig. 4.2 Vacuum tube furnace used for the stress relief annealing.

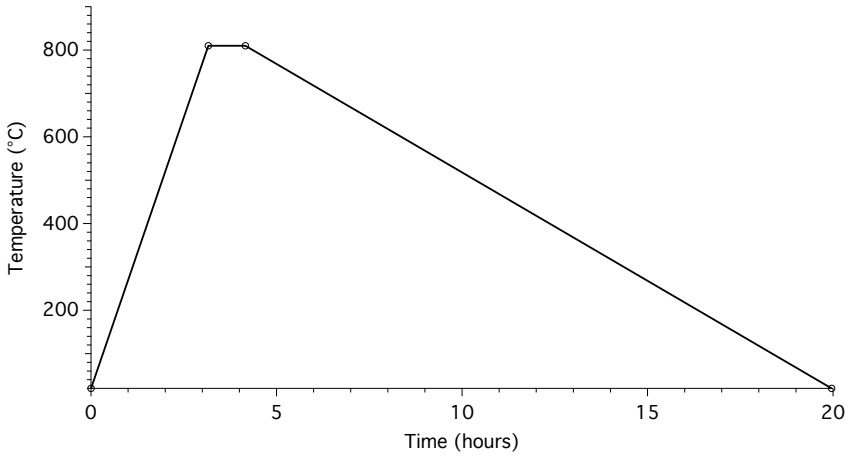

Fig. 4.3 Stress relief annealing at 10^{-6} atm.

Referring to Standard IEC 60404-2, the Epstein frame was built as shown in Fig. 4.4. The fixed windings are composed of two sets of four coils connected in series, distributed uniformly over a minimum length of 190 mm, as shown in Fig. 4.5. The measuring winding (secondary winding) coil carries 175 turns of one copper wire with a nominal cross-sectional area of 0.8 mm^2 wound in one layer. The outer magnetisation winding (primary winding) coil carries 175 turns of two copper wires connected in parallel, each with a nominal cross-sectional area of approximately 1.8 mm^2, wound side by side in three layers. Both windings therefore have the same total number of turns equal to 700.

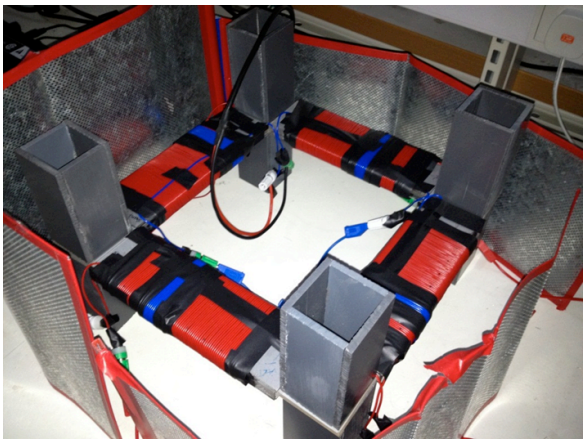

Fig. 4.4 Epstein frame for the measurement of magnetic properties of GO steels.

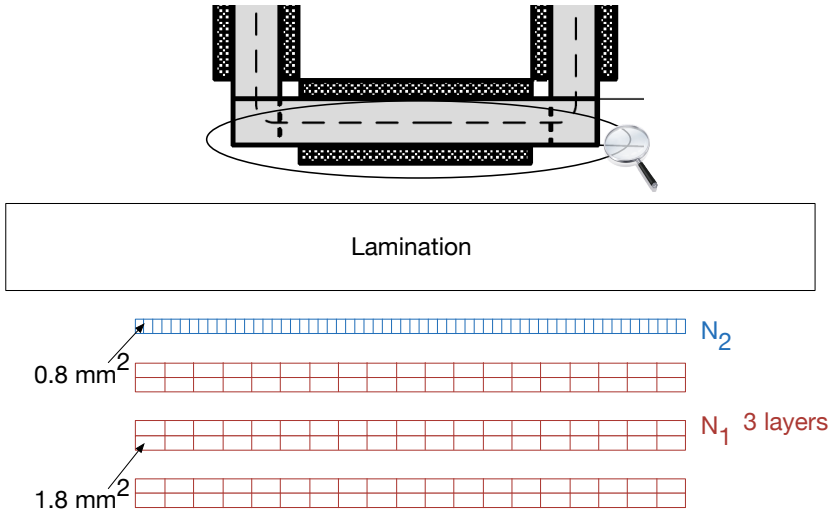

Fig. 4.5 Schematic winding coil settings for Epstein frame.

To enable the automatic control and further update convenience, National Instruments (NI) data acquisition (DAQ) board USB-6229 BNC (16 Bits, 250 kS/s) and the graphical programming language LabVIEW® are used for the measurement, data logging and processing. Some trials such as [45] a high bandwidth linear amplifier can be used as the power source to excite the primary winding. Using an amplifier rather than a conventional autotransformer benefits the integration of output control and data recording with NI DAQ system. Hence, EUROPOWER EP2500 2400 W power amplifier was adopted to amplify the voltage signal generated by the DAQ board. It can produce 20 A maximum current (RMS) and 80 A maximum peak current. Fluke i30s current clamp with 1% accuracy was used to measure the primary magnetisation current. The measurement circuit is presented in Fig. 4.6.

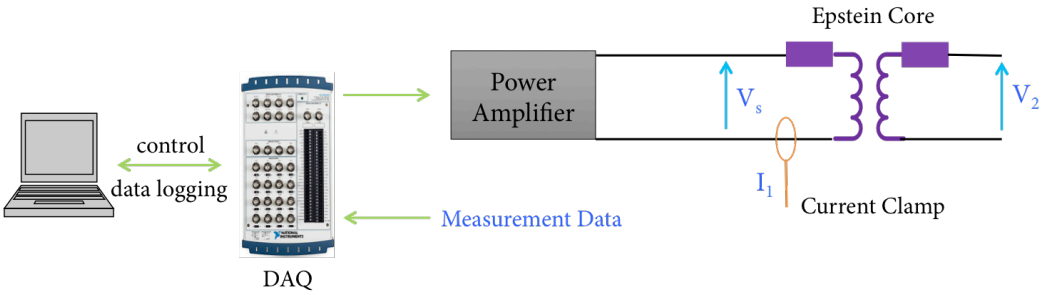

Fig. 4.6 Block diagram of the measurement circuit using DAQ with Epstein method.

As illustrated in Fig. 4.7, the friendly user interface panel allows flexible inputs including number of winding turns, area of core and effective magnetic loop length to adapt different cores. Besides, it will display real-time measurement signals to help monitoring and calculate the r.m.s., peak value and total harmonics distortion (THD) of measured current and voltages, with FFT for harmonics analysis. Furthermore, this programme will also simultaneously draw the hysteresis loop for the certain flux level and give the peak value of B and H along with relative permeability. In addition, all data displayed on UI can be stored for later analysis when 'Save' button is pushed if everything seems normal and stable. More details in terms of the block diagram of programme are attached in the Appendix 3.

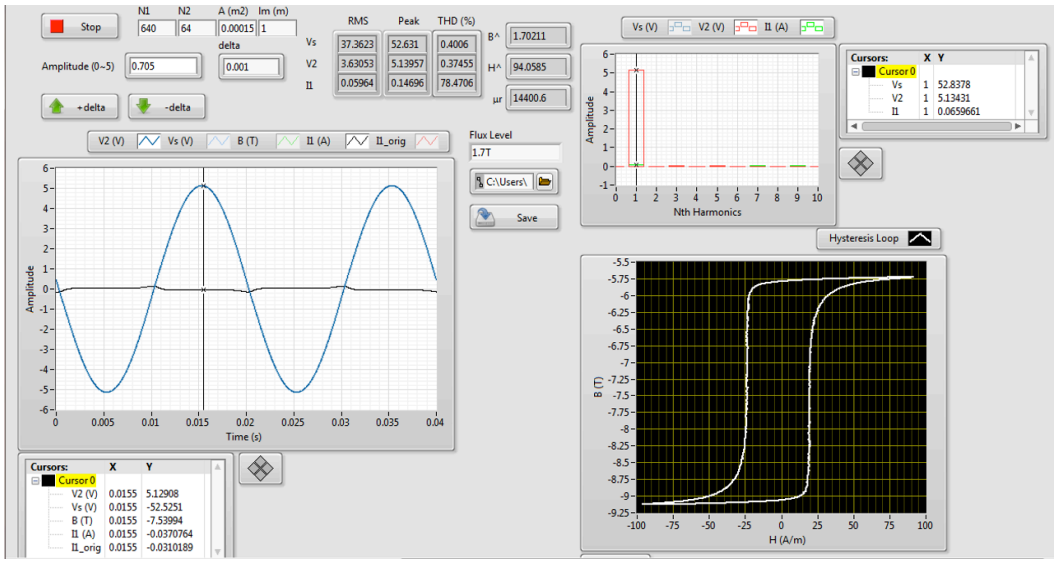

Fig. 4.7 User interface for the digital measurement bench.

4.4 Measurement Results and Discussions with Epstein Frame

4.4.1 Effect of different lamination layers

In IEC 60404-2, the number of sample strips has not been designated. It has been known that the per unit power loss would not change if measured with Epstein core with more than four layers of laminations (16 laminations) [39]. However, no attempt was made to investigate the effect of different lamination layers. With the test bench proposed in Section 4.3, Epstein frames with 4 layers, 12 layers and 15 layers were tested. The measured B-H curves and power loss curves are illustrated in Fig. 4.8 and Fig. 4.9 respectively. The curves in colour magenta represent the HGO 105-30 provided by the manufacturer ThyssenKrupp, which were measured with 7-layer Epstein core. Fig. 4.8 confirms the preceding findings in [39] that the measured power loss would not change significantly if more than four layers of laminations used in the Epstein frame. Meanwhile, Fig. 4.9 demonstrates that the measured B-H curve is not notably affected if there are more than four layers of laminations, particularly under 1.8 T. This also confirms the Epstein methodology has an excellent repeatability and reproducibility for the same group of test specimens, in addition to its easy preparation.

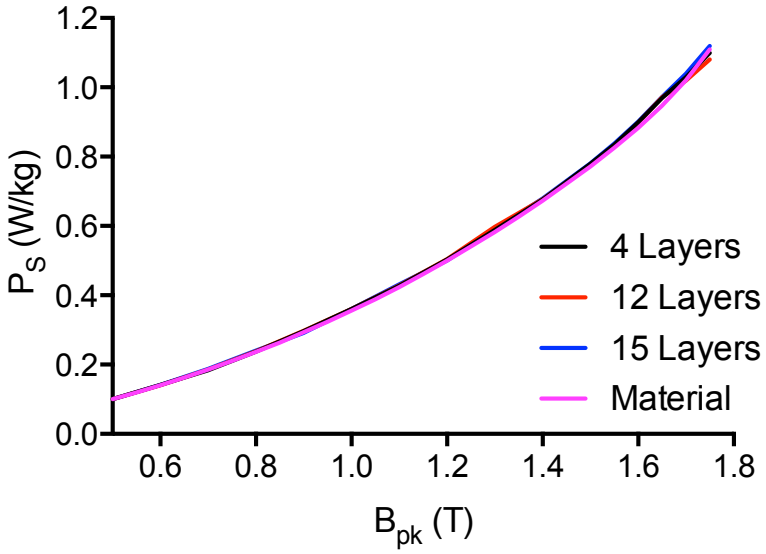

Fig. 4.8 Power loss curves comparison with various layers of laminations for Epstein core.

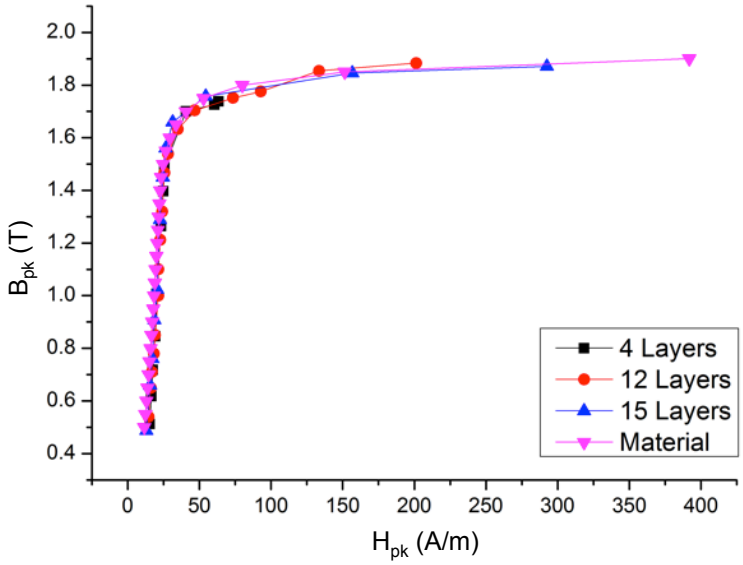

Fig. 4.9 B-H curves comparison with various layers of laminations for Epstein core.

4.4.2 Uncertainty of Epstein method

The accuracy of the Epstein method is still being debated [46], [47]. The sources of uncertainty are mainly from the double-lapped corners, and the related estimation of the magnetic path length l_m. According to the IEC 60404-2, the fixed l_m = 0.94 m is assumed for all the lamination specimens for any flux density levels. This was first suggested by Dieterly after he tested different size of the Epstein frame and compared with the ring-core of the same material for a lot of samples in 1949 [48]. As found in [15], Epstein method can overestimate the power loss by 4% at 0.5 T, and underestimate the power loss by 5% at 1.8 T, caused by the inhomogenous magnetic path due to the double-lapped corners. The latest study [40] repeated in 2007 tried to determine the accurate l_m under sinusoidal magnetisation. The results are presented in Fig. 4.10. It revealed l_m was almost 0.94 m for the CGO sample under 1.5 T. The HGO sample gave l_m around 0.97 m under 1.5 T. Besides, at 1.7 T, l_m droped to 0.90 m for the CGO sample, but increased to 0.98 m for the HGO sample.

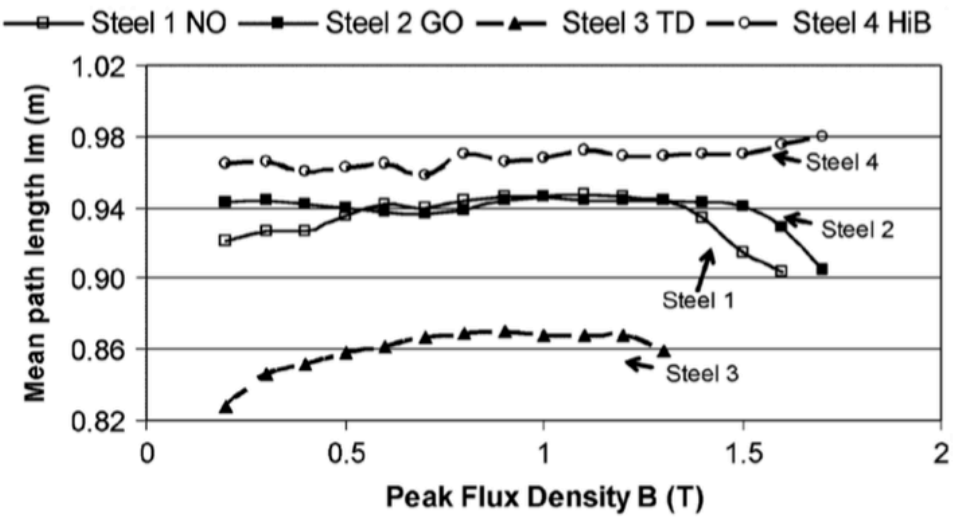

Fig. 4.10 Estimation of the mean magnetic path length for CGO, HGO and NO specimens up to 1.7 T [40].

In addition to the inhomogeneous corner issue, the nonuniformity of the magnetising solenoid can also contribute to the error of the Epstein method. The theoretical distribution of the magnetic field in the magnetisation solenoid windings can be computed using Ampère's law [22]. Fig. 4.11 shows the theoretical magnetic field distributions along the Epstein strip in the magnetisation winding with two different cross-sectional shapes – rectangular and circular. For the traditional circular cross-section in blue, it can be seen that only around 40% central portion of the specimen is magnetised with the expected H calculated from the magnetising current. The real magnetic field close to the end drops fast. The magnetic field at the solenoid ends is almost half of the expected H. Using a rectangular cross-sectional windings, which is shown in orange in Fig. 4.11, can improve the distribution of the magnetic field. About 70% of the specimen is now magnetised with the expected H. That is why the rectangular windings are utilised in the current Epstein frame. However, the uneven distribution of the magnetic field in the magnetising winding is still inevitable, leading to a further measurement error for the Epstein method. This uneven distribution of the magnetic field can be further improved by making the winding turns unevenly distributed, i.e. increase the turns close to the ends.

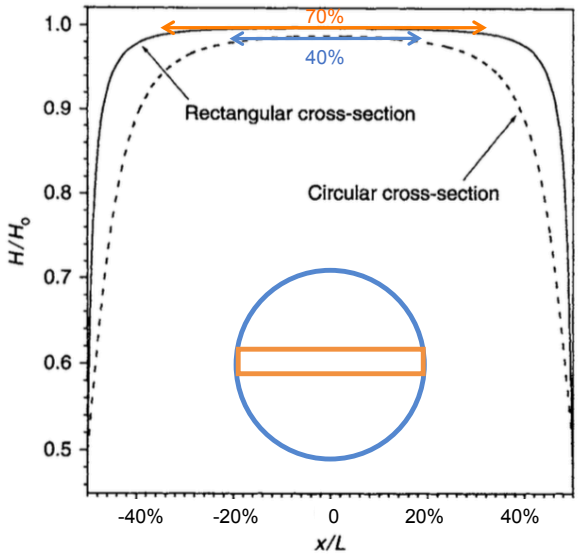

Fig. 4.11 Theoretical magnetic field distributions along the Epstein strip in the magnetisation winding with two different cross-sectional shapes – circular (in blue) and rectangular (in orange) [22].

Nevertheless, due to the good repeatability, reproducibility as discussed before, the Epstein frame is still by far the recommended fixture in IEC 60404-1 [17] and BS 60404-13 [22] to determine the magnetic properties of the grain-oriented steels delivered in the fully processed state, which has a high level of standardization and wide usage.

4.4.3 Using Epstein method at high flux densities

All magnetic simulation software with the finite element method, to name a few, COMSOL, MAGNET and SLIM, require the electrical steel B-H curve as the fundamental input to simulate the flux distribution in the transformer core. However, the B-H characteristics provided by most manufacturers using Epstein are below 1.8 T, which means that the computer has to extrapolate the magnetisation curve from 1.8 T and below to the deep saturation situation. The error brought by the extrapolation might lead to a significantly different flux distribution analysis in the transformer core at high flux densities, and thus result in a misleading conclusion.

Epstein method specified in IEC 60404-2 only covers the tests up to 1.8 T. The main reasons for the incomplete B-H curve are manifold and summarised here:

- Power supply: A much stronger AC power source is needed to give a high enough current, i.e. a high magnetic field H to achieve the high flux density B, while no compromise to the sinusoidal voltage output performance (the voltage and frequency variations shall not exceed ± 0.2% of the required value according to IEC 60404-2).

- Waveform control: The AC magnetisation curve is determined for a certain sinusoidal flux, i.e. a sinusoidal induced secondary voltage. The error of secondary voltage form factor (the ratio of RMS value to average rectified value) should be in ±1%, according to IEC 60404-2. However, at very high flux densities, a large reactive power and current would be drawn from the power source. Meanwhile, the voltage will become highly distorted as well.

  Using MATLAB (see Appendix 4), the harmonic distortion issue studies were conducted, and the results can be seen from Fig. 4.12 and Fig. 4.13. At 1.8 T, the secondary voltage can still maintain a good sinusoidal waveform with a total harmonic distortion (THD) of 1.5%. However, at 2.0 T, voltage THD rises to 30% with a significant amount of 3rd and 5th harmonics.

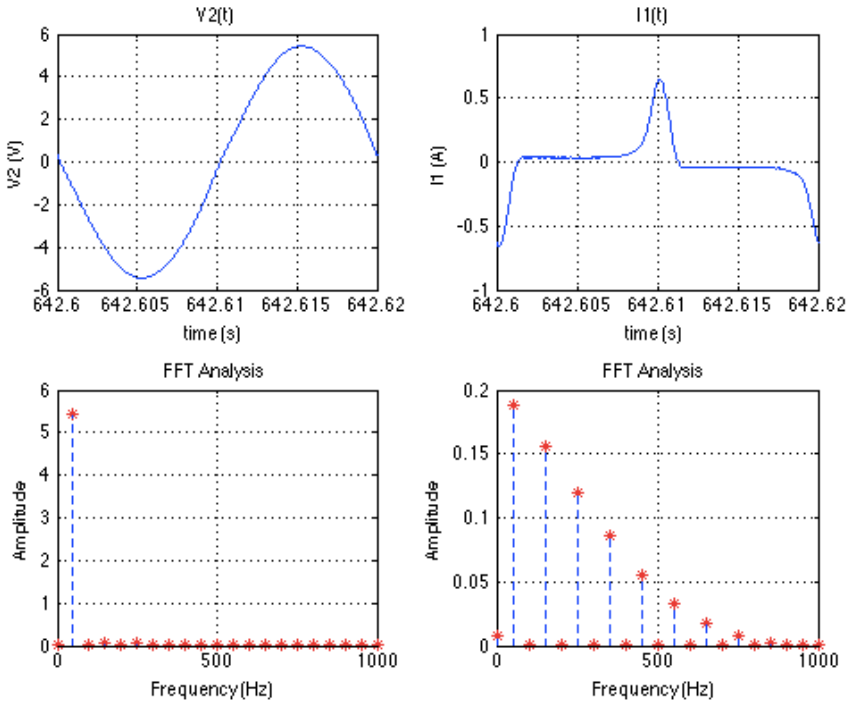

Fig. 4.12 Harmonics analysis of secondary voltage and primary current at 1.8 T using Epstein method.

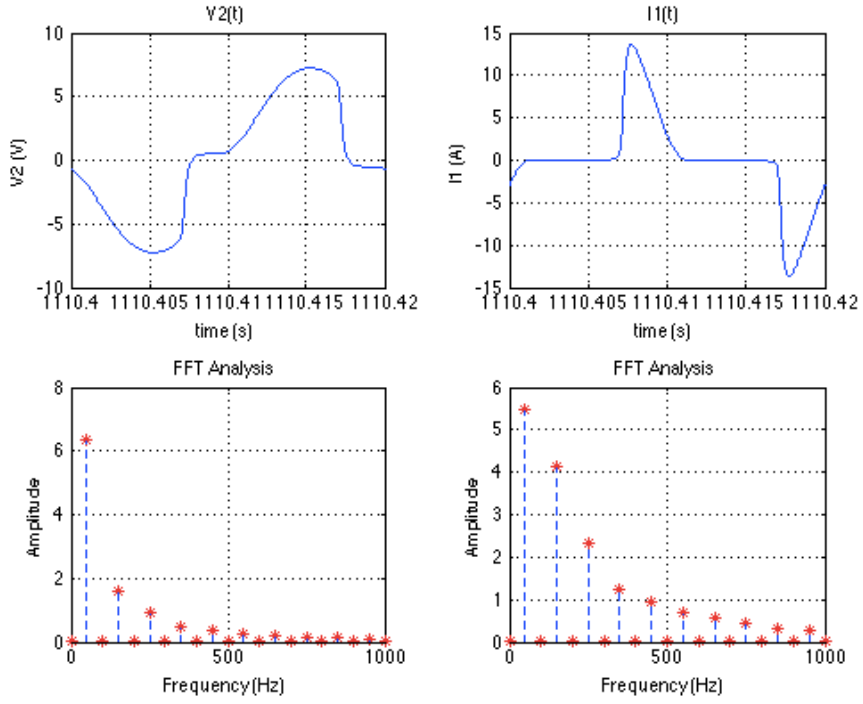

Fig. 4.13 Harmonics analysis of secondary voltage and primary current at 2.0 T using Epstein method.

Recall the practical transformer equivalent circuit in Fig. 3.13, the distortion of V_2 is mainly caused by the significant voltage drop on the primary winding impedance passing through a highly distorted current I_1, while the power source voltage V_s keeps sinusoidal. It is interesting to see, however, the THD of current drops to 91% at 2.0 T compared with 118% at 1.8 T, when the peak value hits up to 13.6 A. The variations of THD for V_2, I_1, and V_s are illustrated in Fig. 4.14. V_2 waveform looks great with THD < 0.5% until 1.75 T, and then THD rises quickly when the core is approaching deep saturation, which is caused by the notable increased current magnitude. The THD of current keeps rising in the linear region of B-H curve, and accelerates climbing speed beyond 1.5 T until 1.9 T. Beyond 1.9 T, the THD of current begins to decrease rapidly, which is not in agreement with some previous work [49].

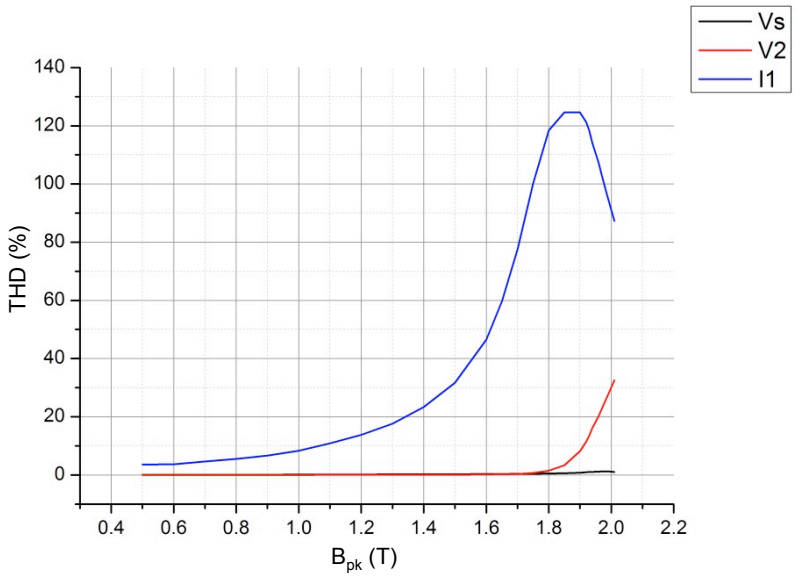

Fig. 4.14 THD of V_2, I_1 and V_s analysis using Epstein method.

The explanation for this phenomenon is that the core branch can be seen as a short-circuit under the situation of deep saturation. The short-circuit current is thus mainly at fundamental frequency. Therefore, this high fundamental component dominates the increase of the total current. As shown in Fig. 4.12 and Fig. 4.13, the fundamental component of current increases 300% at 2.0 T than that at 1.8 T, compared with only 250% increase in 3rd harmonics component. This effect therefore finally decreases the THD.

- Air flux compensation: To comply with IEC 60404-2, the Epstein testing requires an air-core inductor, i.e., mutual inductor, for air flux compensation. The primary winding of the mutual inductor is connected in series with the primary winding of the Epstein frame, and the secondary winding of the mutual inductor is connected to the secondary winding of the Epstein frame in series opposition, as shown in Fig. 4.15.

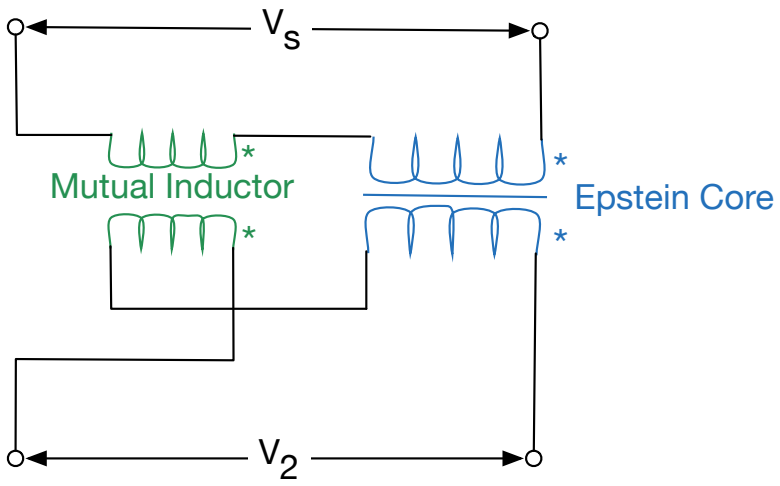

Fig. 4.15 Air flux compensation using a mutual inductor for the Epstein frame.

The adjustment of the mutual inductance is made so that, when passing an alternating current through the primary windings in the absence of the specimen in the apparatus, the voltage measured between the non-common terminals of the secondary windings shall be no more than 0.1% of the voltage appearing across the test apparatus alone. Hence, B can be directly calculated from the induced secondary voltage. Nonetheless, this mutual inductor is not suitable to be used when approaching deep saturation owing to the voltage drop on the windings of the mutual inductor with the highly distorted current. A significant error may therefore arise when deriving B from secondary voltage at high flux densities.

In comparison with the Epstein method, the other standard method recommended by IEC – single sheet/strip tester will be discussed in the following section.

4.5 IEC 60404-3 USING SINGLE SHEET/STRIP TESTER

Single sheet/strip tester (SST) was first developed in the 1970s [50]. As it is an open sample compared with the Epstein frame, an additional yoke is necessary to close the magnetic circuit. The first SST utilises a double horizontal yoke frame by stacking GO strips, cut along the rolling direction, as shown in Fig. 4.16. This design leads to a convenient operation with automatic insertion and extraction of the sheet/strip sample, and it therefore appears attractive to quality control engineers.

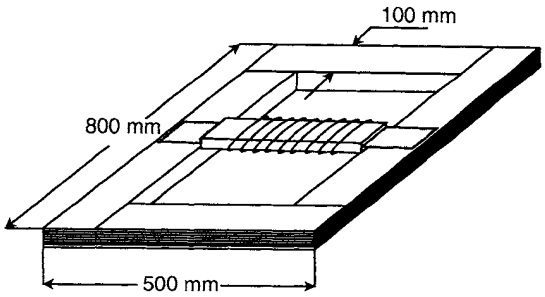

Fig. 4.16 An asymmetric yoke SST system – double horizontal yoke frame [50].

It was later noticed that the eddy currents would appear in the test lamination when the magnetic flux leaves or enters into the yoke (see Fig. 4.17), which is named as "overhang effect" [51]. The overhang effect will bring a systematic error in H as well as extra eddy current losses. This problem can be basically addressed by using a symmetric yoke system, i.e. the test specimen sandwiched between two identical yokes, as shown in Fig. 4.18.

Single sheet tester was first standardised in 1982 by IEC. Due to the strong adherence to Epstein values, this 1982 version SST required calibration of the SST by means of Epstein method. However, this calibration showed considerable scattering, resulting in a poor reproducibility of this SST [43]. After critical revision with studies on single/double yoke construction, lamination modifications, inclusion or exclusion of corrections for the loss in the yoke, H-coil or magnetisation current method to determine H and P, SST was updated in IEC 60404-3 in 1992 [43], [46], [52]. Now it is used more often than the Epstein frame today for it has many advantages such as inexpensiveness and time saving for sample preparation and insertion [20]. In

addition, another important reason is that the conversion of SST values into Epstein values and vice versa has now been sufficiently well established [53].

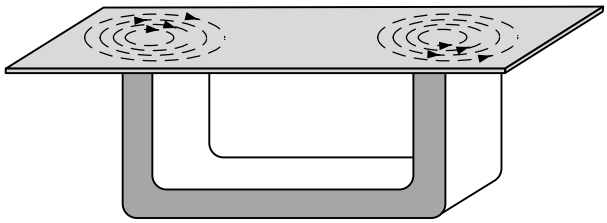

Fig. 4.17 The eddy current generated in the asymmetric yoke system.

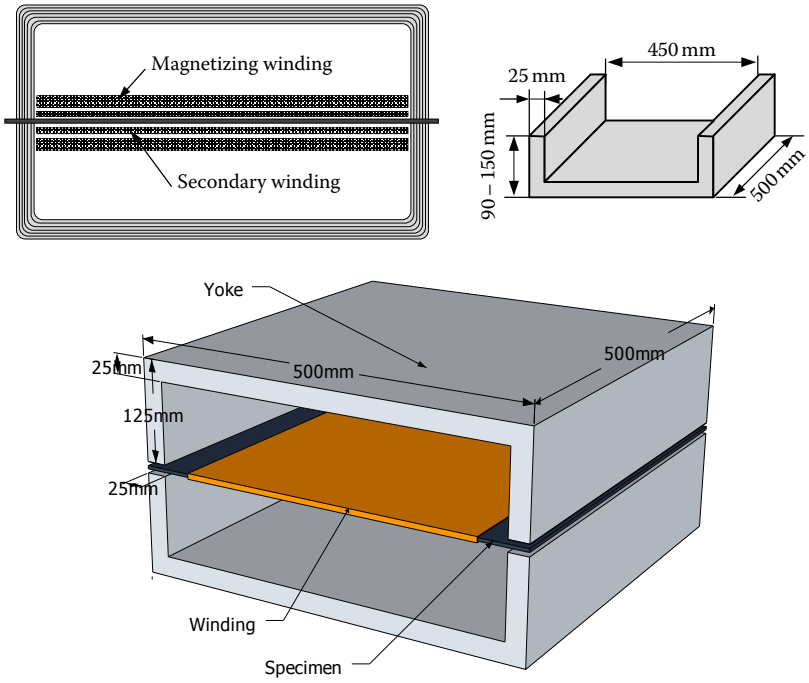

Fig. 4.18 A symmetric yoke SST system – Single sheet tester according to IEC 60404-3.

To comply with IEC 60404-3 [53], the test specimen is 500 mm long and its width can vary between 300 and 500 mm. The double U-yoke, 500 mm wide, is made of either grain-oriented silicon steel or nickel iron alloy with good permeability and low loss. The pole faces are 25 mm thick and are accurately made (coplanar is within 0.5 mm, so no gap is formed between opposite pole faces). The upper yoke is movable upwards to insert the test specimen. The suspension of the upper yoke shall allow part of its weight to be counterbalanced so as to give a force up to 200 N on the test specimen. The primary and secondary windings are at least 440 mm long. The

primary winding can be made of a 400 turn single layer of a 1 mm diameter wire. The number of turns of the secondary winding depends on the characteristic of the measurement instruments.

Similarly to Epstein method, the flux density is derived from the secondary winding voltage using (4.2). For H measurements, there are generally two techniques: directly measurement using the H-coil or indirectly calculation from the primary magnetisation current (MC), as displayed in (4.1). In principle, H-coil method is a more accurate technique, because it avoids the problem of magnetic path length determination. H-coil also helps reduce the non-uniformity of magnetisation of the sample if placed in the central part of the specimen. However, H-coil method was not widely adopted in the industrial practice for the following reasons:

- The output voltage signal by the H-coil is very small and prone to be disturbed by the environment noises.
- The weak output voltage needs further integration chain in order to obtain $H(t)$, which can be another source of instability and possible phase error [54].
- The accuracy of turn-area calibration for H-coil largely affects the accuracy of H measurement.

Consequently, the MC method is preferred because of an excellent reproducibility and reasonably close to the intrinsic steel properties, besides the simplicity and lower cost. The length of magnetic path l_m is thus defined as the distance between the poles of the U-yoke, i.e. 450 mm in IEC 60404-3 [53]. The effects that the two different H measurement techniques bring on measured magnetic properties, particularly at high flux densities, will be further investigated and discussed in the following sections.

4.6 Measurement Bench with Single Strip Tester

4.6.1 Single strip tester

A compact version of single sheet tester – single strip tester (see Fig. 4.19) might be more affordable and suitable in the university lab. The illustrated single strip tester

built by Wolfson Centre for Magnetics has a primary winding 865 turns, secondary winding 250 turns, and l_m just 255 mm. Compared with the single sheet tester, the single strip tester has the following advantages:

- Single sheet tester needs a large sheet sample (500 mm × 500 mm) together with two big and heavy U-yokes, and accompanying high costs; Single strip tester only requires a standard Epstein strip (305 mm × 30 mm), and a much smaller and lighter U-yokes with less pressure on the test specimen (no need for additional suspension structure).

	Epstein	Single sheet tester	Single strip tester
Sample size (mm)	305×30	500×500	305×30

- Results with single strip tester can be compared with the Epstein method more conveniently while using the same test strip.
- It is much more cost-effective to use a small H-coil in the single strip tester providing H-coil technique is applied.
- The smaller size of the test specimen also means less power needed to make the high flux densities measurement available.

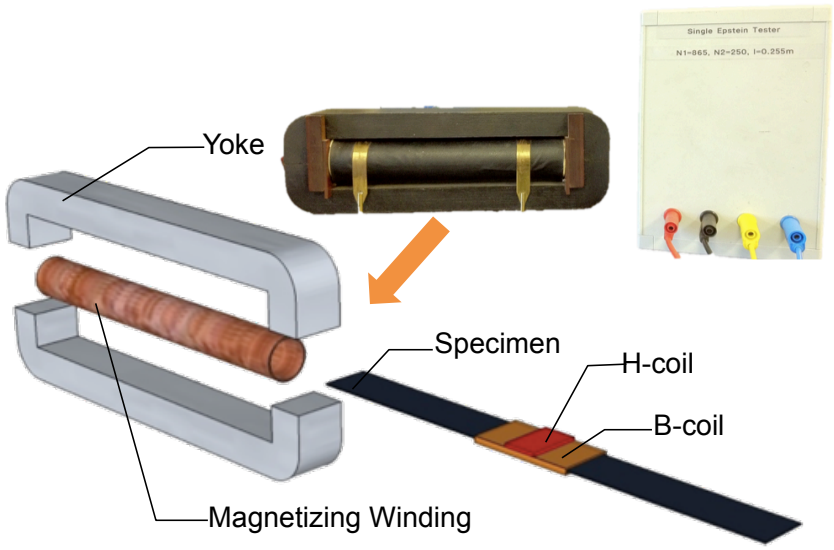

Fig. 4.19 The single strip tester built by Wolfson Centre for Magnetics.

4.6.2 B-coil and H-coil used in the improved SST

B-coil and H-coil were applied in the above single strip tester to further improve its measurement capability particularly for high flux densities.

In order to minimise the errors brought by the air flux, as discussed in Section 4.4.3, a 50-turn, 0.2 mm diameter, thin enameled copper wire was wound directly around the specimen to measure the induced voltage, as the B-coil. The insulation of copper wire must be carefully checked in case it was cut by the sharp edge of the lamination, which leads to the short circuit. The check can be carried out via measuring the resistance between the terminal of the B-coil and the lamination cutting edge with an ohmmeter. Besides, the leads of B-coil must be twisted to remove the effect of the stray magnetic field and increase the reading accuracy, as shown in Fig. 4.20. The effect of B-coil compared with the original secondary winding will be analysed in the following section.

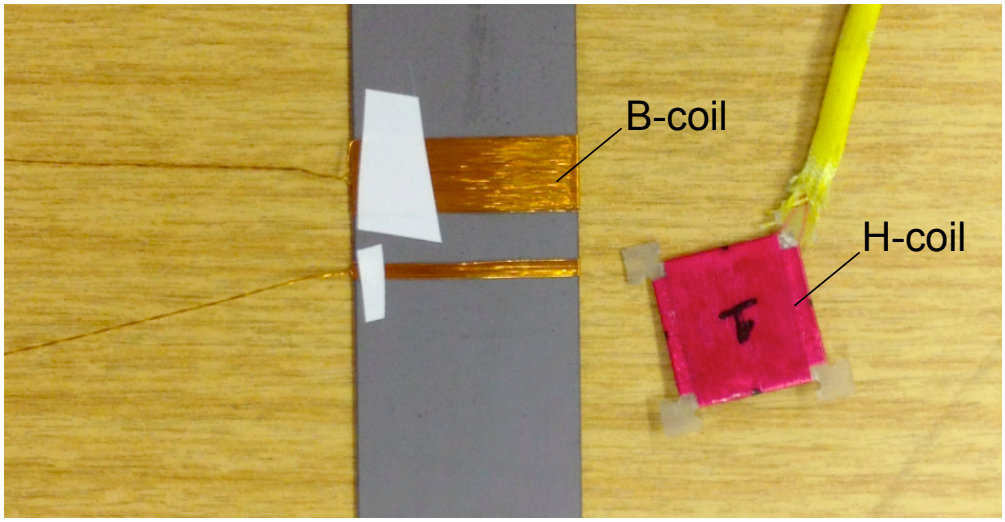

Fig. 4.20 B-coil and H-coil used in the experiments.

H-coil (the red one in Fig. 4.20), made of 1000-turn, 0.02 mm diameter copper wire wound on a glass fiber reinforced plastic (GFRP) frame, was placed on top of the B-coil to read the magnetic field H. The leads of H-coil also need to be twisted to avoid the induced voltage in the leads' loop and, therefore, strengthen the output stability.

It would be useful to compare the H-coil techniques and MC technique when measuring H, especially when B > 1.8 T.

Recall the relationship between B and H in the air under sinusoidal AC magnetisation, the H-coil's average output voltage U_{av} is thus simply given by

$$U_{av} = 200NA\mu_0 H_{pk} = kH_{pk} \tag{4.3}$$

where: N = Number of turns

A = Cross-sectional area of the coil (m^2)

μ_0 = Permeability of free space (H/m)

k = Coefficient constant (V·m/A)

H_{pk} = Peak magnetic field (A/m)

Before H-coil is used for the SST measurement, it first needs the calibration, whose procedures are described as follows:

- H-coil was positioned together with a precision Hall sensor at the centre of a uniformly wound long solenoid, which was fed a 50 Hz sinusoidal voltage.
- The H-coil output was connected to a digital voltmeter to obtain U_{av}.
- H_{pk} read from the Hall sensor together with U_{av} was then used to acquire k through the linear regression.

It should also be noticed that the accuracy of H-coil is easily affected by the background noise especially when the H value is low. The systematic error brought by the Hall sensor (a transducer that varies its output voltage in response to a magnetic field) should also be taken into account.

Both B-coil and H-coil were placed in the central part of the sample to avoid the error caused by the magnetic field distortion near to the ends of the magnetising winding as shown in Fig. 4.11.

Since the H-coil is placed on the surface of the specimen, there still exists the difference between the measured H value and the real H value in the specimen. Applying two H-coils on both upper and down sides of the specimen may help further improve the measurement accuracy by average the two readings. The problem of uncertainty of determination of the length of magnetic path can be also solved by using the compensation method Rogowski–Chattock potenti-ometer (RCP) [17].

4.6.3 The improved SST measurement system

The schematic measurement system is shown in Fig. 4.21. A computer, with virtual instrumentation software LabVIEW and a data acquisition/generation card NI BNC-2110 (DAQ), generates a voltage waveform, which is fed into a power amplifier whose output current is used to magnetise the specimen. An isolation transformer between the power amplifier and the magnetising winding is connected, which removes any DC component in the magnetising current. The measured signals are fed back into the DAQ, where they are acquired with 500 kS/s sampling rate and sent to the computer. Meanwhile, the waveform of B is real-time monitored and controlled to be sinusoidal with the digital feedback control technique developed by Wolfson Centre for Magnetics (to be discussed in the next section). The form factor error can achieve 0.05% (even better than the 1% required by IEC standard).

The complete B-H loops are obtained at set peak B levels, and the specific power loss P_S is calculated through the integration of the B-H loop area. The vertex coordinates (H_{pk}, B_{pk}) for each flux density level are also recorded in steps of 0.1 T from 0.1 T to 2.0 T in order to obtain the magnetisation curve (B-H curve).

The control panel of LabVIEW is displayed in Fig. 4.22. The new features of B-coil and H-coil measurement were added into the standard SST measurement programme in order to compare the different results between the standard SST and improved SST.

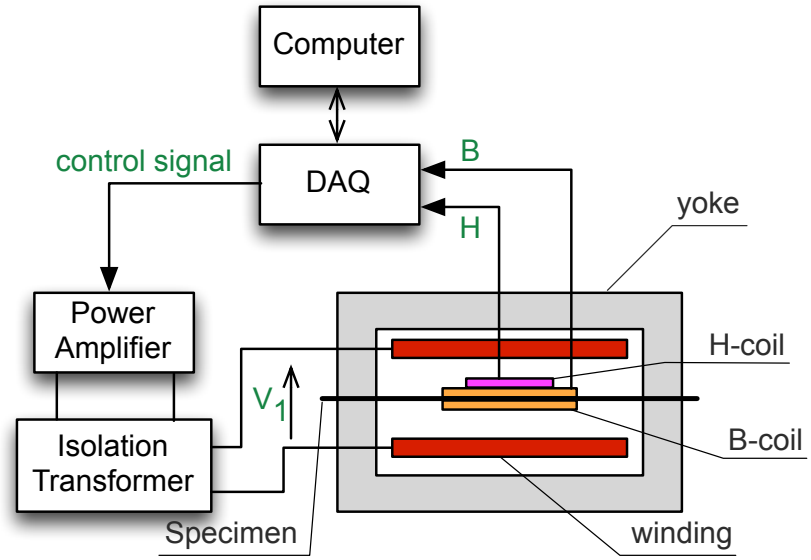

Fig. 4.21 The block diagram of the improved SST measurement system.

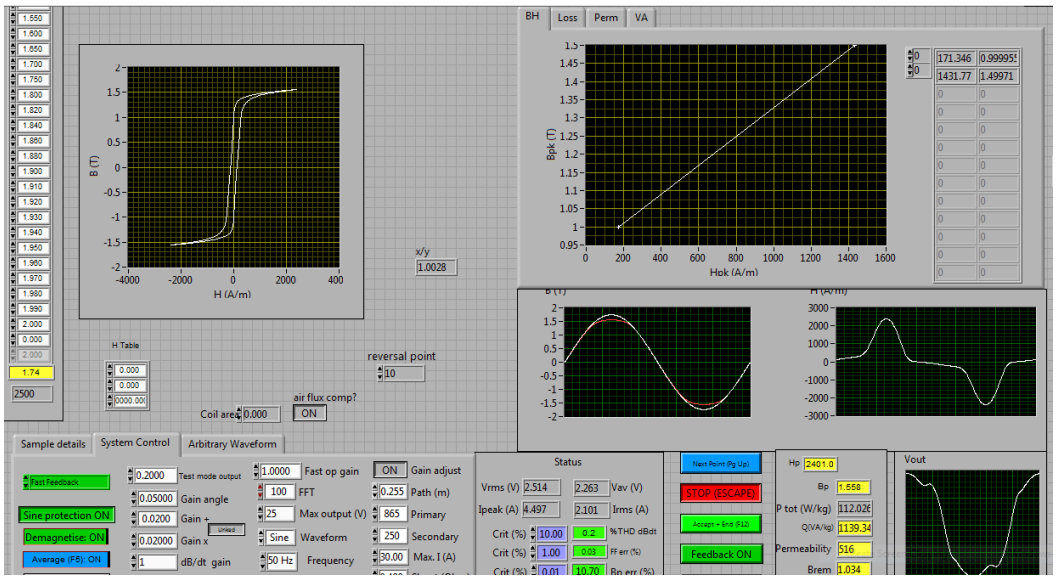

Fig. 4.22 The control panel of the improved SST measurement system.

4.6.4 Digital feedback control scheme

Properties of electrical steels, such as B-H curve and power loss, are very sensitive to the distorted flux. For a higher frequency H component, a lower B will be obtained for the same material due to the reduced permeability. Besides, same peak flux density with higher frequency will contribute much larger losses. In order to make the electrical steels magnetic properties measurement results universally usable and

comparable, one difficulty needs to be overcome is the flux waveform distortion due to the nonlinear characteristics of B-H curve. For this reason, the feedback control must be adopted to keep the flux waveform sinusoidal at certain required frequency, as required by IEC. For the traditional measurement, it seems sufficient to use a simple analog electronic feedback circuit as illustrated in Fig. 4.23. However, for some complicated conditions, e.g. very high flux densities, this analog feedback will fail, which is caused by the oscillation of the magnitude of the controlled signal leading to instability of the closed control loop [55].

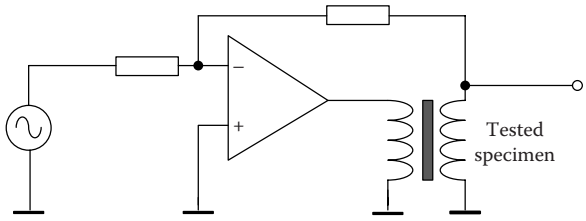

Fig. 4.23 Anolog electronic feedback circuit for a sinusoidal flux waveform control.

The digital feedback control is more versatile and effective. The principle is to change the power source voltage (input signal) in order to obtain the required sinusoidal secondary voltage (response signal). Each time, the response signal changes after the input signal changes. A typical algorithm requires several successive iterative approximation steps until the form factor of response signal satisfies the set criteria.

A possible approach is to apply the fast Fourier analysis to the response signal. If the unexpected harmonics are detected, the computer generates the input signal with negative harmonics (the phase shift needs to be taken into account) to cancel this distortion effect [56]. Another popular digital control methods are fast digital methods – applying the controller or adaptive filter between the wave generator and the test specimen [55]. Fig. 4.24 shows this algorithm of utilising the error signal between required reference signal and measured signals. This algorithm does not need to know properties of the test specimen or the yoke, because the whole control circuit can be treated as a "black box" [17]. It can thus cooperate with various test

systems with full versatility. Recently, waveform control techniques using artificial neural network (ANN) were also proposed with reference signal dB/dt [57].

The digital feedback technique developed by Wolfson Centre for Magnetics and adopted in the improved SST measurement was mainly the fast digital method combing with the FFT. The LabVIEW block diagram is illustrated in Fig. 4.25.

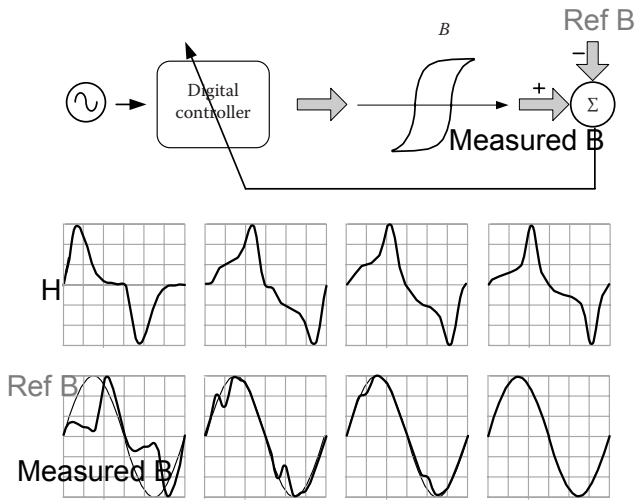

Fig. 4.24 The fast digital feedback control with digital controller.

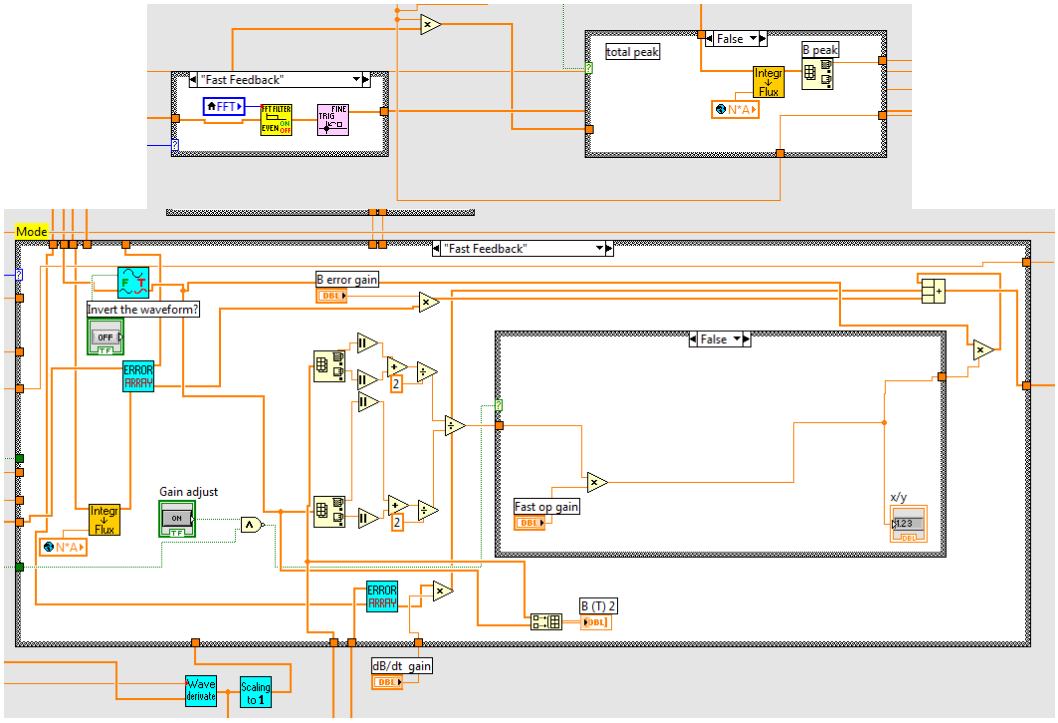

Fig. 4.25 The application of fast digital feedback and FFT techniques in LabVIEW.

4.7 Measurement Results and Discussions

The performance of the proposed SST was assessed by measuring on one commonly used grade of 0.30 mm HGO electrical sample at 50 Hz AC magnetisation. The specimen was firstly measured using the standard SST. Then it was tested with the proposed improved SST using the B-coil to measure the flux density, and H-coil to measure the magnetic field. Finally, the improved SST with B-coil and the standard H measurement methodology was carried out in order to investigate the necessity of H-coil.

4.7.1 Capability verification below 1.80 T

As shown in Fig. 4.26, "Standard SST", "B-coil + H-coil", and "B-coil" represent the properties obtained using the standard SST, improved SST with B-coil + H-coil, and improved SST with only the B-coil (H is obtained using MC technique). The capability of the improved SST has been verified up to 1.80 T by comparing results with values obtained on the same sample tested in a standard SST. From Fig. 4.26, the average relative difference in H and P_S measured with the standard SST and the improved SST is not more than 3% and 2% respectively over the full measurement range. This confirms the improved SST performs well as the standard SST in the normal measurement range.

Fig. 4.26 also shows that the H-coil is good enough to provide the B-H curve. However, it does not give a smooth power loss curve. The explanation for it is that the DAQ has to compromise on the resolution when the measurement range is enlarged. Besides, the output voltage signal by the H-coil is small and prone to be disturbed by environment noises. Therefore, the relatively poor performance of H-coil output when H is very low leads to the error in the B-H loop area integration. For the reasons above, only results over 1.0 T using H-coil are presented here. The P_S computation

and its accuracy are largely dependent upon the H(t) measurement, and the instability of the H(t) waveform from H-coil finally contributes to this deviation, as shown in Fig. 4.26.

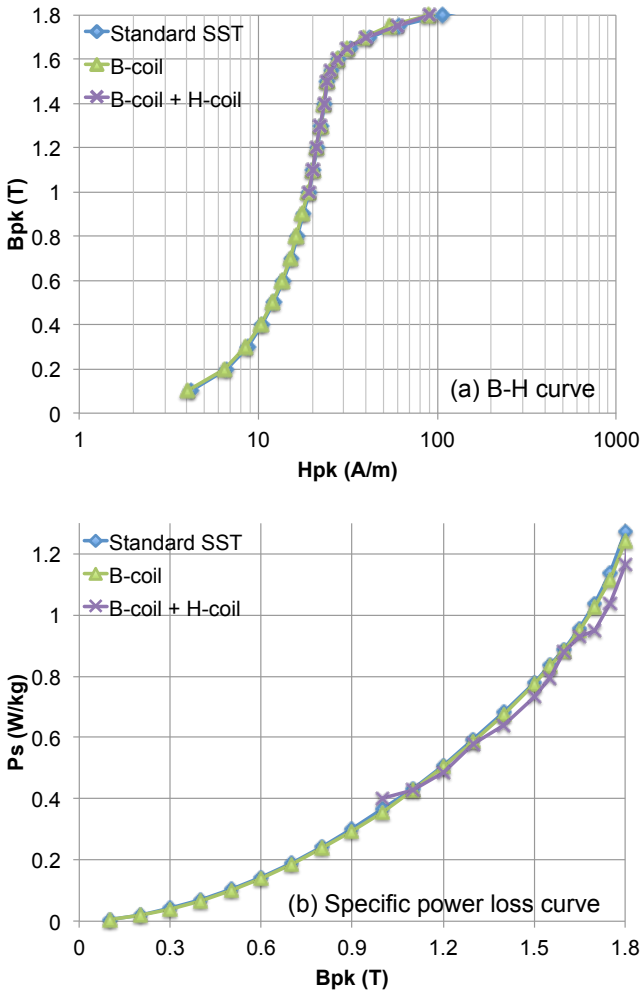

Fig. 4.26 Comparison between magnetic properties from standard SST and improved SST below 1.80 T.

4.7.2 Magnetic properties at high flux densities

As shown in Fig. 4.27, "Standard SST", "B-coil + H-coil", and "B-coil" represent the magnetic properties of the HGO strip at flux densities up to 2.0 T obtained using the standard SST, improved SST with B-coil + H-coil, and improved SST with only the B-coil (H is obtained using MC technique). As expected, the standard SST failed to produce meaningful results at high flux densities. In the standard SST measurement

system, although attempting to control B sinusoidal by using mutual inductor, B obtained from the voltage winding still consists of not only the flux carried by the lamination in deep saturation, but also some highly distorted air flux. The real flux carried by the lamination is also distorted, and the magnetic property of the HGO specimen at 50 Hz is no longer represented with the standard SST. Besides, the control system can hardly keep the measured B to be sinusoidal above 1.96 T, at which point the measurement using the standard SST has to stop according to the standard defined criteria.

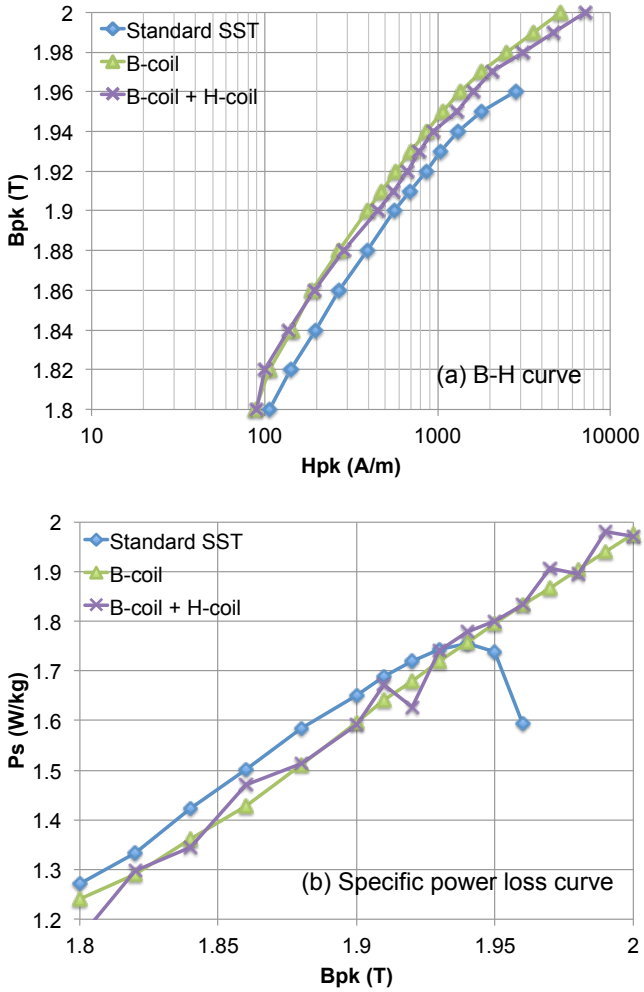

Fig. 4.27 Comparison between magnetic properties from standard SST and improved SST at high flux densities.

Fig. 4.27(b) shows the P_S measured with the standard SST starts to drop after 1.94 T. It can be explained if we look at the B-H loop presented in Fig. 4.28. It is noted that a

crossover appears near (600 A/m, 1.90 T) of the B-H loop measured with the standard SST in the dashed curve. Consequently, it causes a negative loop area integrated from the top right corner part, leading to the drop of P_S.

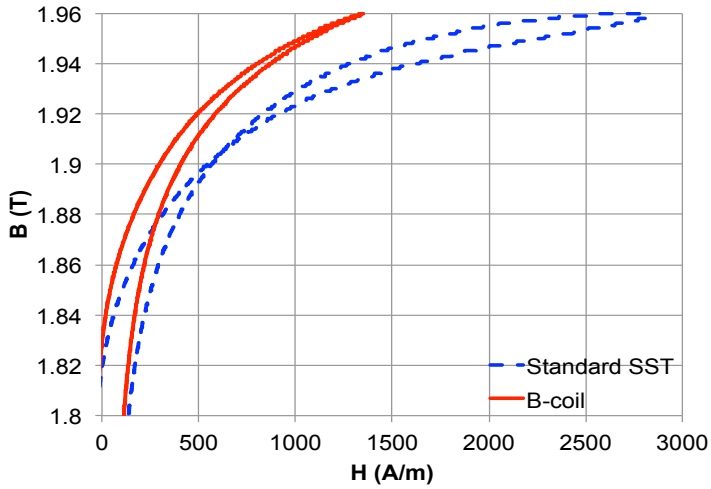

Fig. 4.28 Comparison between B-H loops from standard SST and improved SST at B_{pk}=1.96 T.

This crossover problem can be further analysed through the waveforms of B and H, demonstrated by Fig. 4.29. Contrary to the knowledge of hysteresis characteristics, the H value measured using the standard SST is 1287 A/m at 1.94 T when B is increasing, which is less than 1646 A/m when B is decreasing at 1.94 T. Compared to that, the improved SST always obtains a larger H value when B is decreasing. Therefore, we did not see any crossover problem in the B-H loop using the improved SST owning to the correct measurement.

The test results shown in Fig. 4.27 confirm the capability of the improved SST at high flux densities. Either the "B-coil" or the "B-coil + H-coil" method can achieve 2 T smoothly. Fig. 4.27(a) also shows that the error in the B-H characteristic obtained from the standard SST may lead to an overestimation of H by 50% when B is at 1.9 T, and as much as 108% at 1.96 T for this test specimen. However, the specific power loss difference between the standard SST and the improved SST with B-coil is rather small, i.e., less than 5%, until the crossover problem occurs at 1.94 T. That is because the work done by air flux for the complete loop integration is always equal to null.

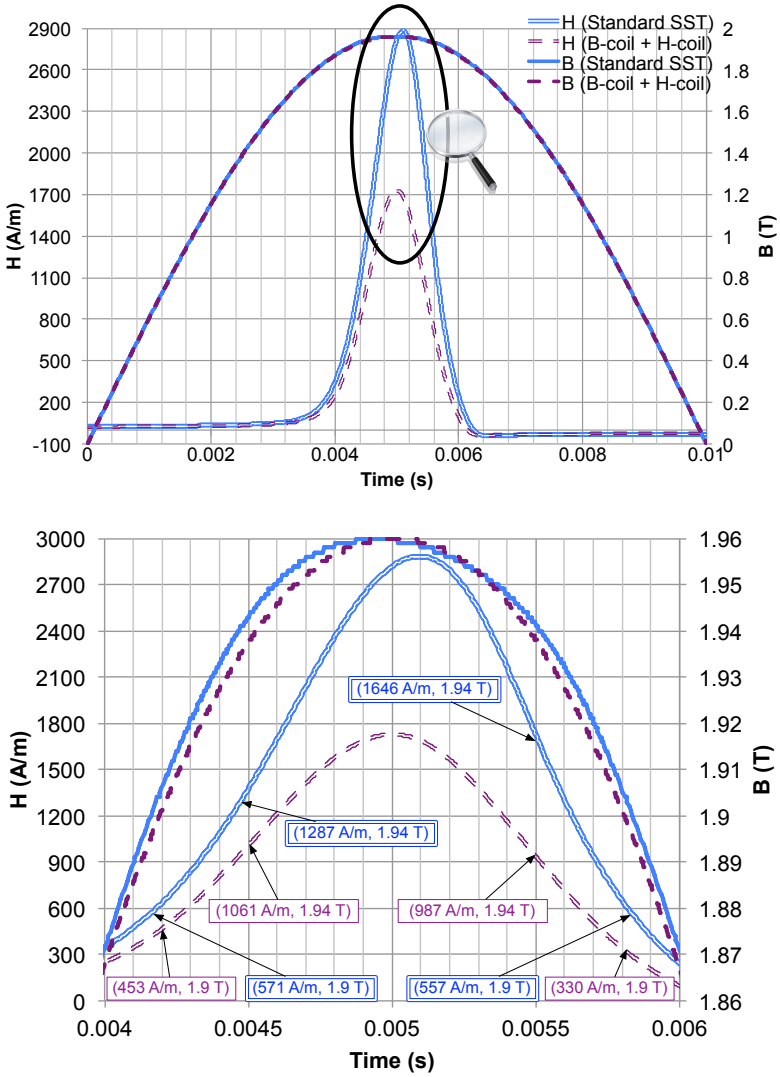

Fig. 4.29 Comparison between B and H waveforms from standard SST and improved SST at 1.96 T.

It is interesting to observe the maximum relative error is less than 15% in the worst condition at 2.0 T when applying the H-coil instead of using H derived from the calculation of the magnetising current, which means the equivalent magnetic path length varies little before deep saturation. However, the H-coil shows its major disadvantage: It is difficult for the DAQ device to maintain sufficient resolution while the magnetisation current range is largely increased particularly into deep saturation. This leads to the error in the specific power loss P_S calculation and thus an unstable increase in P_S as shown in Fig. 4.27(b). Hence, the recommended improved SST suitable for measurement at high flux densities to use the B-coil to avoid the air flux

error and the standard H computation methodologies (MC) to achieve sufficiently accurate magnetic properties at high flux densities, while keeping a good stability and reproducibility. This conclusion from experiments agrees with the previous discussions in Section 4.5.

4.7.3 Reproducibility

Each measurement was repeated five times and the relative standard deviations of H and P_S at various flux density levels are demonstrated in Fig. 4.30. The results comply with the reproducibility requirements (relative standard deviation < 7%) in the IEC standard.

From Fig. 4.30, it can be seen that the SST using MC technique for H measurement achieves much better H and P_S reproducibilities. As shown in Fig. 4.30 (b), it once again verifies the drawback of the H-coil as the relative standard deviation in P_S using the H-coil is about four times higher compared to the MC indirect H computation methodology.

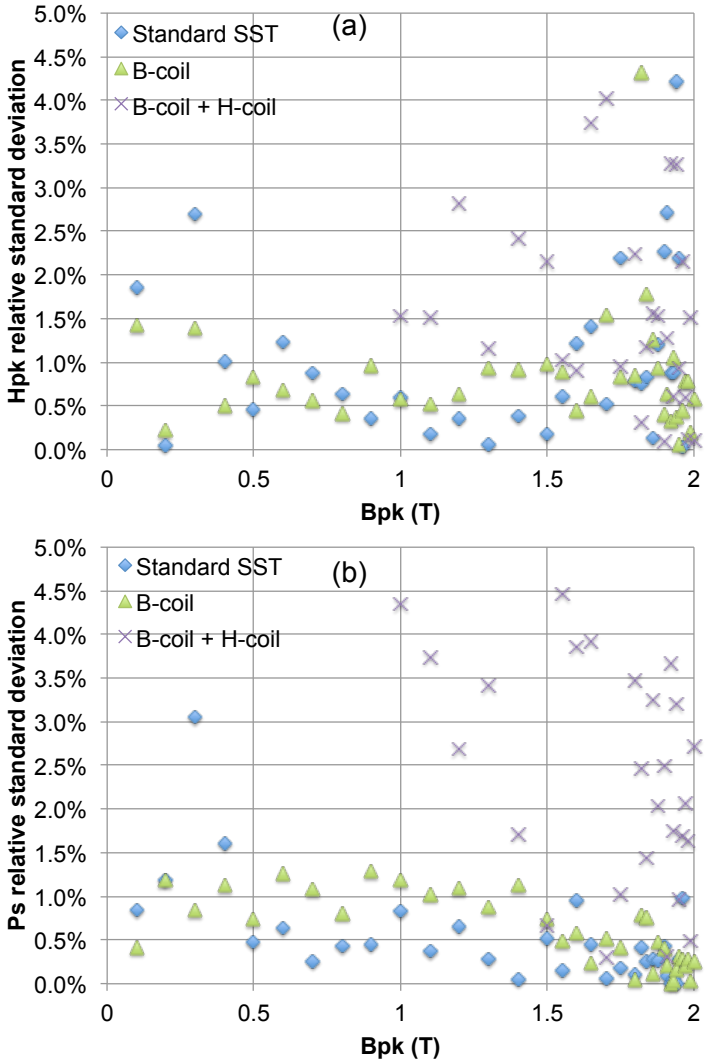

Fig. 4.30 Relative standard deviations for various flux density levels.

4.8 Application of Measured Magnetic Properties at High Flux Densities

Simulation software with finite element method extrapolates the measured B-H curve by curve fitting in order to estimate the saturation condition. This might produce unconvincing flux distributions and possibly lead to an expensive conservative core design [38].

In order to investigate the error brought by the B-H curve extrapolation, the B-H toolbox of AREVA T&D SLIM simulation software is applied to extrapolate the measured standard SST data from 1.9 T to 2.0 T. SLIM divides the B-H curve into two

sections. A nonlinear exponential function is used to approximate the B-H curve at low flux densities, and a linear function is applied at high flux densities. The extrapolated B-H curve is then compared with the measured result using the improved SST, as illustrated in Fig. 4.31. It reveals that the extrapolated curve overestimates the magnetising current at a certain B in deep saturation. The relative error can be up to 60%. That also means the B level is actually underestimated for a certain magnetising current in deep saturation, which might be potentially harmful to the power transformer if this is not considered in the core design.

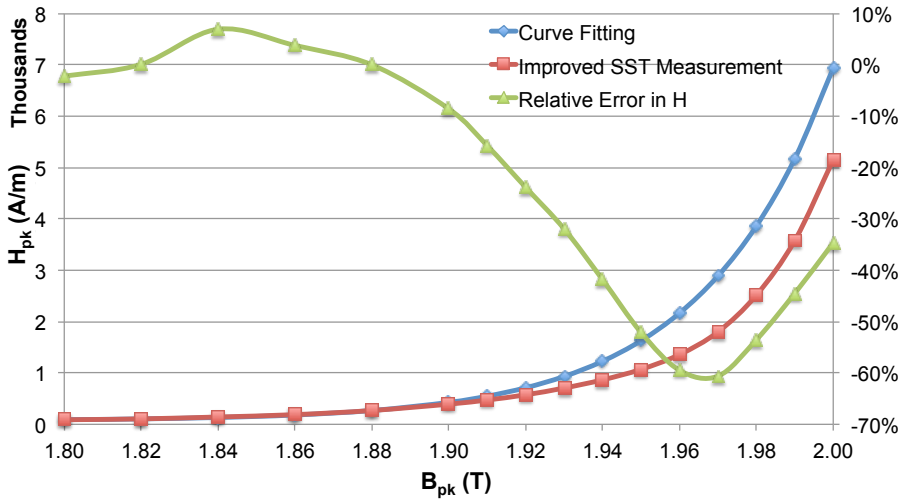

Fig. 4.31 Comparison between B-H curves from measurement and curve fitting using AREVA T&D SLIM simulation software.

The measured B-H curves up to 2.0 T on GO steels can be used to explore better B-H curve fitting and extrapolation equations, which will be discussed in Chapter 5. The improved SST also enables us to measure the P_S at different frequencies until deep saturation, which can be used to separate the iron losses and help build a better mathematical model for core losses.

4.9 Summary

This chapter first critically reviewed the development, standardization of Epstein frame and SST. The digital DAQ test bench with Epstein method was built in the laboratory at The University of Manchester, and the measurements were successfully

conducted on the GO specimens. It was found that the measured B-H curve is not notably affected if there are more than four layers of laminations. The uncertainty of Epstein method is mainly caused by the double-lapped corners, which is not suitable for the magnetic property measurement at high flux densities because of the inevitable air flux error between lamination layers.

An improved single strip tester was made at the Wolfson Centre for Magnetics on the basis of the standard single strip tester. The test results on a HGO sample up to 2.0 T at 50 Hz confirms its good performance in both the conventional measurement region and the deep saturation region. It revealed that it is a must to replace the secondary winding coil by a B-coil to obtain the main flux without air flux between the specimen and the secondary winding for the deep saturation region. Otherwise, a crossover would appear at the B-H loop, leading to the drop of specific power loss at 1.94 T and beyond. The unstable flux eventually results that the standard SST measurement automatically stops at 1.96 T. In terms of H measurement technique, the standard magnetisation current (MC) method as an indirect way performs better than the H-coil method as a direct way. This is mainly owing to the poor accuracy at low H region affected by environment noises. Hence, the suggested improvement SST adopts is the B-coil to measure B and the MC method to measure H.

Using the B-H toolbox of SLIM software, the B-H curve extrapolation was made for the range from 1.9 T to 2.0 T. The results revealed that the extrapolated curve overestimates the magnetising current at a certain B in deep saturation. Reciprocally, it also can underestimate the B level at a certain magnetising current.

The test bench developed can be used to measure the magnetic properties of GO materials up to 2.0 T and covers AC magnetisation frequency up to 400 Hz. It provides a possibility to validate the current extrapolation models for B-H curve, and deepen the understandings on how each component of core losses varies at high flux densities.

5 B-H Curve Approximation and Prediction

5.1 Introduction

As one of the most important magnetic properties of electrical steels, the nonlinear AC magnetisation curve (B-H curve) is key for the design of power transformers and motors to reduce size and improve performance [58]–[60]. The B-H curve is also essential for transformers and reactors modelling in power system switching transient studies such as ferroresonance [41], [61]. Measured *B-H* data in accordance with the IEC standards [44], [53] is usually expressed in a tabular form in steps of 0.10 up to 1.80 Tesla (T). This is used as input for CAD programs, together with an interpolation procedure to produce the B-H curve.

In most cases, it is acceptable to represent the curve by a series of straight lines between fixed points on the curve (linear interpolation). However, kinks caused by the junction of two straight lines are magnified in the solution of a problem, which could lead to instability of the iterative computation [62]. The nonlinear B-H curve expressed in an explicit equation form is therefore particularly useful and is preferred to yield accurate results while saving computer time.

In the past, there have been many attempts to fit equations to experimental B-H data, and the research falls into two main categories: One deals with theoretical formulations based on physical models [60], [63]–[67], producing expressions which are too complex to use in engineering software. The other expresses the magnetisation characteristics in empirical mathematical terms, which are useful for quantitative estimation despite little theoretical basis [62], [67]–[75]. The second category remains popular when attempting the best representative for the B-H characteristic [75].

Since the 1960s, several attempts including exponential, power series and Froelich's hyperbolic functions, have been made to express the magnetisation characteristic [62], [68]–[73]. None of these, however, makes a satisfactory approximation over the full useful range of B-H curve (0 - 2.00 T). After failing to find the best suitable single

fitting function, some researchers tried to subdivide the magnetisation curve into a large number of sections and employ numerical piecewise interpolation, such as cubic Bézier spline [76]–[78]. Fourier Series [68], [79] and Fuzzy modelling [80] have recently been introduced to give an accurate approximation. Nevertheless, the resulting complex expression and the required artifice for those methods are improper to use in current CAD software.

The previous work also suffer from the following weaknesses: (i) the fitting quality was rarely quantified or compared among different approximation expressions except [76], [81]; (ii) little validation was made using the experimental results of modern electrical steels; (iii) the performance of fitting at high flux densities (>1.80 T) and the extrapolation capability have not been tested yet due to limited experimental data.

Based on the measured B-H characteristic of modern commercial grain-oriented (GO) electrical steels over a wide range up to 2.00 T using the proposed improved SST in Section 4.6, the 10 most popular fitting equations proposed previously were critically evaluated in this chapter. A new simple explicit empirical function is then proposed here. Its performance verifications are also given in terms of both approximation and prediction capability where high flux density data are not available from steel manufacturers.

5.2 Nonlinear B-H Curve Fitting Consideration

5.2.1 Merit function consideration

In order to find the best-fit B-H curve, we have to find parameter values that minimise the difference between the observed experimental data points and the chosen fitting equation model. It is thus usual to see the entire model-fitting process described in terms of minimization of an error function (merit function). The most common representation of the merit function for regression models is based on the chi-square (χ^2) distribution, which has been used in the statistics to assess "goodness-of-fit" [82]. There are three merit functions used in the previous studies [62], [74], [75], where H_i

and B_i are the ith measured peak magnetic field strength and peak flux density. $B=f(H)$ is the approximation function for the N-points B-H data.

1) Sum of absolute errors

$$\sum_{i=1}^{N}\left[B_i - f\left(H_i\right)\right] \text{ is a minimum}$$

The absolute error for a certain point can remain rather great, where the sum of absolute errors is small, if the errors distribute symmetrically.

2) Maximum error

$$\max\left[B_i - f\left(H_i\right)\right] \text{ is a minimum}$$

Although it appears to be justified in the metrology field, the application turns out delicate because the convergence is not always assured for nonlinear systems.

3) Sum of squares of errors

$$\sum_{i=1}^{N}\left[B_i - f\left(H_i\right)\right]^2 \text{ is a minimum}$$

The third merit function also known as "least squares" is taken here because of its best-fit compromise between the former two, and the convenience to handle mathematically.

5.2.2 Regression algorithm

The merit function for linear models is quadratic in nature, and is thus amenable to an exact analytical solution. In contrast, nonlinear problems such as B-H curve must be solved iteratively. This procedure can be summarised as follows:

1) Define the merit function;

2) Start with a set of initial guesses of the parameters and determine the value of the merit function for this set of guesses;

3) Adjust the parameter guesses and recalculate the merit function. If the merit function is improved, then keep the parameter values as new guesses;

4) Iterate step 3. When further iterations yield a negligible improvement ($\varepsilon = 1.0 \times 10^{-6}$ is selected here) in the fit, stop adjusting the parameter guesses and generate the curve based on the last set of estimates.

The rules for adjusting the parameters of the nonlinear model are based on matrix algebra and are formulated as computer algorithms. There are three widely used algorithms: the gradient search, Gauss-Newton, and Levenberg-Marquardt (LM) [82], [83]. The gradient search works well in the initial iterations, but tends to drag as it approaches a minimum value. Gauss-Newton works best when employed close to the surface minimum, but works poorly in initial iterations. The LM method refines the scaling problem and derives a series of equations which can simulate the gradient search method at early iterations and Gauss-Newton method at later stages closer to the minimum, exploiting the best features of both. The LM method is therefore chosen in this chapter for the following nonlinear B-H curve regression.

5.2.3 Fitting quality assessment

There is a growing demand of the best-fitted B-H curve for the electromagnetic analysis, which makes it paramount to measure the goodness-of-fit quantitatively.

The sum of squares of errors (SSE) is the quantity that most researchers turn to because it is also used for the merit function. The smaller the SSE value, the better is the fitting quality. In general, the more parameters that are added to a model, the greater is the likelihood of observing a very close fit of the regression curve to the data, and thus a smaller SSE. However, this comes at the cost of degrees of freedom (total number of data points N minus the number of model parameters K). $S_{y.x}$ is

accordingly defined as the square root of SSE divided by the degrees of freedom to measure the standard deviation of the residuals:

$$S_{y.x} = \sqrt{\frac{SSE}{N-K}} \tag{5.1}$$

$S_{y.x}$ value is mainly dependent on the magnitude of fitted points. It is therefore difficult to compare the fitting performances between $B=f(H)$ models and $H=f(B)$ models because the order of magnitude of B is much smaller than that of H. Perhaps the R^2 value (coefficient of determination) is more appropriate as a measure of goodness-of-fit in this case:

$$R^2 = 1 - \frac{SSE}{SSTotal} \tag{5.2}$$

where $SSTotal$ is the sum of the squared differences between each fitted point and the average of all fitted points. The closer to unity R^2 value is, the closer the model fits the dataset. Similar to the SSE, the model with more parameters is easier to achieve a higher R^2. Adjusted R^2 can then be applied to compare different fitting equations with different numbers of parameters:

$$\text{Adjusted } R^2 = 1 - \frac{SSE/(N-K)}{SSTotal/(N-1)} \tag{5.3}$$

Although useful, R^2 value is simply an index of how close the data points are to the regression curve, not necessarily an index of the correctness of the model. Hence, while R^2 may be used as a starting point in the assessment of goodness-of-fit, it should be used in conjunction with other criteria such as the normality test of residuals.

If the fitting equation is adequate in describing the behavior of the measured data, the scatter of points around the curve follows a Gaussian distribution. The normality test will give the probability of obtaining data whose residuals deviate from a

Gaussian distribution as much (or more so) as the data does. The versatile and powerful D'Agostino-Pearson normality test [84]is thus applied here to verify the fitting performance [85]. It first computes the skewness and kurtosis to quantify how far the distribution is from Gaussian in terms of asymmetry and shape. It then calculates how far each of these values differs from the value expected with a Gaussian distribution, and computes a single P value from the sum of these discrepancies. A large P value means that the data are consistent with the regression assumptions.

5.3 Nonlinear B-H Curve Approximation

5.3.1 Theoretical expressions based on physical models

For convenience, the magnetisation curve is traditionally divided into three parts.

The first part, known as Rayleigh region, corresponds to weak fields and is believed to be entirely controlled by domain wall motion. The magnetisation curve has a quadratic shape as given as [86]:

$$B = \left(\mu_0 + \chi_0\right) H + \nu H^2 \tag{5.4}$$

where μ_0, χ_0 and ν are the permeability of free space, initial susceptibility and the Rayleigh constant respectively.

The central portion of the magnetisation curve is a problematic region, because the main processes occurring here are large Barkhausen jumps, which causes domain wall motion to become jerky and discontinuous. The shape of this portion of the magnetisation curve varies widely from material to material.

In high fields, on the other hand, domain rotation is the predominant effect, and magnetisation generally follows the "law of approach" expressed as a series of H^{-1} terms as follows:

$$B = B_S\left[1 - \frac{a}{H} - \frac{b}{H^2} - \cdots\right] \tag{5.5}$$

where B_S is the material saturation flux densities; a, b, etc., are constants for a given material and temperature. The constant a is generally interpreted as being related to microstress, and constant b to crystal anisotropy. However, there are both practical and theoretical difficulties in the use of this equation. The practical difficulty is in deciding what is the exact range of fields to apply this law: the field should be chosen high enough so that all domain wall motion is complete, but there is no clear criterion to determine when this condition is reached. The theoretical difficulties are of two kinds. Firstly, the physical significance of the a/H term has been variously interpreted, with no consensus. Secondly, $1/H$ and $1/H^2$ terms are not the only possibilities: $1/H^{1/2}$ and $1/H^{3/2}$ have been proposed with theoretical grounds [86]. It may therefore be concluded that the understanding of the approach to saturation is still in a distinctly unsatisfactory state.

5.3.2 Explicit approximation expressions

In engineering applications, the magnetisation curve can be expressed explicitly as either a function of magnetic field strength H, i.e. $B=f(H)$, or a function of magnetic flux density B, i.e. $H=f(B)$. Ten common approximation expressions are listed in Table 5.1, comprising four in the form $H=f(B)$ and six in form $B=f(H)$, together with the proposed new empirical function (11) in the last row.

Table 5.1 Approximation expressions for B-H curve.

No.	Expression	Number of parameters
(1)	$H = a_0 + a_1 B + \ldots + a_9 B^9$	10
(2)	$H = aB + bB^n$	3
(3)	$H = ae^{bB}$	2
(4)	$H = \left(ae^{bB^2} + c\right)B$	3
(5)	$B = a_0 + a_1 H - a_2 H^{-1}$	3
(6)	$B = \frac{a_0 + a_1 H + a_2 H^2}{1 + b_1 H + b_2 H^2} + \mu_0 H$	6
(7)	$B = a - be^{-cH}$	3
(8)	$B = a_0 + a_1 e^{-b_1 H} + \cdots + a_4 e^{-b_4 H}$	9
(9)	$B = a\tan^{-1}\left(bH\right) + cH$	3
(10)	$B = a(\coth\frac{H}{b} - \frac{b}{H}) + c$	3
(11)	$B = \frac{a}{1 + \frac{b}{H} + \frac{c}{H^2}} + d\left(\coth\frac{H}{e} - \frac{e}{H}\right) + fH$	6

5.3.3 Approximation performance validation in the 0-2.00 T region

Using the B-H curves of CGO and HGO samples measured with the improved SST at 50 Hz introduced in Section 4.6.3, B-H data with 36 data points is used in this section to evaluate the performances of different approximation equations over the full useful range of B-H curves (B up to 2.00 T and H up to 10 kA/m). The fitting quality assessment was conducted using MATLAB Curve Fitting Toolbox and GraphPad Prism. The fitting results for the CGO and HGO samples are displayed in Fig. 5.1 (a) and Fig. 5.1 (b) respectively.

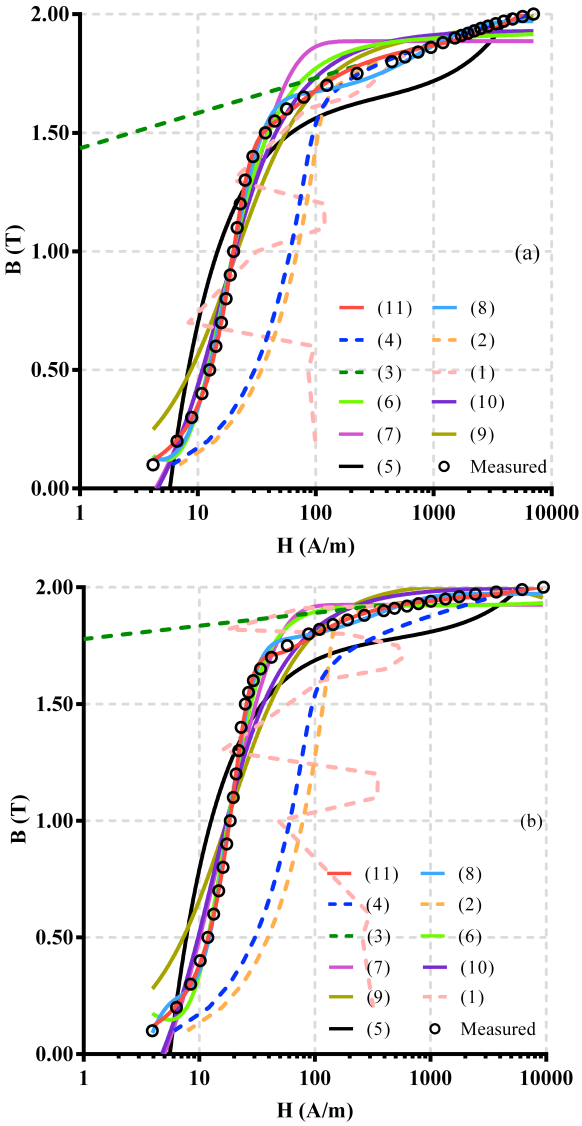

Fig. 5.1 B-H curve fitting results: (a) results for CGO samples; (b) results for HGO samples.

In order to analyse the fitting results in detail, the B-H curves are zoomed in and segmented into three parts, as shown in Fig. 5.2 and Fig. 5.3.

Fig. 5.2 compares the fitting qualities among different approximation expressions for the CGO sample, and their fitting quality quantitative analysis is given in Table 5.2.

Fig. 5.3 compares the fitting qualities among different approximation expressions for the HGO sample, and their fitting quality quantitative analysis is given in Table 5.3.

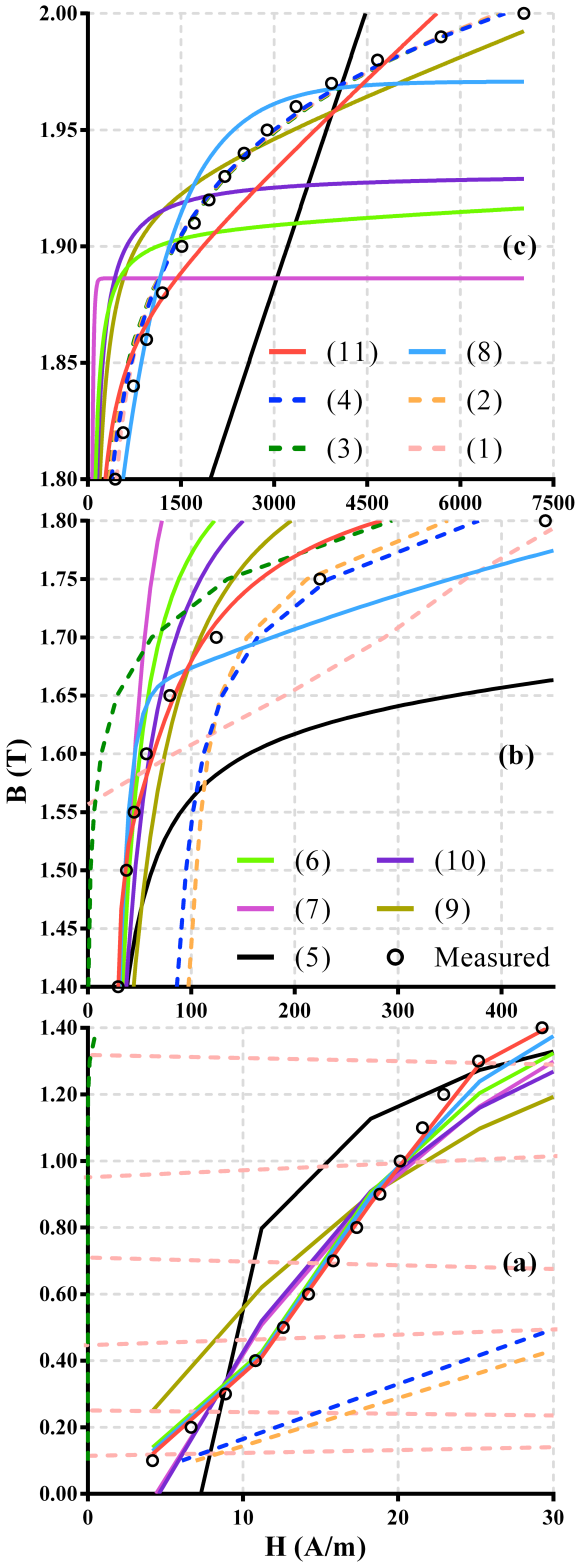

Fig. 5.2 B-H curve fitting quality comparison for CGO sample: (a) low induction portion; (b) knee area portion; (c) saturation portion.

In the low induction linear portion shown in Fig. 5.2 (a), $B=f(H)$ series approximations perform much better than $H=f(B)$ series: Equation (1) suffers the highly oscillatory problem due to the high order polynomials, known as Runge's Phenomenon. Equations (2), (3) and (4) also deviate from the measured data where the error exceeds 100%. The central portion shown in Fig. 5.2 (b) confirms that the knee area is very difficult to approximate. $H=f(B)$ series are still not good enough to track the measured characteristic in this region. For the $B=f(H)$ cluster, only (8) and (11) can basically follow the trend of the measured B-H properties. Equations (6), (7), (9) and (10) apparently overestimate the flux density while (12) underestimate about 10% at 1.75 T. Interestingly, all $H=f(B)$ functions approximate B-H character closely at high flux densities. Fig. 5.2 (c) suggests the $B=f(H)$ functions would encounter the flat head situation which overestimates the induction field H needed for a certain flux density, such as (7) and (8).

Table 5.2 summarises the overall curve fitting performances of 11 functions sorted by the adjusted R^2. It reveals that the proposed expression (11) can approximate the AC magnetisation curve well with the adjusted $R^2 = 0.9992$, It also shows that (2) and (4) does not pass the normality test, despite high ranking in terms of the adjusted R^2, which indicates that they are not good approximation expression options. Equation (5) should not be used because it behaves badly in both the curve fitting and normality test.

Table 5.2 B-H curve fitting quality comparison for CGO (up to 2.0 T).

No.	Expression	Adjusted R^2	Normality Test Passed
(11)	$B=\frac{a}{1+\frac{b}{H}+\frac{c}{H^2}}+d\left(\coth\frac{H}{e}-\frac{e}{H}\right)+fH$	0.9992	Yes
(8)	$B=a_0+a_1e^{-b_1H}+\cdots+a_4e^{-b_4H}$	0.9971	Yes
(4)	$H=\left(ae^{bB^2}+c\right)B$	0.9968	No
(2)	$H=aB+bB^n$	0.9956	No
(3)	$H=ae^{bB}$	0.9953	Yes
(1)	$H=a_0+a_1B+\ldots+a_9B^9$	0.9928	Yes
(6)	$B=\frac{a_0+a_1H+a_2H^2}{1+b_1H+b_2H^2}+\mu_0H$	0.9898	Yes
(10)	$B=a(\coth\frac{H}{b}-\frac{b}{H})+c$	0.9844	Yes
(7)	$B=a-be^{-cH}$	0.9779	Yes
(9)	$B=a\tan^{-1}\left(bH\right)+cH$	0.9646	Yes
(5)	$B=a_0+a_1H-a_2H^{-1}$	0.8604	No

The fitting quality of these 11 equations was also checked using the HGO sample, as shown in Fig. 5.3. Compared to the CGO sample result, the poor approximation ability of $H=f(B)$ functions below 1.80 T is confirmed again. Nevertheless, the fitting quality increases when it enters the saturation zone, as can be clearly observed in Fig. 5.3 (c), (2) and (3) as an example. A relatively poor performance of $B=f(H)$ functions except (11) is found in saturation, which is consistent with the preceding CGO results.

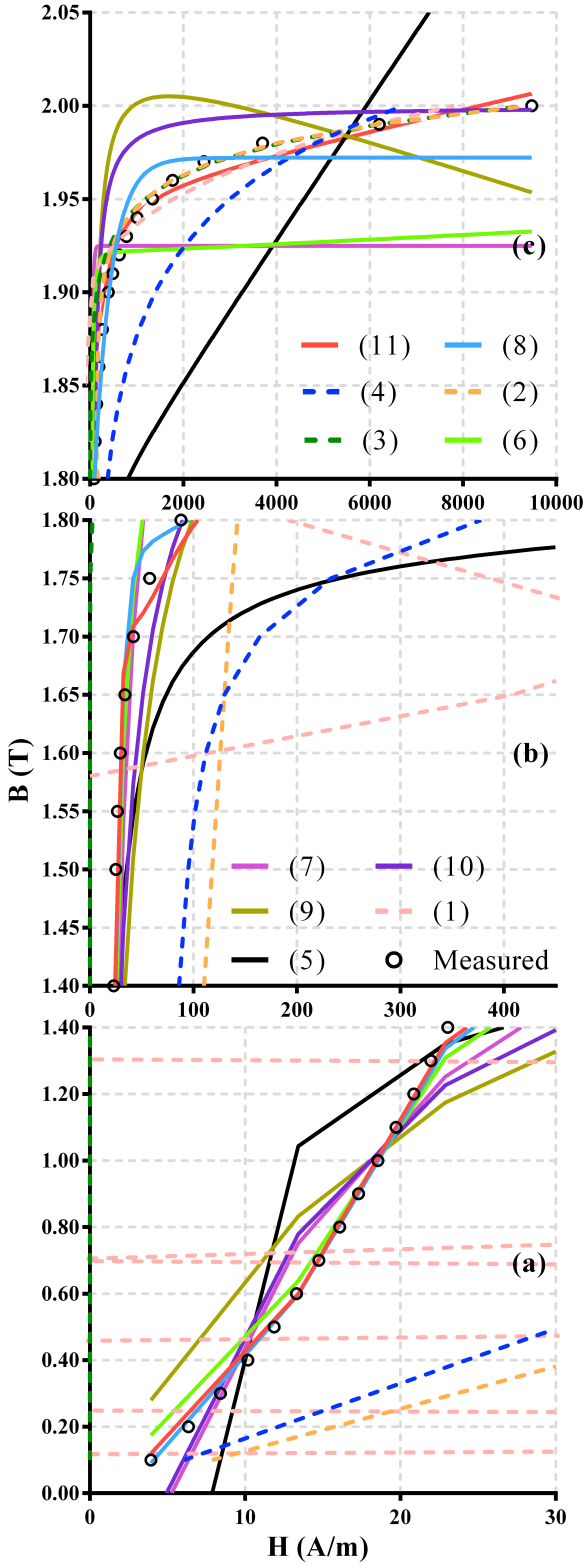

Fig. 5.3 B-H curve fitting quality comparison for HGO sample: (a) low induction portion; (b) knee area portion; (c) saturation portion.

A further detailed statistical analysis is conducted and presented in Table 5.3. Although six out of eleven equations can obtain adjusted R^2 > 0.99, only (8) and (11) are among the runners-up because (2), (3), and (4), (6) did not pass the normality test on the HGO sample, and the CGO sample respectively. Equation (11) again proves its good curve approximation ability on the HGO sample with the best adjusted R^2 performance.

Table 5.3 B-H curve fitting quality comparison for HGO (up to 2.0 T).

No.	Expression	Adjusted R^2	Normality Test Passed
(11)	$B=\frac{a}{1+\frac{b}{H}+\frac{c}{H^2}}+d\left(\coth\frac{H}{e}-\frac{e}{H}\right)+fH$	0.9993	Yes
(8)	$B=a_0+a_1e^{-b_1H}+\cdots+a_4e^{-b_4H}$	0.9975	Yes
(4)	$H=\left(ae^{bB^2}+c\right)B$	0.9968	Yes
(2)	$H=aB+bB^n$	0.9963	Yes
(3)	$H=ae^{bB}$	0.9945	No
(6)	$B=\frac{a_0+a_1H+a_2H^2}{1+b_1H+b_2H^2}+\mu_0H$	0.9901	No
(7)	$B=a-be^{-cH}$	0.9733	Yes
(10)	$B=a(\coth\frac{H}{b}-\frac{b}{H})+c$	0.9643	Yes
(9)	$B=a\tan^{-1}\left(bH\right)+cH$	0.9272	Yes
(1)	$H=a_0+a_1B+\ldots+a_9B^9$	0.9109	No
(5)	$B=a_0+a_1H-a_2H^{-1}$	0.8173	No

In the above fitting quality assessments, four expressions in the form $H=f(B)$ achieved good adjusted R^2 values (>0.99) due to the great similarity to the measured results in the high flux densities region, but none of them is suitable for describing the full B-H curve because of the poor approximation in the low and medium induction region. In addition, none of the four expressions passed all the normality tests. Finally, only five of eleven approximation expressions, i.e. (7), (8), (9), (10) and

(11) passed all the normality tests on both samples. Furthermore, among those five, just (8) and (11) achieved adjusted $R^2 > 0.99$.

The parameters of (8) and (11) for the two samples are hence presented in Table 5.4.

Table 5.4 Fitting parameters of (8) and (11) for the CGO and HGO approximation.

	No.	Parameters	Values	95% Confidence Intervals
CGO	(11)	a	0.2781	0.1955 to 0.3607
		b	-38.19	-41.39 to -34.99
		c	583.5	547.4 to 619.6
		d	1.588	1.501 to 1.675
		e	20.27	17.94 to 22.61
		f	2.450e-5	1.974e-5 to 2.927e-5
	(8)	a0	1.971	1.942 to 1.999
		a1	0.3342	0.2640 to 0.4044
		b1	0.001182	2.273e-5 to 0.002341
		a2	-0.1135	(Very wide)
		b2	36.65	(Very wide)
		a3	-52.64	(Very wide)
		b3	0.1305	(Very wide)
		a4	53.72	(Very wide)
		b4	0.1238	(Very wide)
HGO	(11)	a	0.3246	0.2610 to 0.3883
		b	-38.74	-40.72 to -36.77
		c	583.6	560.9 to 606.3
		d	1.631	1.563 to 1.699
		e	19.65	17.89 to 21.42
		f	5.579e-6	2.136e-6 to 9.021e-6
	(8)	a0	1.972	1.946 to 1.998
		a1	0.2246	0.1645 to 0.2846
		b1	0.002775	0.001091 to 0.004459
		a2	-8554	(Very wide)
		b2	0.2224	(Very wide)
		a3	4298	(Very wide)
		b3	0.2284	(Very wide)
		a4	4260	(Very wide)
		b4	0.2165	(Very wide)

The 95% confidence intervals of parameters were computed using GraphPad Prism. The confidence intervals are always centred on the best-fit value of the parameter, and extend above and below that value a distance equal to the parameter's standard error multiplied by a critical value from the *t*-distribution [87]. It indicates how accurate the estimated parameters are for the measured data. Apparently, the major problem with (8) is the resulting ambiguous parameters with very wide confidence intervals because of redundant parameters. In contrast, the proposed expression (11) has only half the number of parameters that (8) needs. Besides, all six parameters of (11) have narrow confidence intervals.

The good approximation capability of (11) is further confirmed with three other B-H characteristics: GO-M6 from COMSOL Multiphysics, PowerCore H 105-30 from ThyssenKrupp Electrical Steel, and 30RGH120 reported in [88]. The adjusted R^2 are 0.9954, 0.9991, and 0.9964 respectively, and meanwhile the fitted equations for the three materials have also passed all the normality tests. The approximation results are illustrated in Fig. 5.4. Therefore, (11) appears to be the most preferable simple analytical approximation expression for curve-fitting GO steels' B-H characteristic. Furthermore, (11) demonstrates good universal adaption on Non-Oriented steels (adjusted R^2 = 0.9930 for NGO 50PN270 from COMSOL Multiphysics).

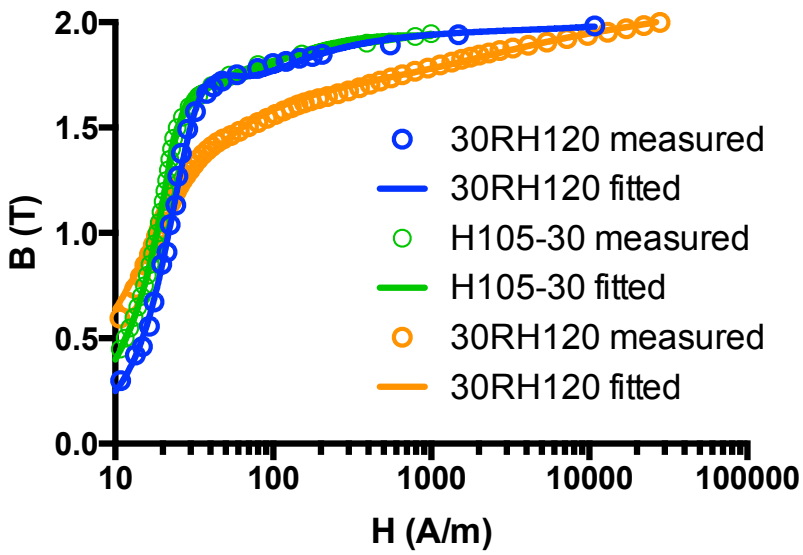

Fig. 5.4 Approximation capability tests for (11) on B-H data from other sources.

5.4 NONLINEAR B-H CURVE EXTRAPOLATION

In engineering practice, the high flux density data (> 1.80 T) are often not available from steel manufacturers. Hence it would be useful if the fitting expression has the capability of extrapolating the existing curve to the saturation region with sufficient accuracy.

The four expressions (7), (9), (10), and (11) with relatively strong approximation abilities from Section 5.3.3 were selected to explore their extrapolation capabilities, tested on both CGO and HGO samples. The experimental data from 0.10 T to 1.80 T was first used to find the parameters of the approximation expressions, as shown in Table 5.5. The flux density values extrapolated in the saturation region 1.80 to 2.00 T are then compared with the measured B-H property, as illustrated in Fig. 5.5.

It can be seen that, for the CGO sample, all parameter values of (11) in Table 5.4 are within the 95% confidence intervals of fitting parameters in Table 5.5, which means (11) extrapolates the curve well because the parameters estimated are very close to the original ones, as shown in Fig. 5.5 (a).

Table 5.5 Fitting parameters of (7), (9), (10) and (11) for prediction.

	No.	Parameters	Values	95% Confidence Intervals
CGO	(11)	a	0.3124	0.2391 to 0.3858
		b	-37.04	-39.74 to -34.35
		c	580.3	550.7 to 609.8
		d	1.519	1.434 to 1.603
		e	20.00	18.13 to 21.88
		f	2.439e-5	1.904e-5 to 2.974e-5
	(7)	a	1.798	1.710 to 1.887
		b	2.277	2.057 to 2.496
		c	0.05099	0.04222 to 0.05975
	(9)	a	1.265	1.144 to 1.387
		b	0.04692	0.03657 to 0.05726
		c	9.346e-7	-5.160e-5 to 5.347e-5
	(10)	a	2.348	2.116 to 2.579
		b	8.456	6.768 to 10.14
		c	-0.4133	-0.6506 to -0.1760

HGO	(11)	a	0.2695	0.1990 to 0.3399
		b	-40.03	-42.21 to -37.84
		c	582.3	558.3 to 606.3
		d	1.798	1.659 to 1.936
		e	20.60	18.31 to 22.90
		f	-6.809e-6	-1.745e-5 to 3.836e-6
	(7)	a	1.956	1.797 to 2.114
		b	2.594	2.313 to 2.875
		c	0.05701	0.04475 to 0.06927
	(9)	a	1.587	1.279 to 1.896
		b	0.04080	0.02720 to 0.05440
		c	-5.173e-5	-0.0001167 to 1.329e-5
	(10)	a	2.681	2.355 to 3.007
		b	8.028	5.873 to 10.18
		c	-0.5169	-0.8537 to -0.1802

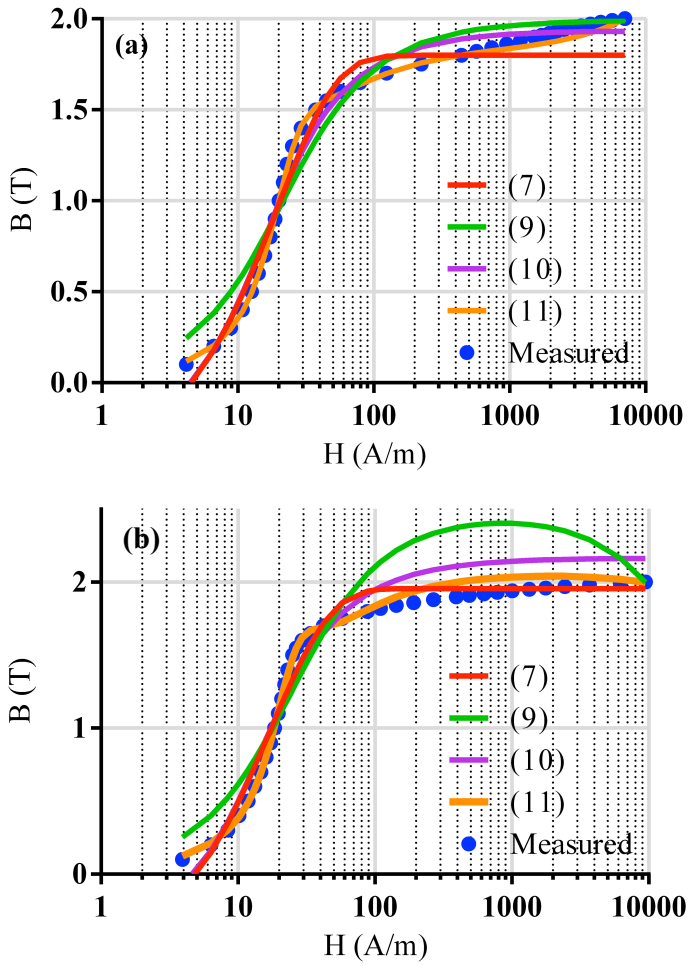

Fig. 5.5 B-H curve high flux densities (1.80 – 2.00 T) extrapolation capability test using 0.10 – 1.80 T measured data: (a) CGO prediction results; (b) HGO prediction results.

The B-H characteristics prediction quality in terms of the adjusted R^2 are summarised in Table 5.6. It is obvious from Table 5.6 that the proposed expression (11) with the incomplete input data is able to provide a reliable B-H curve prediction for both GO samples, whose adjusted R^2 is maintained above 0.9913 for the overall region. At the same time, a good approximation performance is kept in the region 0.10 – 1.80 T as well (adjusted $R^2 > 0.9990$). The other three, however, demonstrate relatively weak prediction abilities as compared with (11). The approximation quality of (7) and (10) decreases to 0.93 when tested on the HGO sample. The unsteady prediction quality of (10) is unstable, falling to 0.92 on HGO compared with 0.98 on CGO. The unsatisfactory performance of (7) and (10) is again mainly owing to their flat head shape and inflexibility, naturally determined by their mathematical functional form. Table VI also reveals that (9) is not appropriate for the B-H characteristic extrapolation owing to the poor prediction result (adjusted $R^2 = 0.7257$) and a large relative error (25%) at 1.90 T, as seen from Fig. 5.5 (b).

Table 5.6 B-H curve prediction quality comparison.

	Range (T)	Adjusted R^2			
		(7)	(9)	(10)	(11)
CGO	0.10-1.80	0.9702	0.9121	0.9652	0.9994
	0.10-2.00	0.9624	0.9577	0.9828	0.9974
HGO	0.10-1.80	0.9385	0.8642	0.9332	0.9990
	0.10-2.00	0.9692	0.7257	0.9227	0.9913

For the HGO sample result in Table 5.5, it is interesting to observe that the parameter f changes to negative (-6.809e-6) in the prediction compared with the positive value in the approximation (5.579e-6). The main reason behind that is the limited input data. At 1.8 T, for the CGO sample, H is around 450 A/m, but only 88 A/m for the HGO sample. The slope of the B-H curve (dB/dH) for the HGO is twice as steep as that of the CGO at low induction region while thrice as moderate as that of the CGO when B > 1.9 T. The sudden change of trend therefore requires a negative fH term to pull the extrapolated B-H curve down, owing to no BH data points above 88 A/m for the curve fitting. From Fig. 5.5 (b), it is apparent that (9) demonstrates a poor

extrapolation capability, whereas (11) obviously benefits from the negative fH term to achieve a better result.

Table 5.7 illustrates the incremental relative permeability ($dB/dH/\mu_0$) for the measured B-H and predicted B-H curves at 2 T using (11), which should be ideally equal to 1 in the full saturation situation. However, it can be seen the incremental relative permeability changes to negative due to the negative fH term for the HGO sample's B-H curve extrapolation with limited data points up to (88A/m, 1.8 T). This suggests more measured BH points are necessary to obtain better prediction results for the HGO materials if possible. Three more BH points up to (192 A/m, 1.86 T) are hence added here to enhance the prediction performance for the HGO sample. The new obtained fitted f = 2.636e-6 secures a positive incremental relative permeability, while an improved adjusted R^2 = 0.9991 for the prediction in the range 0.10-2.00 T is achieved using (11). The improved extrapolation performance is verified by the new $dB/dH/\mu_0$ = 2.3 (see Table 5.7), which is very close to the measured result.

Table 5.7 Incremental relative permeability comparison using (11) for the approximation and the extrapolation.

		$dB/dH/\mu_0$
CGO	Measured	6.0
	Approximation	19.9
	Extrapolation using B-H data (0.1-1.80 T)	19.7
HGO	Measured	2.4
	Approximation	4.6
	Extrapolation using B-H data (0.1-1.80 T)	-5.2
	Extrapolation using B-H data (0.1-1.86 T)	2.3

5.5 SUMMARY

Based on the latest experimental results of two different modern graded grain-oriented electrical steels measured up to 2.00 Tesla under AC 50 Hz with the improved SST proposed in the last chapter, the existing ten popular analytical approximation functions for AC magnetisation curves are critically evaluated. The

fitting quality indices – adjusted R^2, normality test, the number of parameters, and 95% confidence intervals are adopted here to give a comprehensive assessment.

Between $B=f(H)$ series and $H=f(B)$ series, $B=f(H)$ series generally perform better when the flux density is not high. $H=f(B)$ series expressions yet reflect the B-H characteristic better in the saturation region. None of the ten approximation functions, however, is capable of making a satisfactory approximation over the full useful range (0 - 2.00 Tesla), if taking account of all the fitting quality indices.

After many trials of different fitting equations, a new explicit simple empirical function (11) with enough robustness to produce good approximation and prediction/extrapolation results is proposed. The fitting quality of (11) has been validated in all flux density ranges not only on the CGO and HGO samples measured with the improved SST but also on the B-H data obtained from other sources. It is simple to use (six parameters) and sufficiently accurate (adjusted $R^2 \geq 0.9992$) to represent the AC magnetisation curve.

In the B-H curve prediction capability tests, Equation (11) also performs well (adjusted $R^2 \geq 0.9913$) for extrapolating the AC magnetisation curve into the high flux density region (1.80 - 2.00 Tesla) when only using the available experimental data in the region 0 - 1.80 Tesla from steel manufacturers. The extrapolation tests also suggests it is important to use enough experimental B-H data points as the input, particularly for the good GO materials with a large change in permeability. In this test, for instance, two more B-H points around 200 A/m for the HGO sample would enhance the prediction performance while giving a reasonable incremental relative permeability.

6 Electrical Steel's Power Loss Separation and Prediction

6.1 Introduction

Core loss is an important parameter of electrical steel, which largely determines the grades and the prices. The loss, i.e. wasted energy, is mainly dissipated as the heat. Although the efficiency can be as high as 99% for the modern power transformers, it still has been estimated that the cost of no-load core losses in transformers in the UK alone was estimated to be £110 million during 1987/1988 [89]. Today, more than 1 billion units of electricity each year are wasted in this way in the UK distribution transformers. This requires 7 million barrels of oil and releases 35,000 ton of SO_2 and 4 million ton of CO_2 into the atmosphere [23].

Considerable research and development resources have been consequently applied to electrical steels, which are used to build transformer cores, towards lower core losses, because even small improvement contributes to significant economical and environmental benefits.

Fig. 6.1 illustrates the timeline for the improvement in core loss of electrical steel over the past 100 years. The loss has been reduced very close to the theoretical value 0.4 W/kg from the initial 15 W/kg at 1.5 T under 50 Hz AC magnetisation [17]. The four milestones during this history are: addition of Si in 1900; Goss texture in 1934; HGO steel in 1970; amorphous material in 1980.

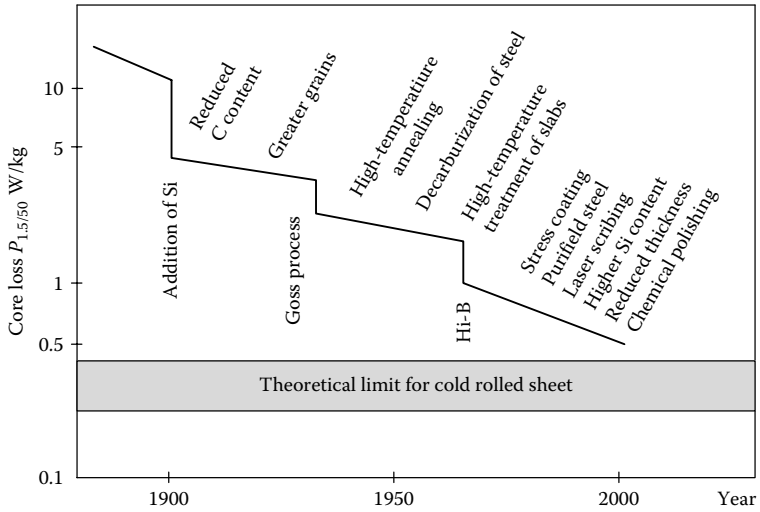

Fig. 6.1 The timeline for the improvement in core loss of electrical steel [17].

The specific power loss can be measured using the Epstein method or SST method as described in Chapter 4, and calculated through the integration of B-H loop applying (2.15). As mentioned in Section 2.4.3, the power loss can be expressed as the sum of three parts in (6.1):

$$P_{total} = P_h + P_e + P_a \tag{6.1}$$

where, P_h is the hysteresis loss; P_e is the classical eddy current loss; P_a is the anomalous loss.

The first part hysteresis loss P_h is related to the static hysterias loss and is proportional to the area of static hysteresis loop and the frequency. Hence, P_h is a characteristic of the material and a function of the peak flux density. The well-known Steinmetz hysteresis loss empirical formula was first proposed in 1892 [90], as illustrated in (6.2):

$$P_h = fk_h B_{pk}^n \tag{6.2}$$

where f is the AC magnetisation frequency, k_h is the constant for the material, n is called the Steinmetz exponent. n was originally taken constant as 1.6 by Steinmetz. In 1926, [12] found n varies a lot with the flux density. Based on AC test on Epstein strips samples in [12], it was found that Steinmetz's exponent did not change significantly

below 1.0 T with the value of 1.6. n increased to 2.5 near 1.5 T and dropped again to 1.6 or even lower after 1.6 T. Brailsford also attempted to account for the anomalous loss using the increased hysteresis loss brought about by the severe flux distortion inside the lamination, although this explanation was not widely accepted [13].

The second part classical eddy current loss P_e is related to the loss caused by eddy currents inevitably induced by the main flux B. The classical eddy current loss for a constant permeability can be calculated from (6.3):

$$P_e = \frac{\pi^2}{6\rho} d^2 f^2 B_{pk}^2 \tag{6.3}$$

where ρ is steel lamination resistivity, d is the thickness of the lamination. P_e can be reduced by building the core from a stack of thin laminations with high resistivity to restrict the flow of eddy current (see Fig. 6.2).

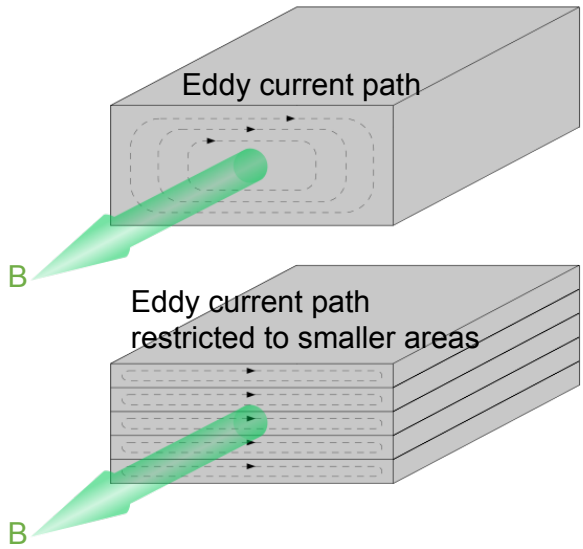

Fig. 6.2 Schematic diagram of the eddy current path in a solid core and a laminated core.

The third part P_a is called anomalous loss (or excess loss), because it was found that there always exists a difference between the measured specific power loss and the sum of theoretical calculated hysteresis loss and classical eddy current loss. This

discrepancy in modern GO steel can be up to 50% of the total core loss at power frequency [14]. This anomalous loss was not explained well until the domain wall model was proposed by Pry and Bean in 1958 [15], as illustrated in Fig. 6.3. P_a is thought to be proportional to the domain wall spacing 2L and inversely proportional to the sheet thickness d. This relationship helps us to understand the reason why domain refined HGO mentioned in Chapter 3 improves the magnetic performance. From Fig. 6.4, it can be seen that after the domain refinement process by the laser scribing, the domain wall spacing is decreased, resulting in a lower anomalous loss.

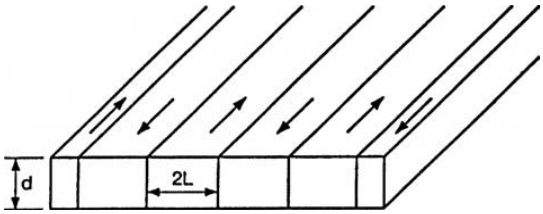

Fig. 6.3 Domain wall model for anomalous eddy current loss by Pry and Bean [15].

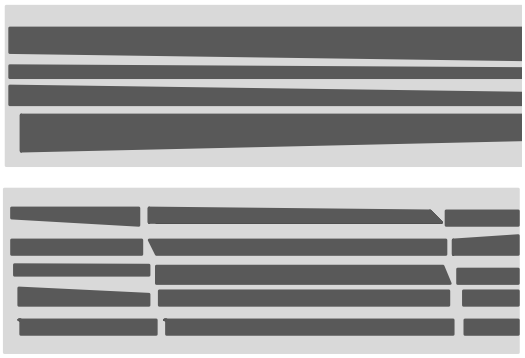

Fig. 6.4 Domain refinement of GO steel by the laser scribing.

Further extension of the anomalous loss study following Pry and Bean were presented by Bertotti [20], [91], [92], which can be simplified using (6.4), where k_a is the material constant.

$$P_a = k_a f^{1.5} B_{pk}^{1.5} \tag{6.4}$$

The three components of the total core loss can thus be separated if the total specific core power loss curves at various frequencies are measured. The separated power

losses will benefit the prediction of the specific power loss and the transformer core loss modelling for the future studies using the finite element method. Some papers such as [66], [93], [94], give the methodologies and formulae to estimate the eddy current loss and anomalous loss for arbitrary distorted flux waveform without minor hysteresis loops, which have addressed the power loss prediction issue under the distorted flux waveform for the harmonics components presented in T joints of three phase transformer. However, the current popular power loss separation algorithms, based on the four formulae (6.1), (6.2), (6.3), and (6.4), were not tested on the latest commercial GO steels, and particularly there was little measurement data at high flux densities [95], [96].

In this chapter, the current popular hysteresis loss models are briefly introduced and compared. Jiles-Atherton model is discussed in details and the application of this model in 3D FEM with COMSOL is developed. The effect of the assumption of constant permeability for the GO steel, as compared with the accurate and changing permeability, on the eddy current loss calculation is also investigated. The power loss curves for the CGO and HGO steels up to 2.0 T from 50 Hz to 400 Hz are measured using the improved SST proposed in Chapter 4. With the measured data, different power loss separation algorithms are tested and compared. Besides, a new simple power loss separation algorithm is proposed and its performance is verified using the latest experimental results.

6.2 Hysteresis Loop and Its Losses

6.2.1 Hysteresis loop models comparison

One of the first attempts for the hysteresis loop modelling is made by Rayleigh in 1887 [17]. Rayleigh model assumes there is a linear relationship between the permeability and the magnetic field, and B can be expressed with a quadratic function of H, as shown in Fig. 6.5, where ν is the Rayleigh constant; μ_i is the initial permeability; $\hat{H}$ and $\hat{B}$ are the peak value of magnetic field and magnetic flux density respectively.

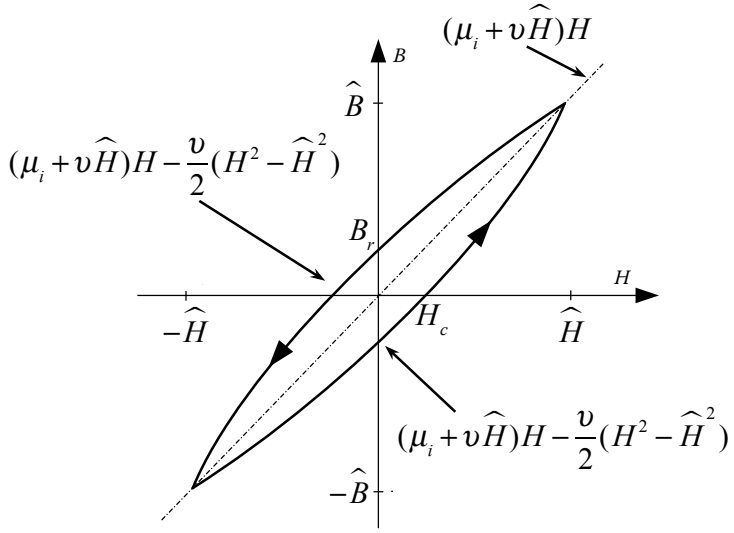

Fig. 6.5 Rayleigh hysteresis loop model.

The residual flux density B_r and coercive magnetic field H_c can then be determined using the following two equations:

$$B_r = \frac{\upsilon}{2} H^2 \tag{6.5}$$

$$H_c = \sqrt{\widehat{H}^2 + \frac{\mu_i^2 - \mu_i}{\nu}} \tag{6.6}$$

The hysteresis loss can then be derived:

$$P_h = 2\int_{-\hat{B}}^{\hat{B}} H\, dB = \frac{4}{3}\nu\widehat{H}^3 \tag{6.7}$$

Rayleigh hysteresis model is not able to describe the complete characteristics of magnetisation particularly when entering into the saturation region where the constant permeability assumption is no longer reasonable.

In the 1980s, Jiles and Atherton proposed a model including the irreversible and reversible domain wall motion [97], [98]. The total magnetisation is then given in (6.8), as shown in Fig. 6.6.

$$\mathbf{M}_{tot} = \mathbf{M}_{irr} + \mathbf{M}_{rev} \tag{6.8}$$

The relationship between the two magnetisation components is given by (6.9).

$$\mathbf{M}_{rev} = c\left(\mathbf{M}_{an} - \mathbf{M}_{irr}\right) \tag{6.9}$$

where the coefficient c represents the reversible wall motion. The Langevin function was chosen by Jiles and Atherton to approximate the DC initial B-H curve approximation function, i.e. anhysteretic function $\mathbf{M}_{an}$:

$$\mathbf{M}_{an} = M_s\left(\coth\frac{|\mathbf{H}_e|}{a} - \frac{a}{|\mathbf{H}_e|}\right) \tag{6.10}$$

where, M_s is the saturation magnetisation; a is the coefficient characterizing the shape of the anhysteric magnetisation; $\mathbf{H}_e$ is the effective applied magnetic field determined by (6.11), and α is a parameter to describe the inter-domain coupling.

$$\mathbf{H}_e = \mathbf{H} + \alpha\mathbf{M} \tag{6.11}$$

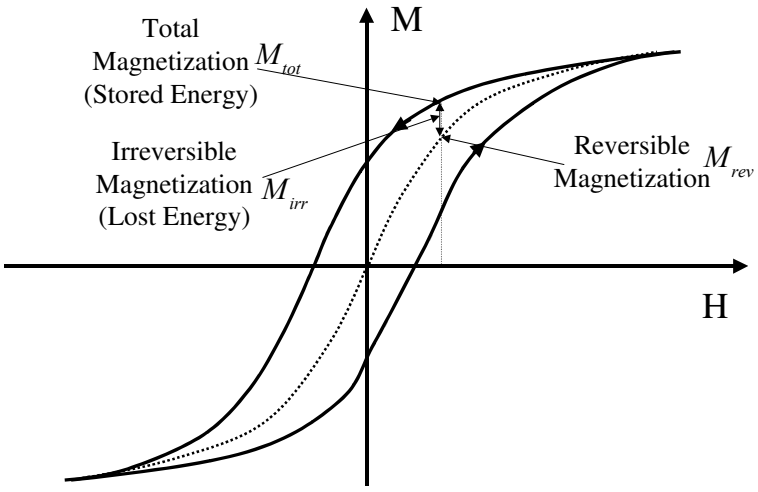

Fig. 6.6 Jiles and Atherton hysteresis loop model.

The irreversible magnetisation process can be described using (6.12) considering the domain wall pinning energy [98]:

$$\frac{d\mathbf{M}_{irr}}{d\mathbf{H}_e} = \frac{\mathbf{M}_{an} - \mathbf{M}_{irr}}{\delta k} \tag{6.12}$$

where δ is a directional parameter (1 for positive slope of H, and -1 for negative slope of H); k is the parameter reflecting the pinning effect. Recall (2.10), the B-H hysteresis loop can then be obtained.

One advantage of this model is that the four coefficients (a, k, c, and α) have a certain physical meaning which would be useful when the temperature factor is considered. The other advantage is that the separate equations used for the reversible and irreversible magnetisations allow the power loss directly calculated. However, the extraction of model parameters from the experiment results needs complicated iterations, which is not easy [63], [99]. Meanwhile Jiles-Atherton model lacks the frequency dependence, bringing difficulties for the practical simulations [100].

6.2.2 Implementation of Jiles-Atherton model in COMSOL

The Jiles-Atherton (JA)'s model described in the last section, was implemented on a 3D model in COMSOL Multiphyisics. As shown in Fig. 6.7, a cylinder core is wired with 1000-turn coils and surrounded in a sphere fulfilled with air.

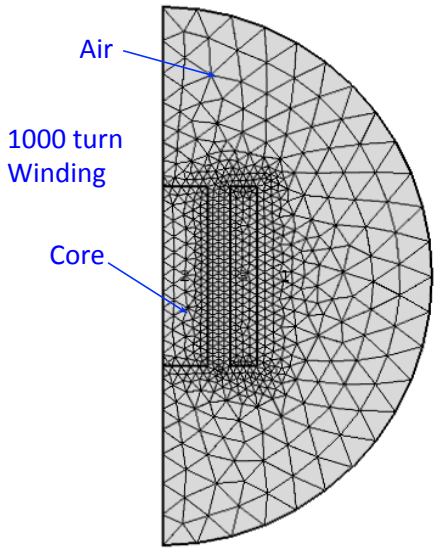

Fig. 6.7 3D model in COMSOL to implement Jiles-Atherton hysteresis model.

In order to implement Jiles-Atherton hysteresis model in a 3D situation, H, B, and M should be decomposed into the x, y, and z direction respectively, shown as the below equations used in COMSOL. The differential equations have been derived to take advantage of the time dependent study in COMSOL. The ***flsmhs*** function is a smooth step function used in COMSOL to replace the ideal δ step function. Fig. 6.8 illustrates the simulation results when different magnetising currents are charged, where a=1000 A/m, k=700A/m, c=0.22, α=1.4e-4, and M_s=1.615e6 A/m.

$$H_{ex} = H_x + \alpha M_x;\ \text{y,z...}$$

$$|H_e| = \sqrt{H_{ex}^{\ 2} + H_{ey}^{\ 2} + H_{ez}^{\ 2}}$$

$$B_{ex} = \mu_0 (H_x + M_x)$$

$$M_{anx} = M_s \left(\coth \frac{H_{ex}}{a} - \frac{a}{H_{ex}} \right) \frac{H_{ex}}{|H_e|};\ \text{y,z...}$$

$$M_{revx} = \frac{c}{1-c} \left(M_{anx} - M_x \right); \text{y,z...}$$

$$\frac{dM_x}{dt} = (1-c)\frac{dM_{irrx}}{dt} + c\frac{dM_{anx}}{dt}; y, z...$$

$$|M_{rev}| = \sqrt{M_{revx}^{\ 2} + M_{revy}^{\ 2} + M_{revz}^{\ 2}}$$

$$\frac{dM_{irrx}}{dt} = flsmhs\left(\frac{M_{revx}}{ck} \cdot \frac{dH_{ex}}{dt} + \frac{M_{revy}}{ck} \cdot \frac{dH_{ey}}{dt} + \frac{M_{revz}}{ck} \cdot \frac{dH_{ez}}{dt} \right) \frac{M_{revx}}{|\mathrm{M}_{rev}|}; y, z...$$

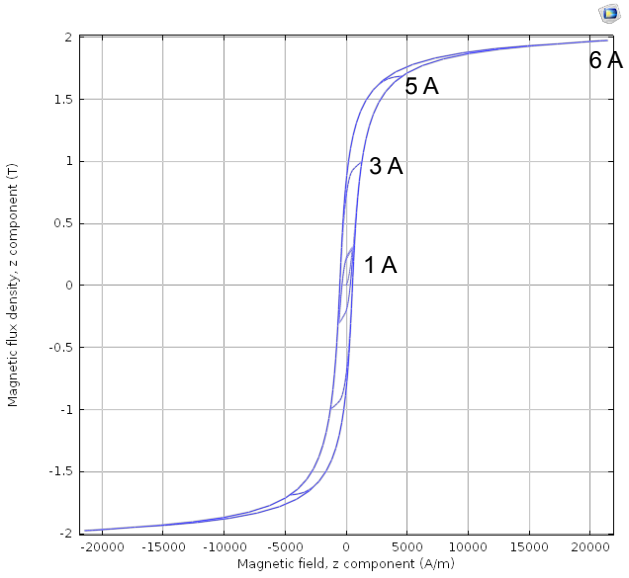

Fig. 6.8 Hysteresis loops with different magnetising currents in COMSOL.

In order to further examine the effects brought about by the four coefficients (k, a, c, and α) on the hysteresis loop, the sensitivity studies were carried out, and the results are shown in Fig. 6.9.

From Fig. 6.9(a), we can see that the coercive magnetic field H_c increases from 400 A/m to around 650 A/m when k increases from 500 to 900. The residual flux density B_r almost keeps constant. The peak magnetic field $\hat{H}$ is found to increase 400 A/m when k increases 400. Fig. 6.9(b) shows the change of a will not bring any change to H_c, but reduce B_r from 0.9 T to 0.5 T. Meanwhile, the increase of a also boosts $\hat{H}$.

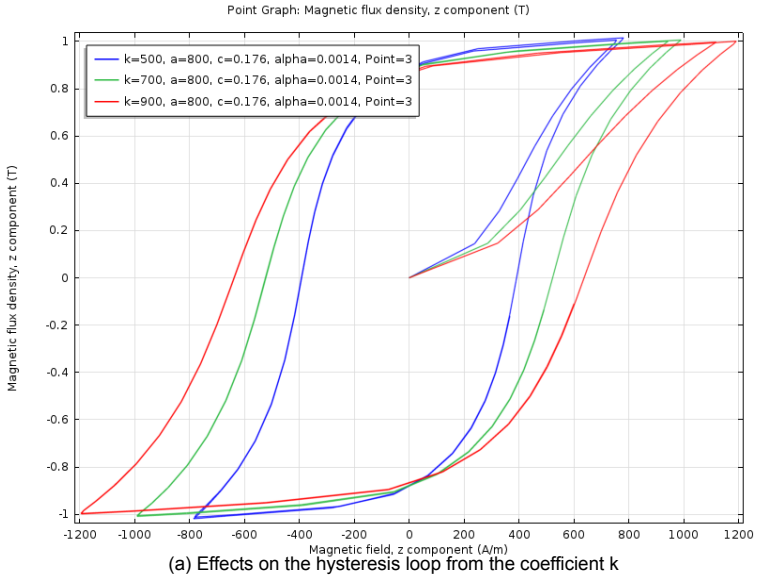

(a) Effects on the hysteresis loop from the coefficient k

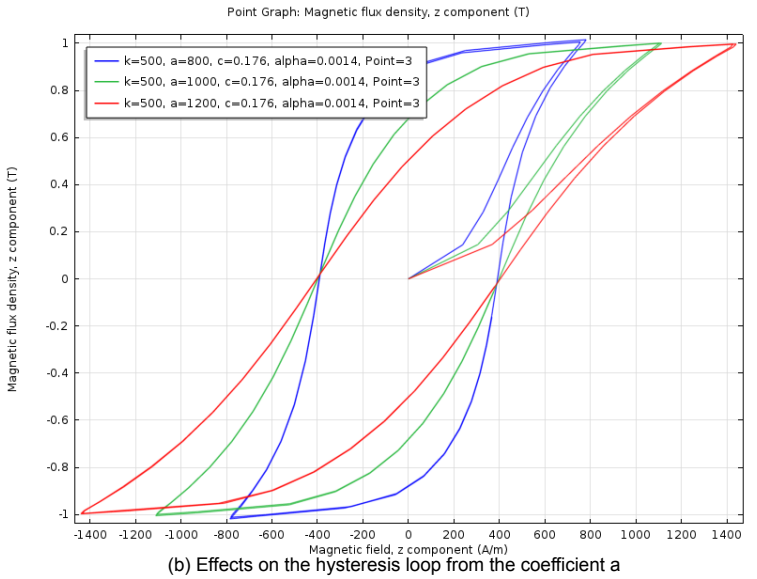

(b) Effects on the hysteresis loop from the coefficient a

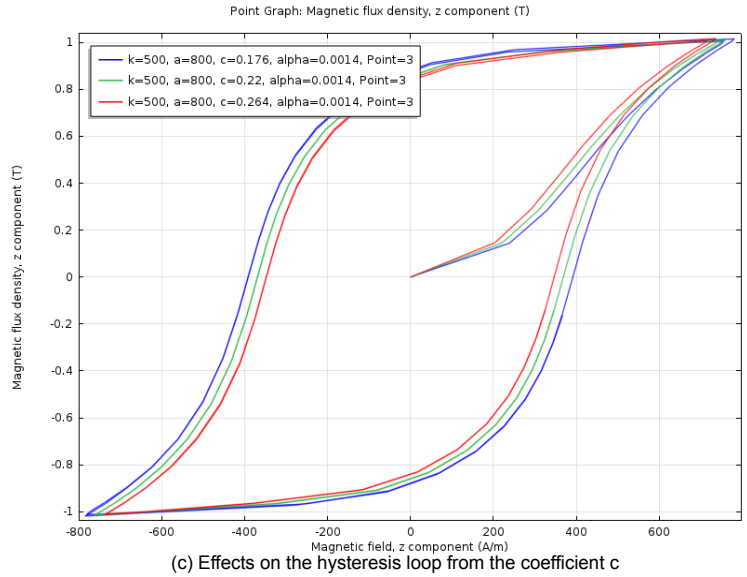

(c) Effects on the hysteresis loop from the coefficient c

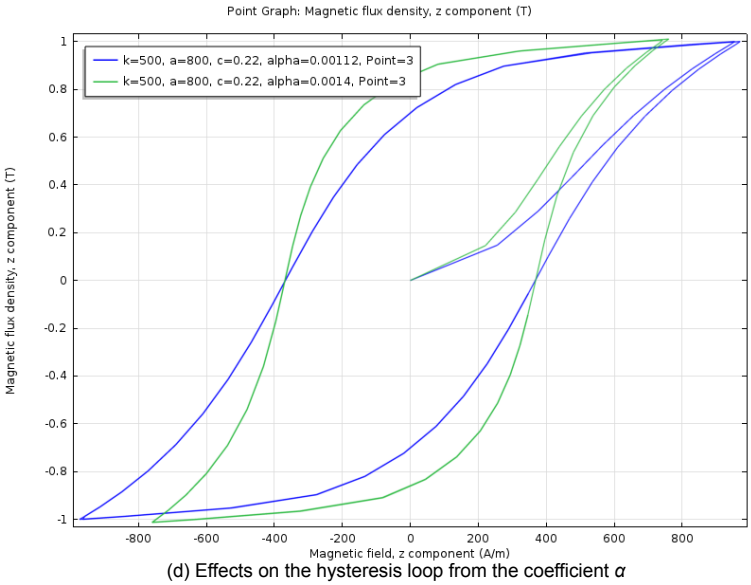

(d) Effects on the hysteresis loop from the coefficient α

Fig. 6.9 Sensitivity studies to investigate the effects of variation of coefficients (k, a, c, and α) in JA's model.

Compared with the effects of a and k, the increase of c shrinks the hysteresis loop, where H_c, B_r, and $\hat{H}$ are all decreased, as can be seen from Fig. 6.9(c). Fig. 6.9(d) illustrates the H_c does not be affected, and both $\hat{H}$ and B_r decrease with the increase of α.

Table 6.1 summarises the meaning of those four coefficients, and their effects on the hysteresis loop. It is interesting to observe the increase of k and c will respectively

increase and decrease the hysteresis loop area, i.e. the hysteresis loss. However, the change of a and α will not make significant difference in the hysteresis loop area because of the diverse results of $\hat{H}$ and B_r.

Table 6.1 Summary of the effects on the hysteresis loop from the coefficients in JA's model.

Coefficients in JA's model	**Physical meaning**	**Effects on the hysteresis loop due to the increased coefficients**			
		H_c	B_r	$\hat{H}$	Hysteresis loss
k	Reflecting the pinning effect	↗	→	↗	↗
a	Characterizing the shape of the anhysteric magnetisation	→	↘	↗	→
c	Representing the reversible wall motion	↘	↘	↘	↘
α	Describing the inter-domain coupling	→	↗	↘	→

The hysteresis loss calculation can also be implemented in COMSOL by applying (6.13).

$$P_h = \frac{1}{t}\int_0^t \left(\mathbf{H} \cdot \frac{\partial \mathbf{B}}{\partial t} \right) dt \tag{6.13}$$

A JA's hysteresis loop under 50 Hz AC magnetisation was generated in a 3D model in COMSOL, as shown in Fig. 6.7. The hysteresis loop and its accompanying hysteresis loss can be clearly seen in Fig. 6.10. Fig. 6.10 (a) shows the hysteresis loops of the material in 0.1 seconds. Fig. 6.10 (b) demonstrates the calculated real-time hysteresis loss using (6.13). In order to achieve an accurate result for the average hysteresis loss, the time-dependent study with a longer simulation time (>80 ms) is recommended. For this case, the average hysteresis loss is around 0.115 W/kg.

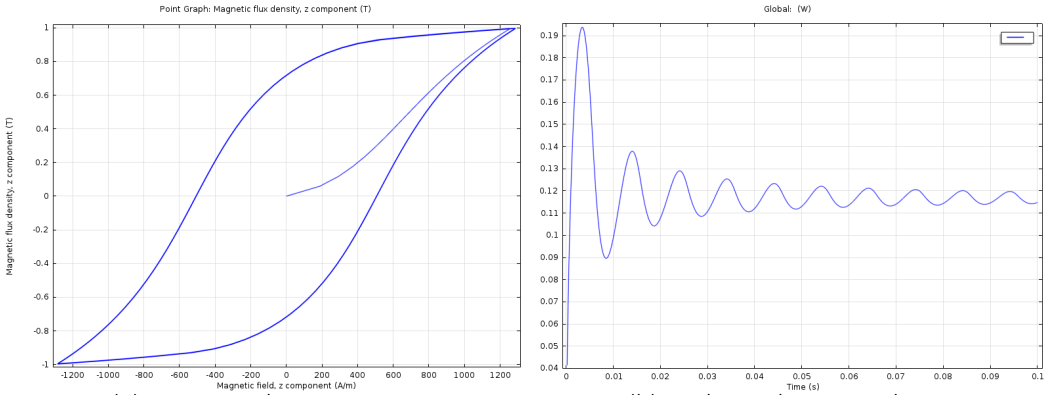

(a) Hysteresis loops in 0.1 s (b) Real-time hysteresis loss

Fig. 6.10 The JA's hysteresis loop model and its hysteresis loss evaluation in COMSOL.

If we take the dynamic losses (eddy current loss and anomalous loss) to consideration, the static hysteresis loop (under DC magnetisation) will be widened as shown in Fig. 6.11. Some researchers have also made some trials on the improved JA's models to take into account the dynamic losses, but they introduce more parameters which are hard to be extracted [100]–[102].

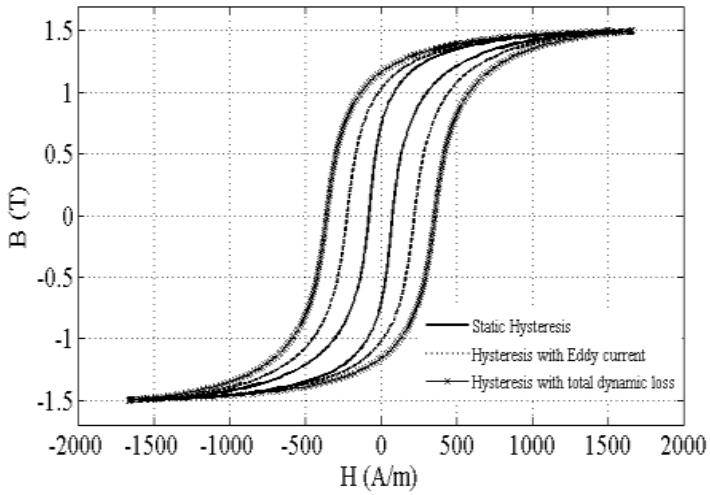

Fig. 6.11 Static hysteresis loop and its dynamic loss extension [103].

6.3 Eddy Current Loss and Its Variation with Permeability

The comprehensive formula for the classical eddy current loss is shown as (6.14) below [104]:

$$P_e = \frac{p\rho B_{pk}^2}{16d\pi^2\mu_r^2} \times \frac{\sinh pd - \sin pd}{\cosh pd + \cos pd} \tag{6.14}$$

where,

p	$2\pi\sqrt{\frac{\mu_r f}{\rho}}$
ρ	resistivity of lamination
d	thickness of lamination
f	frequency
B_{pk}	the peak value of the flux density
μ_r	relative permeability at B_{pk}

When pd is very small, i.e. $pd \rightarrow 0$, the Taylor expansion for the second part in (6.14) can be demonstrated in (6.15).

$$\frac{\sinh pd - \sin pd}{\cosh pd + \cos pd} \rightarrow \frac{(pd)^3}{6} - \frac{17(pd)^7}{2520} + O(x^{11}) \tag{6.15}$$

(6.14) can then be simplified to (6.3), as derived in (6.16):

$$\begin{aligned} P_e &\approx \frac{p\rho B_{pk}^2}{16d\pi^2\mu_r^2} \times \frac{(pd)^3}{6} = p^4 \times \frac{\rho d^2 B_{pk}^2}{96\pi^2\mu_r^2} \\ &= \frac{16\pi^4\mu_r^2 f^2}{\rho^2} \times \frac{\rho d^2 B_{pk}^2}{96\pi^2\mu_r^2} \\ &= \frac{\pi^2}{6\rho} d^2 f^2 B_{pk}^2 \end{aligned} \tag{6.16}$$

Equation (6.3) has already been widely used as an empirical formula. However, it was rarely seriously reviewed particularly after modern CGO and HGO material were developed. Apparently, two assumptions are supposed to be reconsidered. Firstly, pd was very small for an old electrical steel. But for the current GO steels, the pd can be as large as 45 due to a high relative permeability. Hence, the Taylor expansion will not be able to accurately reflect the real value. Secondly, only the first term with the 3rd order in Taylor series was used for simplification. The advantage for this assumption is

to eliminate μ_r in the final formula. Therefore, this simplification will also lead to the error in the classical eddy current loss computation.

In order to investigate the difference between the comprehensive formula (6.14) and the simplified formula (6.3), the measured relative permeability curves, as shown in Fig. 6.12, for the commercial HGO sample (HGO 105-30) from ThyssenKrupp at various frequencies are used here. The thickness of lamination d=0.3 mm, and the resistivity ρ=0.48 μΩm.

From Fig. 6.12, it can be seen that the relative permeability first increases with the peak flux density level. The highest relative permeability for this HGO sample is about 50k when the peak flux density is about 1.5 T at 50 Hz. After that, the relative permeability begins to decrease until the deep saturation. Meanwhile, the relative permeability falls when the magnetisation frequency rises.

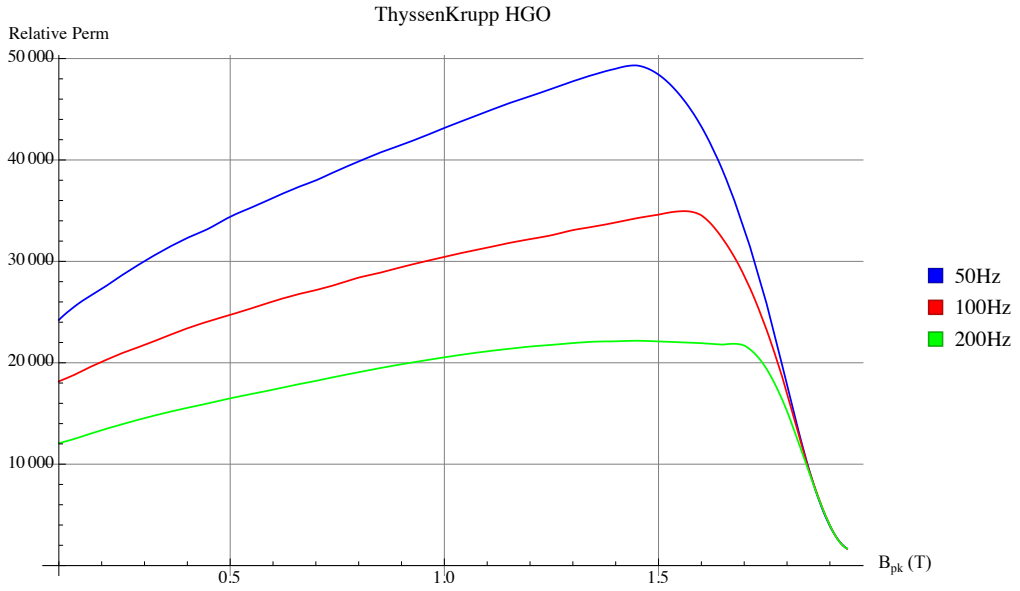

Fig. 6.12 The relative permeability curve of the HGO specimen from ThyssenKrupp.

Fig. 6.13 presents the specific total power loss curves, and the classical eddy current loss computed from both the simplified and the accurate formulae. The dashed lines represent the total loss provided by the manufacturer; the thick lines represent the accurate eddy current loss; and the thin lines represent the simplified eddy current loss. Undoubtedly, there is no surprise that the total loss is higher than the calculated

eddy current loss, since the eddy current loss is a part of the total loss. Compared with the eddy current loss calculated with the accurate formula (6.14), the simplified one using (6.16) always overestimates the classical eddy current loss, as illustrated in Fig. 6.13.

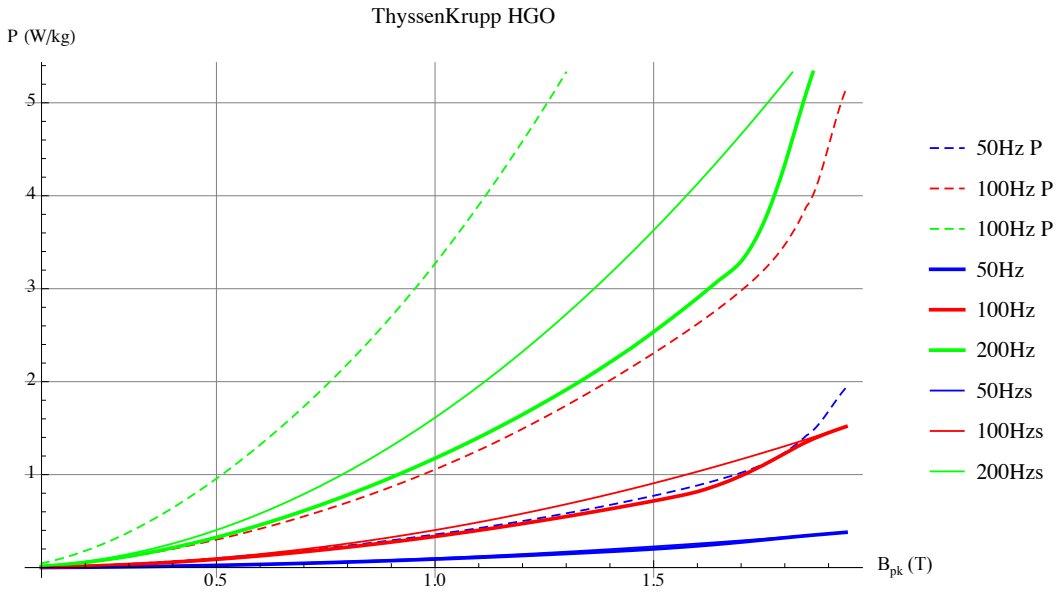

Fig. 6.13 The total power loss curves and classical eddy current loss curves computed from the accurate and the simplified formula. (dashed lines: total power loss; thick lines: accurate eddy current loss; thin lines: simplified eddy current loss)

The relative error overestimated is sketched in Fig. 6.14. At a certain frequency, the variation of this relative error follows the trend of the relative permeability: gradual rising to the maximum relative permeability and sharp dropping after that. It means the largest overestimation error is expected to be observed at around 1.5 T for the current GO materials. This overestimation error would also be enlarged with the magnetisation frequency. For this HGO sample, the simplified eddy current formula will overestimate up to 12% at 50 Hz. A larger relative error will be seen when the frequency is increased, which is up to 42% at 200 Hz. Besides, due to the much lower relative permeability of the material at high flux densities, the overestimation error falls steeply, which is also true even at a higher frequency.

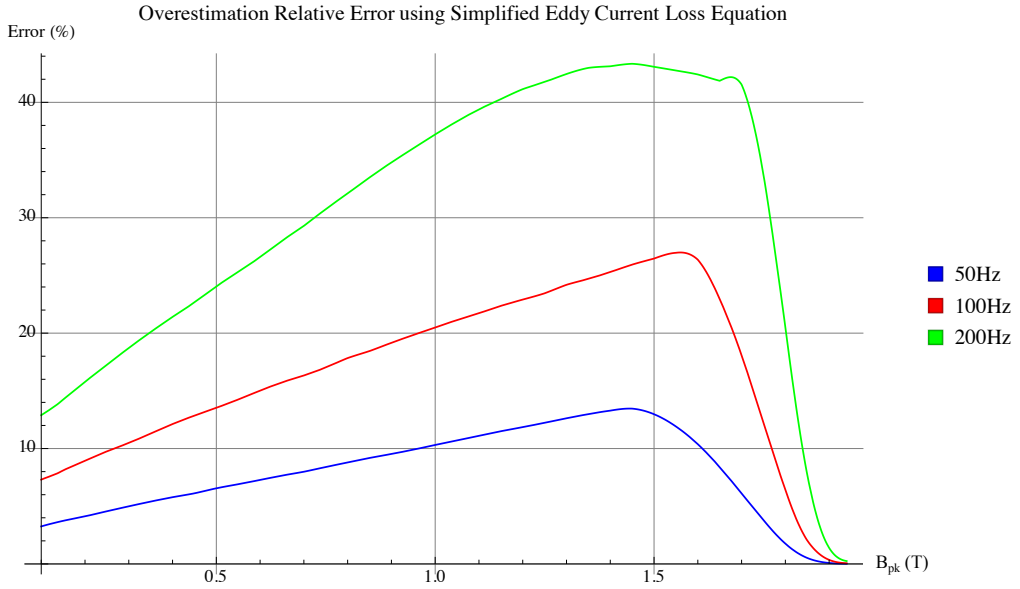

Fig. 6.14 The overestimated relative error using the simplified eddy current loss formula.

Fig. 6.15 illustrates the share of the calculated classical eddy current loss in the measured total power loss.

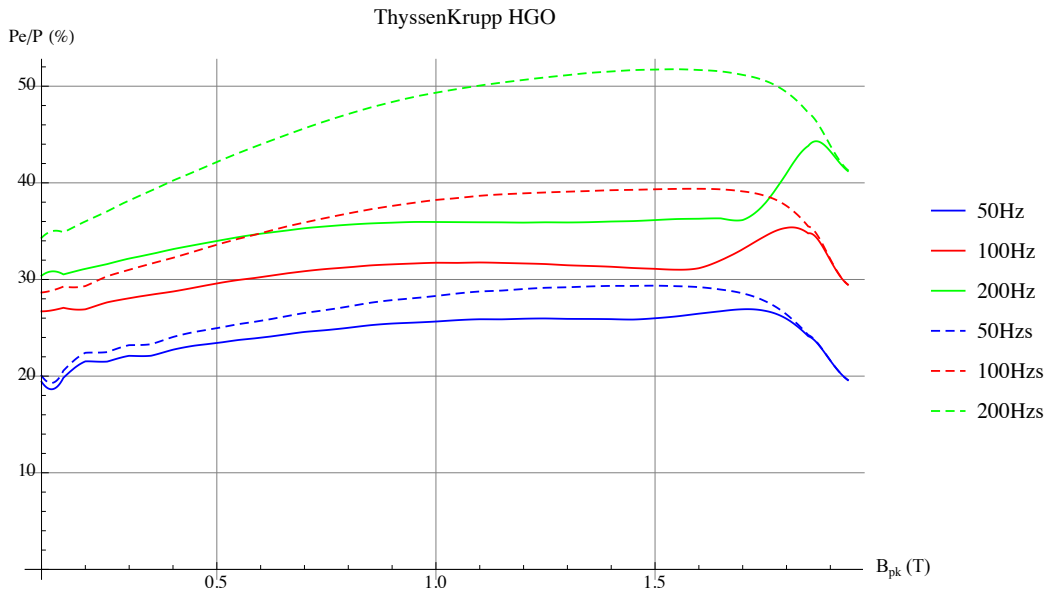

Fig. 6.15 The percentage of the classical eddy current loss to the total power loss at different frequencies. (dashed lines: with the simplified formula; solid lines: with the accurate formula)

With the simplified eddy current loss formula in the dashed line, the percentage of eddy current loss steadily creeps until the knee region. After that, it drops fast in the saturation region. Compared with that, the accurate eddy current loss formula actually provides a lower percentage before saturation. Because of the declined permeability in saturation, as discussed before, the shares of eddy current loss using two formulae are much closer. With the accurate eddy current loss formula, the share of eddy current loss also first slowly rises until the maximum relative permeability point, but suddenly boosts after that before dropping, which is noteworthy at high frequencies.

This interesting result can be explained with the help of Fig. 6.16.

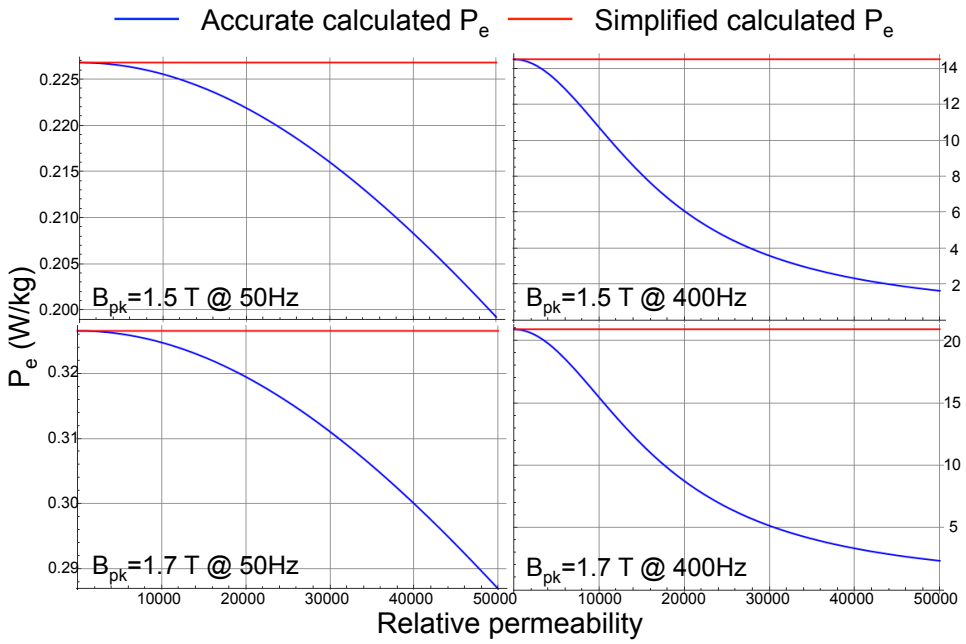

Fig. 6.16 The effects of B_{pk}, f and relative permeability on the accurate eddy current loss model.

Before approaching the maximum permeability point, the relative permeability keeps increasing, which leads to a falling effect on P_e. Considering the rising effect from the increased B_{pk}, the total effect on P_e is a slight increase. After the maximum permeability point, the relative permeability keeps decreasing, which results in a rising effect on P_e. Stacking it together with the rising effect from the increased B_{pk}, the total P_e therefore gains a boosting during this stage. From Fig. 6.16, it can also be

seen that this effect will be enlarged at a higher frequency, leading to a greater boosting for the percentage of P_e, as shown in Fig. 6.15.

Fig. 6.13 clearly illustrates that the rate of increase for the total power loss is much higher than that for P_e at very high flux densities. The drop in the percentage of P_e is hence observed at high flux densities after boosting in Fig. 6.15. The reason behind that is a much faster increase for P_h and P_a in the deep saturation, which will be discussed in the following section.

6.4 Core Loss Separation

6.4.1 Evaluations on the current multi-frequency separation methods

Substituting (6.2), (6.3) and (6.4) into (6.1), the total core loss can be expressed as (6.17), based on the statistical loss model proposed by Bertotti [20], [91], [92].

$$P_{total} = fk_h B_{pk}^n + \frac{\pi^2}{6\rho} d^2 f^2 B_{pk}^2 + k_a f^{1.5} B_{pk}^{1.5} \tag{6.17}$$

After divided by f for both sides of (6.17), it gives:

$$\frac{P_{total}}{f} = k_h B_{pk}^n + k_e B_{pk}^2 \left(\sqrt{f}\right)^2 + k_a B_{pk}^{1.5} \left(\sqrt{f}\right) \tag{6.18}$$

(6.18) shows that P_{total}/f is a quadratic function of square root of frequency at a certain flux density. In the conventional model, values of coefficients k_e, k_a, k_h, and n are assumed constants.

As discussed in Section 6.1, n does change when B_{pk} changes. So n was suggested to be replaced by a flux density dependent term $a + bB_{pk} + cB_{pk}^2$, where a, b, and c will change with f [95]. Therefore, we have,

$$\frac{P_{total}}{f} = k_h B_{pk}^{a+bB_{pk}+cB_{pk}^2} + k_e B_{pk}^2 \left(\sqrt{f}\right)^2 + k_a B_{pk}^{1.5} \left(\sqrt{f}\right) \tag{6.19}$$

As shown in Fig. 6.17, the algorithm developed to find the coefficients in (6.19) can be described as follows:

- Sketch the P_{total}/f versus at a certain B_{pk} from the measurement;
- Find k_a and k_e through the curve fitting;
- Find the four parameters k_h, a, b, and c at a certain frequency through solving the linear equation sets $\log P_h(B_{pk}) = \log k_h + \log f + \left(a + bB_{pk} + cB_{pk}^2\right)\log B_{pk}$.
- The total core loss together with the three components can then be obtained using (6.17).

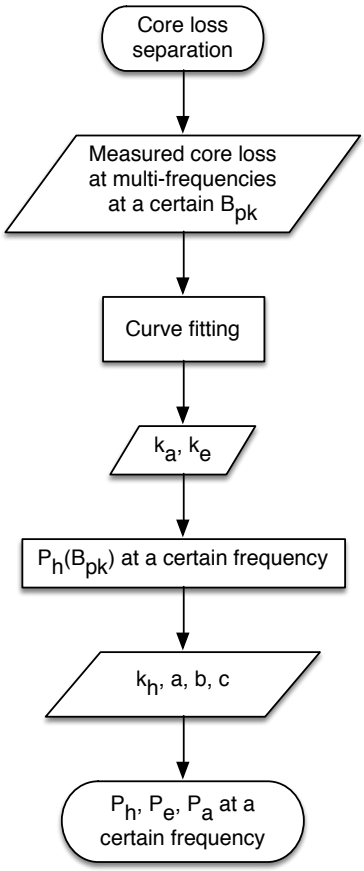

Fig. 6.17 Core loss separation algorithm assuming k_a and k_e are constants.

This algorithm was then tested using the measured core loss curves for a CGO steel sample from the improved SST at 25, 50, 100, 200, 250 and 400 Hz. The measured data for the core loss separation is illustrated in Fig. 6.18.

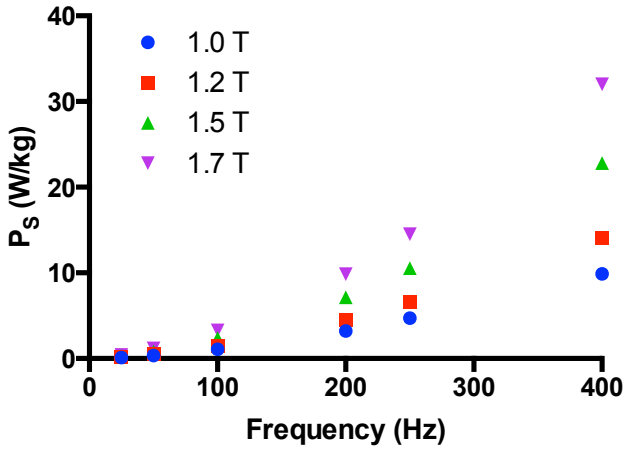

Fig. 6.18 Total core loss for a CGO sample measured with the improved SST at various frequencies.

Using the measured core losses at 1.5 T, the fitted k_a and k_e are 0.0008142 and 2.720e-5 respectively. The four coefficients for the hysteresis loss formula are solved using Mathematica (see Appendix 5) at 50 Hz: k_h 0.000124737, a 52.9091, b -55.9507, c 17.1992. The core loss separation results for the CGO sample at 50 Hz is then shown in Fig. 6.19.

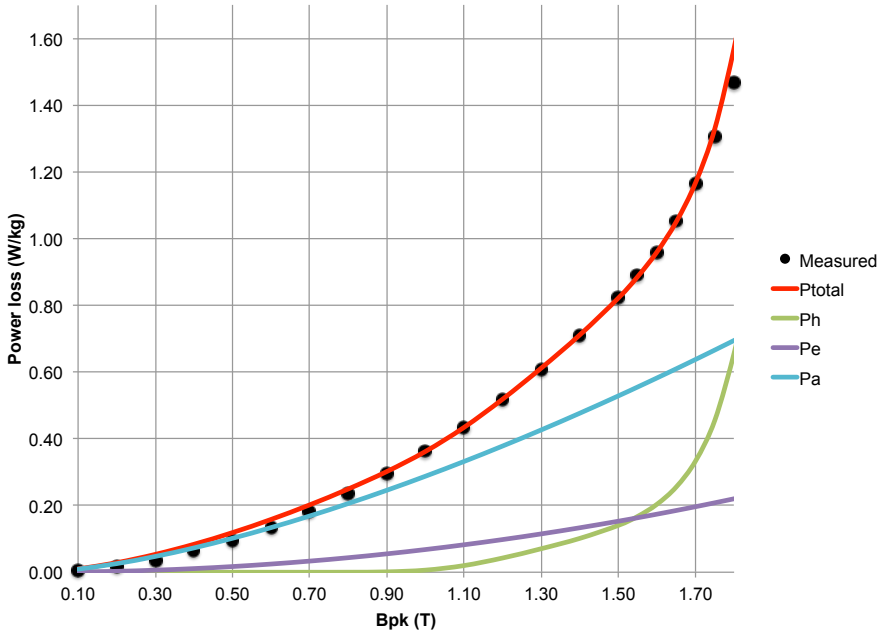

Fig. 6.19 Core loss separation results for the CGO sample at 50 Hz assuming k_a and k_e are constants.

It can be seen that the calculated P_{total} matches well with the measured result. The classical eddy current loss and the anomalous loss rise steadily together with the flux density level. However, the hysteresis loss climbs rapidly after the knee region (around 1.6 T), which dominates the increase of the total core loss.

Fig. 6.20 compares the contribution of each loss component at different flux destines.

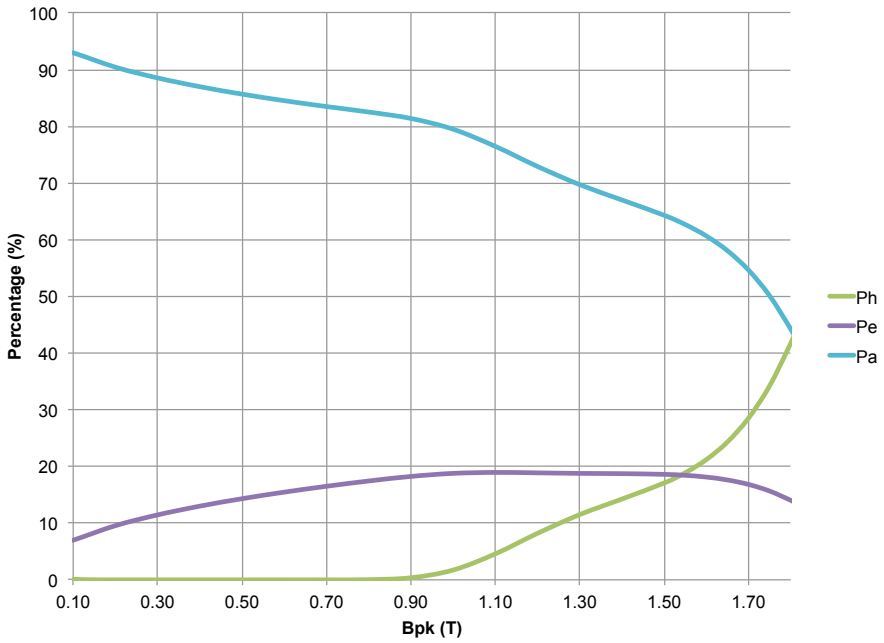

Fig. 6.20 Percentage of three loss components for the CGO sample at 50 Hz assuming k_a and k_e are constants.

It is apparent that the anomalous loss contributes more than half of the total loss for the power transformer operational region below 1.7 T. The percentage of the hysteresis loss is very small at low flux density levels. However, it increases sharply due to the increase of the Steinmetz exponent value after 0.9 T. This leads to the drop of the percentage of the anomalous loss between 0.9 T and 1.5 T where the eddy current loss does not change significantly. The behaviour of the hysteresis loss coincides with the results reported in [105], [106]. The trend of the eddy current loss behaves similar to the theoretical results using the simplified formula as discussed in Section 6.3. The faster increase of eddy current loss in the low induction region causes the decline of anomalous loss's share. Approaching saturation, the eddy

current loss is not increasing as fast as the hysteresis loss, causing a drop of its percentage in the total core loss. As we can see, the dropping slope of the eddy current loss's percentage is gentler than that of the anomalous loss, i.e. the eddy current loss is rising faster with B_{pk} than the anomalous loss. The reason behind that is the eddy current loss has 2 as its B_{pk}'s exponent compared with 1.5 for the anomalous loss.

The first issue for the preceding power loss separation algorithm is the assumption that k_a and k_e are independent from the flux density. However, Fig. 6.21 clearly shows they do vary with the induction levels. It seems that the two coefficients have somehow complementary trend, i.e. k_a increases while k_e decreases initially; k_a turns down while k_e begins to rise after 1.2 T, which agrees with the findings reported in [96].

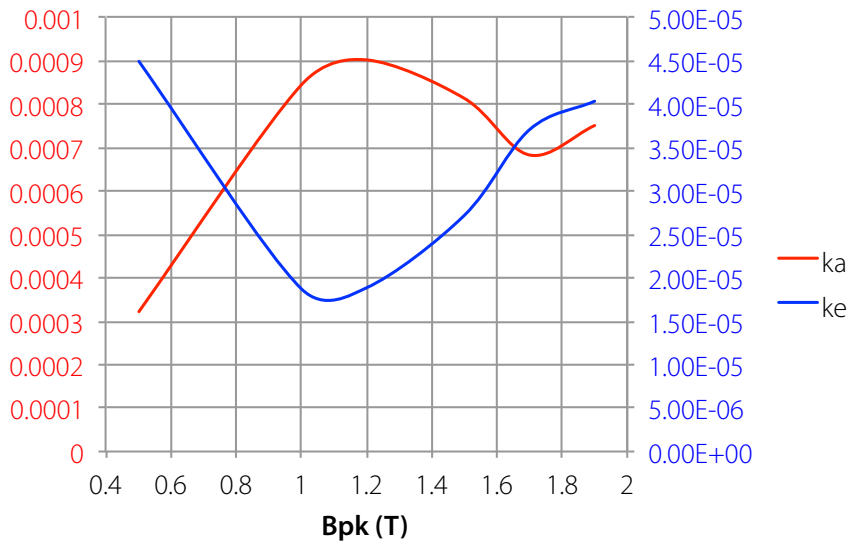

Fig. 6.21 Variation of classical eddy current coefficient k_e and anomalous loss coefficient k_a with the flux density levels.

The possible explanations for this might be the anomalous loss formula expression [96] and/or the separation of anomalous and eddy current loss is still questionable [107]. It could also be caused by the overestimation of the classical eddy current loss using the simplified equation ignoring the variation of the permeability as discussed in the last section, which leads to a dropping of k_e as a compensation. This

compensation effect is reduced after 1.2 T, at which the permeability is the highest. The rise of k_e is therefore observed because the error difference is reduced when approaching the saturation.

In Fig. 6.22 and Fig. 6.23, the differences brought by different fitted k_a and k_e using the power loss data measured at 1.5 T and 1.7 T are compared. It is interesting to see that P_{total} is almost the same for the two cases. However, it does bring the differences to the percentages of three loss components. Computed with the data at 1.7 T, the new percentages of classical eddy current loss and the hysteresis loss increase, while the anomalous loss' share drops by around 10%. This again indicates the current power loss separation method needs further improvement. One trial, for example [96], suggested to replace the constants k_e and k_a with third order polynomials such as $k = a + bB_{pk} + cB_{pk}^2 + dB_{pk}^3$. Nevertheless, it may introduce more uncertainties because of the additional curve fittings such as ambiguous fitted parameters. It could also produce the coefficients with complex values and negative total core loss under 0.3 T, which would have no physical meanings.

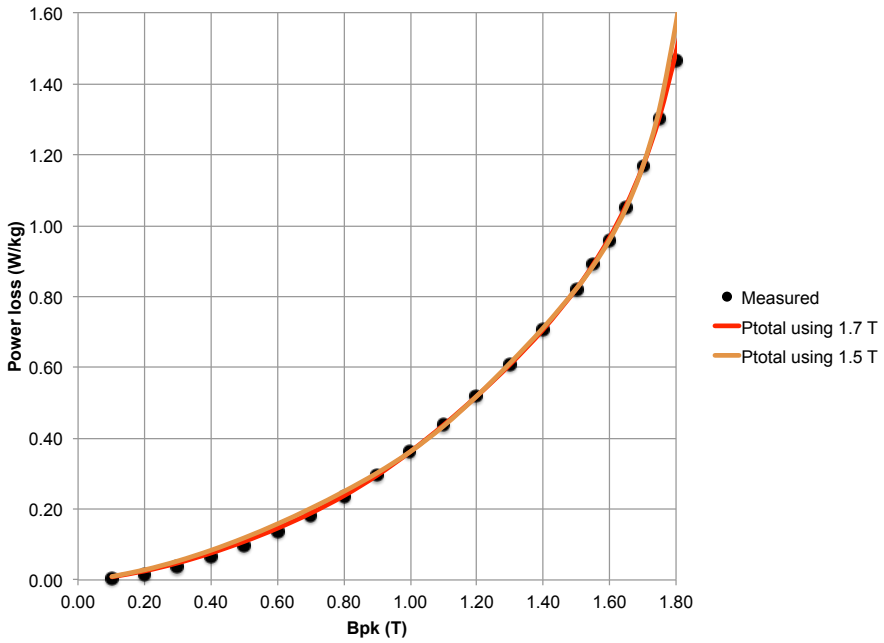

Fig. 6.22 The comparison between the calculated total core loss using different fitted k_a and k_e values.

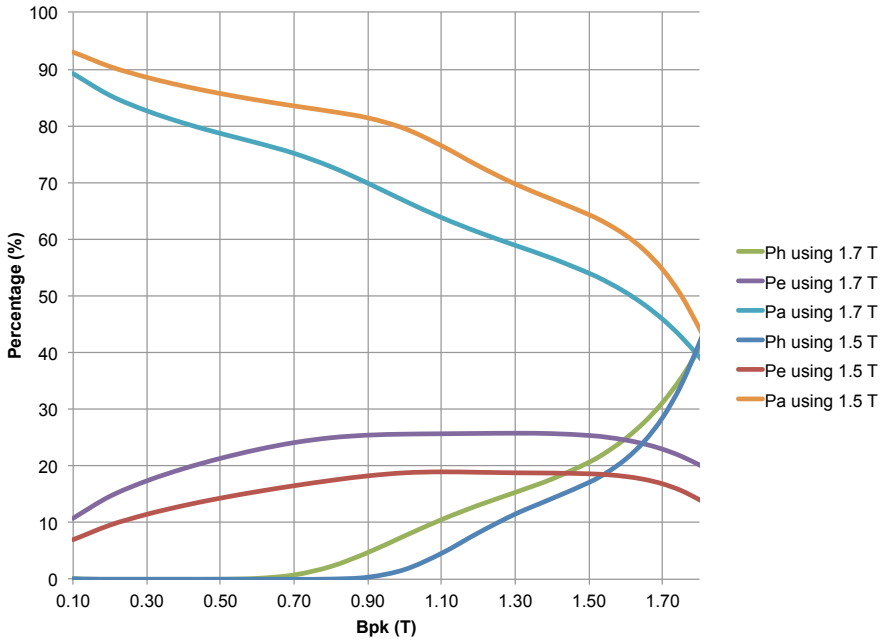

Fig. 6.23 The comparison between the percentage of three loss components using different fitted k_a and k_e values.

The second issue for the preceding power loss separation algorithm is the poor performance in the saturation region, as shown in Fig. 6.24. Using the data sets at 1.0 T, 1.2 T, 1.5 T and 1.7 T as illustrated in **Error! Reference source not found.**, P_{total} rises to a ridiculous high value in the saturation region, which is caused by the error in the four coefficients of the hysteresis loss formula. In order to minimise this error, the proposed solution here is to pick up the representative values in each region of the power loss curve. Hence, the data at 0.5 T, 1.2 T, 1.5 T, and 1.9 T are used instead to solve the hysteresis loss equation sets. Fig. 6.24 clearly shows the benefits of this improvement: the difference gaps between the measured core loss and the calculated one at both low and high flux densities are significantly narrowed.

This suggests choosing appropriate data sets for coefficients computation largely determines the accuracy of core loss modelling, since only four data sets can be used to determine the four coefficients k_h, a, b, and c. Hence, the typical power loss data at low, medium, and high flux destines are recommended to be used to represent the linear, knee, and saturation regions.

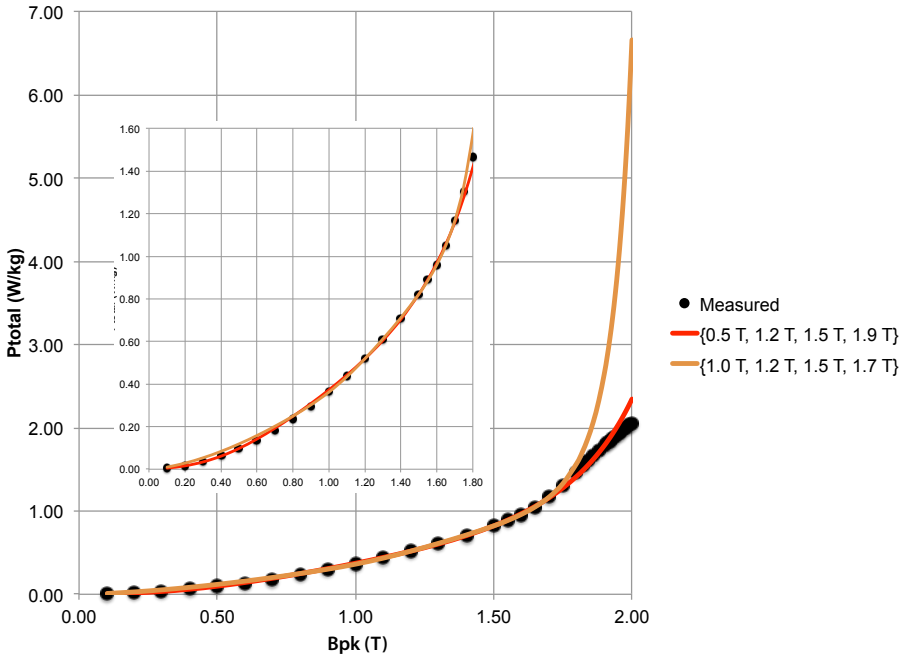

Fig. 6.24 Comparison between the resulting core loss curves using different B sets for the four coefficients of the hysteresis loss formula.

6.4.2 Improved core loss separation algorithm

In order to overcome the problems discussed for the preceding power loss separation algorithm, a new simple and accurate power loss separation algorithm is proposed here. Recall the accurate eddy current loss calculation formula (6.14), P_e for each flux density level at any frequency can be obtained. The sum of hysteresis loss and anomalous loss can then be expressed as P_{ha}, which equals to the difference between the measured P_{total} and the calculated P_e. Recall the original anomalous loss formula for a sinusoidal flux [108]:

$$P_a = 8.76\sqrt{\sigma GSV_0(B_{pk})}f^{1.5}B_{pk}^{1.5} \tag{6.20}$$

where, σ is the conductivity of the material (2.08×10^7 S/m); G is a dimensionless coefficient (0.1356); S is the cross sectional area of the lamination (9×10^{-6} m^2); $V_0(B_{pk})$ is a parameter characterizing the statistics of the local coercive fields that the individual domain walls have to overcome along the magnetisation reversal [94], which is a function of the flux density.

Equation (6.2) reveals the hysteresis loss per cycle is only dependent on the flux density level. Hence we can extract the coefficient $V_0(B_{pk})$ values through the subtraction between two P_{ha}/f at the same flux density level but different frequencies, derived from (6.20), as shown below:

$$V_0(B_{pk}) = \left(\frac{P_{ha}\left(B_{pk}, f_1\right)/f_1 - P_{ha}\left(B_{pk}, f_2\right)/f_2}{8.76 B_{pk}^{1.5}\left(\sqrt{f_1} - \sqrt{f_2}\right)} \right)^2 / \sigma GS \qquad (6.21)$$

We therefore only needs two power loss curves measured at any two frequencies to obtain the relationship between $V_0(B_{pk})$ and B_{pk}. The anomalous loss at a certain frequency can then be obtained through (6.20). The hysteresis loss component can then be easily obtained using the measured total power loss minus the calculated P_a and P_e.

The new improved core loss separation algorithm is then conducted on the same CGO sample. The two core loss measurement results at 50 Hz and 200 Hz are selected here to obtain $V_0(B_{pk})$. The final separated three loss components are summarised in Fig. 6.25. The percentage of three components can be further analysed with Fig. 6.26.

It can be seen that the eddy current loss component is overestimated using the previous algorithm, which agrees with the conclusion in Section 6.3. Compared with the continuous decline trend of the anomalous loss's share using the old separation algorithm, the improved one shows the anomalous loss will remain around 35% beyond 1.3 T. Moreover, although the hysteresis loss dominates the total core loss rise after 1.1 T, the new separated result shows it is not increasing with such a steep slope as calculated from the previous separation algorithm.

The physical reason behind the variation of the percentage of hysteresis loss can be explained using Fig. 2.2. With a larger magnetic field, the domain walls' movements are irreversible, as shown in Fig. 2.2 (c), boosting the percentage of hysteresis loss. When the magnetisation rotates into the direction parallel with the applied field, and

the material is fully saturated, as shown in Fig. 2.2 (e). The percentage of hysteresis loss is expected to remain constant.

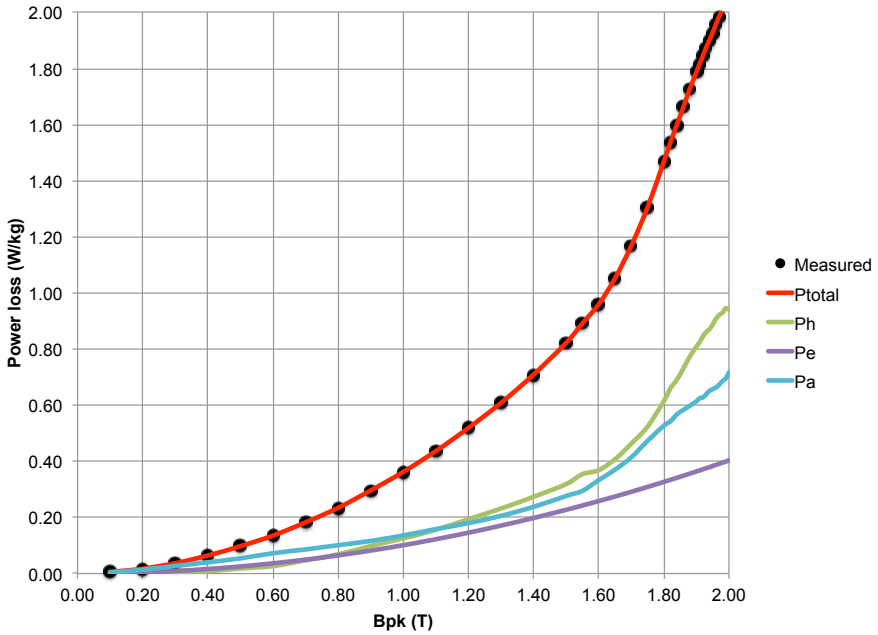

Fig. 6.25 Core loss separation results for the CGO sample at 50 Hz using the improved core loss separation algorithm.

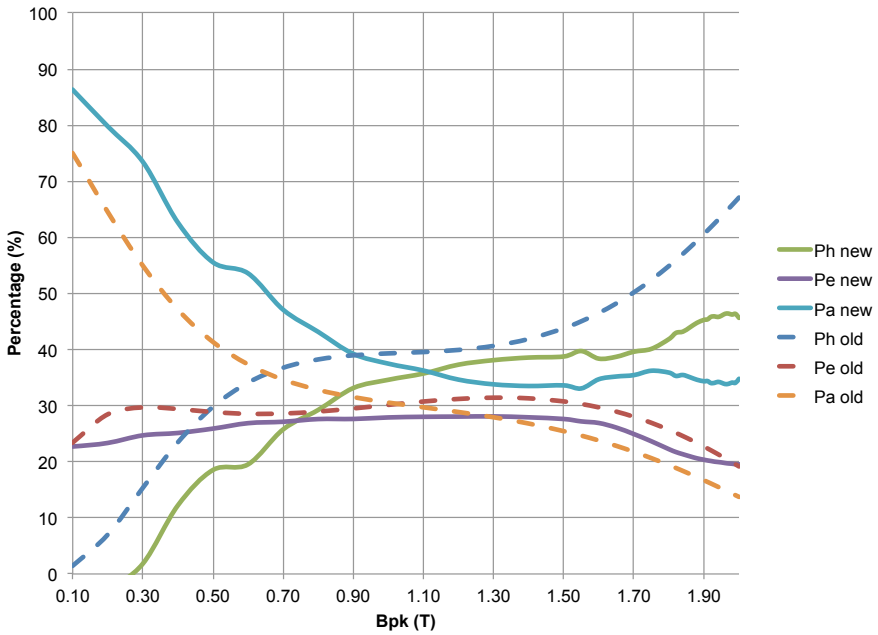

Fig. 6.26 The comparison between the percentages of three loss components with the old and new separation algorithm.

6.5 Summary

This chapter first discusses the three components of the core loss (hysteresis loss, eddy current loss and anomalous loss) and their physical meanings, as well as their calculation formulae.

Two hysteresis loop models – Rayleigh model and Jiles and Atherton's model are critically reviewed. The Jiles and Atherton's hysteresis loop model is then applied in a 3D finite element simulation. The sensitivity studies carried out show the effects on the hysteresis loop brought about by the coefficients in JA's model. The hysteresis loss based on the JA's hysteresis loop model can be determined with the time-dependent finite element study.

The difference in the calculated eddy current loss with the accurate formula and the simplified formula are thoroughly discussed in this chapter. The results reveal that the simplified formula leads to an overestimation on the eddy current loss, particularly in the region where the relative permeability is high. This overestimation gap would be broaden at high frequencies. However, the overestimated error can be ignored at high flux densities because of a much smaller permeability than those in the operational region.

The popular power loss separation algorithms require curve fittings, and this has been specifically discussed here. This algorithm is tested on a CGO sample measured with the improved SST proposed in Chapter 4. The results show that, two critical problems for this separation algorithm bring uncertainties and errors into the models of core loss and its three components: (1) The assumption, that k_a and k_e are constants and do not vary with the flux densities, is not appropriate. Although it will not bring significant difference to the total power loss, it will change the percentages of the three loss components in the total loss. (2) The data sets chosen for solving the four coefficients in the hysteresis loss formula largely affects the performance of the core loss model. It is suggested to pick up the representative values in each region of the power loss curve, such as sets of 0.5 T, 1.2 T, 1.5 T, and 1.9 T, in order to minimise the error.

In order to overcome the two problems mentioned above, a simpler and more accurate power loss separation algorithm is proposed in this chapter. It avoids the curve fitting and data sets selection issues. It only requires the measured data at two different frequencies rather than six frequencies in the old algorithm without any comprise to the accuracy of the core loss modelling. The separation results give a trend in the percentage of eddy current loss similar to the previous algorithm as revealed in Section 6.3. The percentage of the anomalous loss first drops to around 35% at 1.3 T, and almost remains the same value until the saturation. The percentage of the hysteresis loss, however, steadily increases with the flux density levels for the whole range.

The proposed models can be useful for the finite element software packages to analyse the core power losses and the corresponding temperatures. This is particularly important when the hotspots caused by core saturation and magnetic flux redistribution are concerned. Better understandings of the variation of the core loss and its three components with the flux density levels are thus beneficial to help design a good power transformer with a lower loss and a higher efficiency.

7 Calculation of Distributions of Magnetic Flux and Power Loss with FEM

7.1 Introduction

The prediction accuracy of core losses for a transformer in design stage is vitally important, and empirical methods derived from previously tested core structures were generally adopted by industry in addition to basic material loss calculation formulae [109]. The accuracy of empirical methods was reasonably acceptable for standard designs. However, the accuracy drops when non-standard designs are considered or new materials used. Therefore, it is desirable to use the finite element computational method based on Maxwell's equations together with measured magnetic properties of electrical steels leads to help achieve a more accurate predication about the transformer core losses, and nowadays it is widely applied by the transformer manufacturers.

The core joint area contains the air gaps and overlaps, that forces the magnetic flux to jump into adjacent laminations. This deviation of magnetic flux from the rolling direction of electrical steel laminations results in a local high magnetic flux density, which therefore increases losses. Hence, it is essential to understand the magnetic flux distribution inside the core, and particularly at the joints to estimate the core losses. This flux distribution will be also useful to predict the core hotspot positions.

Several researchers have measured the magnetic flux distribution in the joint area with arrays of single turn search coils [19], [39], [110]–[112]. Double-lapped, butt and lap, and 45° mitred corner joints were compared. It was found that the 45° mitred corner joint configuration has an advantage in lower power loss due to less deviations of magnetic flux from the rolling direction of electrical steels [39]. Moses [113] suggested that the areas of high localised loss at T-joints in three-phase transformers can be directly related to the presence of a rotating component of flux, normal flux, and third harmonic flux. Many studies were also conducted with finite element method to simulate the magnetic flux distributions at the joints in 2D and

3D models. With 2D finite element analysis, Mechler [114] investigated the magnetic flux distribution behavior in the single-step-lapped (SSL) and multi-step-lapped (MSL) joints, which confirmed the benefits of MSL joints in reducing core losses, noise, and excitation current. TeNyenhuis [115], based on the 2D transformer core model, discussed the effects of operating flux density, excitation frequency, and core material on the local joints losses. However, many 2D simulations do not take account of the flux transfers at the joints, which overestimated the magnetic flux compared with the experimental results [109]. Girgis [116] concluded that the contributions of air gaps in joints to nonuniform flux distribution results in even more distorted flux waveshapes, higher harmonic contents and hence higher losses. However, only a few 3D finite element simulations considered both the air gaps and the anisotropic magnetic properties of laminations [117], [118]. Hihat [117] studied the simple butt and lap square core in 3D considering air gaps. Unfortunately, the most popular joint configuration 45° mitred corner was not discussed there. Hernández [118] analysed the flux transfers in the 45° mitred corner joint, but the unrealistic constant relative permeability 10000 was taken for the transverse and normal direction of core laminations. Moreover, the majority of simulations with finite element methods are focusing on the behavior at normal operating flux densities [114]–[118]. Recent concerns on overflux challenges brought by geomagnetically induced currents or quadrature booster operations, encourage more flux distribution analysis at high flux densities [119], [120].

This chapter first briefly introduces the numerical computation with the finite element method and one commercial application package – COMSOL Multiphysics. The derivation of differential equations used in COMSOL is illustrated as well. Following that, the realistic scenario of magnetic flux transfer is considered, including the effects of stacking air gaps, joint air gaps, and the anisotropic characteristics of laminations. The magnetic flux distributions in SSL and MSL joints in the 2D and 3D models are presented. The effects of higher operating flux densities on the SSL and MSL joints are investigated. In addition, an alternative way is adopted to reflect the effect of very thin air gaps, which does not produce any mesh or study difficulties for the 3D 45° mitred corner model. For the single-phase Schneider 1 MVA 6.6 kV/433 V

transformer core, the main flux, as well as the leakage flux with clamping structures are analysed and discussed. The distributions of the power loss in both core and clamping structures are also presented.

7.2 Finite Elements Method and COMSOL

The finite element method (FEM) is one of the most powerful numerical techniques for solving a system of differential equations related with physics or engineering problems. The principle of FEM is to divide a whole structure into a finite number of small elements. The collection of these elements is called the finite element mesh. One advantage of the subdivision is allowing each small element to have a simpler shape, which leads to an accurate approximation of the complex geometry. Another advantage is that FEM can capture the local effects, and reflect the effects of dissimilar material properties. A set of simultaneous algebraic and/or differential equations gained by connecting elements together, will be solved via the piecewise polynomial interpolation technique, such as the Galerkin's method [121].

The finite element analysis is an implementation of FEM to performing a computational engineering analysis. A typical FEA procedure adopted by commercial software is shown in Fig. 7.1 [122]. After choosing a suitable analysis type and element type, such as a stationary study for a 3D model, one of the most important things might be the mesh generation, which largely determines the accuracy and even the convergence of the solution. The three widely used meshing methodologies are advancing front technique, Delaunay technique, and artificial neural networks (ANN) [123], [124]. The modern advancing front technique is often chosen due to a high-quality point distribution though it is less efficient since it generates a large number of nodes. Delaunay technique is good in terms of the efficiency, measured in complexity or CPU time. However, Delaunay technique may encounter the problem of boundary recovery for a 3D model, and other robustness together with quality issues, as reported in [123]. ANN shows a good adaptive capability in generating mesh. Nevertheless, it needs training and the time of calculation is questionable due to the continuous refinement. Hence, a sound automatic mesh function is an important selling point for FEA commercial software. COMSOL Multiphysics, for

example, uses the physics-controlled mesh as default, which takes the analysis type, geometry, and the materials, etc. into account to determine the parameters for meshing: the max/min element size, max element growth rate, curvature factor and the resolution of narrow regions. In practice, it is often necessary to manually mesh the model for a satisfactory result.

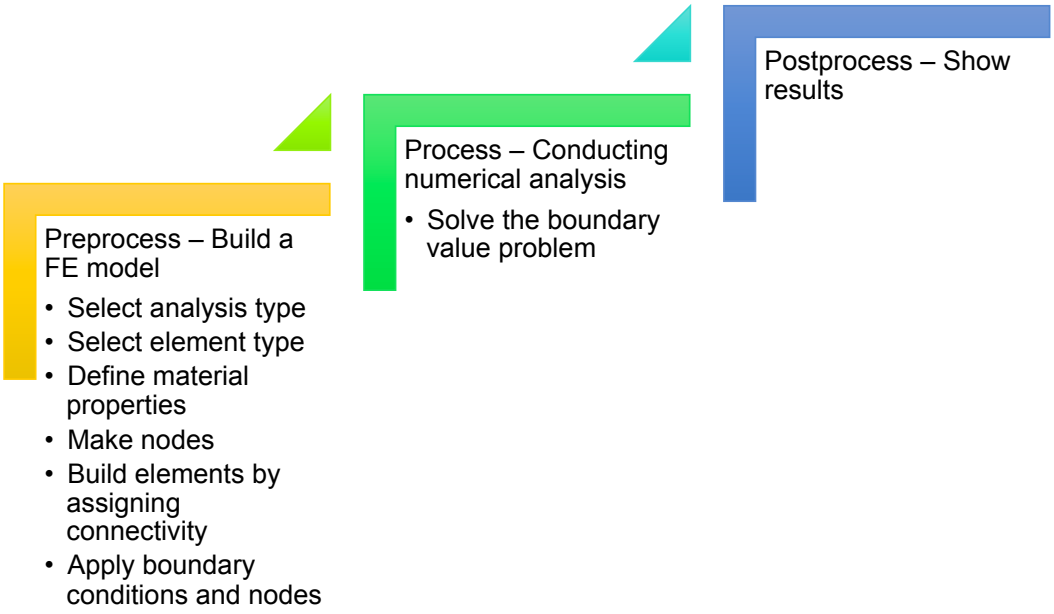

Fig. 7.1 The typical procedure of FEA commercial software.

For electromagnetic analysis, the process of FEA is actually solving Maxwell's equations. The standard Maxwell equations for the electromagnetic FEA are illustrated below:

$$\nabla \times \mathbf{E} = -\frac{\partial \mathbf{B}}{\partial t} \tag{7.1}$$

$$\nabla \times \mathbf{H} = \mathbf{J} + \frac{\partial \mathbf{D}}{\partial t} \tag{7.2}$$

$$\nabla \cdot \mathbf{B} = 0 \tag{7.3}$$

where, $\mathbf{E}$ is the electric field strength; $\mathbf{J}$ is the current density; $\mathbf{D}$ is the electric flux density. In order to make solving the Maxwell's equations simple, the magnetic vector potential $\mathbf{A}$ is usually introduced to formulate the problems, which is given by:

$$\mathbf{B} = \nabla \times \mathbf{A} \tag{7.4}$$

Equation (7.3) and (7.4) give

$$\nabla \cdot \left(\nabla \times \mathbf{A} \right) = 0 \tag{7.5}$$

For the static situation, recalling (2.11), (7.2) can be simplified as below:

$$\nabla \times \left(\mu^{-1} \nabla \times \mathbf{A} \right) = \mathbf{J} \tag{7.6}$$

For time-varying magneto-dynamic fields, the quasi-static approximation can be used by neglecting the displacement current ($\frac{\partial \mathbf{D}}{\partial t} = 0$) when the conductivity is much larger than the product of radian frequency and permittivity, i.e. $\sigma \gg 2\pi f \varepsilon$ [125]. For convenience, the electric scalar potential V can be defined from the transformation of (7.1), as shown in (7.7).

$$\nabla V = -\left(\mathbf{E} + \frac{\partial \mathbf{A}}{\partial t} \right) \tag{7.7}$$

Considering $\mathbf{J} = \sigma \mathbf{E} + \mathbf{J}_e$ ($\mathbf{J}_e$ is an externally generated current density) and (7.7), we have

$$\mathbf{J} = \sigma \left(-\nabla V - \frac{\partial \mathbf{A}}{\partial t} \right) + \mathbf{J}_e \tag{7.8}$$

Equation (7.6) and (7.8) yield the formulation

$$\mathbf{J}_e = \nabla \times \left(\mu^{-1} \nabla \times \mathbf{A} \right) + \sigma \nabla V + \sigma \frac{\partial \mathbf{A}}{\partial t} \tag{7.9}$$

The numerical analysis can then be done by the FEA software solving the above equation (7.9).

The postprocess step is mainly to show the calculated results properly and data export for further analysis. Take COMSOL Multiphysics as example, it has a powerful result visualization tool to generate 1D plots (e.g. line graphs, point graphs, global parameters graphs), 2D plots (e.g. surface plots, contour plots, arrow plots), 3D plots (e.g. volume and surface plots) together with the physical model geometry, which makes it convenient to present the FEA results.

7.3 Distribution of Flux at Corner Joints

7.3.1 Transformer Core Joint Models for FEA

The schematic geometry of 2D transformer core joint region with SSL and MSL joints are illustrated in Fig. 7.2 (a) and (b). The electrical steel laminations are coloured in grey, and the air gaps are highlighted in blue. The number of lamination layers used in this finite element simulation is 10, considering the number of mesh elements and accuracy [39], [114]. In Fig. 7.2, the air gaps in the joint region consist of joint airgaps in the same lamination layer and stacking airgaps between adjacent layers. The joint air gap g in the real full-size transformers takes a value in the range of 1 to 3 mm [126]. g=2 mm is selected here to represent an ordinary building accuracy. The stacking airgaps are very tiny, but can be estimated using the stacking factor and the lamination thickness. In this 2D study, 0.01 mm stacking airgaps would be selected for the 0.3 mm laminations with 97% stacking factor. A typical overlap length o=9 mm is applied in the 5-step MSL joint model as many researchers used [114], [126]. For the convenience of comparing the flux distribution behavior between SSL and MSL joint configurations, the overlap length in SSL model is set to 42 mm in order to make an identical joint region length (overlaps plus joint airgaps) to that of the MSL model.

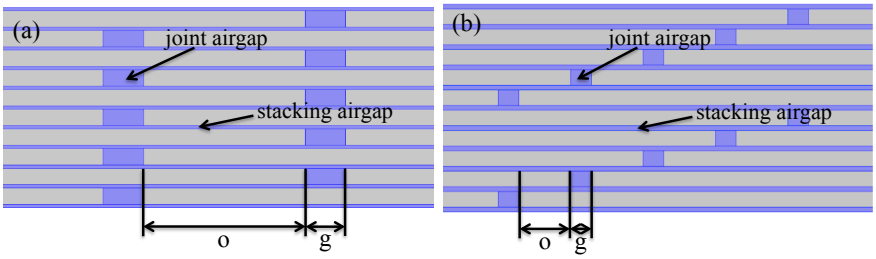

Fig. 7.2 Transformer core joint region in 2D: (a) SSL joint (b) MSL joint. (not to scale)

For the 3D study, the 45° mitred SSL configuration is built in this paper to validate the alternative air gaps modelling method. As illustrated in Fig. 7.3, the joint is built with 10 layers of 0.3 mm laminations, 2 mm joint airgaps, and 0.01 mm stacking airgaps. Besides, the same joint region length is kept in the 3D models as well.

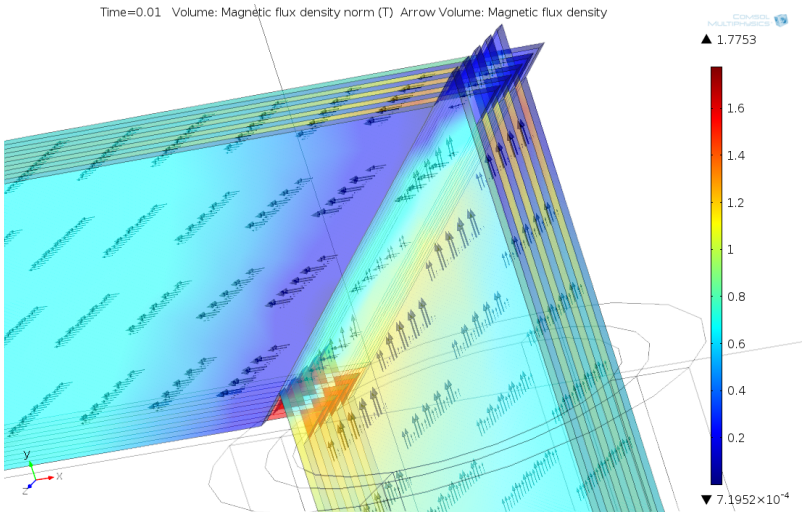

Fig. 7.3 Transformer core with SSL 45° mitred joint in 3D. (not to scale)

The magnetic properties of grain-oriented electrical steels currently used for power transformers are anisotropic. It is therefore vital to involve the anisotropic magnetisation curves (B-H) into the 2D and 3D finite element simulations. As no measured material properties in normal direction is available, the assumption is made that the magnetisation in normal direction behaves similar to that in transverse direction, which is reasonable from the aspect of crystalline structure of grain-oriented steels [119]. The anisotropic B-H characteristics of silicon steel GO M-6 provided by COMSOL Multiphysics, as shown in Fig. 7.4, would be used to evaluate the magnetic flux distribution behaviour of core joints.

All the simulations in this paper were performed in the commercial finite element software package COMSOL Multiphysics 4.4. The number of elements for 2D models is about 3 million. The direct linear solver is used to obtain a fast convergence. For the 3D model, due to a much higher degree of freedom, and the more severe nonlinear situation including normal direction, the iterative linear solver is chosen to meet the memory limit requirement and keep the convergence.

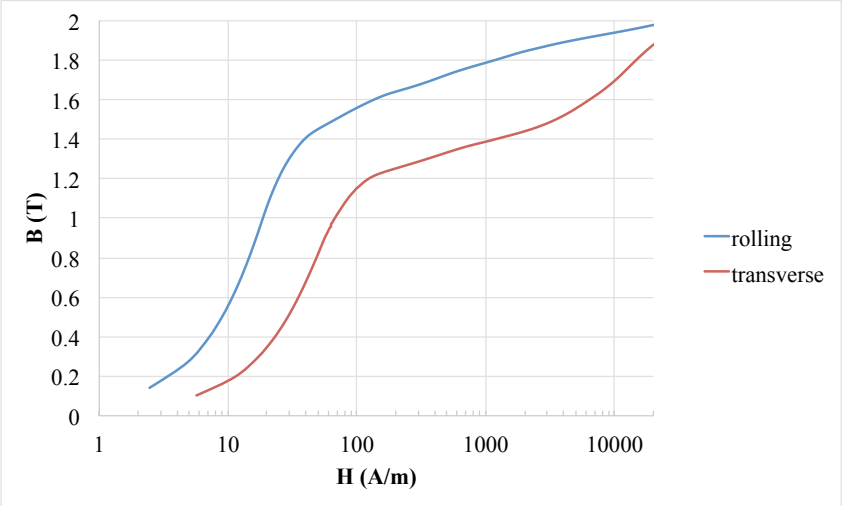

Fig. 7.4 Anisotropic B-H characteristics of silicon steel GO M-6 from COMSOL Multiphysics.

7.3.2 Magnetic Flux Distributions with the 2D Model

When the overall induction level is 1.5 T (normal operation level), the rolling direction component of magnetic flux (Bx) in the SSL joint configuration is presented in Fig. 7.5. Far from the joint air gaps, the flux density is almost evenly distributed throughout all the laminations, equal to 1.5 T. As approaching to the joint air gaps, the magnetic flux density drops and is transferred into the adjacent lamination layers.

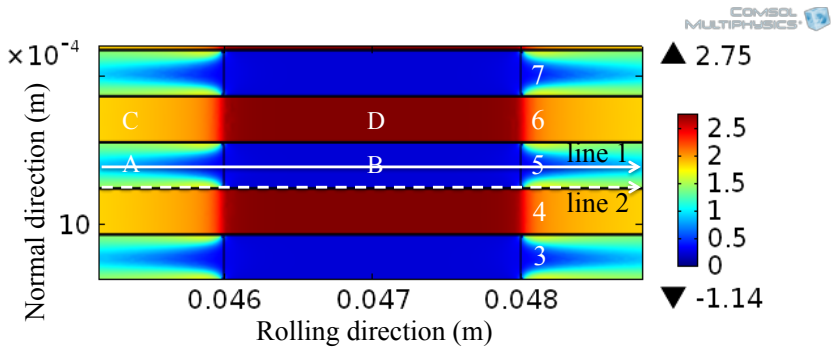

Fig. 7.5 Bx in the SSL joint configuration at 1.5 T.

In order to further analyse this scenario, Bx along the middle of lamination 5 (line 1) is plotted in Fig. 7.6. It can be seen that Bx is dropping to only 0.25 T in the region approaching the joint air gap. Part of Bx is transferred into the normal direction (Bz) and penetrates into the adjacent layers 4 and 6, leading to a higher flux density than 1.5 T in region C. In the joint air gap, i.e. region B, a flux density around 0.25 T is observed. Region D in the adjacent layers 4 and 6 is highly saturated with the flux density up to 2.75 T, although this area is very small (2 mm).

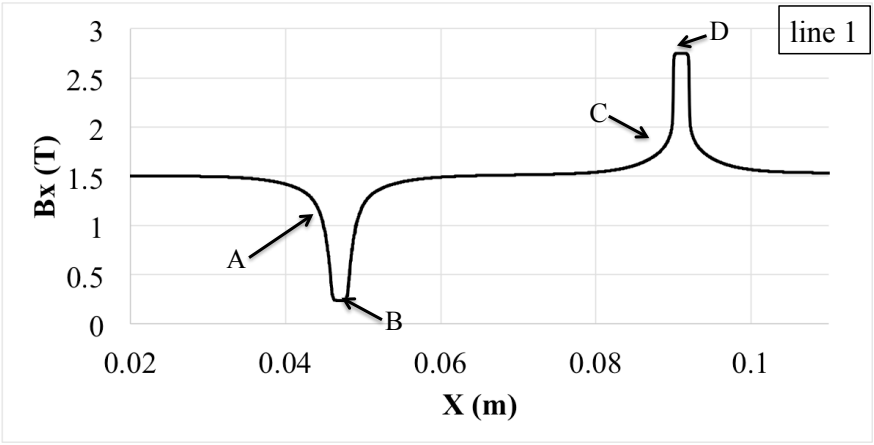

Fig. 7.6 Variation of Bx along the path line 1 in the lamination for the SSL model.

Fig. 7.7 shows how the magnetic flux varies in the stacking air gap between the layer 4 and layer 5 along the middle path line 2. The magnitude of the normal flux density is 1.25 T keeping the flux conservation. It also reveals the flux transfer only occurs in a very narrow region, just 1 mm before and after the joint air gap. The root cause for that is the magnetic flux will always distribute in the least reluctance loop path. The

high relative permeability μ_r (around 20,000 at 1.5 T) in the rolling direction provides a lower reluctance path, making the flux "waiting" until very close to the joint air gaps to be transferred with the A-C-D path. The equilibrium is thus retained between the A-C-D path and the A-B path, where the reluctance is mainly affected by the following three parameters: the low μ_r for the normal flux in the laminations, the decreased μ_r for the rolling direction flux due to saturation, and the ratio between the air gap length and the lamination thickness. Meanwhile, the uneven flux distribution Bz in region A is hard to be measured with search coils, which is also one of the advantage of finite element computation over the experiments [39].

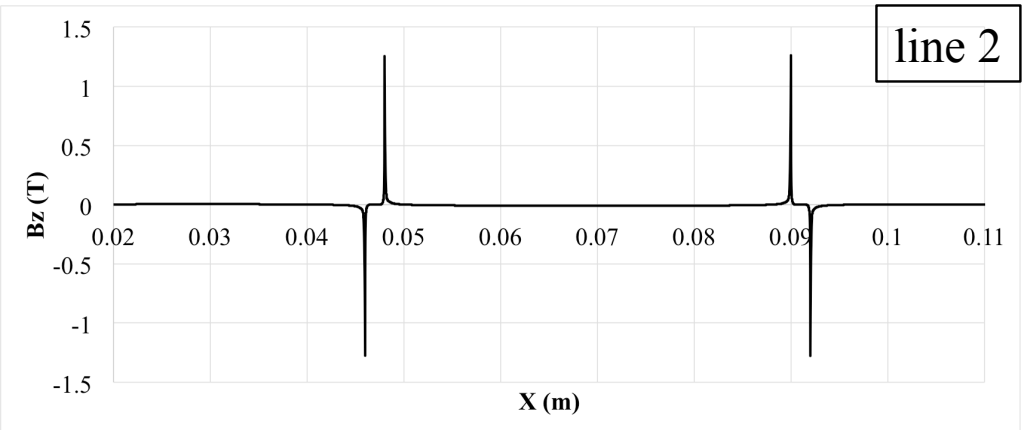

Fig. 7.7 Variation of Bz along the path line 2 in the stacking air gap for the SSL model.

In order to make the flux transfer smooth, 5-step MSL joints are introduced. Fig. 7.8 clearly shows the highest flux density appeared in the MSL model is just 1.9 T as compared to 2.75 T in the SSL model. The magnetic flux density variations along the rolling direction Bx in each step are plotted in Fig. 7.9. It demonstrates there hardly any magnetic flux travels in the joint airgaps (around 4 mT). The flux is then redistributed almost equally (around 1.88 T) among the other four laminations, which means the peak flux density is reduced by around 30% as compared with the SSL joints. This study confirms the benefits of applying the MSL joints configuration to transformer cores, which helps improve the flux distribution, resulting in lower power losses as well as lower noise level for a power transformer.

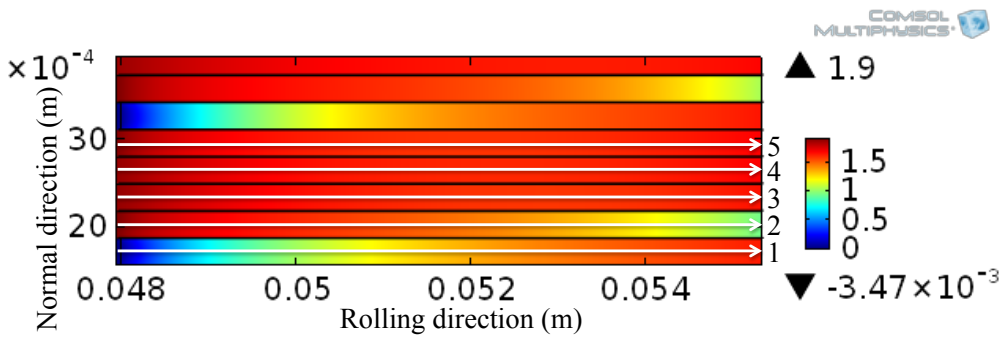

Fig. 7.8 Bx in the MSL joint configuration at 1.5 T.

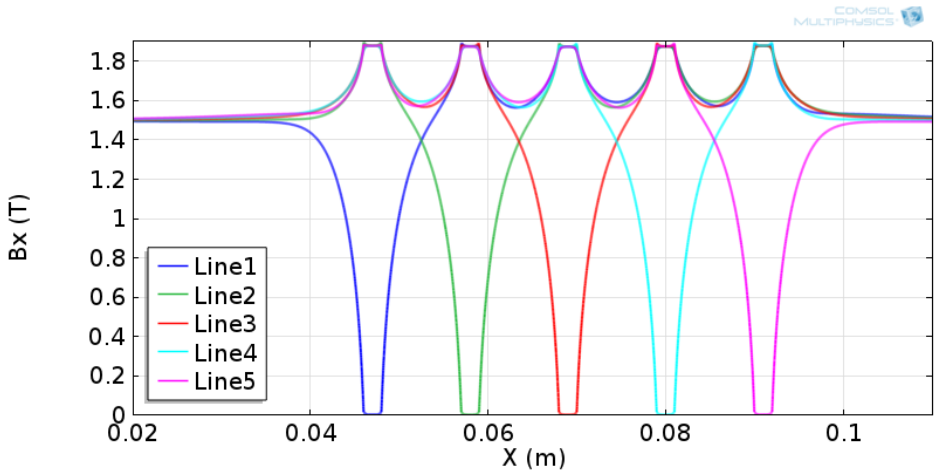

Fig. 7.9 Variation of Bx along the path lines 1, 2, 3, 4, and 5 in the laminations for the MSL model.

Fig. 7.10 and Fig. 7.11 show the effects of various operating flux densities, particularly at very high flux densities, on the flux distribution pattern in the core joint region. For the SSL joint configuration operated at high flux density Bx=1.9 T, the peak flux density in the narrow region beyond the joint air gaps can even achieve 3.4 T (this unrealistic high value is computed based on the assumption of linear extrapolation of B-H curves), as shown in Fig. 7.10. Simultaneously, this extreme saturation makes the flux transfer between the adjacent layers terribly inefficient, causing a slight increase at the edge of the joint air gap and two times higher leakage flux travelling in the air.

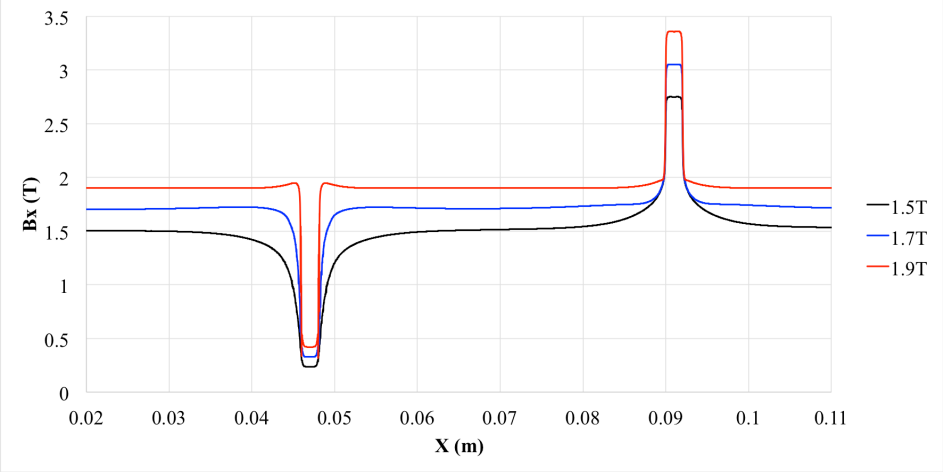

Fig. 7.10 Variation of Bx in the lamination for the SSL model at different operating flux densities.

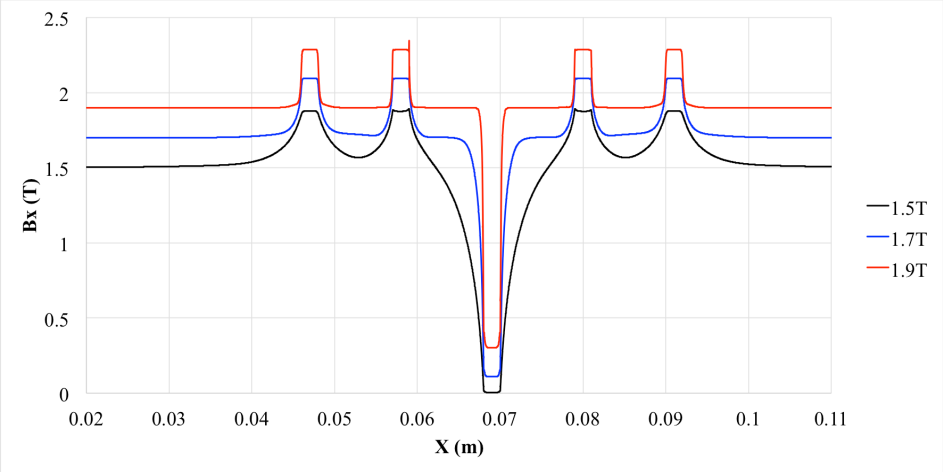

Fig. 7.11 Variation of Bx in the lamination for the MSL model at different operating flux densities.

Correspondingly, the peak flux density in the MSL joint configuration is just 2.3 T, which is 33% less than that in the SSL model. The fluxes travelling in the joint air gaps are 0.1 T and 0.3 T when the operating Bx equals to 1.7 T and 1.9 T respectively. Overall, the MSL configuration still shows a better distribution pattern than the SSL one at high flux densities, although the relative advantage of using an MSL joint over an SSL joint is less due to both joints being fully saturated.

The effect of different joint air gap g on the magnetic flux distribution for the MSL configuration is also investigated. As shown in Fig. 7.12, the flux density traveling in

the electrical steels almost follows the same pattern with the same peak flux when g varies from 1 mm to 3 mm. The joint air gap therefore has no major influence on the flux distribution. It indicates that the imperfection in core laminate stacking with some errors in joint air gaps will not produce a significant impact on the flux distributions, which can be another benefit by using MSL joints.

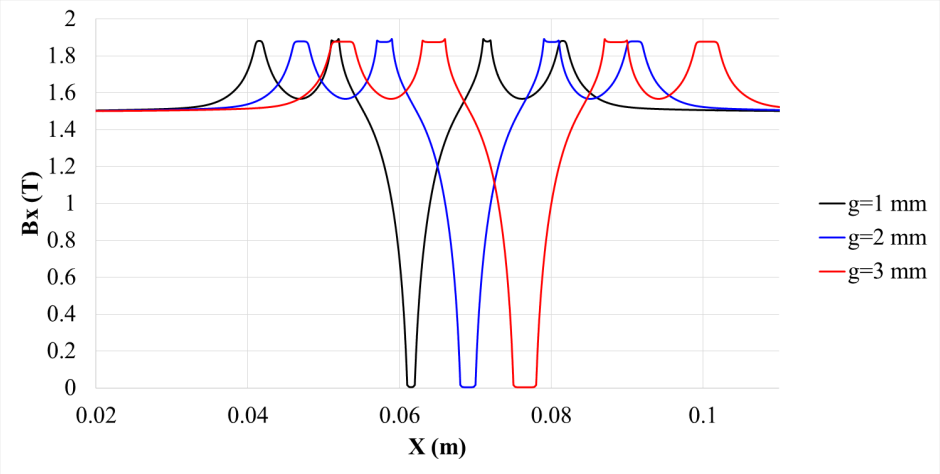

Fig. 7.12 Variation of Bx in the lamination for the MSL model with different joint air gap g at 1.5 T.

7.3.3 Magnetic Flux Distributions with the 3D Model

For the 3D joint model, the consideration of air gaps brings technical challenges to the elements meshing. The requirement of a high number of elements with good quality makes it impossible to successfully obtain a convergent solution. Hence, the thin low permeability gap is introduced here. The thin low permeability gap adds boundary conditions on an internal boundary, which allows for a discontinuity in the magnetic scalar potential. It represents a thin air layer in the electrical steels while avoiding a real thin air gap in geometry and consequently meshing for it. The physical air gap is thus removed from the FEA modelling structure, and the gap is accounted for by applying the following boundary condition. As shown in , the difference between the normal component of magnetic flux $\mathbf{B}_1$ and $\mathbf{B}_2$ through this boundary is:

$$\mathbf{n}\cdot(\mathbf{B}_1-\mathbf{B}_2)=\mu_0\frac{V_m^d-V_m^u}{d_s} \tag{7.10}$$

where V_m^u and V_m^d are the magnetic scalar potentials on the upside and downside of the stacking air boundary respectively; d_s is the thickness of the stacking air gap, i.e. 0.01 mm.

Fig. 7.13 demonstrates the flux distribution result in the 5th lamination layer with SSL 45° mitred joints at an operating flux density of 1.5 T. The colour denotes the magnitude of flux density. The black cones represent the direction of flux densities in the horizontal plane, whose length is proportional to the flux density levels.

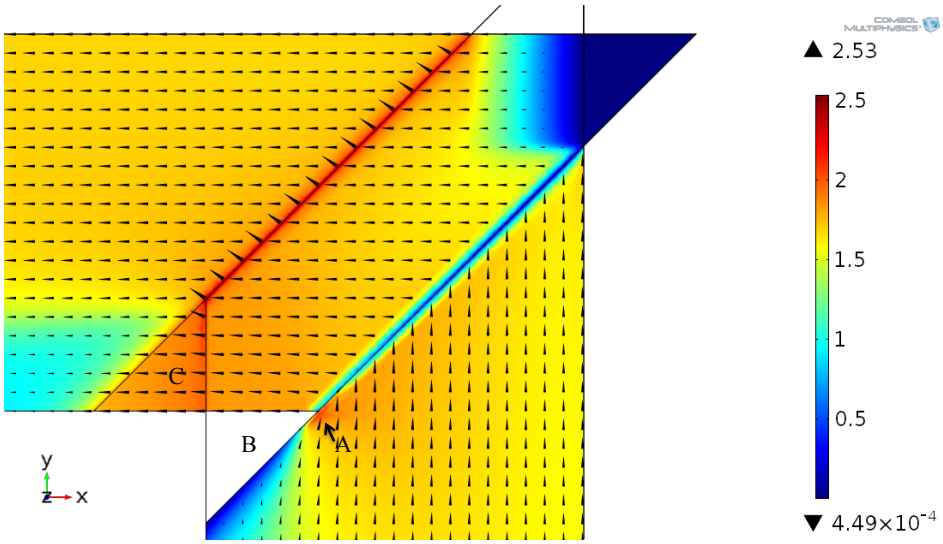

Fig. 7.13 The 3D flux distribution result in the 5th lamination layer with SSL 45° mitred joints at operating flux density 1.5 T.

It can be seen that the flux in the inner side tends to deviate towards the centre of the lamination when approaching the overlap region because of the triangle air gap ahead. This deviation leads to a local saturation (around 2.0 T) in a small region, region A shown in Fig. 7.13. Meanwhile, some of the fluxes in the inner side also travel into the adjacent laminations layer 4 and layer 6, which increases their flux density levels in the triangle region – region B. For the same reason, a high flux density level is observed in the triangle region, region C. The flux distribution behaviour in 3D model

is similar to the previous 2D simulation results. About 0.2 T is found traveling in the joint air gap, and the corresponding areas in the adjacent layers, 4 and 6, rise to saturation. The flux always picks the lowest reluctance loop path, so the flux density at the inner corner joint (2.5 T) is higher than that at the outer corner joint (2.0 T) along the joint air gap. The good agreement between this 3D simulation result and the experimental result from [39] confirms the benefits of air gap modelling with the thin low permeability gap. It should also be noticed that the magnetic flux distribution behaviour in this 3D model is largely dependent on the dimensions of the lamination, overlap length, air gap length, and of course the B-H characteristics of the material.

7.4 Distribution of Flux in the Single-Phase Transformer Core

7.4.1 Transformer Core Model for FEA

In order to investigate the distribution of the main flux and the leakage flux, particularly at high flux densities, a single-phase transformer core model is built to describe the Schneider 1 MVA 6.6kV/433 V power transformer, as shown in Fig. 7.14.

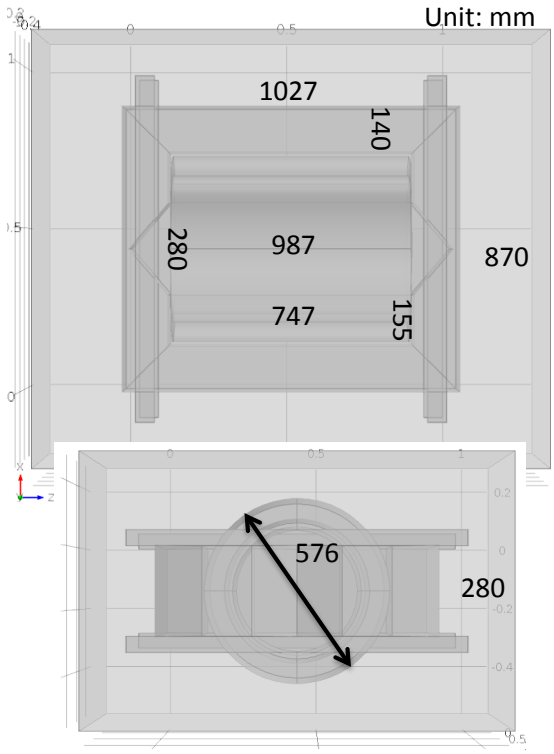

Fig. 7.14 FEA model in 3D for the Schneider 1 MVA 6.6kV/433 V power transformer.

The key parameters of this power transformer is described in Table 7.1, where the clamping structure's relative permeability is assumed as a constant 50, suggested in [88].

Table 7.1 Key parameters for the FEA transformer model in 3D.

Item	Dimension
Leg	140 mm*1027 mm
Centre Limb	280 mm*987 mm
Yoke	140 mm*870 mm
Window	155 mm*747 mm
Core thickness	280 mm
HV winding's diameter/thickness	576 mm/63 mm
HV winding's turn number	300
HV winding's wire cross-section area	22 mm^2
LV winding's turn number	12
LV winding's wire cross-section area	583 mm^2
Wire's conductivity	1.163e7 S/m
Clamping structure's relative permeability	50
Clamping structure structure's dimension	1054 mm*50 mm*58 mm

The CGO steel's B-H characteristics up to 2 T, measured with the improved SST in Chapter 4, is used for the core material, whose relative permeability is illustrated in Fig. 7.15.

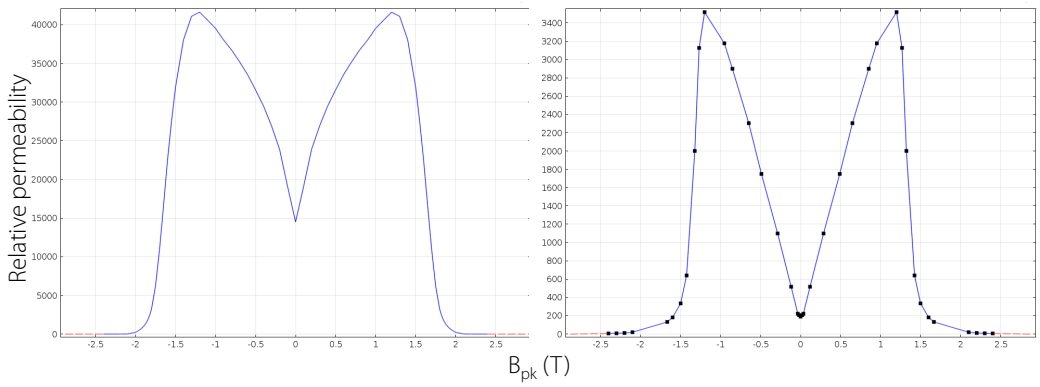

Fig. 7.15 The relative permeability for the core material in FEA model. (left for the rolling direction; right for the transverse/normal direction)

7.4.2 Distribution of Main Flux

The HV winding on the centre limb is connected with an ideal strong voltage source to give the 50 Hz sinusoidal outputs in order to magnetise the core. The LV winding is open circuit without any loadings. Recall (3.2), the peak main flux in the core can be adjusted by changing the voltage source outputs. The phase angle of the flux is lagging that of the voltage by 90°, for which the peak value of the main flux is expected to be seen at 0.01s in a cycle.

The overview of the main flux distribution in the transformer core at various flux densities is illustrated in Fig. 7.16. The colour indicates the normalised flux density, i.e. $\sqrt{B_x^{\,2} + B_y^{\,2} + B_z^{\,2}}$. In order to compare the distribution pattern of the flux qualitatively, the letter N is used to represent the region where the normalised B is around the average value in the centre limb. Similarly, L notes the region whose normalised B is lower than that in N region; S indicates the region whose normalised B is higher than that in N region; LL notes the region whose normalised B is lower than that in L region; SS indicates the region whose normalised B is higher than that in S region; SSS represents the highest flux density region.

Fig. 7.16 reveals the highest flux density will always appear at the inner corner of mitred joints, while the lowest flux density will be found at the top position of the T-joint. The reason behind is that the flux tends to pick the path with a shorter magnetic loop length. This also leads to the uneven flux distribution in limbs and yokes, which is particularly obvious at a lower flux density in Fig. 7.16 (a). However, the flux is distributed more evenly when the average induction level is increased. This is caused by the reduction of the relative permeability at a higher flux density level, resulting in a larger reluctance and pushing the flux out of the shorter inner corner path.

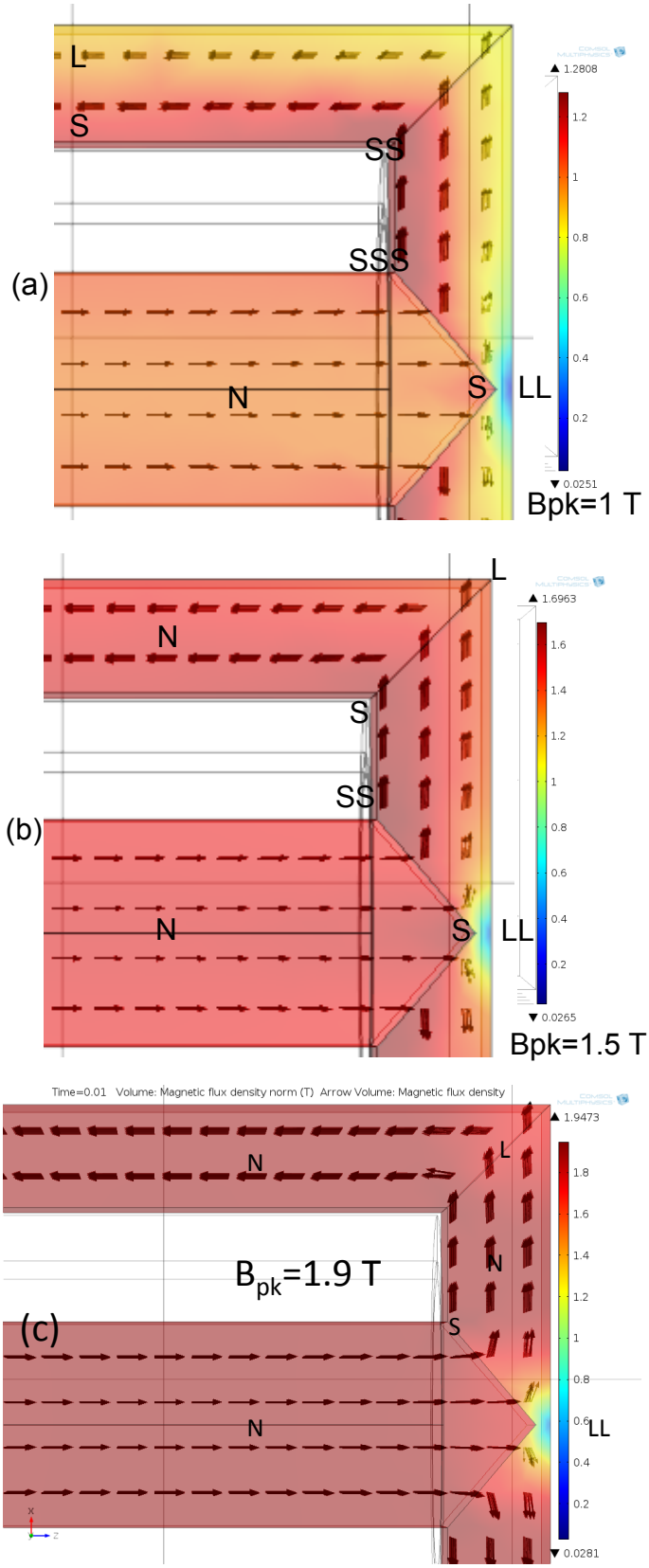

Fig. 7.16 The overview of the main flux distribution at various flux densities: (a) 1.0 T; (b) 1.5 T; (c) 1.9 T (zoomed).

To further analyse the main flux in the transformer core quantitatively, a cut plane and a cut line are made in the middle of the limb, which is illustrated in Fig. 7.17. Under the 50 Hz AC magnetisation, the main flux distributions in limbs, whose peak flux density is set around 1 T during a half cycle (0.01 s), are demonstrated in Fig. 7.18. The upper 2D cut plane figure shows the distribution of the normal flux, while the lower one shows the values of the normal flux density along the cut line at different time in the half cycle between 0 and 0.01 s. In the centre limb, it is found that the flux density in the outer part (1.02 T) is 4% higher that that in the inner part (0.98 T). This difference is much larger at a lower flux density: about 11% at 0.9T, and 25% at 0.5 T. In the side limb, a severe uneven flux distribution can be observed. The flux density in the inner side is much higher than that in the outer side. Along the cut line, around 22% of the side limb has a flux density of 1.17 T; 34% of the limb sees the flux density of 1.02 T; and only 0.9 T is found in the outer 44% of the side limb. The flux in the inner side leg is also higher than that in the centre limb. This difference is also enlarged with the increase of the average main flux density. At 1 T, about 16% higher flux density in the inner side limb compared with the centre limb. This difference is increased to 19% at 0.9 T and 26% at 0.5 T, respectively.

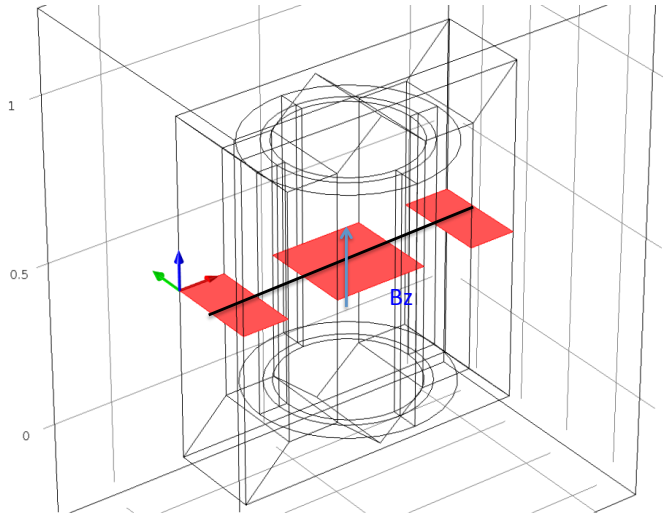

Fig. 7.17 The cut plane and the cut line in the middle of the limb.

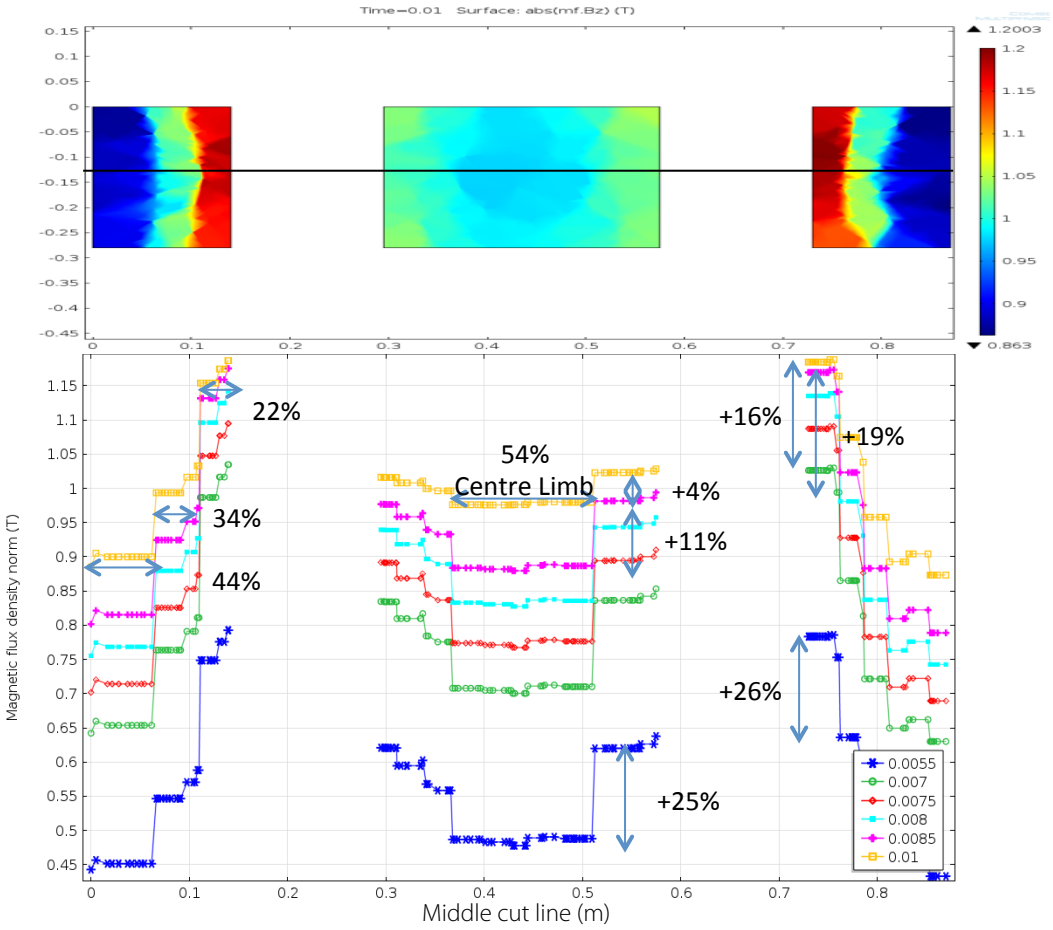

Fig. 7.18 The main flux distribution in limbs whose peak flux density is around 1 T during a quarter cycle for the 50 Hz AC magnetisation.

When the excitation is increased, the core enters into saturation with the peak flux density around 1.8 T, as shown in Fig. 7.19. In the centre limb, the flux will be almost evenly distributed when the flux density value is larger than 1.55 T. In the side limb, however, the flux is still unevenly distributed at 1.55 T, where the inner side is 1.6 T and the outer side is 1.5 T. The flux only starts to distribute evenly when the flux density value is larger than 1.7 T. This is mainly due to the effects of the flux deviation at T-joint, where more flux is squeezed into the inner side of the yoke, which can be also seen in Fig. 7.16 (b).

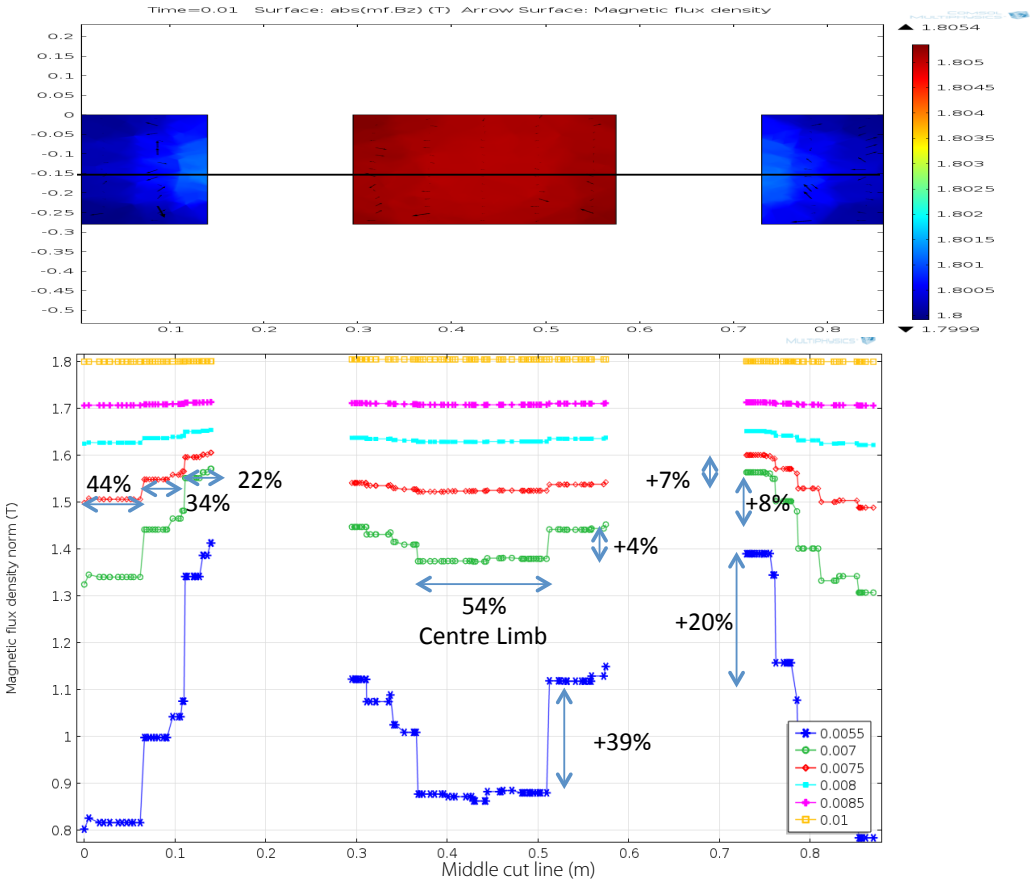

Fig. 7.19 The main flux distribution in limbs whose peak flux density is around 1.8 T during a half cycle for the 50 Hz AC magnetisation.

In the very deep saturation situation (B_{pk} =1.9 T), as shown in Fig. 7.20, the flux distributions in both centre limb and side limb are distributed evenly. Meanwhile, it is interesting to observe that the flux density level in the centre limb now is even higher than that in the side limb. For example, approximate 0.01 T and 0.004 T higher flux density values are found in the centre limb as compared with the side limb, when the flux density level is 1.9 T and 1.81 T respectively. This indicates there exists a considerable leakage flux out of the core in the deep saturation stage, leading to the reduction of the flux density level in the side limb.

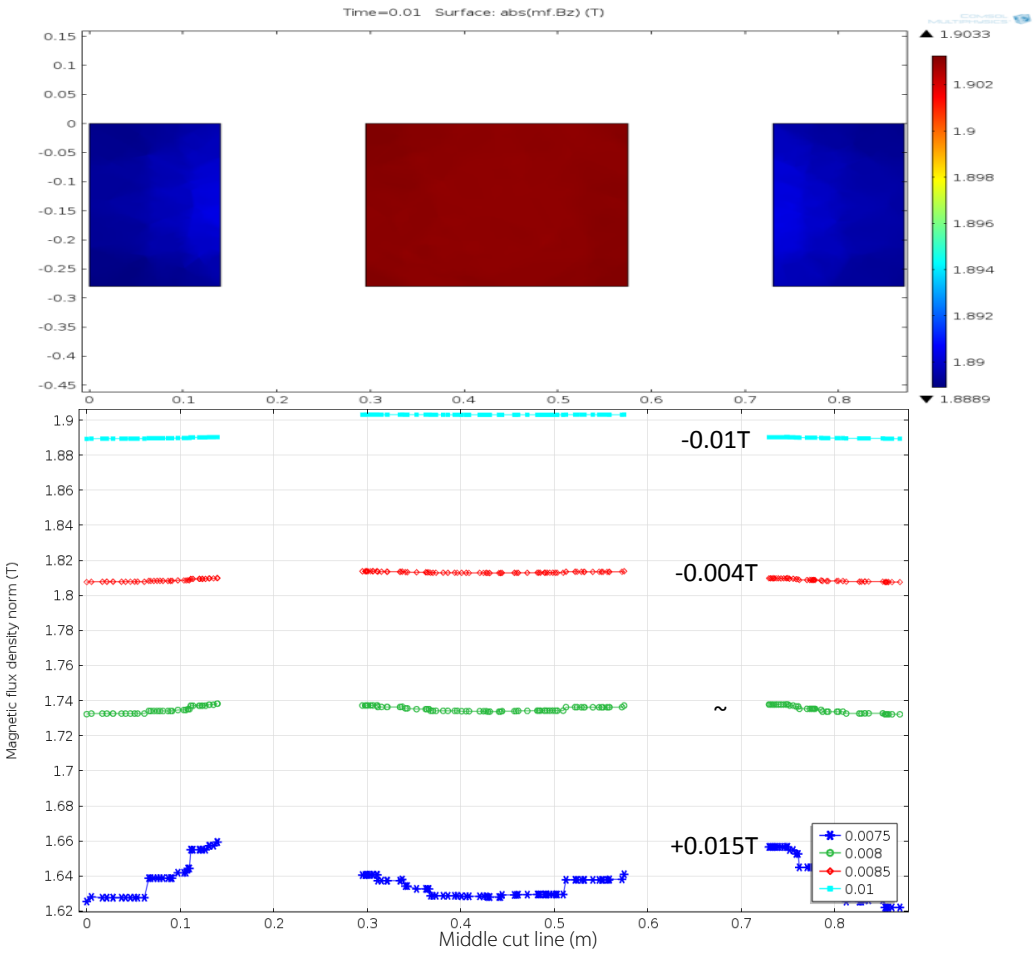

Fig. 7.20 The main flux distribution in limbs whose peak flux density is around 1.9 T during a quarter cycle for the 50 Hz AC magnetisation.

Regarding the main flux in the yoke, it would be helpful if a 2D cut plane is made in the middle of the yoke, as shown in Fig. 7.21. This plane divides the yoke into three zones: zone A is a part of the centre limb; zone B is a part of the yoke; and zone C is a part of the side limb. The main flux distribution for the three zones at various flux densities are summarised in Fig. 7.22. For zone A before the saturation, i.e. the T-joint region of the centre limb, a higher flux density in the middle part can be observed when compared with the side parts. This is because the flux tends to deviate from the centre limb into the yokes earlier to obtain a lower reluctance path length. But in saturation, the flux cannot increase in the inner side of the yoke, making the flux travel in the main limb longer before turning into the x direction. It thus explains the reason why we see a flat line in zone A for the flux density in the z direction.

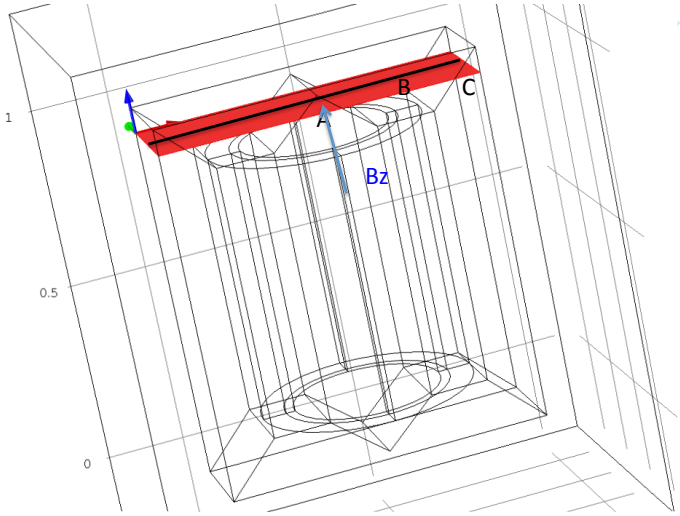

Fig. 7.21 The cut plane and the cut line in the middle of the yoke.

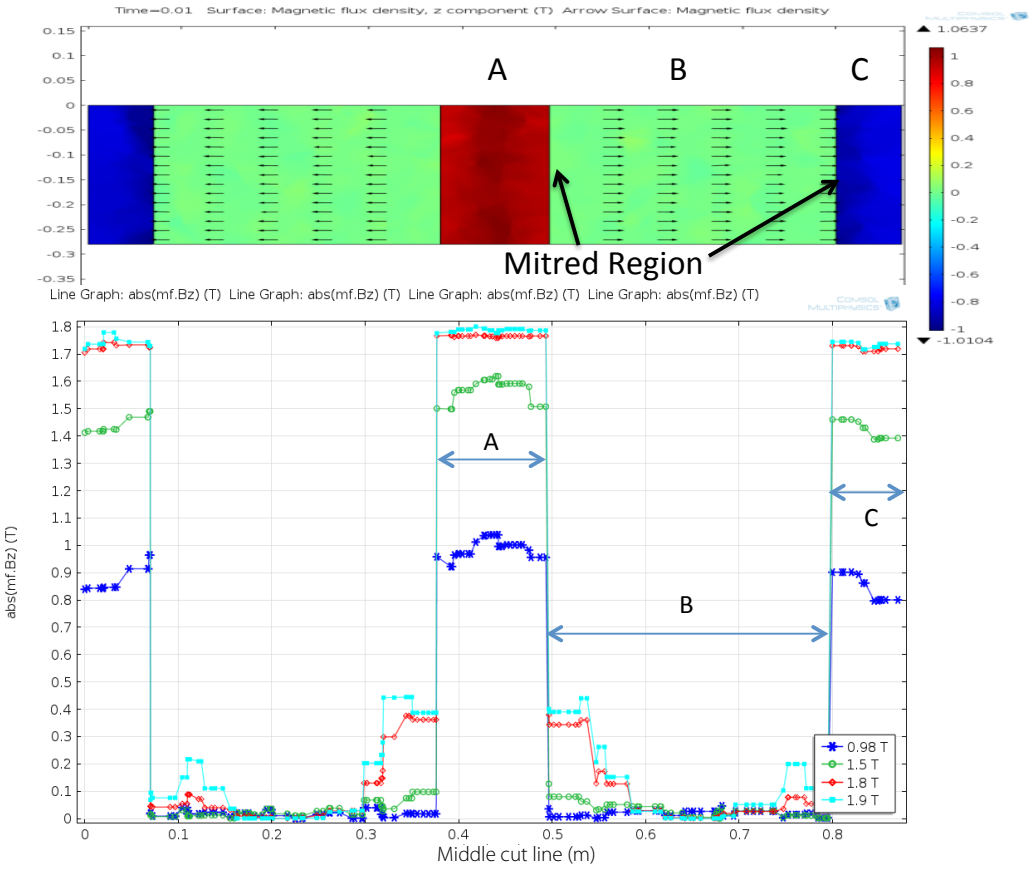

Fig. 7.22 The main flux distribution in the centre yoke at various flux densities during a quarter cycle for the 50 Hz AC magnetisation.

For zone B before saturation, little flux component in the z direction can be seen in the yoke. When the inner yoke is deeply saturated at 1.9 T, the flux (about 0.4 T) will

continue to travel in the z direction to the outer part of the yoke where the permeability is higher before turning into the x direction. Similarly, it explains the flux component around 0.2 T in the z direction found, which is deviating into the side limb at 1.9 T, while all the flux has already turned into the side limb before the cut plane at lower flux densities. A similar distribution pattern in zone C to the middle part of the side limb described previously is also found here, due to the same reason as mentioned above.

7.4.3 Distribution of Leakage Flux

The leakage flux in a transformer is generally very small and difficult to be measured accurately with the search coils. Hence, it would be very useful to see the distribution of the leakage flux at different flux densities with the help of FEA.

For the convenience of analysis, a cut plane for the leakage flux in the middle height of the core is used, as shown in Fig. 7.23. The distributions of the leakage flux in the middle height of the core are then illustrated in Fig. 7.24, when the main flux is increased from 1 T to 1.9 T.

For the normal operation situation, the order of the magnitude of leakage flux densities surrounding the core is 10^{-5} T. The value of the leakage flux is almost increasing linearly with the induction at low flux density levels while the core is operated in the linear region of the B-H curve. In the deep saturation (1.9 T), the leakage flux climbs sharply to the value with the order of the magnitude 10^{-3} T, which is contributed from the flux squeezed out of the centre limb due to the drop of the permeability. The leakage flux in the deep saturation of 1.9 T is around 30 times and 40 times higher than that at 1.8 T and 1.5 T respectively. Fig. 7.24 also reveals that the distribution of the leakage flux in the middle part of the core is almost uniform no matter what the main flux density level is, which corresponds well with the common understanding.

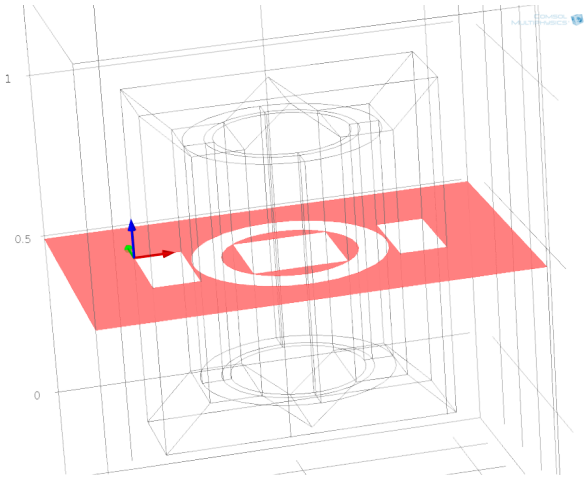

Fig. 7.23 The cut plane for the leakage flux in the middle height of the core.

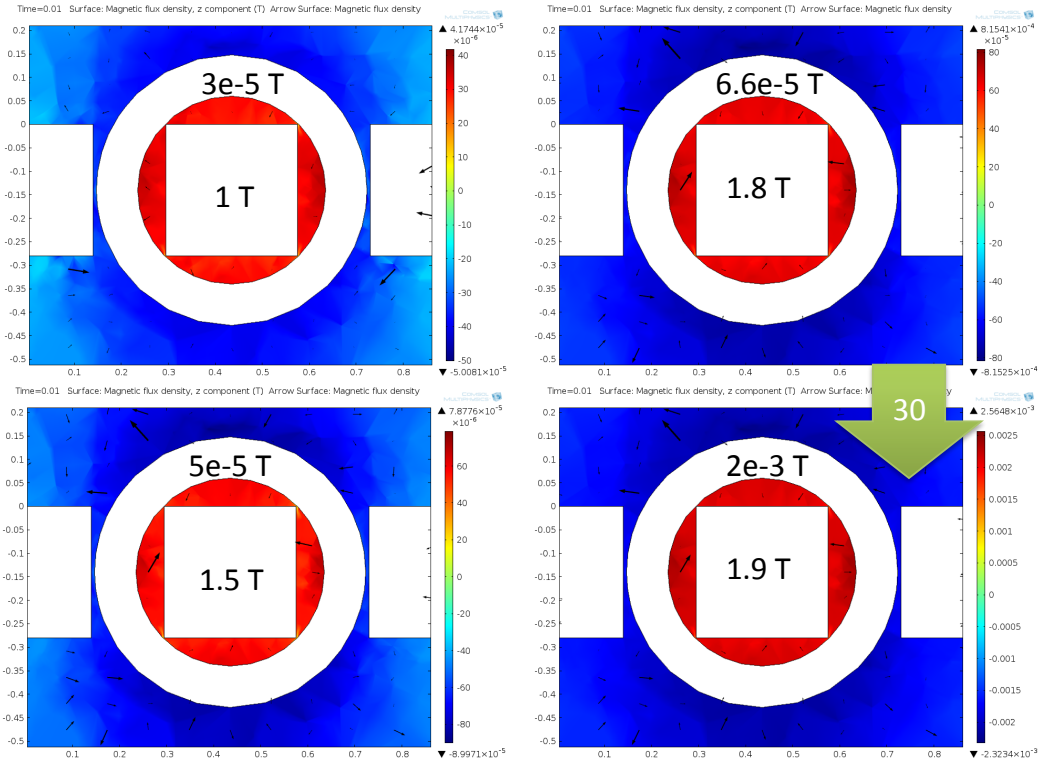

Fig. 7.24 The distribution of the leakage flux in the middle of the core at various flux densities.

Another cut plane for the leakage flux analysis is made at the height position as the same as the top windings, as shown in Fig. 7.25. In contrast to the middle height of the core, the leakage flux is unevenly distributed. The leakage flux tends to concentrate in the region under the yoke. When the main flux is 1.5 T, the leakage flux under the yoke region is 13×10^{-5} T, which is 2.2 time higher than that out of the yoke'

projection (6×10^{-5} T). This trend grows with the main flux density level. At 1.9 T, the concentration ratio between the region under the yoke and out of the yoke rises to 3.6. Besides, the leakage flux in the surrounding space in the deep saturation 1.9 T is about 33 times higher than that under the normal operation around 1.5 T, which may bring stray loss issues if it enters into the adjacent metal components.

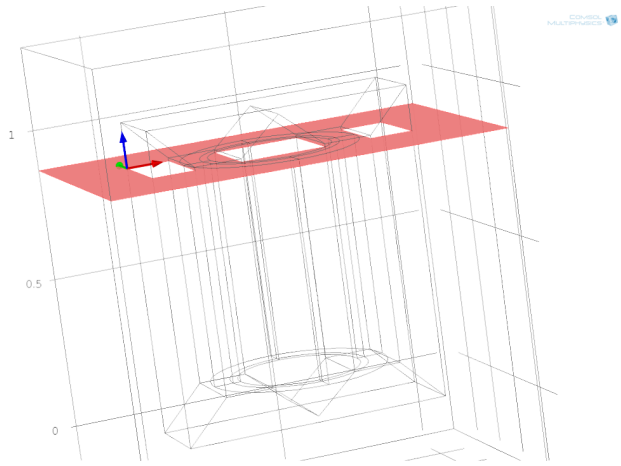

Fig. 7.25 The cut plane for the leakage flux at the top windings.

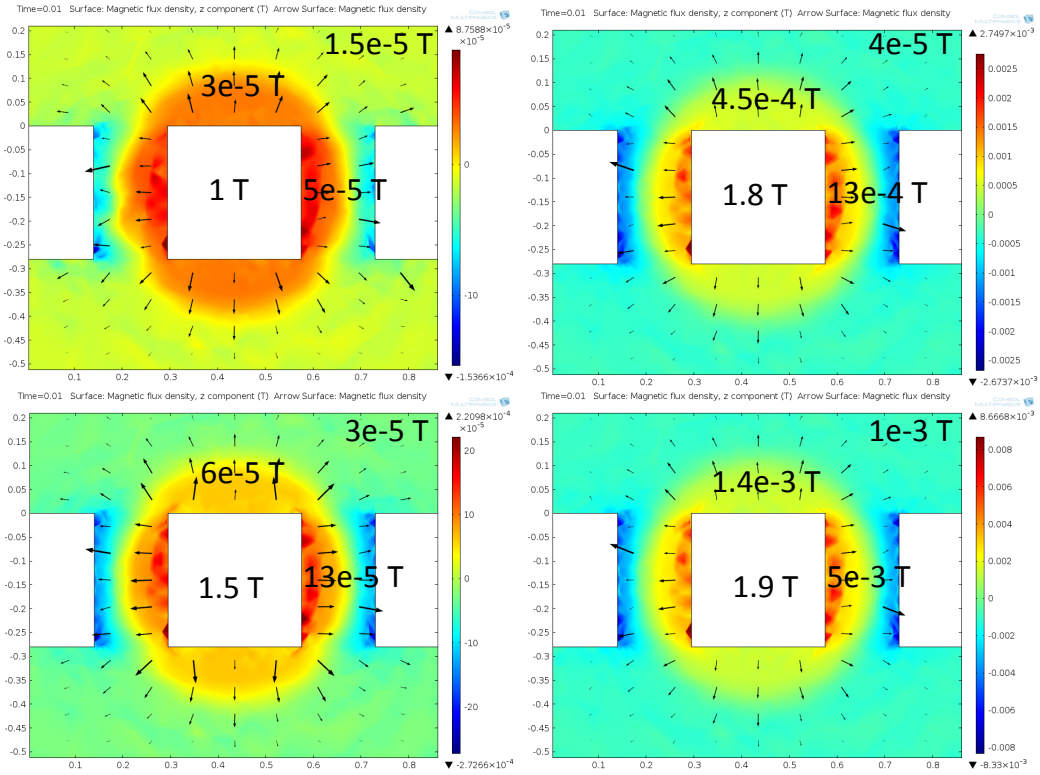

Fig. 7.26 The distribution of the leakage flux at the top windings at various flux densities.

Since the leakage flux may be carried in part by the yokes, this must be taken into account in the transformer design to ensure that overfluxing does not occur in the yokes, particularly for the quadrature booster [40]. A 2D cut plane just under the bottom of the upper yoke is made to analyse the leakage flux, which enters in or out from the yoke, as shown in Fig. 7.27. Fig. 7.28 demonstrates the distribution pattern of the leakage flux. A relative large leakage flux enters into the yoke in the first third section of the core window ①. The leakage flux with a half lower value enters into the yoke in the next third section of the core window ②. And the leakage flux will leave the yoke in the last third section of the core window ③.

Fig. 7.29 clearly shows the specific values of the leakage flux entering into the yokes along the middle cut line of the 2D cut plane. Under normal operation (B<1.5 T), it is hard to observe the leakage flux enters into or out of the yoke. However, a significant leakage flux about 4 mT transfers into the yoke close to the T-joint when the main flux is 1.9 T. Meanwhile, the flux around 5 mT is found jumping out of the yoke at the corner joint. This increased leakage flux in the deep saturation, as compared with transformer operational conditions, is because of the deep saturation of both inner T-joint and inner corner joint. The flux prefers to choose a shortcut in the air to optimise its reluctance loop path.

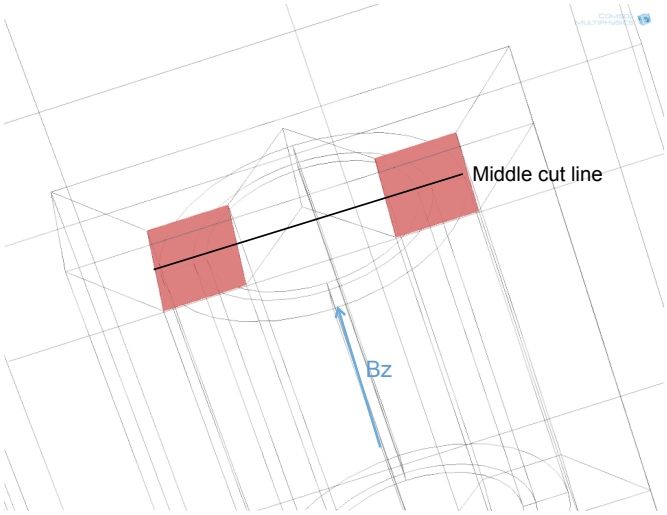

Fig. 7.27 The cut plane for the leakage flux under the bottom of the upper yoke.

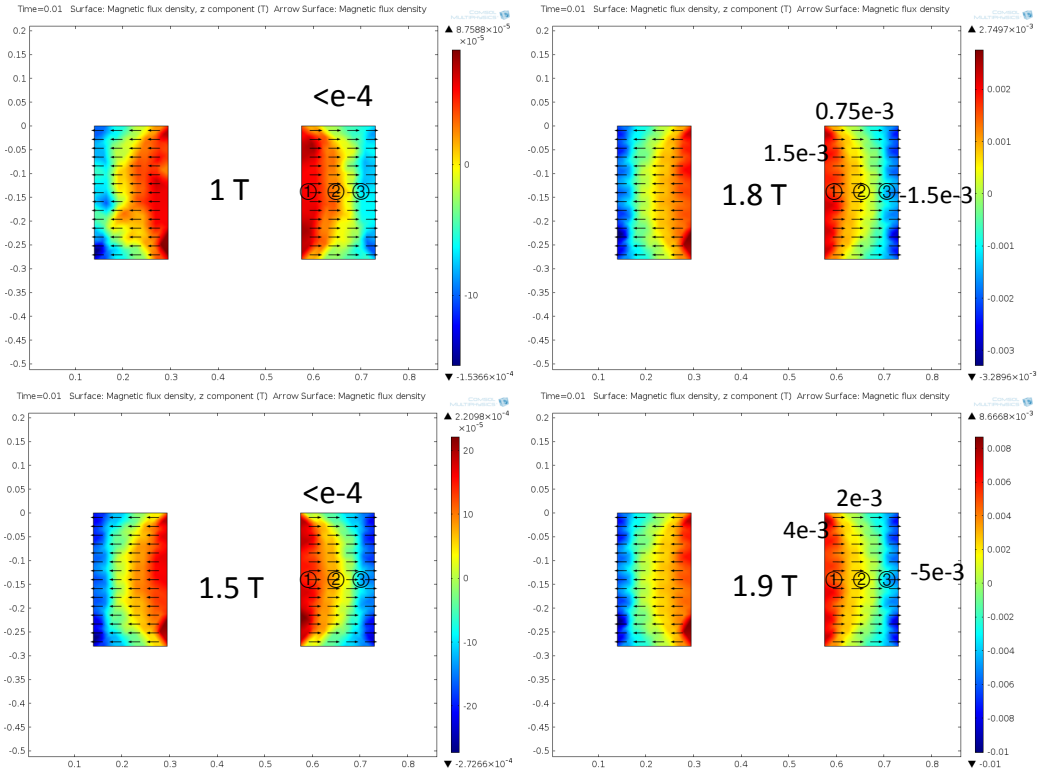

Fig. 7.28 The distribution of the leakage flux into and out of the yoke at various flux densities.

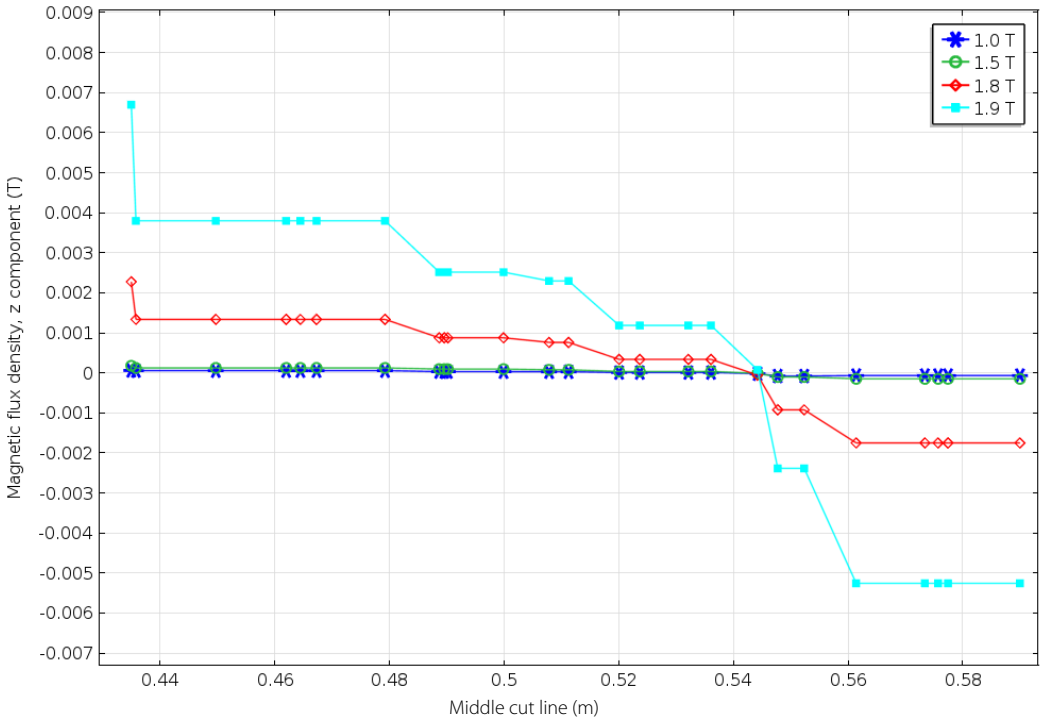

Fig. 7.29 The leakage flux into and out of the yoke along the middle cut line at various flux densities.

7.4.4 Distribution of Flux in the Clamping Structure

The winding hotspot temperature could increase about 30 °C (from 120 °C to 150 °C) due to the transformer's half-saturation in a GIC event [127]. Gassing can also result from the overheated transformer cores, even when the core hotspot temperatures are as low as 110-120 °C [128]. Undoubtedly, there is no surprise to see a higher core hotspot temperature and the accompanying gassing phenomenon when the core goes into deep saturation.

Some researchers [129], [130] believe the major heat sources for the hotspots are the metal components in the tank: The magnetic flux flows through adjacent paths such as the transformer tank or core-clamping structures, rather than inside the core at high flux densities. These components are often made of stainless steel, with a much larger power loss compared with the electrical steel, resulting to the hotspots. Nevertheless, hotspots are also probably related to the heating generated by core itself under saturation. Hence, it would be useful to see the magnetic flux distribution in the transformer clamping structures at high flux densities with the help of FEA, as shown in Fig. 7.30. Four clamping beams with the dimension of 1054 mm*50 mm*58 mm are located in contact with the yokes. The relative permeability of the clamping beams is assumed as a constant 50, suggested in [88].

It can be seen from Fig. 7.30 that the flux in the clamping structures is below 0.01 T when the main flux in the core is under 1.5 T. In the saturation, the highest flux in the clamping structures appears at the centre yoke between the two mitred regions (illustrated with the black arrow line), which is higher than 0.08 T.

This flux in the clamping beams is generally contributed by two components: one is leaked from the main flux in the yoke; the other is from the leakage flux entering through the bottom of the clamping structure, which are clearly demonstrated in Fig. 7.31 and Fig. 7.32 respectively.

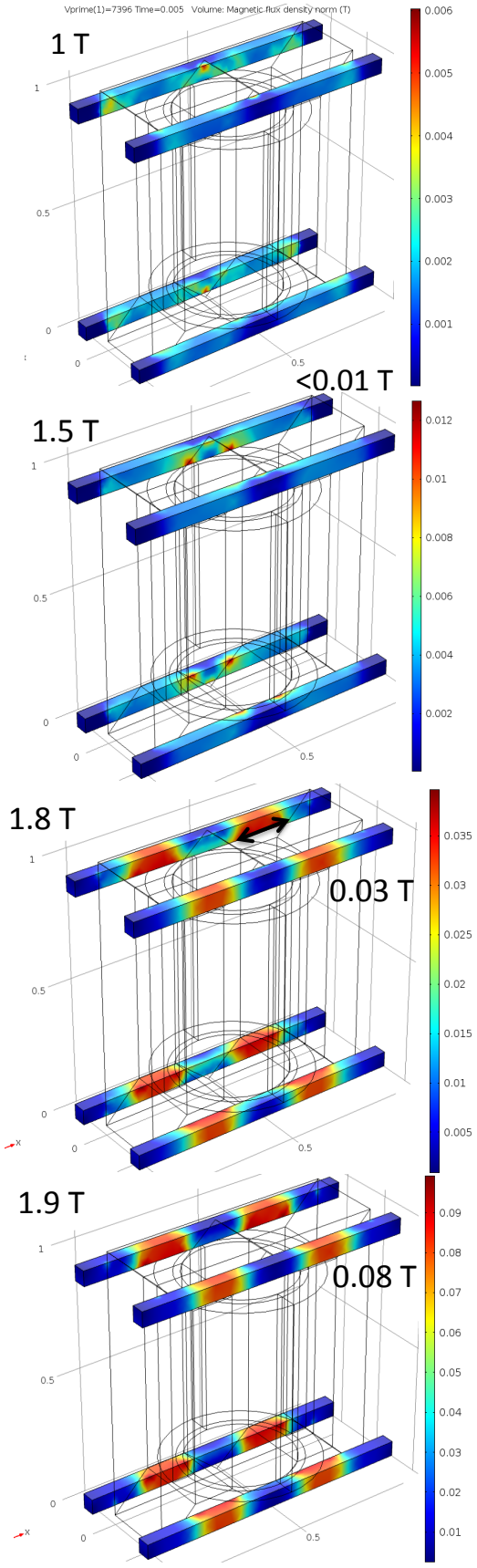

Fig. 7.30 The magnetic flux distribution in the transformer clamping structures.

Fig. 7.31 shows that a small amount of flux (< 0.01 T) lies outside of the centre limb and transfers itself into the clamping structure when the main flux is 1.9 T. A larger leakage flux, up to 0.1 T, comes from the yoke just after the mitred region of the T-joint. Traveling along the clamping structure for a while, the flux jumps back to the yoke again before the corner joint.

Compared with the yoke's leakage flux, the leakage flux that enters the clamping structure through the bottom of the clamping structure is only about 5% of the yoke's leakage flux, just 5 mT shown in Fig. 7.32. Fig. 7.32 also reveals that the flux into the clamping structure mainly concentrates in the winding projection area. Outside of the winding projection area, the flux begins to jump out of the clamping structure into the air.

Hence, the major leakage flux contributing to the flux seen in clamping structures should be from the yokes.

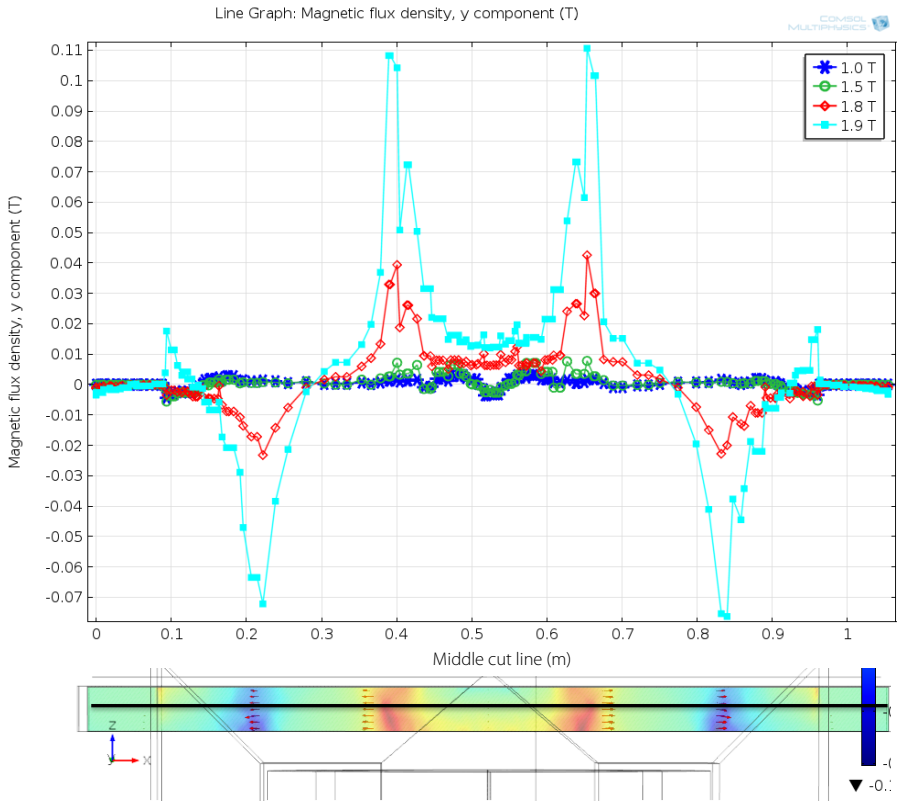

Fig. 7.31 Flux entering into the clamping beam from the contact face with the yoke.

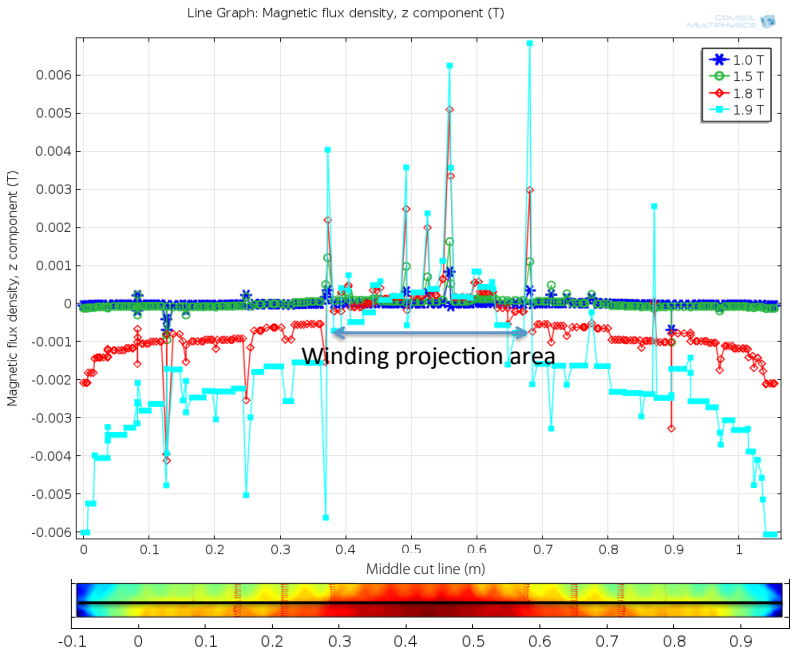

Fig. 7.32 Flux entering into the clamping structure from its bottom.

7.5 Power Loss Distribution in the Transformer Core with Clamping Structures

In order to use FEA to give a simplified estimation for the power loss distribution in the core with clamping structures, the power loss curves (P-B functions) measured for the rolling, transverse and normal directions are used for the 3D model, as shown in Fig. 7.33.

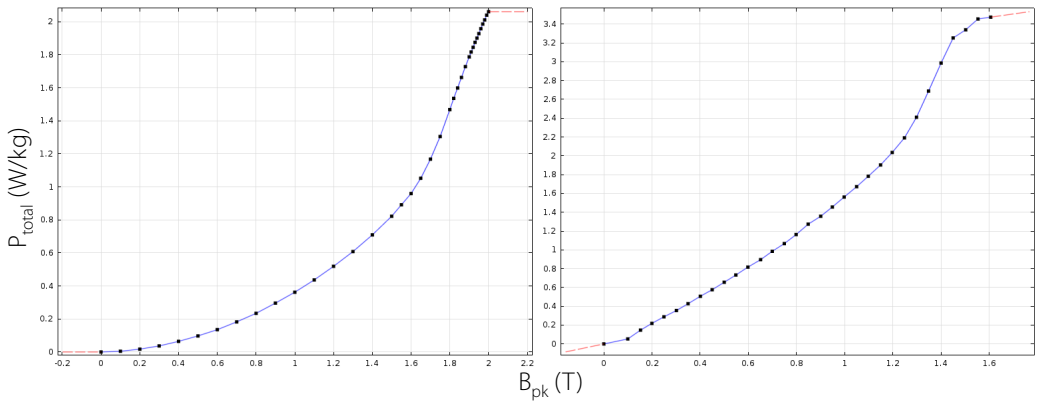

Fig. 7.33 The specific power loss for the core steel in the rolling direction (left) and transverse/normal direction (right).

Firstly, the values of magnetic flux density components at each element for the direction x, y, z (B_x, B_y, B_z) are computed as above section. The corresponding (P_x, P_y, P_z) for each element can be obtained using the P-B functions shown in Fig. 7.33. Finally, the specific total power loss P_{total} for each element can be roughly estimated using (7.11) [96]:

$$P_{total} = P_x + P_y + P_z \tag{7.11}$$

The power loss distribution pattern at 1.5 T and 1.9 T are then illustrated in Fig. 7.34 and Fig. 7.35 respectively. At 1.5 T, the specific power loss of the CGO material in the rolling direction is about 0.8 W/kg, and 0.8 W/kg is therefore observed in the centre limb. Due to the concentrated flux in the inner side of the core, a 25% higher power loss (> 1 W/kg) can be seen in the inner side of the yoke. Besides, the deviation of the flux in the T-joint and the corner joint from the rolling direction produces an additional power loss in the mitred regions. This power loss estimation result is confirmed by the simulation result presented in [131].

In the deep saturation (1.9 T), the specific power loss now rises to 1.8 W/kg in the three limbs. The highest power losses up to 2.8 W/kg are generated at the inner corners of the core windows. In contrast with the power loss distribution at 1.5 T, the mitred region at T-joint has a lower power loss because the flux is forced to travel longer in the rolling direction rather than deviate into the transverse direction. This therefore leads to a relative lower power loss compared with the surrounding area.

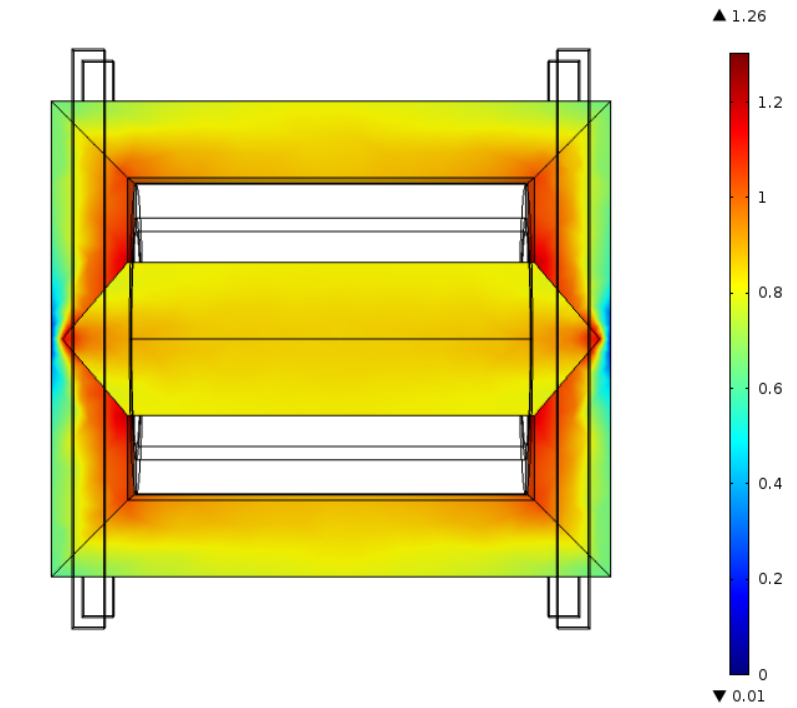

Fig. 7.34 The power loss distribution in the transformer core with the clamping structures when the main flux is 1.5 T.

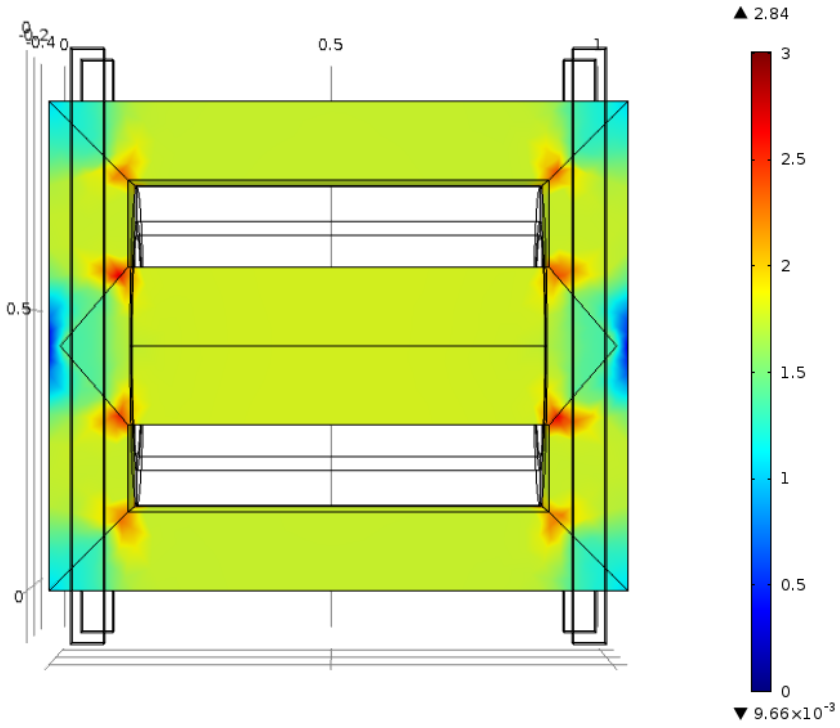

Fig. 7.35 The power loss distribution in the transformer core with the clamping structures when the main flux is 1.9 T.

The typical clamping structure is made of the mild steel, which is not laminated. Hence, a very high eddy current loss is expected when the transformer core goes into deep saturation. For the clamping beam with the dimension of 1054 mm*50 mm*58 mm, the constant relative permeability of 50, and the resistivity of 0.15 μΩm, COMSOL provides a convenient tool to automatically calculate the eddy current loss (in W/m^3) for each element of the beam. A further function was added to convert the eddy current loss to W/kg by divided by its density 7.85 g/cm^3.

As shown in Fig. 7.36, an average eddy current loss about10 W/kg is seen in the middle part of the yoke with the area around 171 cm^2 (295 mm*58 mm). Besides, the highest loss can even hit more than 20 W/kg at the edge of the clamping structure's bottom. The simulation results reveals that although the flux in the clamping structure is quite small (just 0.08 T) when core goes into deep saturation, the power loss can still be 5 to 10 times higher than that in the core, which would be the main reason for the hotspots at high flux densities.

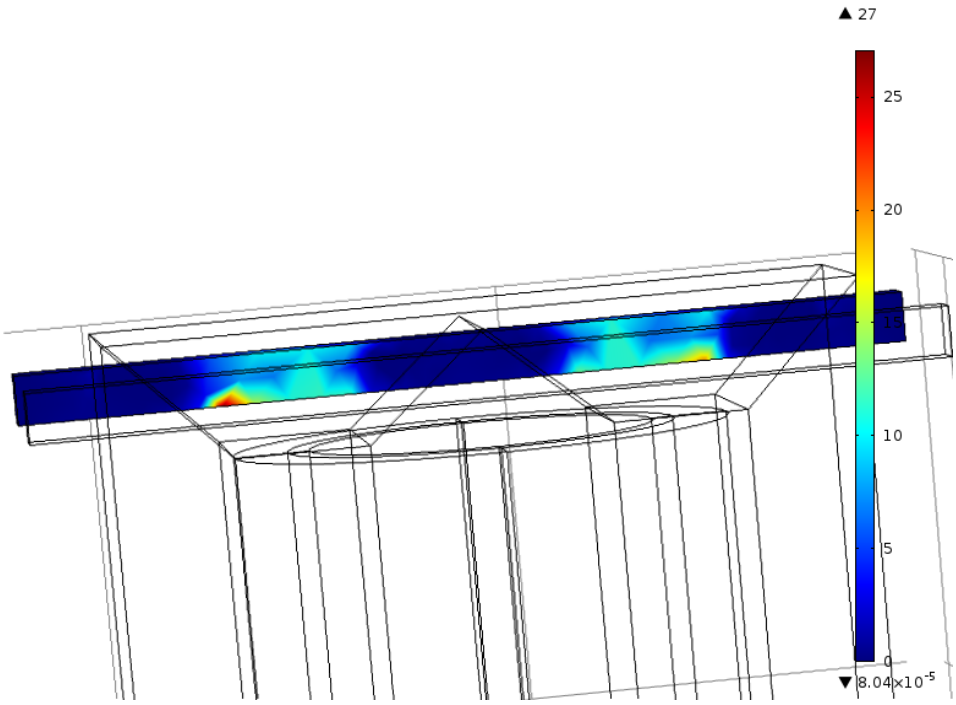

Fig. 7.36 The eddy current loss distribution in the clamping structure.

7.6 Summary

The magnetic flux distributions at the transformer core joints are simulated in the 2D and 3D finite element models, considering the anisotropic permeability together with the air gaps. The smoother flux transfer at various flux densities guarantees a lower power loss using the MSL joint compared with the SSL joint. Besides, it is found that the imperfection in core laminate stacking with some errors in joint air gaps will not produce a significant impact on the flux distributions with MSL joints. Thin low permeability gap method avoids the high number of mesh elements, and therefore makes the 3D finite element calculation possible without the compromise of dismissing the air gaps, which was done previously when simulating a real size transformer. The simulation results agree well with the existing experimental data on the SSL 45° mitred joint configuration.

The simulation results for an "imaginary" single-phase three-limb transformer core based on Schneider 1 MVA 6.6 kV/433 V power transformer show that the highest flux density always appear at the inner corner of mitred joints. At lower flux densities, it is the geometry that dominates the reluctance loop path, leading to an uneven distribution of the flux in the centre and side limbs. The flux in the centre limb also tends to deviate into the yoke earlier and follow a lower reluctance loop path. Approaching deep saturation, the permeability of the material at the area, where the flux density is high, decreases sharply, and this helps the flux distribute more evenly in the limbs. Meanwhile, the flux from the centre limb now prefers to travel longer in the rolling direction, because the inner corner has been fully saturated.

The leakage flux distributes almost evenly in the middle of the centre limb inside the windings. When it is approaching the top of the windings, it tends to concentrate under the yoke's projection region. This concentration trend increases with the main flux level. Under normal operation, the leakage flux value only has the order of the magnitude 10^{-5} T, and it is hard to observe the leakage flux enters into the yoke. In the deep saturation (1.9 T), the leakage flux value climbs 30 times higher, and about 4 mT of leakage flux enters into the yoke area close to the T-joint. This result indicates such

a large leakage flux may bring stray loss issues if it enters into the adjacent metal components in the transformer tank.

The mild steel clamping structures are hereby added to the FEA model to see the flux distribution inside the clamping beams. It reveals that the majority of the flux travelling in the clamping beams is contributed by the leakage flux from the yokes. The power loss distribution for the transformer core with the clamping structures is estimated and presented in this chapter. Under normal operation, the highest power loss appears in the inner side of the yoke. The deviation of the flux in the joints from the rolling direction produces an additional power loss in the mitred regions. In deep saturation, the highest power loss generated in the transformer core is 2.8 W/kg concentrated at the inner corners of the core windows. However, the eddy current loss generated by the clamping structures can be 5 to 10 times higher than the power loss in the core, which supports the argument that the major heat sources for the hotspots in the saturation are the metal components surrounding the core. This suggests using non-magnetic components in the transformer tank would help avoid the extremely high eddy current loss caused by the increased leakage flux when the core goes into saturation.

8 CONCLUSIONS AND FUTURE WORK

8.1 CONCLUSIONS

This thesis focuses on the magnetic properties of electrical steels and power transformer core particularly at high flux densities. Through the experimental investigations, simulations with FEM, and data analysis, the PhD research project's objectives have been achieved.

The main original contributions made by this thesis are highlighted as follows:

- A digital DAQ test bench with Epstein method was built. An improved single strip test bench, which is able to up to 2.0 T, has been used to measure the magnetic properties of modern grain-oriented electrical steels under AC magnetisation up to 400 Hz.

- A new single explicit expression is proposed to accurately approximate and predict the AC magnetisation curve over a wide range up to 2.0 T.

- A simple and accurate power loss separation algorithm is proposed, which requires the measured power loss data of electrical steels for two different frequencies.

- Considering the realistic air gaps, anisotropic properties of electrical steels, the magnetic flux distribution at different corner joints in the deep saturation are obtained with FEM.

- The distribution of the main flux, leakage flux, together with the power loss in the transformer core and adjacent clamping structures under the deep saturation conditions are acquired with FEM.

The main results and findings in this thesis are summarised as follows:

For the measurement with Epstein frame, it was found that the measured B-H curve is not notably affected if there are more than four layers of laminations. The uncertainty of Epstein method is mainly caused by the double-lapped corners, which is not suitable for the magnetic property measurement at high flux densities because of the inevitable air flux error between lamination layers. The THD of current in real transformer can be a good index of saturation level, because there exists a watershed, beyond which the THD of current begins to drop. In contrast, the THD of voltage continues increasing with the flux density level.

It is a must to replace the secondary winding coil by a B-coil to obtain the main flux without air flux between the specimen and the secondary winding for the deep saturation region. Otherwise, a crossover would appear at the B-H loop, leading to the drop of specific power loss at 1.94 T and beyond. The unstable flux eventually results that the standard SST measurement automatically stops at 1.96 T. In terms of H measurement technique, the standard magnetisation current (MC) method as an indirect way performs better than the H-coil method as a direct way. This is mainly owing to the poor accuracy at low H region affected by environment noises. Hence, the suggested improvement SST adopts is the B-coil to measure B and the MC method to measure H. Using the B-H toolbox of SLIM software, the B-H curve extrapolation was made for the range from 1.9 T to 2.0 T. The results revealed that the extrapolated curve overestimates the magnetising current at a certain B in deep saturation. Reciprocally, it also can underestimate the B level at a certain magnetising current.

None of the ten approximation functions is capable of making a satisfactory approximation over the full useful range (0 - 2.00 Tesla), if taking account of all the fitting quality indices – adjusted R^2, normality test, the number of parameters, and 95% confidence intervals. Between $B=f(H)$ series and $H=f(B)$ series, $B=f(H)$ series generally perform better when the flux density is not high. $H=f(B)$ series expressions yet reflect the B-H characteristic better in the saturation region. It has been verified that the new simple explicit empirical function has enough robustness to produce

good approximation and prediction/extrapolation results. Besides, the extrapolation tests suggests it is important to use enough experimental B-H data points as the input, particularly for the good GO materials with a large change in permeability.

The sensitivity studies of JA's hysteresis model shows the increase of k and c will respectively increase and decrease the hysteresis loop area, i.e. the hysteresis loss. However, the change of a and α will not make significant difference in the hysteresis loop area because of the diverse results of $\hat{H}$ and B_r. The comparison between the accurate and simplified formula for the eddy current loss calculations reveals that the simplified formula leads to an overestimation on the eddy current loss, particularly in the region where the relative permeability is high. This overestimation gap would be broaden at high frequencies. However, the overestimated error can be ignored at high flux densities because of a much smaller permeability than those in the operational region.

There are two critical problems for this separation algorithm bringing uncertainties and errors into the models of core loss and its three components: (1) The assumption, that k_a and k_e are constants and do not vary with the flux densities, is not appropriate. Although it will not bring significant difference to the total power loss, it will change the percentages of the three loss components in the total loss. (2) The data sets chosen for solving the four coefficients in the hysteresis loss formula largely affects the performance of the core loss model. It is suggested to pick up the representative values in each region of the power loss curve, such as sets of 0.5 T, 1.2 T, 1.5 T, and 1.9 T, in order to minimise the error.

The smoother flux transfer at various flux densities guarantees a lower power loss using the MSL joint compared with the SSL joint. Besides, it is found that the imperfection in core laminate stacking with some errors in joint air gaps will not produce a significant impact on the flux distributions with MSL joints. Thin low permeability gap method avoids the high number of mesh elements, and therefore makes the 3D finite element calculation possible without the compromise of dismissing the air gaps, which was done previously when simulating a real size

transformer. The simulation results agree well with the existing experimental data on the SSL 45° mitred joint configuration.

At lower flux densities, it is the geometry that dominates the reluctance loop path, leading to an uneven distribution of the flux in the centre and side limbs. The flux in the centre limb also tends to deviate into the yoke earlier and follow a lower reluctance loop path. Approaching deep saturation, the permeability of the material at the area, where the flux density is high, decreases sharply, and this helps the flux distribute more evenly in the limbs. Meanwhile, the flux from the centre limb now prefers to wait and travel longer in the rolling direction, because the inner corner has been fully saturated.

The leakage flux distributes almost evenly in the middle of the centre limb inside the windings. When it is approaching the top of the windings, it tends to concentrate under the yoke's projection region. This concentration trend increases with the main flux level. Under normal operation, the leakage flux value only has the order of the magnitude 10^{-5} T, and it is hard to observe the leakage flux enters into the yoke. In the deep saturation (1.9 T), the leakage flux value climbs 30 times higher, and about 4 mT of leakage flux enters into the yoke area close to the T-joint. This result indicates such a large leakage flux may bring stray loss issues if it enters into the adjacent metal components in the transformer tank.

The majority of the flux travelling in the clamping beams is contributed by the leakage flux from the yokes. The power loss distribution for the transformer core with the clamping structures is estimated and presented in this chapter. Under normal operation, the highest power loss appears in the inner side of the yoke. The deviation of the flux in the joints from the rolling direction produces an additional power loss in the mitred regions. In deep saturation, the highest power loss generated in the transformer core is 2.8 W/kg concentrated at the inner corners of the core windows. However, the eddy current loss generated by the clamping structures can be 5 to 10 times higher than the power loss in the core, which supports the argument that the major heat sources for the hotspots in the saturation are the metal components surrounding the core. This suggests using non-magnetic components in the

transformer tank would help avoid the extremely high eddy current loss caused by the increased leakage flux when the core goes into saturation.

8.2 Future Work

In this thesis, some useful conclusions are made on the magnetic properties of electrical steels and the transformer core. However, there are still a significant amount of research work need to be done in order to have a realistic transformer model which can incorporate the analysis work needed for a transformer under extreme conditions, such as sustained ferroresonance, GIC and QBs. It is therefore recommended, that further research to be undertaken in the following areas:

- Toroid core can be another good test bench to avoid the uneven distribution of H, and reduce the effects from the change of the equivalent magnetic loop length. However, a strong power source is required to make the measurement at a very high flux density due to the increase of the electrical steel materials.

- It would be useful, if based on the measured magnetic properties and experience gained through this PhD research, a simple parameter extraction algorithm is developed for JA's model.

- The meshing strategy for the laminated transformer core model with 45° mitred joint needs further improvement to overcome the problem brought by the thin thickness of the lamination compared with its length and width. The triangle air gaps left due to the 45° mitred lapped joints should be also incorporated into the model.

- The distributions of magnetic flux and power loss in the three-phase three-limb and three-phase five-limb transformers under AC magnetisation at high flux densities, need to be studied with FEM, which will give more useful information for the transformer designer.

- It would be interesting to know if any difference between the half-cycle saturation caused by GIC and the full-cycle AC saturation.

- In order to reflect the whole transformer's external characteristics, i.e. V-I characteristics, the methodology to convert the material's B-H characteristics combining the effects of core types, building factors, core bolts, etc. are supposed to be developed.

- The industries are concerned about the value of temperature of the windings, core, and surrounding insulating oil. Therefore, it would be important to take the heat transfer modules in the simulation to identify the exact temperature rise at high flux densities and evaluate the risks of hotspots.

APPENDIX 1 QB'S OPERATION AND THE OVERFLUX PROBLEM

The most commonly used circuit for two-core design QB is presented in Fig. A.1. One is the shunt transformer unit with Y/Y connection; the other is series transformer unit with open-delta/delta connection. The advantage of this design is that the regulating winding and tapchanger of shunt unit are not exposed to transmission network directly to avoid onerous voltage insulation duty [24], increasing the flexibility in selecting the step voltage and the current of the regulating winding [132]. From Fig. A.1 and Fig. A.2, we can see how QB works: $\Delta\mathbf{V}$ provided by QB is in quadrature with $\mathbf{V}_{\text{in}}$; the magnitude and direction of $\Delta\mathbf{V}$ could be adjusted by the tapchanger and ground switch respectively in shunt unit. The output voltage $\mathbf{V}_{\text{out}}$ then equals the sum of $\mathbf{V}_{\text{in}}$ and $\Delta\mathbf{V}$. If $\mathbf{V}_{\text{out}}$ leads $\mathbf{V}_{\text{in}}$, QB is boosting active power flow, recalling that the active power flows from the point with leading voltage phase angle to the point with lagging one. When $\mathbf{V}_{\text{out}}$ lags $\mathbf{V}_{\text{in}}$, QB is bucking power. In reality, however, there will be a voltage drop due to the internal impedance of QB, which increases actual $\Delta\mathbf{V}$ (red arrow) when bucking and decreases actual $\Delta\mathbf{V}$ (blue arrow) when boosting, displayed in Fig. A.2.

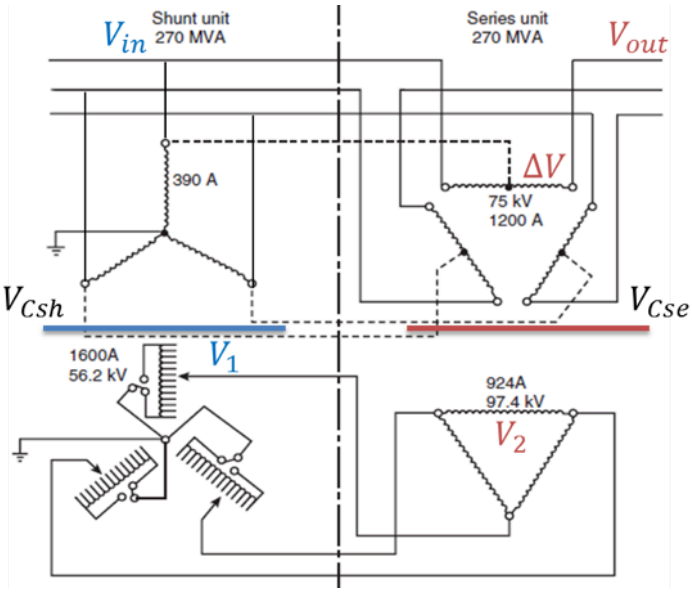

Fig. A.1 Commonly used circuit for two-core 400kV QB design [24].

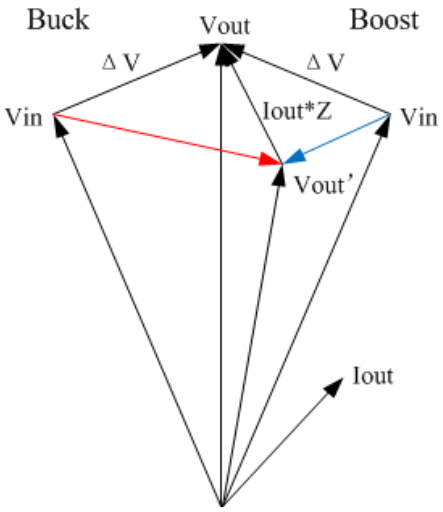

Fig. A.2 Phasor diagram of QB.

Jarman [40] shows how the preceding overvoltage ΔV produces the overflux problem. Fig. A.3 provides the equivalent model originated Fig. A.1, combining turns ratio and phase shift of series and shunt units into a single ideal transformer with a phase shift of 90° as well as turns ratio n. N stands for the maximum turns ratio. The impedances of series and shunt units are split into high voltage and low voltage impedances (not easy to obtain the accurate values), with a T network approach assuming a notional search coil wound close to core limb. According to $E = 4.44 fBAN$, the p.u. voltage E appearing at T point, therefore, is equivalent to the p.u. flux density B in the core. Similarly, V_{Csh} and V_{Cse} can be seen as p.u. core flux density of shunt and series units as well.

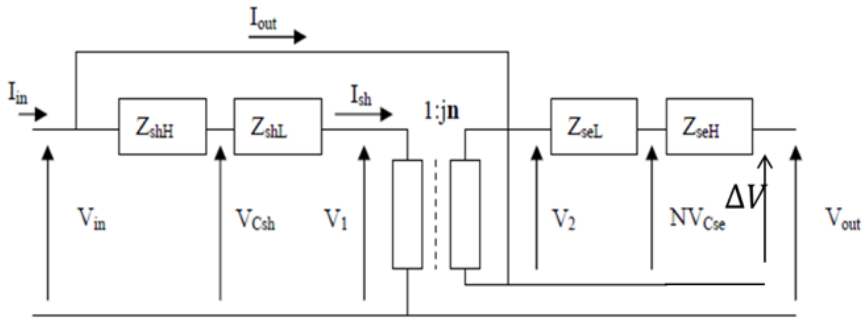

Fig. A.3 QB's equivalent circuit [40].

From the above model, we have:

$$
\begin{aligned}
I_{in} &= I_{out} + I_{sh} \\
V_1 &= V_{in} - I_{sh}\left(Z_{shH} + Z_{shL}\right) \\
V_{out} &= V_{in} + V_2 - I_{out}\left(Z_{seL} + Z_{seH}\right) \\
V_2 &= jnV_1 \\
I_{sh} &= -jnI_{out}
\end{aligned}
$$

The following equations can then be derived from the above equation sets:

$$
\begin{aligned}
V_1 &\cong V_{in} - nI_{out}\left(X_{shH} + X_{shL}\right) \\
V_{Csh} &\cong V_{in} - nI_{out}X_{shH} \\
V_{Cse} &\cong \frac{-j}{N}\left(-nV_{in} + I_{out}\left(n^2\left(X_{shH} + X_{shL}\right) + X_{seL}\right)\right) \\
\Delta V &\cong -j\left(-nV_{in} + I_{out}\left(X_{seL} + X_{seH}\right)\right)
\end{aligned}
$$

According to the above four equations, when QB is bucking, i.e. $\mathbf{n}$<0, it is apparent that $\mathbf{V}_1$, $\mathbf{V}_{Csh}$, $\mathbf{V}_{Cse}$, $\Delta\mathbf{V}$ will increase with the load current $\mathbf{I}_{out}$, which means overvoltage on regulating winding, overflux on shunt unit core, overvoltage on series winding, and overflux on series unit core. The degree of overvoltage and overflux depends on the load current $\mathbf{I}_{out}$ and impedances of QB. In other words, the limits of flux in the cores will constrain the maximum current output $\mathbf{I}_{out}$, that is to say, the QB's capability of power flow control.

Here is an example to show the effect of the flux limit on the QB's power control capability. For a 400kV, 2750 MVA QB with total 33-tap positions design, the overload capability is 4331 MVA considering that maximum overload rating is 1.5 p.u. when operating voltage is 1.05 p.u.. If the flux limits for the core are set to 1.9 T, the power rating limits due to flux limits at different tap positions can be shown in Fig. A.4. Clearly, the power flow capability is reduced to 3682 MVA at position 32 and 2642 MVA at position 33. If the limits of flux are increased to 1.95 T, the power flow capability rises to 4083 MVA at position 32 and 3000 MVA at position 33. From this example, it is apparent that the QB's design with higher flux limit values will improve the performance of power flow control, providing no other side effects in the deep saturation.

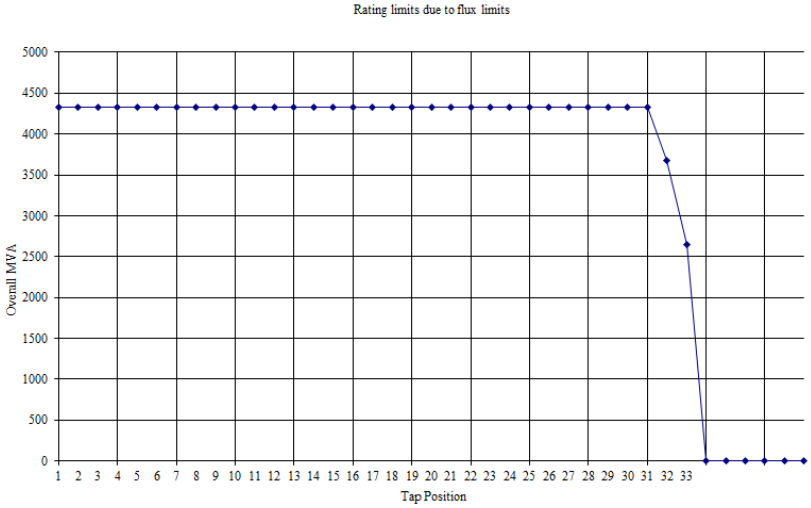

Fig. A.4 Power rating limits due to flux limits of 1.9 T

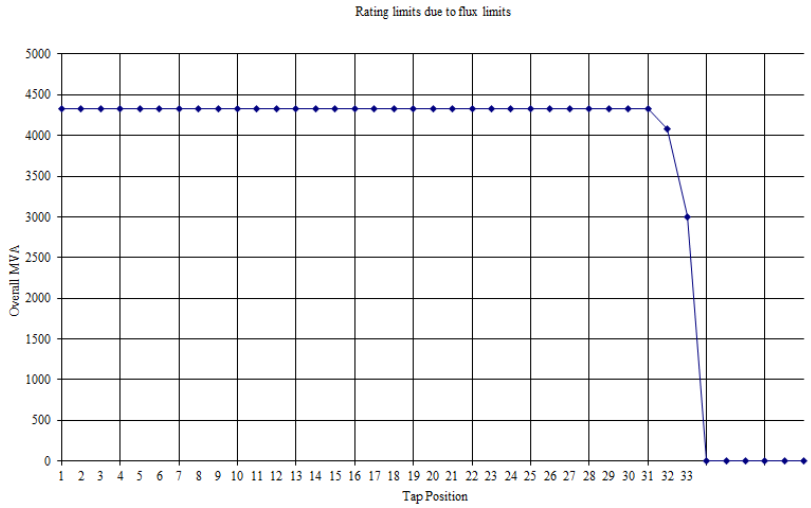

Fig. A.5 Power rating limits due to flux limits of 1.95 T

APPENDIX 2 LIST OF IEC 60404 SERIES FOR TESTING MAGNETIC MATERIALS

IEC 60404-1 "Magnetic materials. Part 1: Classification"

IEC 60404-2 "Magnetic materials. Part 2: Methods of measurements of the magnetic properties of electrical steel sheet by means of an Epstein frame"

IEC 60404-3. "Magnetic materials. Part 3: Methods of measurement of the magnetic properties of magnetic sheet and strip by means of a single sheet tester"

IEC 60404-4 "Magnetic materials. Part 4: Methods of measurement of the dc magnetic properties of magnetically soft materials"

IEC 60404-5 "Magnetic materials. Part 5: Permanent magnet (magnetically hard) materials. Methods of measurement of magnetic properties"

IEC 60404-6 "Magnetic materials. Part 6: Methods of measurement of the magnetic properties of magnetically soft metallic and powder materials at frequencies in the range 20 Hz to 200 kHz by the use of ring specimen"

IEC 60404-7 "Magnetic materials. Part 7: Method of measurement of the coercivity of magnetic materials in an open magnetic circuit"

IEC 60404-8 "Magnetic materials. Part 8-1: Specifications for individual materials - Magnetically hard materials"

IEC 60404-9 "Magnetic materials. Part 9: Methods of determination of the geometrical characteristics of magnetic steel sheet and strip"

IEC 60404-10 "Magnetic materials. Part 10: Methods of measurement of magnetic properties of magnetic sheet and strip at medium frequencies"

IEC 60404-11. "Magnetic materials. Part 11: Method of test for the determination of surface insulation resistance of magnetic sheet and strip"

IEC 60404-12. "Magnetic materials. Part 12: Guide to methods of assessment of temperature capability of interlaminar insulation coatings"

IEC 60404-13. "Magnetic materials. Part 13: Methods of measurement of density, resistivity, and stacking factor of electrical steel sheet and strip

IEC 60404-14. "Magnetic materials. Part 14: Methods of measurement of the magnetic dipole moment of a ferromagnetic material specimen by the withdrawal or rotation method"

APPENDIX 3 BLOCK DIAGRAM OF LABVIEW PROGRAMME FOR TEST BENCH WITH EPSTEIN FRAME

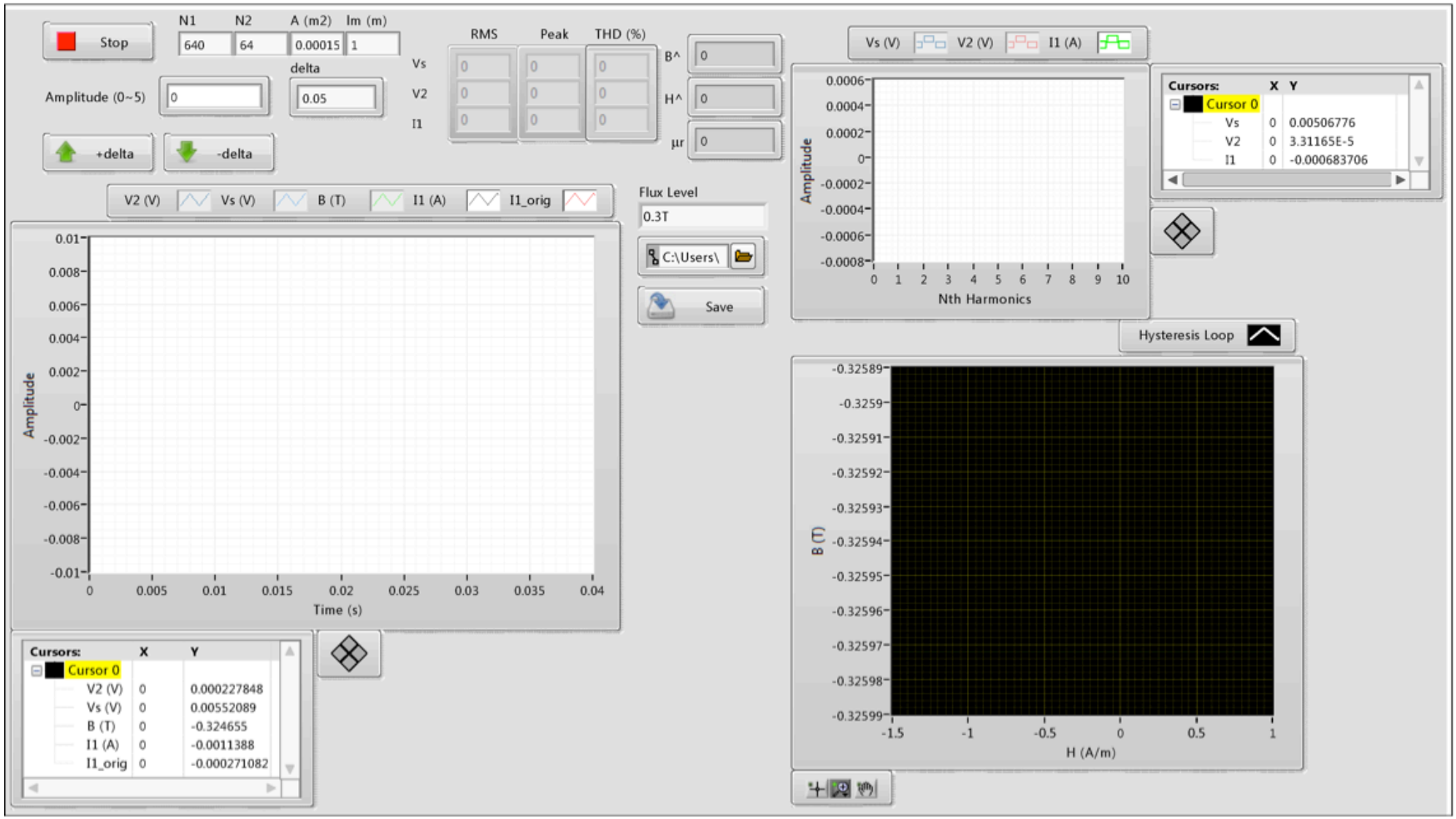

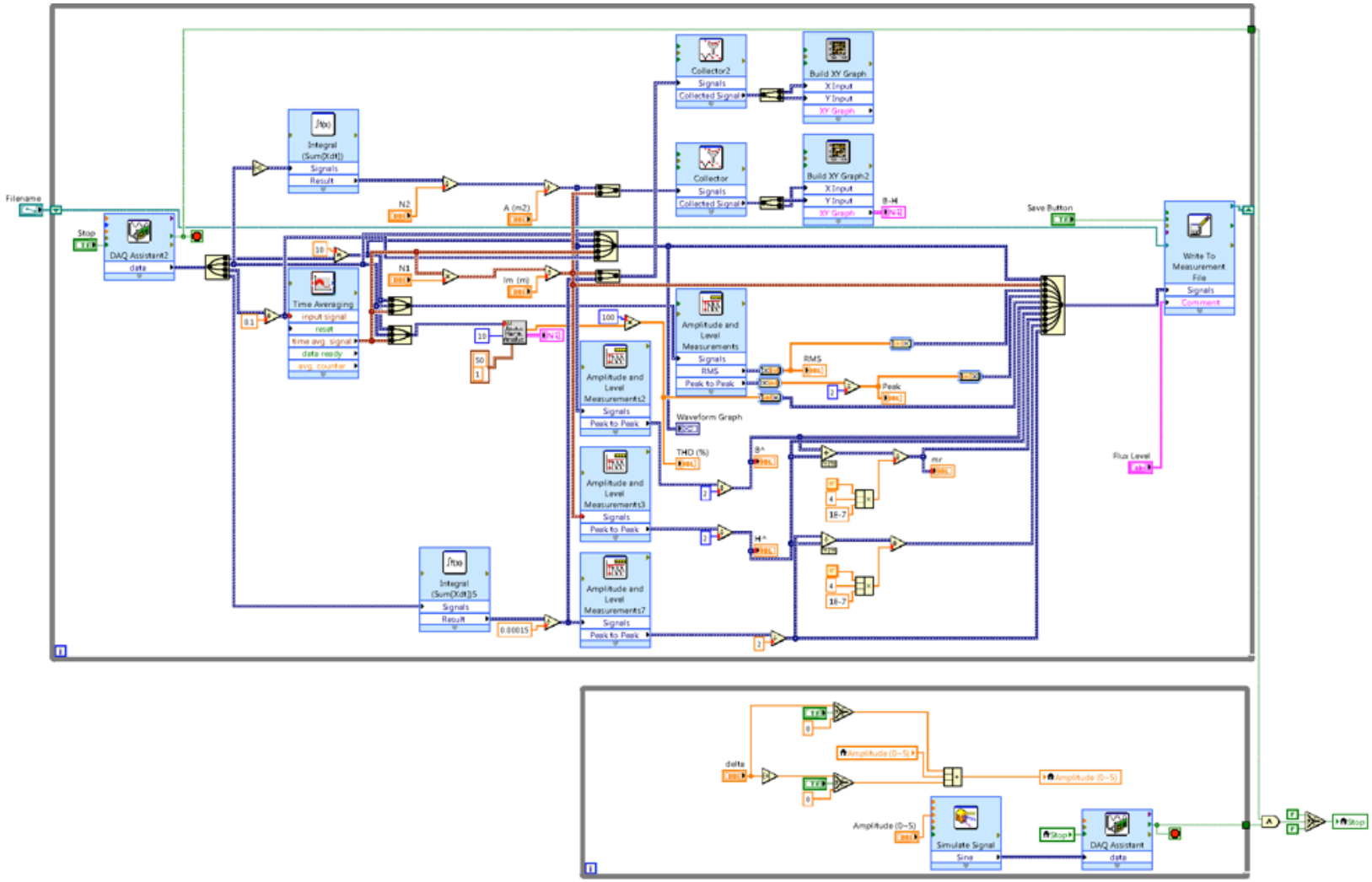

Write To Measurement File
Write To Measurement File
Writes data to text-based measurement files (.lvm) or binary measurement files (.tdm or .tdms).

Convert to Dynamic Data
Convert to Dynamic Data
Converts numeric, Boolean, waveform and array data types to the dynamic data type for use with Express VIs.

Convert from Dynamic Data
Convert from Dynamic Data
Converts the dynamic data type to numeric, Boolean, waveform, and array data types for use with other VIs and functions.

Convert to Dynamic Data2
Convert to Dynamic Data
Converts numeric, Boolean, waveform and array data types to the dynamic data type for use with Express VIs.

Convert from Dynamic Data2
Convert from Dynamic Data
Converts the dynamic data type to numeric, Boolean, waveform, and array data types for use with other VIs and functions.

Amplitude and Level Measurements
Amplitude and Level Measurements
Performs voltage measurements on a signal.

This Express VI is configured as follows:

Measurement: RMS
Measurement: Peak to Peak
Voltage Window: Off

Convert to Dynamic Data3
Convert to Dynamic Data
Converts numeric, Boolean, waveform and array data types to the dynamic data type for use with Express VIs.

Build XY Graph2
Build XY Graph
formats the data displayed on an X-Y Graph.

This Express VI is configured as follows:

Clear data on each call: On

Collector
Collector
Collects input signals and returns the most recent data, up to the specified maximum number of samples per channel. When you call this Express VI repeatedly and the Express VI reaches the maximum number of samples per channel, the Express VI discards the oldest data and adds the newest data to the collected samples.

This Express VI is configured as follows:

Number of Points to Collect: 1000

Amplitude and Level Measurements3
Amplitude and Level Measurements
Performs voltage measurements on a signal.

This Express VI is configured as follows:

Measurement: Peak to Peak

Build XY Graph
Build XY Graph
formats the data displayed on an X-Y Graph.

This Express VI is configured as follows:

Clear data on each call: On

Collector2
Collector
Collects input signals and returns the most recent data, up to the specified maximum number of samples per channel. When you call this Express VI repeatedly and the Express VI reaches the maximum number of samples per channel, the Express VI discards the oldest data and adds the newest data to the collected samples.

This Express VI is configured as follows:

Number of Points to Collect: 1000

Time Averaging
Time Averaging
Averages a time waveform or scalar input signal over time. Time Averaging can perform a running or block average.

Amplitude and Level Measurements2
Amplitude and Level Measurements
Performs voltage measurements on a signal.

This Express VI is configured as follows:

Measurement: Peak to Peak

Integral (Sum[Xdt])
Time Domain Math
Performs one of several math functions on time domain signals.

This Express VI is configured as follows:

Math Operation: Integral
Calculation Mode: Continuous Calculation

Amplitude and Level Measurements7
Amplitude and Level Measurements
Performs voltage measurements on a signal.

This Express VI is configured as follows:

Measurement: Peak to Peak

Integral (Sum[Xdt])5
Time Domain Math
Performs one of several math functions on time domain signals.

This Express VI is configured as follows:

Math Operation: Integral
Calculation Mode: Continuous Calculation

Simulate Signal
Simulate Signal
Simulates a sine wave, square wave, triangle wave, sawtooth wave, or noise signal.

This Express VI is configured as follows:

Signal Type: Sine
Frequency: 50 Hz
Amplitude: 1
Phase: 0
Offset: 0
Sampling Rate: 100000 Hz
Number of Samples: 10000 (Automatic)
Timing: Run as fast as possible
Timestamps: Relative

DAQ Assistant2
DAQ Assistant
Creates, edits, and runs tasks using NI-DAQmx. Refer to the NI-DAQmx Readme for a complete listing of devices NI-DAQmx supports.

When you place this Express VI on the block diagram, the DAQ Assistant launches to create a new task. After you create a task, you can double-click the DAQ Assistant Express VI to edit that task. For continuous measurement or generation, place a while loop around the DAQ Assistant Express VI.

For continuous single-point input or output, the DAQ Assistant Express VI might not provide optimal performance. Refer to the Cont Acq&Graph Voltage-Single Point Optimization VI in examples\DAQmx\Analog In\Measure Voltage.llb for an example of techniques to create higher-performance, single-point I/O applications.

DAQ Assistant
DAQ Assistant
Creates, edits, and runs tasks using NI-DAQmx. Refer to the NI-DAQmx Readme for a complete listing of devices NI-DAQmx supports.

When you place this Express VI on the block diagram, the DAQ Assistant launches to create a new task. After you create a task, you can double-click the DAQ Assistant Express VI to edit that task. For continuous measurement or generation, place a while loop around the DAQ Assistant Express VI.

For continuous single-point input or output, the DAQ Assistant Express VI might not provide optimal performance. Refer to the Cont Acq&Graph Voltage-Single Point Optimization VI in examples\DAQmx\Analog In\Measure Voltage.llb for an example of techniques to create higher-performance, single-point I/O applications.

APPENDIX 4 MATLAB CODE FOR HARMONICS ANALYSIS

```
function myfftv(data)
fs=1/(data(2,1)-data(1,1));
fs=round(fs);
data=data(1:fs/50+1,:);
t=data(:,1);
N=length(t)-1;
p=data(:,2);

subplot(2,2,1);
plot(t,p);
grid on
title('V2(t)');
xlabel('time (s)')
ylabel('V2 (V)')

Y=fft(p);
magY=abs(Y(1:1:N/2))*2/N;
f=(0:N/2-1)'*fs/N;

subplot(2,2,3);
h=stem(f(1:21),magY(1:21),'fill','--');
set(h,'MarkerEdgeColour','red','Marker','*')
grid on
title('FFT Analysis');
xlabel('Frequency (Hz)')
ylabel('Amplitude')
```

```
global myfftv_result;
myfftv_result=[f(2:2:20),magY(2:2:20)];

function myffti(data)
fs=1/(data(2,1)-data(1,1));
fs=round(fs);
data=data(1:fs/50+1,:);
t=data(:,1);
N=length(t)-1;
p=data(:,2);

subplot(2,2,2);
plot(t,p);
grid on
title('I1(t)');
xlabel('time (s)')
ylabel('I1 (A)')

Y=fft(p);
magY=abs(Y(1:1:N/2))*2/N;
f=(0:N/2-1)'*fs/N;

subplot(2,2,4);
h=stem(f(1:21),magY(1:21),'fill','--');
set(h,'MarkerEdgeColour','red','Marker','*')
grid on
title('FFT Analysis');
xlabel('Frequency (Hz)')
ylabel('Amplitude')

global myffti_result;
myffti_result=[f(2:2:20),magY(2:2:20)];
```

APPENDIX 5 MATHEMATICA CODE FOR THE CORE LOSS SEPARATION

```
ClearAll["Global`*"];
pl[hys_, ka_, ke_, f_, B_] := f*(hys + ka*Sqrt[f]*B^1.5 + ke*f*B^2)
data1 = {0.0004713, 0.0008446, 1.877*^-5, f, 1.0};
data12 = {0.0007346, 0.0009027, 1.886*^-5, f, 1.2};
data15 = {0.002779, 0.0008142, 2.720*^-5, f, 1.5};
data17 = {0.006898, 0.0006835, 3.708*^-5, f, 1.7};
f = 50; pl1 = 0.3621; pl12 = 0.5189; pl15 = 0.8223; pl17 = 1.168;


pa1e3 = data15[[2]]*(f*data1[[5]])^1.5; pe1e3 = data15[[3]]*(f*data1[[5]])^2; ph1e3 =
pl1 - pe1e3 - pa1e3;
pa12e3 = data15[[2]]*(f*data12[[5]])^1.5; pe12e3 = data15[[3]]*(f*data12[[5]])^2;
ph12e3 = pl12 - pa12e3 - pe12e3;
pa15e3 = data15[[2]]*(f*data15[[5]])^1.5; pe15e3 = data15[[3]]*(f*data15[[5]])^2;
ph15e3 = pl15 - pa15e3 - pe15e3;
pa17e3 = data15[[2]]*(f*data17[[5]])^1.5; pe17e3 = data15[[3]]*(f*data17[[5]])^2;
ph17e3 = pl17 - pa17e3 - pe17e3;


so3 = Solve[Log[ph1e3] == Log[kh] + Log[f] + (a + b*data1[[5]] +
c*data1[[5]]^2)*Log[data1[[5]]] && Log[ph12e3] == Log[kh] + Log[f] + (a +
b*data12[[5]] + c*data12[[5]]^2)*Log[data12[[5]]] && Log[ph15e3] == Log[kh] + Log[f]
+ (a + b*data15[[5]] + c*data15[[5]]^2)*Log[data15[[5]]] && Log[ph17e3] == Log[kh] +
Log[f] + (a + b*data17[[5]] + c*data17[[5]]^2)*Log[data17[[5]]], {kh, a, b, c}]

pl300e3[B_] := f*(kh*B^(a + b*B + c*B^2) + data15[[2]]*Sqrt[f]*B^1.5 +
data15[[3]]*f*B^2) /. {so3[[1, 1]], so3[[1, 2]], so3[[1, 3]], so3[[1, 4]]};
```

```
ph300e3[B_] := f*kh*B^(a + b*B + c*B^2) /. {so3[[1, 1]], so3[[1, 2]], so3[[1, 3]], so3[[1,
4]]}; pa300e3[B_] := f*data15[[2]]*Sqrt[f]*B^1.5 /. {so3[[1, 1]], so3[[1, 2]], so3[[1, 3]],
so3[[1, 4]]}; pe300e3[B_] := f*data15[[3]]*f*B^2 /. {so3[[1, 1]], so3[[1, 2]], so3[[1, 3]],
so3[[1, 4]]};

plotpl300e3 = Plot[pl300e3[x], {x, 0, 2}, PlotStyle -> Green];
plotph300e3 = Plot[ph300e3[x], {x, 0, 2}, PlotStyle -> Green];
plotpa300e3 = Plot[pa300e3[x], {x, 0, 2}, PlotStyle -> Green];
plotpe300e3 = Plot[pe300e3[x], {x, 0, 2}, PlotStyle -> Green];
plotph300e3per = Plot[ph300e3[x]/pl300e3[x]*100, {x, 0, 2}, PlotStyle -> Green,
PlotRange -> {0, 100}];
plotpa300e3per = Plot[pa300e3[x]/pl300e3[x]*100, {x, 0, 2}, PlotStyle -> Green,
PlotRange -> {0, 100}];
plotpe300e3per = Plot[pe300e3[x]/pl300e3[x]*100, {x, 0, 2}, PlotStyle -> Green,
PlotRange -> {0, 100}];
```

APPENDIX 6 UNCERNTAINTY BUDGET FOR THE MEASUREMENT

The calculations of uncertainty budgets in this thesis are made based on [22], whose combined uncertainty is obtained with the below equation:

$$\text{combined uncertainty} = \sqrt{\sum_{i=1}^{n}\left(c_i \frac{u_i}{d_i}\right)^2}$$

where,

c_i the sensitivity coefficient for each uncertainty source

u_i the relative uncertainty for each uncertainty source

d_i the divisor of distribution function for each uncertainty source

n the total number of the uncertainty sources

The expended uncertainty can then be obtained by multiplying the combined uncertainty and the coverage factor for a confidence level of 95%.

Table A.1 illustrates the uncertainty budget in the measurement of B_{pk} at 50 Hz using the improved compact SST. The relative uncertainty for the DAQ board and frequency setting were obtained from the DAQ board (NI BNC-2110)'s manual. The mass of sample was weighed using Avery Berkel FB31 whose accuracy is 0.01%. The density of sample was quoted from the manufacturer with the relative uncertainty 0.03%. The length of the sample was measured using a ruler with the resolution 0.5 mm. Its uncertainty was assumed as the half of the resolution divided by the nominal length of the sample, i.e. about 0.1%. The LabVIEW programme was able to maintain B_{pk} and its form factor with the relative error 0.01% and 0.05% respectively. The relative standard deviation for the 5 trials was 0.01%. With the coverage factor k=2, the declared uncertainty in the measurement of B_{pk} at 50 Hz using the improved compact SST is 0.17%.

Table A.1 Uncertainty budget in the measurement of B_{pk} at 50 Hz using the improved compact SST.

Source of uncertainty	**Distribution function**	**Divisor (d_i)**	**Relative uncertainty (u_i)**	**Sensitivity coefficient (c_i)**	**Degrees of freedom**
DAQ board	Normal	1	0.05%	1	∞
Frequency setting	Normal	1	0.01%	1	∞
Sample mass	Rectangular	$\sqrt{3}$	0.01%	1	∞
Sample density	Rectangular	$\sqrt{3}$	0.03%	1	∞
Sample length	Rectangular	$\sqrt{3}$	0.1%	1	∞
B_{pk} control	Rectangular	$\sqrt{3}$	0.01%	1	∞
Form factor control	Rectangular	$\sqrt{3}$	0.05%	1	∞
Repeatability	Normal	1	0.01%	1	4
Combined uncertainty			0.085%		
Expanded uncertainty (coverage factor k=2)			0.17%		
Declared uncertainty (95% confidence level)			**0.17%**		

Table A.2 illustrates the uncertainty budget in the measurement of P_S at 50 Hz using the improved compact SST. The relative uncertainty for the DAQ board and frequency setting were obtained from the DAQ board (NI BNC-2110)'s manual. The mass of sample was weighed using Avery Berkel FB31 whose accuracy is 0.01%. The sensitivity coefficient for the dependence of P_S on B_{pk} can be calculated via $\frac{dP_S}{dB_{pk}}$ using the measured specific power loss curve, i.e. 3.6. The relative standard deviation for the 5 trials was 0.25%. With the coverage factor k=2, the declared uncertainty in the measurement of P_S at 50 Hz using the improved compact SST is 1.32%.

Table A.2 Uncertainty budget in the measurement of P_S at 50 Hz using the improved compact SST.

Source of uncertainty	**Distribution function**	**Divisor (d_i)**	**Relative uncertainty (u_i)**	**Sensitivity coefficient (c_i)**	**Degrees of freedom**
DAQ board	Normal	1	0.05%	1	∞
Frequency setting	Normal	1	0.01%	1	∞
Sample mass	Rectangular	$\sqrt{3}$	0.01%	1	∞
Dependence of P_S on B_{pk}	Normal	1	0.17%	3.6	∞
Repeatability	Normal	1	0.25%	1	4
Combined uncertainty			0.66%		
Expanded uncertainty (coverage factor k=2)			1.32%		
Declared uncertainty (95% confidence level)			**1.32%**		

APPENDIX 7 LIST OF PUBLICATIONS

- Peer-reviewed Journal Papers in SCI

[1] Q. Tang, Z. Wang, P. Anderson, P. Jarman, and A. Moses, "Approximation and prediction of AC magnetisation curves for power transformer core analysis," *IEEE Trans. Magn.*, in Press, 2015.

[2] Q. Tang, S. Guo, and Z. Wang, "Magnetic flux distribution in power transformer core with mitred joints," J. Appl. Phys., in Press, 2015.

- International Conference Contributions

[3] Q. Tang, S. Guo, and Z. Wang, "Magnetic flux distribution in power transformer core with mitred joints," presented at 59th Annual Magnetism & Magnetic Materials Conference. Honolulu, US, 2014.

[4] Q. Tang, P. Anderson, Z. Wang, P. Jarman, and A. Moses, "Measurement of electrical steels magnetic properties at very high flux densities using improved single sheet tester," in *18th International Symposium on High Voltage Engineering*, 2013, pp. 27–32.

[5] Q. Tang, Z. Wang, and P. Jarman, "Electrical steels and power transformer cores in deep saturation," in *International Conference on Condition Monitoring and Diagnosis*, 2012, pp. 1035–1038.

[6] Q. Tang, P. Anderson, Z. Wang, P. Jarman, and A. Moses, "Measuring electrical steels magnetic properties up to theoretical saturation limit using improved single sheet tester," presented at 6th UHVnet Colloquium. Glasgow, UK, 2013.

[7] Q. Tang, Z. Wang, P. Jarman, and A. Moses, "Performance of electrical steels and power transformer cores in deep saturation," presented at 2012 EuroDoble Colloquium. Manchester, UK, 2012.

References

[1] L. Bolduc, "GIC observations and studies in the Hydro-Qu{é}bec power system," *J. Atmos. Solar-Terrestrial Phys.*, vol. 64, no. 16, pp. 1793–1802, 2002.

[2] T. S. Molinski, "Why utilities respect geomagnetically induced currents," *J. Atmos. Solar-Terrestrial Phys.*, vol. 64, no. 16, pp. 1765–1778, 2002.

[3] ABB, *Transformer handbook*. Z{ü}rich: ABB Ltd., 2004.

[4] E. M. Carlini, G. Manduzio, and D. Bonmann, "Power Flow Control on the Italian network by means of phase-shifting transformers," in *CIGRE*, 2006.

[5] "Alstom Grid boosted by new Quadrature contract." Feb-2011.

[6] D. J. Fallon, P. M. Balma, W. J. McNutt, P. S. Electric, G. Company, and D. E. Company, *The destructive effects of geomagnetic induced currents in power transformers*. Doble Engineering Co., 1990.

[7] L. Shu-hua, "Origine de la boussole II. aimant et boussole," *Isis*, vol. 45, no. 2, p. 175, Jan. 1954.

[8] W. Gilbert and P. F. Mottelay, *De magnete*. New York: Dover Publications, 1958.

[9] D. Ball, "Maxwell's equations, part VII," *Spectroscopy*, vol. 27, no. 6, pp. 20 – 27, 2012.

[10] F. T. Ulaby, E. Michielssen, and U. Ravaioli, *Fundamentals of applied electromagnetics*. Boston: Prentice Hall, 2010.

[11] B. D. Cullity and C. D. Graham, *Introduction to Magnetic Materials*. Hoboken, NJ, USA: John Wiley & Sons, Inc., 2008.

[12] C. E. Webb, "The power losses in magnetic sheet material at high flux densities," *Electr. Eng. J. Inst.*, vol. 64, no. 352, pp. 409–427, 1926.

[13] F. Brailsford, "Investigation of the eddy-current anomaly in electrical sheet steels," *Electr. Eng. - Part I Gen. J. Inst.*, vol. 95, no. 88, pp. 175–177, 1948.

[14] M. J. Heathcote, *The J & P transformer book : a practical technology of the power transformer*. Amsterdam; London; Oxford: Elsevier ; Newnes, 2007.

[15] R. H. Pry and C. P. Bean, "Calculation of the energy loss in magnetic sheet materials using a domain model," *J. Appl. Phys.*, vol. 29, no. 3, pp. 532–533, 1958.

[16] J. W. Coltman, "The transformer [historical overview]," *Ind. Appl. Mag. IEEE*, vol. 8, no. 1, pp. 8–15, 2002.

[17] S. Tumański, "Handbook of magnetic measurements." CRC Press, Boca Raton, FL :, 2011.

[18] F. Brailsford and R. E. E. P. of the I. of Fogg, "Anomalous iron losses in cold-reduced grain-oriented transformer steel," in *Electrical Engineers, Proceedings of the Institution of*, 1964, pp. 1463–1467.

[19] A. J. Moses, B. Thomas, and J. Thompson, "Power loss and flux density distributions in the T-joint of a three phase transformer core," *Magn. IEEE Trans.*, vol. 8, no. 4, pp. 785–790, 1972.

[20] G. Bertotti, "General properties of power losses in soft ferromagnetic materials," *Magn. IEEE Trans.*, vol. 24, no. 1, pp. 621–630, 1988.

[21] T. Nakata, N. Takahashi, K. Fujiwara, and M. Nakano, "Measurement of magnetic characteristics along arbitrary directions of grain-oriented silicon steel up to high flux densities," *Magn. IEEE Trans.*, vol. 29, no. 6, pp. 3544–3546, 1993.

[22] F. Fiorillo and I. D. Mayergoyz, *Characterization and Measurement of Magnetic Materials*. Burlington: Elsevier, 2004.

[23] A. J. Moses, "Electrical steels: past, present and future developments," *Phys. Sci. Meas. Instrumentation, Manag. Educ. IEE Proc. A*, vol. 137, no. 5, pp. 233–245, 1990.

[24] J. H. Harlow, *Electric power transformer engineering : electric power engineering handbook*. Boca Raton, Fla.; London: CRC, 2007.

[25] J. A. Salsgiver, "A comparison of CGO silicon steels, high performance domain refined silicon steels and amorphous core materials in distribution transformers by Total Ownership Cost (TOC) modeling," *Phys. Scr.*, vol. 39, no. 6, p. 775, 1989.

[26] "Magnetic properties." [Online]. Available: www.aksteel.com. [Accessed: 17-Jan-2014].

[27] "Magnetic properties." [Online]. Available: www.thyssenkrupp.com. [Accessed: 17-Jan-2014].

[28] "Magnetic properties." [Online]. Available: www.jfe-steel.co.jp. [Accessed: 17-Jan-2014].

[29] "Magnetic properties." [Online]. Available: www.arcelormittal.com. [Accessed: 17-Jan-2014].

[30] "Magnetic properties." [Online]. Available: www.nssb.nssmc.com. [Accessed: 17-Jan-2014].

[31] "Magnetic properties." [Online]. Available: www.cogent-power.com. [Accessed: 17-Jan-2014].

[32] "Magnetic properties." [Online]. Available: www.posco.com. [Accessed: 17-Jan-2014].

[33] V. Sankar, "Preparation of transformer specifications," 2012.

[34] S. V Kulkarni and S. A. Khaparde, *Transformer engineering : design and practice*. New York: Marcel Dekker, Inc., 2004.

[35] "Transformer." [Online]. Available: http://www.energy.siemens.com/hq/en/power-transmission/transformers/. [Accessed: 19-Aug-2014].

[36] "Further processing hints." [Online]. Available: http://www.tkes.com/web2010/tkeswebcms.nsf/www/en_Anwendungshinweise_c.html. [Accessed: 19-Aug-2014].

[37] H. W. Kerr and S. Palmer, "Developments in the design of large power transformers," *Proc. Inst. Electr. Eng.*, vol. 111, no. 4, p. 823, 1964.

[38] R. M. Del Vecchio, *Transformer design principles : with applications to core-form power transformers*. Amsterdam: Gordon and Breach Science Publishers, 2001.

[39] M. Jones, A. J. Moses, and J. Thompson, "Flux distribution and power loss in the mitered overlap joint in power transformer cores," *Magn. IEEE Trans.*, vol. 9, no. 2, pp. 114–122, 1973.

[40] P. Jarman, P. Hynes, T. Bickley, A. Darwin, H. Hayward, and N. Thomas, "The specification and application of large quadrature boosters to restrict post-fault power flows," in *CIGRE*, 2006.

[41] C. A. Charalambous, Z. D. Wang, P. Jarman, and M. Osborne, "2-D finite-element electromagnetic analysis of an autotransformer experiencing ferroresonance," *Power Deliv. IEEE Trans.*, vol. 24, no. 3, pp. 1275–1283, 2009.

[42] J. G. Kappenman, "Geomagnetic storms and their impact on power systems," *Power Eng. Rev. IEEE*, vol. 16, no. 5, p. 5, 1996.

[43] J. Sievert, "The measurement of magnetic properties of electrical sheet steel - Survey on methods and situation of standards," *J. Magn. Magn. Mater.*, vol. 215–216, pp. 647–651, 2000.

[44] "Magnetic materials - part 2: methods of measurement of the magnetic properties of electrical steel sheet and strip by means of an epstein frame," 1996.

[45] T. L. Mthombeni, P. Pillay, and R. M. W. Strnat, "New Epstein frame for lamination core loss measurements under high frequencies and high flux densities," *Energy Conversion, IEEE Trans.*, vol. 22, no. 3, pp. 614–620, 2007.

[46] J. Sievert, "Determination of AC magnetic power loss of electrical steel sheet: Present status and trends," *Magn. IEEE Trans.*, vol. 20, no. 5, pp. 1702–1707, 1984.

[47] P. Marketos, S. Zurek, and A. J. Moses, "A method for defining the mean path length of the epstein frame," *IEEE Trans. Magn.*, vol. 43, no. 6, pp. 2755–2757, 2007.

[48] D. Dieterly, "DC Permeability Testing of Epstein Samples with Double-Lap Joints," *Symp. Magn. Mater.*, 1948.

[49] I. Daut, S. Hasan, S. Taib, R. Chan, and M. Irwanto, "Harmonic content as the indicator of transformer core saturation," in *2010 4th International Power Engineering and Optimization Conference (PEOCO)*, 2010, pp. 382–385.

[50] T. Yamamoto and Y. Ohya, "Single sheet tester for measuring core losses and permeabilities in a silicon steel sheet," *Magn. IEEE Trans.*, vol. 10, no. 2, pp. 157–159, 1974.

[51] K. Matsubara, T. Nakata, N. Takahashi, K. Fujiwara, and M. Nakano, "Effects of the overhang of a specimen on the accuracy of a single sheet tester," *Phys. Scr.*, vol. 40, no. 4, pp. 529–531, Oct. 1989.

[52] H. Ahlers, J. D. Sievert, and Q. -ch. QU, "Comparison of a single strip tester and Epstein frame measurements," *J. Magn. Magn. Mater.*, vol. 26, no. 1–3, pp. 176–178, Mar. 1982.

[53] "Magnetic materials - part 3: methods of measurement of the magnetic properties of electrical steel strip and sheet by means of a single sheet tester," IEC 60404-31992.

[54] H. Pfutzner and P. Schonhuber, "On the problem of the field detection for single sheet testers," *IEEE Trans. Magn.*, vol. 27, no. 2, pp. 778–785, Mar. 1991.

[55] S. Zurek, P. Marketos, T. Meydan, and A. J. Moses, "Use of novel adaptive digital feedback for magnetic measurements under controlled magnetizing conditions," *Magn. IEEE Trans.*, vol. 41, no. 11, pp. 4242–4249, 2005.

[56] N. Chatziilias, T. Meydan, and C. Porter, "Real time digital waveform control for magnetic testers," in *Journal of Magnetism and Magnetic Materials*, 2003, vol. 254–255, pp. 104–107.

[57] S. Baranowski, S. Tumański, and S. Zurek, "Comparison of digital methods of the control of flux density shape," *Przegląd Elektrotechniczny*, no. 1, pp. 93–95, 2009.

[58] E. A. Erdélyi, S. V Ahamed, and R. D. Burtness, "Flux distribution in saturated DC machines at no-Load," *Power Appar. Syst. IEEE Trans.*, vol. 84, no. 5, pp. 375–381, 1965.

[59] S. V Ahamed and E. A. Erdélyi, "Nonlinear theory of salient pole machines," *Power Appar. Syst. IEEE Trans.*, no. 1, pp. 61–70, 1966.

[60] J. Rivas, J. M. Zamarro, E. Martin, and C. Pereira, "Simple approximation for magnetization curves and hysteresis loops," *Magn. IEEE Trans.*, vol. 17, no. 4, pp. 1498–1502, 1981.

[61] S. Prusty and M. V. S. Rao, "New method for predetermination of true saturation characteristics of transformers and nonlinear reactors," in *IEE Proceedings C: Generation Transmission and Distribution*, 1980, pp. 106–110.

[62] G. F. T. Widger, "Representation of magnetisation curves over extensive range by rational-fraction approximations," in *Electrical Engineers, Proceedings of the Institution of*, 1969, pp. 156–160.

[63] D. C. Jiles, J. B. Thoelke, and M. K. Devine, "Numerical determination of hysteresis parameters for the modeling of magnetic properties using the theory of ferromagnetic hysteresis," *IEEE Trans. Magn.*, vol. 28, no. 1, pp. 27–35, 1992.

[64] M. S. Maklad and M. Fahmy, "An analytical investigation of a ferroresonant circuit," *Magn. IEEE Trans.*, vol. 16, no. 2, pp. 465–468, 1980.

[65] M. Le Floc'h, "Analytical expression of the first magnetization curve in soft magnetic polycrystalline materials," *J. Appl. Phys.*, vol. 67, no. 1, p. 405, 1990.

[66] F. Fiorillo, L. R. Dupre, C. Appino, and A. M. Rietto, "Comprehensive model of magnetization curve, hysteresis loops, and losses in any direction in grain-oriented Fe-Si," *Magn. IEEE Trans.*, vol. 38, no. 3, pp. 1467–1476, 2002.

[67] I. Mészáros and G. Vértesy, "Modelling of normal magnetization curves of soft magnetic alloys," *Mater. Sci. Forum*, vol. 659, pp. 429–434, Sep. 2010.

[68] F. H. Middleton, "Analytic hysteresis function," *J. Appl. Phys.*, vol. 32, no. 3, pp. S251–S252, 1961.

[69] M. K. El-Sherbiny, "Representation of the magnetization characteristic by a sum of exponentials," *Magn. IEEE Trans.*, vol. 9, no. 1, pp. 60–61, 1973.

[70] W. K. Macfadyen, R. R. S. Simpson, R. D. Slater, and W. S. Wood, "Representation of magnetisation curves by exponential series," in *Electrical Engineers, Proceedings of the Institution of*, 1973, pp. 902–904.

[71] J. W. Teape, R. R. S. Simpson, R. D. Slater, and W. S. Wood, "Representation of magnetic characteristic, including hysteresis, by exponential series," in *Electrical Engineers, Proceedings of the Institution of*, 1974, pp. 1019–1020.

[72] J. R. Brauer, "Simple equations for the magnetization and reluctivity curves of steel," *Magn. IEEE Trans.*, vol. 11, no. 1, p. 81, 1975.

[73] S. Prusty and M. V. S. Rao, "A direct piecewise linearized approach to convert rms saturation characteristic to instantaneous saturation curve," *Magn. IEEE Trans.*, vol. 16, no. 1, pp. 156–160, 1980.

[74] M. AKBABA, "A modified Froelich's type equation for accurate modeling of magnetising characteristic of magnetic cores," *Electr. Mach. Power Syst.*, vol. 19, no. 3, pp. 303–311, May 1991.

[75] M. Jaafar, V. Markovski, and M. Elleuch, "Modelling of the differential permeability and the initial magnetization curve for ferromagnetic materials," in *Industrial Technology, 2004. IEEE ICIT '04. 2004 IEEE International Conference on*, 2004, pp. 460–465.

[76] F. Trutt, E. Erdelyi, and R. Hopkins, "Representation of the magnetization characteristic of DC Machines for computer use," *IEEE Trans. Power Appar. Syst.*, vol. PAS-87, no. 3, pp. 665–669, Mar. 1968.

[77] Q. Wu, Z. Cui, and L. Li, "Research on application of interpolation and fitting method in magnetization curve numeralization," in *Intelligent Control and Information Processing (ICICIP), 2011 2nd International Conference on*, 2011, pp. 1076–1078.

[78] K. Fujiwara, T. Adachi, and N. Takahashi, "A proposal of finite-element analysis considering two-dimensional magnetic properties," *IEEE Trans. Magn.*, vol. 38, no. 2, pp. 889–892, Mar. 2002.

[79] J. G. Santesmases, J. Ayala, and A. H. Cachero, "Analytical approximation of dynamic hysteresis loop and its application to a series ferroresonant circuit," in *Electrical Engineers, Proceedings of the Institution of*, 1970, pp. 234–240.

[80] P. H. Huang and Y. S. Chang, "Qualitative modeling for magnetization curve," *J. Mar. Sci. Technol.*, vol. 8, no. 2, pp. 65–70, 2000.

[81] J. Fischer and H. Moser, "Die nachbildung von magnetisierungskurven durch einfache algebraische oder transzendente funktionen," *Arch. für Elektrotechnik*, vol. 42, no. 5, pp. 286–299, May 1956.

[82] W. H. Press, *Numerical Recipes in C: The Art of Scientific Computing*. Cambridge: Cambridge University Press, 1992.

[83] A. Christopoulos and M. J. Lew, "Beyond eyeballing: fitting models to experimental data," *Crit. Rev. Biochem. Mol. Biol.*, vol. 35, no. 5, pp. 359–391, 2000.

[84] GraphPad Software Inc., "Normality tests of residuals." [Online]. Available: http://www.graphpad.com/guides/prism/6/curve-fitting/index.htm?reg_diagnostics_tab_6_2.htm. [Accessed: 26-Nov-2014].

[85] R. B. D'Agostino, *Goodness-of-Fit-Techniques*. CRC Press, 1986.

[86] B. D. Cullity, *Introduction to magnetic materials*. London: Addison-Wesley.

[87] GraphPad Software Inc., "How standard errors and confidence intervals are computed." [Online]. Available: http://www.graphpad.com/guides/prism/6/curve-fitting/index.htm?reg_how_standard_errors_are_comput.htm.

[88] C. Zhiguang, N. Takahashi, B. Forghani, G. Gilbert, J. Zhang, L. Liu, Y. Fan, X. Zhang, Y. Du, J. Wang, and C. Jiao, "Analysis and Measurements of Iron Loss and Flux Inside Silicon Steel Laminations," *Magn. IEEE Trans.*, vol. 45, no. 3, pp. 1222–1225, 2009.

[89] M. Daniels, "Power from designer domains," *Phys. World*, pp. 33–36, 1988.

[90] C. P. Steinmetz, "On the Law of Hysteresis," *Trans. Am. Inst. Electr. Eng.*, vol. IX, no. 1, pp. 1–64, Jan. 1892.

[91] G. Bertotti, "Physical interpretation of eddy current losses in ferromagnetic materials. I. Theoretical considerations," *J. Appl. Phys.*, vol. 57, no. 6, p. 2110, Mar. 1985.

[92] G. Bertotti, "Physical interpretation of eddy current losses in ferromagnetic materials. II. Analysis of experimental results," *J. Appl. Phys.*, vol. 57, no. 6, p. 2118, Mar. 1985.

[93] F. Fiorillo and A. Novikov, "An improved approach to power losses in magnetic laminations under nonsinusoidal induction waveform," *Magn. IEEE Trans.*, vol. 26, no. 5, pp. 2904–2910, 1990.

[94] E. Barbisio, F. Fiorillo, and C. Ragusa, "Predicting loss in magnetic steels under arbitrary induction waveform and with minor hysteresis loops," *IEEE Trans. Magn.*, vol. 40, no. 4 I, pp. 1810–1819, 2004.

[95] C. Yicheng and P. Pillay, "An improved formula for lamination core loss calculations in machines operating with high frequency and high flux density excitation," in *Industry Applications Conference, 2002. 37th IAS Annual Meeting. Conference Record of the*, 2002, pp. 759–766 vol.2.

[96] D. M. Ionel, M. Popescu, S. J. Dellinger, T. J. E. Miller, R. J. Heideman, and M. I. McGilp, "On the variation with flux and frequency of the core loss coefficients in electrical machines," *IEEE Trans. Ind. Appl.*, vol. 42, no. 3, pp. 658–667, May 2006.

[97] D. C. Jiles and D. L. Atherton, "Theory of ferromagnetic hysteresis (invited)," *J. Appl. Phys.*, vol. 55, no. 6, pp. 2115–2120, 1984.

[98] D. C. Jiles and D. L. Atherton, "Theory of ferromagnetic hysteresis," *J. Magn. Magn. Mater.*, vol. 61, no. 1–2, pp. 48–60, 1986.

[99] a. P. S. Baghel and S. V. Kulkarni, "Parameter identification of the Jiles–Atherton hysteresis model using a hybrid technique," *IET Electr. Power Appl.*, vol. 6, no. 9, p. 689, 2012.

[100] P. R. Wilson, J. N. Ross, and A. D. Brown, "Simulation of magnetic component models in electric circuits including dynamic thermal effects," *IEEE Trans. Power Electron.*, vol. 17, no. 1, pp. 55–65, 2002.

[101] D. C. Jiles, "Frequency dependence of hysteresis curves in conducting magnetic materials," *J. Appl. Phys.*, vol. 76, pp. 5849–5855, 1994.

[102] J. V Leite, Vale, x, M. ncia Ferreira da Luz, N. Sadowski, and P. A. da Silva, "Modelling Dynamic Losses Under Rotational Magnetic Flux," *Magn. IEEE Trans.*, vol. 48, no. 2, pp. 895–898, 2012.

[103] A. P. S. Baghel and I. I. T. Bombay, "Modern Trends in Design and Manufacturing Practices of the Core in Power Transformers," in *5th International Conference on Large Power Transformers- Modern Trends in Applications, Installation, Operation and maintenance*, 2013.

[104] R. L. Stoll, *The analysis of eddy currents*. Oxford: Clarendon Press, 1974.

[105] F. E. E. J. of the I. of Brailsford, "Alternating Hysteresis Loss in Electrical Sheet Steels," *Electr. Eng. J. Inst.*, vol. 84, no. 507, pp. 399–407, 1939.

[106] K. Narita and T. Yamaguchi, "Rotational and alternating hysteresis losses in 4% silicon-iron single crystal with the {110} surface," *IEEE Trans. Magn.*, vol. 11, no. 6, pp. 1661–1666, Nov. 1975.

[107] A. Boglietti, A. Cavagnino, M. Lazzari, and M. Pastorelli, "Predicting iron losses in soft magnetic materials with arbitrary voltage supply: an engineering approach," *IEEE Trans. Magn.*, vol. 39, no. 2, pp. 981–989, Mar. 2003.

[108] G. Bertotti, *Hysteresis in magnetism : for physicists, materials scientists, and engineers*. San Diego: Academic, 1998.

[109] A. J. Moses, "Comparison of transformer loss prediction from computed and measured flux density distribution," *Magn. IEEE Trans.*, vol. 34, no. 4, pp. 1186–1188, 1998.

[110] Joslin, P. C., A. J. Moses, and J. E. Thompson, "Some aspects of effects of longitudinal and normal stress on power loss and flux distribution within a transformer core," *Electr. Eng. Proc. Inst.*, vol. 119, no. 6, pp. 709–716, 1972.

[111] A. J. Moses and B. Thomas, "Measurement of rotating flux in silicon iron laminations," *Magn. IEEE Trans.*, vol. 9, no. 4, pp. 651–654, 1973.

[112] M. Jones and A. J. Moses, "Comparison of the localized power loss and flux distribution in the butt and lap and mitred overlap corner configurations," *Magn. IEEE Trans.*, vol. 10, no. 2, pp. 321–326, 1974.

[113] A. J. Moses and B. Thomas, "The spatial variation of localized power loss in two practical transformer T-joints," *Magn. IEEE Trans.*, vol. 9, no. 4, pp. 655–659, 1973.

[114] G. E. Mechler and R. S. Girgis, "Magnetic flux distributions in transformer core joints," *Power Deliv. IEEE Trans.*, vol. 15, no. 1, pp. 198–203, 2000.

[115] E. G. teNyenhuis, R. S. Girgis, and G. F. Mechler, "Other factors contributing to the core loss performance of power and distribution transformers," *Power Deliv. IEEE Trans.*, vol. 16, no. 4, pp. 648–653, 2001.

[116] E. G. teNyenhuis, G. F. Mechler, and R. S. Girgis, "Flux distribution and core loss calculation for single phase and five limb three phase transformer core designs," *Power Deliv. IEEE Trans.*, vol. 15, no. 1, pp. 204–209, 2000.

[117] N. Hihat, E. Napieralska-Juszczak, J. Lecointe, J. K. Sykulski, and K. Komeza, "Equivalent Permeability of Step-Lap Joints of Transformer Cores: Computational and Experimental Considerations," *Magn. IEEE Trans.*, vol. 47, no. 1, pp. 244–251, 2011.

[118] I. Hernández, F. De León, J. M. Cañedo, and J. C. Olivares-Galván, "Modelling transformer core joints using Gaussian models for the magnetic flux density and permeability," *IET Electr. Power Appl.*, vol. 4, no. 9, pp. 761–771, 2010.

[119] Q. Tang, Z. D. Wang, and P. Jarman, "Electrical steels and power transformer cores in deep saturation," in *International Conference on Condition Monitoring and Diagnosis*, 2012, pp. 1035–1038.

[120] Q. Tang, Z. D. Wang, P. I. Anderson, and A. J. Moses, "Measurement of magnetic properties of electrical steels at high flux densities using an improved single sheet tester," in *18th International Symposium of High Voltage*, 2013.

[121] P. P. Silvester and R. L. (Ronald L. Ferrari, *Finite elements for electrical engineers*. Cambridge: Cambridge University Press, 1996.

[122] E. Becker, *Finite elements : an introduction*. Englewood Cliffs N.J.: Prentice Hall, 1981.

[123] Q. Du and D. Wang, "Recent progress in robust and quality Delaunay mesh generation," *J. Comput. Appl. Math.*, vol. 195, no. 1–2, pp. 8–23, Oct. 2006.

[124] K. Srasuay, A. Chumthong, and S. Ruangsinchaiwanich, "Mesh generation of FEM by ANN on iron-core transformer," pp. 1885–1890.

[125] C. W. Steele, *Numerical computation of electric and magnetic fields*. New York ; London: Chapman & Hall, 1997.

[126] F. Loffler, "Relevance of step-lap joints for magnetic characteristics of transformer cores," *IEE Proc. - Electr. Power Appl.*, vol. 142, no. 6, p. 371, 1995.

[127] R. Girgis and K. Vedante, "Effects of GIC on power transformers and power systems," in *PES T&D 2012*, 2012, pp. 1–8.

[128] G. F. Mechler and R. S. Girgis, "Calculation of spatial loss distribution in stacked power and distribution transformer cores," *Power Deliv. IEEE Trans.*, vol. 13, no. 2, pp. 532–537, 1998.

[129] P. R. Price, "Geomagnetically Induced Current Effects on Transformers," *Power Eng. Rev. IEEE*, vol. 22, no. 6, p. 62, 2002.

[130] N. Takasu, T. Oshi, F. Miyawaki, S. Saito, and Y. Fujiwara, "An experimental analysis of DC excitation of transformers by geomagnetically induced currents," *Power Deliv. IEEE Trans.*, vol. 9, no. 2, pp. 1173–1182, 1994.

[131] E. G. teNyenhuis, R. S. Girgis, G. F. Mechler, and Z. Gang, "Calculation of core hot-spot temperature in power and distribution transformers," *Power Deliv. IEEE Trans.*, vol. 17, no. 4, pp. 991–995, 2002.

[132] "IEC/IEEE Guide for the Application, Specification, and Testing of Phase-Shifting Transformers," *IEC 62032-2005 IEEE C57.135-2005*, pp. 1–50, 2005.